Mathematical Modelling of Circadian Signalling in *Arabidopsis*

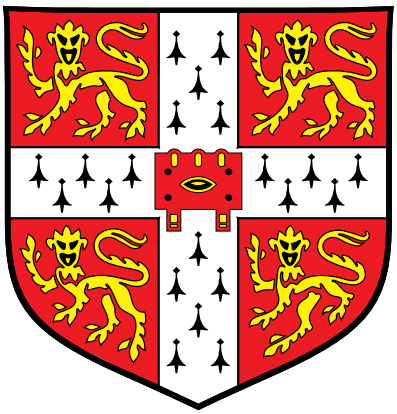

A dissertation submitted to the
University of Cambridge in partial
fulfilment of the requirements for the
degree of Doctor of Philosophy by

Neil Dalchau

Downing College, Cambridge

December 2008

Summary

Mathematical Modelling of Circadian Signalling in *Arabidopsis*
Neil Dalchau

The circadian signalling network in *Arabidopsis thaliana* generates oscillations with negative feedback loops of transcription factor binding, and regulates many developmental and physiological processes. Mathematical models have been proposed which describe the transcriptional and post-translational feedback loops generating oscillations, though do not incorporate the interactions with cytosolic messengers such as Ca^{2+} and cADPR, or with metabolites such as sucrose. The aim of this thesis is to use mathematical modelling to investigate how the circadian clock regulates $[Ca^{2+}]_{cyt}$, how a cADPR-based feedback loop modulates circadian oscillations, and also how the circadian clock perceives changes in the availability of sucrose. Delay linear systems of ordinary differential equations were used to demonstrate how $[Ca^{2+}]_{cyt}$ is co-regulated by two pathways operating on different timescales, the first dependent on the transcription factor *CIRCADIAN CLOCK ASSOCIATED 1* (*CCA1*), and a light/dark-dependent circadian clock-independent pathway. Simulated mutant analysis provided a potential role for the red-light sensing *PHYTOCHROME A* (*PHYA*) in the light-dependent pathway and offered predictions for the dynamics of $[Ca^{2+}]_{cyt}$ when system components are removed. A proposed feedback loop between the second messenger cADPR and the circadian clock was investigated *in silico* using a pairwise parameter perturbation method on mathematical models of the *Arabidopsis* central oscillator. Experimental observations from transient and persistent manipulations to cADPR synthesis could be explained with time-varying parametric perturbations to mathematical oscillator models representing the effects of cADPR on clock gene expression, supporting the hypothesised cADPR-based feedback loop. Finally, the dependency of circadian oscillations in darkness on exogenous sucrose availability was investigated using the *Three Loop model* of the circadian clock. Mathematical analyses and experimental validation demonstrated the involvement of *GIGANTEA* (*GI*) in the sucrose-sensing by the circadian clock, either by a transcriptional or post-translational mechanism. Further experimental evidence is presented supporting the hypothesis that sucrose up-regulates *GI* transcription. This thesis identifies components of the circadian clock which serve as entry or exit points for cytosolic signalling and metabolic pathways involved in key physiological processes, and demonstrates the use of mathematics to generate non-intuitive hypotheses for subsequent experimental validation in complex biological systems.

Acknowledgements

By undertaking this project, I was committing to learning an entire academic discipline from scratch. It is impossible to remember the many people who have explained biological principles to me during my time in Cambridge, though I thank each and every one of them. The enormity of this task would not have been possible without the patience and seemingly infinite enthusiasm of my supervisor, Dr. Alex Webb. I also applaud his ambition in combining the spheres of Biology and Engineering for the purpose of this project. I must also thank my second supervisor, Dr. Jorge Gonçalves, who provided stimulating discussions on the more mathematically rigorous considerations of mathematical modelling and control theory. Also from the engineering community, I am very grateful to Dr. Guy-Bart Stan, who in addition to critically reading my entire thesis has provided many interesting ideas to this project. I am also very grateful to most excellent Dr. Antony Dodd, with whom I had the pleasure of publishing an article in *Science*, and discussing a wealth of academic and completely non-academic topics. All of the other members of the Signal Transduction group contributed greatly to my scientific life over the last three years, particularly Leon Baek, Dr. Katharine Hubbard and Dr. Carlos Hotta. In particular, they have provided much of the data contained within this thesis, which has been used to great extent in the construction of mathematical models.

The majority of the funding for this project has come from the Biotechnology and Biological Sciences Research Council (BBSRC), to whom I am very grateful. Additional funding has come in the form of a studentship from Downing College in memory of Dr. John Treherne and a studentship from the Department of Plant Sciences in memory of Frank Smart.

On a personal level, I am eternally grateful to my fantastic parents who have supported me through the good and bad, with the provision of good food and liquidity (beer and otherwise). Also, my late grandmother Kathleen Dalchau, whose enthusiasm for numeracy sparked a love of mathematics which has never faltered. My sanity has been kept in check by my close friends Gordon Francis, Andrew Dreier, Dr. Fiona Robertson and Anuphon Laohavisit, the latter providing a competitive element to thesis submission and great Thai food. Finally, I am grateful to Dr. Katy Coxon for being a fantastic girlfriend, providing me with food, beer and money, and even for being an occasional dictionary of biological concepts.

Disclaimer

This dissertation does not exceed the word limit for the School of the Biological Sciences Degree Committee and is the result of my own work and includes nothing which is the outcome of work done in collaboration except where specifically indicated in the text. Parts of this dissertation are already published (Dodd *et al.*, 2007) but no part of it has been submitted to another qualification.

Table of Contents

List of Figures

List of Tables

List of Abbreviations

For ease of reference, this list of abbreviations has been separated into gene names and other abbreviations.

List of Gene Name Abbreviations

A	mathematical representation of *PRR7/9* in Locke *et al.* (2006)
AEQ	*AEQUORIN*
CAB2	*CHLOROPHYLL A/B BINDING PROTEIN 2*
CaM	*CALMODULIN*
CAS	*CALCIUM SENSOR*
CAT	*CATALASE* (*2* and *3*)
CCA1	*CIRCADIAN CLOCK ASSOCIATED 1*
CCL	*CCR-LIKE*
CCR	*COLD CIRCADIAN RHYTHM RNA BINDING* (*1* and *2*; *CCR2* is also *GRP8*, *CCR2* is also *GRP7*)
CK	*CASEIN KINASE* (*1* and *2*)
CML	*CALMODULIN-LIKE* (*23* and *24*)
CO	*CONSTANS*
CRY	*CRYPTOCHROME* (*1*, *2* and *3*)
CUL1	*CULLIN 1*
ELF	*EARLY FLOWERING* (*3* and *4*)
FIO1	*FIONA 1*
FKF1	*FLAVIN-BINDING, KELCH REPEAT, F-BOX 1*
FLC	*FLOWERING LOCUS C*
FT	*FLOWERING LOCUS T*
GI	*GIGANTEA*
GRP	*GLYCINE RICH PROTEIN* (*7* and *8*; *GRP7* is also *CCR2*, *GRP8* is also *CCR1*)
LHY	*LATE ELONGATED HYPOCOTYL*
LKP2	*LOV/KELCH PROTEIN 2*
LUC	*LUCIFERASE*

LUX	*LUX ARRHYTHMO* (also *PCL1*)
PCL1	*PHYTOCLOCK 1* (also *LUX*)
PHOT	*PHOTOTROPIN* (*1* and *2*)
PHY	*PHYTOCHROME* (*A*, *B*, *C*, *D* and *E*)
PIF3	*PHYTOCHROME INTERACTING FACTOR 3*
PRR	*PSEUDO RESPONSE REGULATOR* (*1*, *3*, *5*, *7* and *9*)
SFR6	*SENSITIVE TO FREEZING 6*
SKP1	*S-PHASE KINASE-ASSOCIATED PROTEIN 1*
SOC1	*SUPPRESSOR OF OVEREXPRESSION OF CONSTANS 1*
TIC	*TIME FOR COFFEE*
TOC1	*TIMING OF CAB2 EXPRESSION 1* (also *PRR1*)
X	hypothetical gene proposed by Locke *et al.* (2005b)
Y	hypothetical gene proposed by Locke *et al.* (2005b)
ZTL	*ZEITLUPE*

Other Abbreviations

35SCaMV	35S cauliflower mosaic virus promoter
ABA	abscisic acid
ABRE	ABA-responsive element
ADPRc	ADP-ribosyl cyclase
AIC	Akaike Information Criterion
AIC_c	second-order bias correction to AIC
BL	blue light
BRN	biochemical reaction network
$[Ca^{2+}]_{cyt}$	concentration of cytosolic-free Ca^{2+}
CaBP	Ca^{2+}-binding proteins
cADPR	cyclic adenosine diphosphate ribose
cAMP	3′, 5′-cyclic monophosphate
CBS	CCA1-binding site
CICR	calcium-induced calcium release
CONTSID	continuous time systems identification toolbox (for MATLAB^{TM})
CT	circadian time
DD	constant dark
EE	evening element
ER	endoplasmic reticulum
EtOH	ethanol
FOH	first-order hold
IP_3	inositol 1,4,5-triphosphate
L12/D12	12 h light, 12 h dark
L16/D8	16 h light, 8 h dark
L8/D16	8 h light, 16 h dark

LD	light-dark (no specific duration implied)
LED	light emitting diode
LL	constant light
LOV	Light, Oxygen and Voltage
LSQ	least-squares
LT	low temperature
LTI	linear time-invariant
ME	morning element
MeOH	methanol
MH	Metropolis Hastings
MIMO	multi-input multi-output
MS	Murashige and Skoog medium
MYB	V-Myb avian myeloblastosis viral oncogene
NAADP	nicotinic acid adenine dinucleotide phosphate
NaClO	sodium hypochlorite
NASC	Nottingham Arabidopsis Stock Centre
ODE	ordinary differential equation
PEM	prediction-error method
PI-PLC	phosphatidyl inositol-specific phospholipase C
PRC	phase response curve
QSSA	quasi steady state assumption
QTL	quantitative trait loci
RAE	relative amplitude error
RL	red light
RyR	ryanodine receptor
S1P	sphingosine 1-phosphate
SA	simulated annealing
SAM	shoot apical meristem
SCF	skp1/cullin/F-box
SCN	suprachiasmatic nucleus
SID	systems identification toolbox (for MATLAB^{TM})
SISO	single-input single-output
SPP	sucrose phosphate phosphatase
SPS	sucrose phosphate synthase
SR	sarcoplasmic reticulum
SUS	sucrose synthase
TAP	tandem affinity purification
XVE	17-β-estradiol-inducible chimeric transcription factor
WS	Wassilewskija
ZOH	zero-order hold
ZT	zeitgeber time (i.e. time after dawn)

CHAPTER 1

General Introduction

The majority of eukaryotes and some prokaryotes have a molecular mechanism to synchronize their physiology with changing light availability and temperature resulting from the rotation of the planet. This is an autonomous oscillator known as a circadian clock. The timing of many biochemical processes is controlled by the clock through a series of output pathways which originate from central clock components with different oscillation phases. In addition, the inter-phase relationship of clock components can vary according to the external photoperiod, enabling specific seasonal responses. Circadian clocks have evolved independently in cyanobacteria, plants, mammals and flies, leading to mechanisms with few common elements, though in all cases consist of interlocking feedback loops in transcriptional control (Young & Kay, 2001). In mammals, the suprachiasmatic nucleus (SCN) acts as a central pacemaker which co-ordinates peripheral tissues via entrainment* signals (Bartness *et al.*, 2001). The 'slave oscillators' in peripheral tissues also exhibit autonomous cellular oscillations, which synchronize via intercellular coupling to maintain a robust rhythm (Aton *et al.*, 2005). In plants, it is thought that all cells may sustain circadian rhythms (oscillations) independently, though it is speculated that more than one oscillator mechanism exists (McClung, 2001). Independent oscillators have been demonstrated by entraining different leaves to opposite phases, though the short duration of this experiment does not rule out weak intercellular coupling (Thain *et al.*, 2000). Possession

**Entrainment* is defined by Young & Kay (2001) as establishing the phase of a rhythm by providing an environmental signal, such as a light or temperature cycle, or a biological signal, such as a hormone pulse.

of a circadian clock confers major benefits when its natural frequency (or free-running period) is resonant with that of the external environment (Ouyang *et al.*, 1998; Dodd *et al.*, 2005b). In *Arabidopsis thaliana*, it was shown that seedlings whose free-running clock period was similar to the period of the environmental rhythm grew larger and produced more chlorophyll than when placed in an environmental with an alternative period; wild-type seedlings performed better in 24 h days over 20 h and 28 h days, while short-period mutants performed better in 20 h rhythms, and long-period mutants performed better in 28 h rhythms (Dodd *et al.*, 2005b).

1.1 The Circadian Clock in Plants

1.1.1 Circadian control of physiology

Plant circadian clock output pathways regulate a variety of physiological and biochemical processes, including photosynthesis, leaf movement, hypocotyl elongation, stomatal movement and circumnutation (Gardner *et al.*, 2006). Rhythmic control of these mechanisms enables optimisation of output with respective to the time of day, and also leads to competitive advantage (Dodd *et al.*, 2005b). While little is known about how temporal information is conferred to cell physiology, there are examples of circadian control at many developmental stages (Yakir *et al.*, 2007). In contrast to mammals which have a central pacemaker, plant circadian rhythms are thought to be cell autonomous, enabling circadian oscillations with different phases in different organs (Thain *et al.*, 2000). Furthermore, there are examples of periodic differences between different cells (Thain *et al.*, 2002), and different output pathways (Xu *et al.*, 2007), suggesting there are additional components present in some cells, or even the potential for multiple oscillators in plants.

The circadian clock appears to be signalling temporal information very early in the developmental life-cycle in many plant species, including downy birch (*Betula pubescens*), Lapland diapensia (*Diapensia lapponica*) and leatherleaf (*Chamaedaphne calyculata*), in which germination is controlled by day-length (Yakir *et al.*, 2007). In *Arabidopsis*, circadian gene expression is synchronized as seeds are imbibed, supporting the notion that there is a functional clock in seeds (Zhong *et al.*, 1998). Immediately after germination, hypocotyls extend in a circadian-clock-dependent manner, achieving maximal growth during the subjective evening and minimal growth in the subjcetive morning in constant light (LL; Dowson-Day & Millar, 1999). The posi-

tion of leafs and cotyledons also undergo circadian oscillations in many plants including *Arabidopsis*, in which movements are caused by alternating growth on the upper and lower lamina (Webb, 2003). Perhaps the best-characterized circadian-regulated developmental process however is the transition from vegetative to reproductive growth, or flowering time (Yakir *et al.*, 2007). Flowering time depends on the expression of *FLOWERING LOCUS T* (*FT*) and *SUPPRESSOR OF OVEREXPRESSION OF CONSTANS 1* (*SOC1*), which activate the floral identity genes in the shoot apical meristem (SAM; Imaizumi & Kay, 2006). Prior to inducing signals, the transcription factor *FLOWERING LOCUS C* (*FLC*) represses *FT* expression to maintain the plant in the vegetative phase (Hubbard, 2008). The regulation of *FT*, *SOC1* and *FLC* relies on four major pathways: the autonomous, vernalization, gibberellins and photoperiodic pathways (Boss *et al.*, 2004). The photoperiodic pathway culminates in the potentially indirect transcriptional activation of *FT* by *CONSTANS* (*CO*), which encodes a protein that is stabilised by red and blue light (Suárez-López *et al.*, 2001; Valverde *et al.*, 2004; Imaizumi & Kay, 2006). As *CO* is expressed between 12 and 24 hours after dawn (between *zeitgeber time*[†] 12 or ZT12 and ZT24), and CO protein will only accumulate during light, CO protein abundance is low in short days (8 h light, 16 h dark cycles) and high in long days (16 h light, 8 h dark cycles; Suárez-López *et al.*, 2001). Therefore, indirect *FT* activation by CO occurs more in long days than in short days, which enables photoperiodic control of the plants decision to flower.

Photosynthesis and carbon fixation are two of the most important cellular processes which occur during daylight hours, and are optimised by a circadian clock resonant with the external environment (Dodd *et al.*, 2005b). Microarray analysis demonstrated that a large number of genes involved in the light-harvesting reactions of photosynthesis are under circadian control; most of the 22 circadian-regulated photosynthesis genes peaked around *circadian time 4* (CT4[‡]; Harmer *et al.*, 2000). Photosynthesis results in the production of sugars, which are either consumed, stored, or transported to nonphotosynthetic tissues; genes involved in all processes which determine the fate of metabolic sugars are circadian-regulated (Harmer *et al.*, 2000). Starch mobilisation enzymes are also clock-controlled, indicating that the circadian clock is also involved in maintaining carbon homeostasis (Harmer *et al.*, 2000). At the single cell level, circadian rhythms can be observed in the opening and closing of stomata (pores in the leaf;

[†]*Zeitgeber* is German for time-giver, and refers to stimuli which entrain circadian clocks. The corresponding *zeitgeber* time (ZT) is the time since the last entrainment stimulus.

[‡]*Circadian time* is defined as the subjective time through a 'normal' 24 h day, in which 0 corresponds to subjective dawn.

Somers *et al.*, 1998b). In *Arabidopsis*, the stomatal conductance is higher in the subjective day than subjective night (Somers *et al.*, 1998b), and in *Vicia faba*, rhythmic responsiveness to red and blue light signals has been demonstrated (Gorton *et al.*, 1993). Finally, there are circadian oscillations in the concentration of cytosolic-free Ca^{2+} ($[Ca^{2+}]_{cyt}$; Johnson *et al.*, 1995; Love *et al.*, 2004).

1.1.2 Transcriptional feedback loops and essential central oscillator components in *Arabidopsis*

Significant progress in characterising the molecular mechanisms which generate and sustain oscillations has been made since the identification of the first circadian clock mutants in *Arabidopsis* by (Millar *et al.*, 1995), in which *TIMING OF CHLOROPHYLL A/B BINDING PROTEIN 1/PSEUDO RESPONSE REGULATOR 1* (*TOC1/PRR1*) was identified as an important component. The *toc1*-1 mutation had oscillations in the expression of *CHLOROPHYLL A/B BINDING PROTEIN 2* (*CAB2*) and the movement of primary leaves with a short circadian period[§], indicating *TOC1* to be an important gene in circadian rhythm generation (Millar *et al.*, 1995).

Circadian oscillations are generated by networks of interlocking positive and negative transcriptional feedback control loops (Figure 1.1). The first feedback loop identified involved *CIRCADIAN CLOCK ASSOCIATED 1* (*CCA1*), *LATE ELONGATED HYPOCOTYL* (*LHY*) and *TOC1/PRR1* (Alabadí *et al.*, 2001). *CCA1* and *LHY* encode light-induced MYB-like transcription factors which are expressed in peak abundance around ZT2 (Wang & Tobin, 1998; Schaffer *et al.*, 1998). *TOC1* expression is inhibited by the binding of CCA1/LHY heterodimers to a conserved motif called the evening element (EE; AAATATCT) present in the promoter region of many clock-associated genes, including *TOC1* (Harmer *et al.*, 2000; Alabadí *et al.*, 2001). As CCA1/LHY levels drop during the subjective day, *TOC1* expression increases, and is most highly expressed in the latter part of the subjective day (near ZT12; Alabadí *et al.*, 2001). To complete the loop, TOC1 indirectly activates *CCA1/LHY*, as demonstrated by the decreased expression levels of *CCA1/LHY* in the recessive loss-of-function *toc1*-2 mutant (Alabadí *et al.*, 2001). High constitutive expression of *CCA1* or *LHY* leads to constant low levels of *TOC1*, and abolishes circadian oscillations in LL (Wang & Tobin, 1998; Schaffer *et al.*, 1998; Alabadí *et al.*,

[§]The term *circadian period* will be used throughout this thesis, and refers to the oscillation period in constant light, unless otherwise stated. The term *short period* is used to describe circadian oscillations with a period less than the wild-type oscillation of approximately 24 h, and correspondingly for *long period* rhythms.

2001). As circadian oscillations persist in the *toc1*-2 mutant, the *CCA1/LHY-TOC1* negative feedback loop is not the only loop capable of generating oscillations, a notion further demonstrated by the short period oscillations in *cca1*, *lhy*, and *cca1 lhy* loss-of-function mutants (Alabadí *et al.*, 2001, 2002).

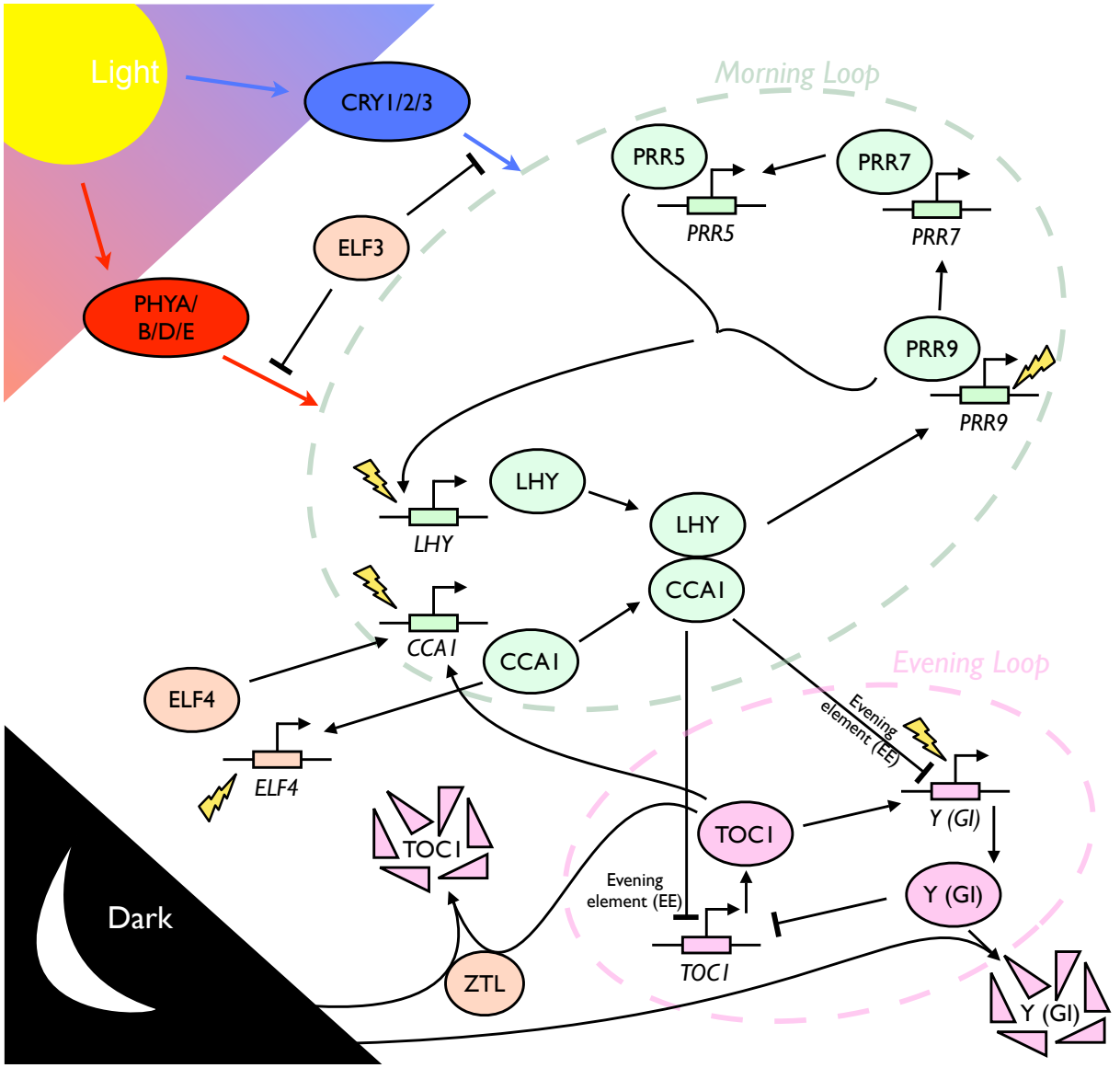

Figure 1.1: A transcriptional/post-translational network describes the *Arabidopsis* circadian clock. The known molecular interactions in the *Arabidopsis* circadian clock may be classified into a 'morning loop' (components represented by light green symbols), an 'evening loop' (pink symbols), red and blue light input pathways, and additional interacting components (peach symbols; see Gardner *et al.*, 2006 for a review). Proteins represented by ovals and mRNA/promoters by box-arrow symbol. Positive influences between components represented by arrows (→) and negative influences by straight line arrows (⊣). Transient light activation represented by crooked yellow arrow. Broken TOC1 and Y (GI) protein symbols represent dark-induced proteolysis.

TOC1/PRR1 belongs to a five gene family of pseudo response regulators which additionally includes *PRR3, 5, 7, & 9* (Michael & McClung, 2003; Mizuno & Nakamichi, 2005; Farré *et al.*,

2005; Nakamichi *et al.*, 2005b; Salomé & McClung, 2005a). The time of peak abundance of these transcripts forms a wave of expression (*PRR9–PRR7–PRR5–PRR3–TOC1/PRR1*) which appears to be positively regulated by *CCA1/LHY* (Mizuno & Nakamichi, 2005). However, mutant analyses have shown that the interconnectivity of these components in not a simple cascade. Loss of function mutants *prr7*-3 and *prr9*-1 have slightly long periods, while *prr7*-3 *prr9*-1 double mutants have periods 6 h longer than wild-type, suggesting there is a degree of redundancy between these two components (Farré *et al.*, 2005; Mizuno & Nakamichi, 2005; Nakamichi *et al.*, 2005b; Salomé & McClung, 2005b). Pseudo response regulators 3 and 5 have an opposite effect on circadian period to *PRR7/9*, as single loss-of-function *prr3*-1 and *prr5*-3 mutants have slightly short periods and *prr3*-1 *prr5*-3 double mutants have a 4 h period reduction (Nakamichi *et al.*, 2005b,a; Salomé & McClung, 2005b). The *prr5*-11 *prr7*-3 *prr9*-1 triple mutant is arrhythmic in LL and DD demonstrating the necessity of the pseudo response regulators in the central oscillator mechanism (Nakamichi *et al.*, 2005b).

A few additional components of the *Arabidopsis* central oscillator have been described as being essential for circadian rhythmicity, such as *LUX ARRHYTHMO/PHYTOCLOCK1* (*LUX/PCL1*), *EARLY FLOWERING 3* and *4* (*ELF3/4*). *LUX* encodes an evening-phased putative Myb-like transcription factor, and has an EE motif in its promoter which is bound by CCA1 and LHY *in vitro* (Hazen *et al.*, 2005; Onai & Ishiura, 2005). *lux*-1 mutants are arrhythmic in LL, while high constitutive expression of *LUX* causes rapid dampening of oscillations in LL and DD after transfer from entrained cycles (Hazen *et al.*, 2005; Onai & Ishiura, 2005). *ELF4* has been proposed to form another feedback with the central oscillator, as light-induced expression of *ELF4* requires CCA1/LHY, while light-induced *CCA1/LHY* expression requires ELF4 (Kikis *et al.*, 2005). *elf4* mutants are arrhythmic in LL, while over-expression of *ELF4* increases circadian period (Doyle *et al.*, 2002; McWatters *et al.*, 2007). *ELF3* negatively regulates light input to the central oscillator, enabling a gated[¶] response to light at different times of day (Covington *et al.*, 2001). *ELF3* encodes a PHYTOCHROME B (PHYB)-interacting protein which peaks in expression during the subjective night, presumably to repress aberrant light resetting of the central oscillator (Covington *et al.*, 2001; Liu *et al.*, 2001). The *elf3*-1 mutant has no detectable oscillations in the expression of classical clock markers *CAB2* and *COLD CIRCADIAN RHYTHM*

[¶]The *gating* hypothesis was proposed by Kay & Millar (1992) to explain how *CAB* gene induction by phytochrome depends on the time of day, enabling transcription during the subjective morning (CT0) and suppressing transcription after CT8. It is the circadian clock that enables this rhythmic responsiveness to regulatory signals.

RNA BINDING 2/GLYCINE RICH PROTEIN 7 (*CCR2/GRP7*) in LL, though oscillations in DD are unaffected (McWatters *et al.*, 2000).

In recent publications, further genes have been found which disrupt circadian rhythms. These include *FIONA 1* (*FIO1*), for which loss-of-function mutants (*fio1*-1) have increased circadian periods (Kim *et al.*, 2008b), and *TIME FOR COFFEE* (*TIC*), for which a severe low amplitude of circadian oscillations is present in *tic*-1 mutants (Hall *et al.*, 2003; Ding *et al.*, 2007). However, these have so far not been positioned within the *Arabidopsis* circadian network.

1.1.3 Mathematical models of the *Arabidopsis* circadian clock

The architecture of circadian clocks is complex, comprising multiple interlocking loops of transcriptional feedback and protein turnover which interact with small molecules and metabolites (Imaizumi *et al.*, 2007). The constituent components can be approximately classified into three basic elements: input pathways whose primary role is to transduce information from the external environment, a central oscillator which maintains oscillations in the absence of external stimuli, and output pathways which control physiology (Dunlap, 1999). However, there is significant crosstalk between all three elements; input pathways are gated by the central oscillator, output pathways can feed back to fine tune clock function, and external signals also contribute to the control of circadian-regulated processes directly. Due to the complex interconnected nature of circadian clocks, and the autonomous oscillatory properties, there has been significant interest from mathematicians. Mathematical models of varying complexity have been derived in many species (Goldbeter, 1995; Leloup *et al.*, 1999; Ueda *et al.*, 2001; Leloup & Goldbeter, 2003; Forger & Peskin, 2003; Locke *et al.*, 2005a,b, 2006; Zeilinger *et al.*, 2006), and have led to the prediction of new components and the uncovering of design principles behind circadian clocks (Locke *et al.*, 2006; Rand *et al.*, 2006).

Mathematical modelling has assisted the identification and positioning of further components in the *Arabidopsis* circadian network which are essential for accurate time-keeping (Locke *et al.*, 2005a,b, 2006; Zeilinger *et al.*, 2006). The first *Arabidopsis* clock model was based on the basic *CCA1/LHY-TOC1* negative feedback loop (Locke *et al.*, 2005a), though was extended to account for the short-period rhythms in *toc1*-1 mutants soon after (Locke *et al.*, 2005b). Two hypothetical genes (X and Y) were incorporated into an *Interlocked Feedback Loop Model* which enabled good agreement between the oscillation phase of *CCA1/LHY* and *TOC1*, and accu-

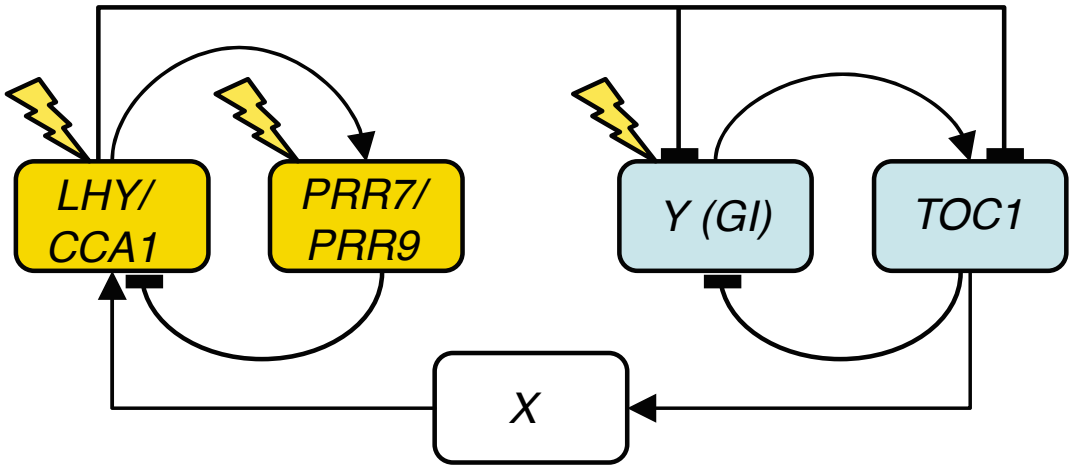

Figure 1.2: The *Three Loop model* of the *Arabidopsis* circadian clock.
Schematic representation of the molecular mechanisms which comprise a three loop mathematical model (Locke *et al.*, 2006). *LHY* and *CCA1* are represented by a single component gene, and similarly for *PRR7/9*. *LHY/CCA1* and *PRR7/9* form the 'morning loop', while *TOC1* and *Y* (*GI*) form the 'evening loop'.

rately predicted the period phenotypes of circadian clock mutants (Locke *et al.*, 2005b). *X* was incorporated as the missing link for indirect TOC1 activation of *CCA1/LHY* transcription. To account for experimental observations in wild-type and *cca1 lhy* double mutants, the *CCA1/LHY*-repressed *Y* gene was required to be both light-inducible and expressed in the late evening, leading to a biphasic expression pattern in light-dark (LD) cycles. Consequently, light-activated transcription of *Y* was increased in the simulated *cca1 lhy* double mutant. By comparing the simulated expression profiles of *Y* with wild-type and *cca1 lhy* double mutant expression data for known circadian-regulated transcripts, *GIGANTEA* (*GI*) was identified as a putative central oscillator component (Locke *et al.*, 2005b). Construction of a *cca1 lhy gi* triple loss-of-function mutant provided experimental evidence that *GI* contributes at least 70% of the function of *Y* (Locke *et al.*, 2006). *GI* had already been established as a circadian-regulated gene which encodes a nuclear-localised protein, is essential for photoperiodic control of flowering time and contains an EE in its promoter (Fowler *et al.*, 1999; Park *et al.*, 1999; Harmer *et al.*, 2000; Huq *et al.*, 2000; Mizoguchi *et al.*, 2005). In *gi* loss of function mutants, the period of oscillation is reduced in LL, and oscillations are abolished in constant dark (DD; Mizoguchi *et al.*, 2005).

Extensions to the *Interlocked Feedback Loop Model* have incorporated the proposed feedback loop between the light-inducible *PRR7 & 9* and *CCA1/LHY* (Figure 1.2; Locke *et al.*, 2006; Zeilinger *et al.*, 2006; Michael & McClung, 2003; Farré *et al.*, 2005). Locke *et al.* (2006) describe a *Three Loop Model* comprising the 'morning loop' (*CCA1/LHY-PRR7/9*), the 'evening loop' (*Y/GI-*

TOC1) and the connecting *CCA1/LHY-X-TOC1* loop. The *PRR7/9* component was added to the network to provide a feedback loop capable of generating circadian oscillations in *toc1*-2 loss-of-function mutants, but also reflect the circadian period phenotypes of mutations to *PRR7* and/or *PRR9* (Locke *et al.*, 2006).

1.1.4 Molecular mechanisms of circadian control

Transcriptional control is probably the best described mode of circadian regulation; as much as 36% of the *Arabidopsis* genome is under circadian control (Harmer *et al.*, 2000; Schaffer *et al.*, 2001; Michael & McClung, 2003; Edwards *et al.*, 2006), and it has been suggested that the transcription factors *CCA1* and *LHY* are central to transcriptional regulation by the clock (Yakir *et al.*, 2007). CCA1 and LHY bind to the EE *in vitro* (Alabadí *et al.*, 2001; Hazen *et al.*, 2005; Harmer & Kay, 2005), a conserved promoter element motif which is over-represented in clock-controlled genes that show peak expression at the end of the subjective day (Harmer *et al.*, 2000). Construction of an artificial promoter comprising four tandem repeats of the EE and a *LUCIFERASE* (*LUC*) bioluminescent reporter demonstrated that the EE is necessary and sufficient to confer evening-phased circadian regulation (Harmer & Kay, 2005). In contrast, there are evening-phased genes which do not have EEs in their promoters, and EEs are also present in the promoters of some morning-phased genes (Harmer *et al.*, 2000). Another conserved motif which differs from the EE by only one base pair is the CCA1-binding site (CBS) sequence (AAAAATCT), which is present in the *CAB1* promoter, but not over-represented in circadian-regulated genes (Wang *et al.*, 1997; Michael & McClung, 2002). However, changing the EE to a CBS motif by site-directed mutagenesis has shown contradictory results, as peak expression of *CCR2* remains unaltered (Harmer & Kay, 2005), while *CATALASE 3* (*CAT3*) is expressed in anti-phase (Michael & McClung, 2002). These results suggest there might be further elements in the *CAT3* promoter required for phase determination in the circadian system. A 'morning element' (ME; AACCACGAAAAT) has been speculated to have a role in phase determination through binding of an unknown transcriptional activator (Harmer & Kay, 2005). There are also motifs such as the light-activation sequence G-box (CCACGTGG) and HEX (TGACGTGG) elements which may play a role, though this has not been verified (Edwards *et al.*, 2006; Michael & McClung, 2003; Hudson & Quail, 2003).

The circadian clock can also exert post-transcriptional control (Yakir *et al.*, 2007). *CCR2*

is a clock-regulated RNA binding protein which regulates the splicing of its own transcript and of the related *COLD CIRCADIAN RHYTHM RNA BINDING 1/GLYCINE RICH PROTEIN 8* (*CCR1/GRP8*; Heintzen *et al.*, 1997; Staiger & Apel, 1999; Staiger *et al.*, 2003). CCR2 binds to the 3'-untranslated region of *CCR1/2* transcripts, favouring alternative splicing of truncated versions of both transcripts, which are unstable and degrade quickly (Staiger *et al.*, 2003). This amounts to an effective negative feedback loop which prevents CCR1/2 from accumulating unchecked. Transcript stability is also subject to circadian control in *CCR-LIKE* (*CCL*) and *SENESCENCE ASSOCIATED GENE 1* (*SEN1*), which have a longer half-life in the morning than afternoon in LL (Lidder *et al.*, 2005).

Post-translational mechanisms add another level of complexity to the function of circadian clocks and are integral for circadian oscillations in protein abundance (Daniel *et al.*, 2004; Dunlap, 1999). The protein kinase CK2 can phosphorylate *CCA1 in vitro*, and is important for normal functioning of the *Arabidopsis* central oscillator (Sugano *et al.*, 1998; Daniel *et al.*, 2004). CK1 and CK2 also phosphorylate at least one protein in the circadian networks of *Drosophila melanogaster*, cyanobacteria, *Neurospora crassa* and mammals, an event which commonly precedes targeting for proteasomal degradation (Gardner *et al.*, 2006). The ubiquitination of the phosphorylated protein is mediated by a conserved ubiquitin ligase complex known as the SCF [Skp1 (S-phase kinase-associated protein 1)/cullin/F-box] complex (Deshaies, 1999). An example of SCF-mediated ubiquitination is found in the *Arabidopsis* circadian clock, in which the F-box protein ZEITLUPE (ZTL) and the related LOV (Light, Oxygen and Voltage)/KELCH PROTEIN 2 (LKP2) target TOC1 protein for degradation (Más *et al.*, 2003b). The importance of the SCF^{ZTL} complex in TOC1 degradation has been demonstrated further by the characterisation of CULLIN 1 (CUL1), as *cul1* loss-of-function mutants have a lengthened circadian period similar to of *ztl* mutants (Harmon *et al.*, 2008; Más *et al.*, 2003b). The LOV domain present in ZTL and LKP2 is similar to the chromophore-binding domain in PHOTOTROPIN (PHOT) photoreceptors, and facilitates a light-induced conformational change which confers dark-dependent degradation of TOC1 (Mizoguchi & Coupland, 2000; Imaizumi *et al.*, 2003). The dark-dependency of TOC1 protein degradation is reflected in all mathematical models of the *Arabidopsis* circadian clock, through an increased rate of degradation in darkness (Locke *et al.*, 2005a,b, 2006; Zeilinger *et al.*, 2006). Another protein containing a LOV domain is FLAVIN-BINDING, KELCH REPEAT, F-BOX (FKF1), which interacts with GI to regulate the expression

of *CONSTANS* in a blue-light dependent manner, contributing to the photoperiodic control of flowering time (Sawa *et al.*, 2007). GI also interacts with ZTL in a blue light-dependent manner, leading to the stabilisation of both proteins (Kim *et al.*, 2007b). GI undergoes a dark-induced proteolysis by the 26S proteasome (N.B. This particular dark-dependent proteolysis mechanism has so far not been incorporated into mathematical models of the *Arabidopsis* circadian clock; David *et al.*, 2006). Therefore, interplay between light signalling and the formation of protein complexes appears to confer photoperiod-dependent regulation of output pathways while additionally regulating central oscillator function.

1.1.5 Input pathways and entrainment

To prevent deviations from a 24 h period accumulating and leading to desynchrony with the external environment, a resetting mechanism shifts the phase of the clock in response to environmental cues. This is known as entrainment. The transition from dark to light at dawn is thought to be the principal entrainment signal in plants (Devlin, 2002). The phase change resulting from a pulse of light is intimately linked to the subjective time it is applied. The resulting phase response curve (PRC) may be plotted, which typically shows phase advances prior to dawn, phase delays after dusk, and invariance during the subjective day (Devlin, 2002). To protect the clock from aberrant environmental light pulses such as lightning flashes, a prolonged period of irradiation is required for entrainment (Nelson & Takahashi, 1991).

Light input to the central oscillator

Photoreception by the *Arabidopsis* circadian clock is mediated by the red-light sensing *PHYTOCHROMES* (*PHY*) *A*, *B*, *D* and *E*, and the blue-light sensing *CRYPTOCHROMES* (*CRY*) *1* and *2* (Somers *et al.*, 2000; Devlin & Kay, 2000). Under low fluence rates of monochromatic red light (RL) or blue light (BL), *phyA* null mutants have an altered circadian period of *CAB2* expression, whereas *phyB* null mutants have altered circadian periods in high-fluence-rate RL (Somers *et al.*, 1998a; Devlin, 2002). *phyA phyB* double mutants have long circadian periods in all fluence rates of RL and low-fluence-rate BL. Conversely, *cry1 cry2* double mutants have long circadian periods in all fluence rates of BL and low fluences of RL, indicating there is some cross-talk between PHYs and CRYs in red- and blue-light responses (Somers *et al.*, 1998a; Devlin & Kay, 2000). The RL sensitivity of *PHYD* and *PHYE* shows partial redundancy with *PHYA*

and *PHYB*, as monogenic *phyD* and *phyE* mutants have wild-type periods, but polygenic *phyA phyB phyD* and *phyA phyB phyE* mutants have longer periods than wild-type and *phyA phyB* plants in RL (Devlin & Kay, 2000; Devlin, 2002). Red-light responses observed in *phyA phyB phyD* and *phyA phyB phyE* have been speculated to be attributable to *PHYC*, though this has not been demonstrated experimentally (Devlin & Kay, 2000; Devlin, 2002). A third photoreceptor family, *PHOTOTROPINS* (*PHOT*), mediate blue light responses in stomatal movements, though there is no evidence for a role in BL input pathways to the clock (Salomé & McClung, 2005b).

While the PHY and CRY photoreceptor families act as inputs to the clock, they are also rhythmic outputs, as their expression oscillates in LL and DD (Tóth *et al.*, 2001). By measuring the luminescence emitted from plants expressing *LUCIFERASE* (*LUC*) under the control of promoters from photoreceptors, the circadian oscillations in photoreceptor expression was analysed (Tóth *et al.*, 2001). *PHYC* was maximally expressed at dawn, followed by *PHYD* and *PHYE* at ZT2, *PHYB*, *CRY1* and *CAB2* at ZT6, and *PHYA* and *CRY2* at ZT10. While transcripts of all PHYs and CRYs have circadian oscillations, only PHYA, PHYB and PHYC appear to oscillate at the protein level (Harmer *et al.*, 2000; Bognár *et al.*, 1999; Hall *et al.*, 2001; Sharrock & Clack, 2002).

The contribution of red- and blue-light photoreceptors to accurate clock function has been well studied, though the pathways through which light is transduced to the central oscillator remain largely unknown. Light has been demonstrated to up-regulate transcription of *CCA1/LHY*, *GI*, *ELF4* and *PRR9* (Wang & Tobin, 1998; Martínez-García *et al.*, 2000; Kim *et al.*, 2003; Farré *et al.*, 2005; Kikis *et al.*, 2005). There is also light/dark-dependent proteolysis of clock proteins by the 26S proteasome (Más *et al.*, 2003b; David *et al.*, 2006). A component important for mediating phytochrome modulation of the circadian clock is the basic helix-loop-helix transcription factor *PHYTOCHROME INTERACTING FACTOR 3* (*PIF3*) which interacts with PHYA and PHYB (Ni *et al.*, 1998). *PIF3* binds specifically to a G-box DNA-sequence motif present in various light-regulated gene promoters, including *LHY* and *CCA1* (Ni *et al.*, 1999; Martínez-García *et al.*, 2000). PIF3 reversibly binds the far-red (active) form of PHYB (PfrB), acting as an entry point for phytochrome induction of G-box-containing promoters (Ni *et al.*, 1999; Martínez-García *et al.*, 2000). There is also an interaction between *PIF3* and PHYA, though this is less well characterised (Ni *et al.*, 1999). More recently, it has been found that PIF3 is

rapidly phosphorylated by PHYA and PHYB, tagging the protein for proteosomal degradation (Al-Sady *et al.*, 2006).

The dynamics of PIF3 abundance was the basis for the light input pathway in mathematical models of the *Arabidopsis* circadian clock, in which *LHY/CCA1*, *PRR7/9* and *Y* (*GI*) are transiently induced by light (Locke *et al.*, 2005a,b, 2006; Zeilinger *et al.*, 2006). For transient light activation, both light and the presence of a PIF3-like protein ($P^{(n)}$; see Appendix A) are required. Only during the early part of the light period – after a transition from darkness – will $P^{(n)}$ be present, during which time it will be degrading quickly. In this way, the coincidence of light and $P^{(n)}$ generates a transient light activation which is additionally capable of entrainment *in silico* (Locke *et al.*, 2005a).

Temperature perception

The circadian clock can also be entrained to temperature cycles (thermocycles), in which the subjective day and night temperatures differ by at least 4°C (Gardner *et al.*, 2006). The involvement of *PRR7* and *PRR9* is probable, as *prr7 prr9* double mutants fail to entrain to 22°C/18°C thermocycles (Salomé & McClung, 2005a,b). However, little else is known about the molecular mechanisms which underpin temperature entrainment (Gardner *et al.*, 2006).

Despite the Q_{10} law (the rate of a biochemical reaction approximately doubles as temperature increases by 10°C within a physiological range), circadian period remains stable over a wide range of temperatures. Therefore, a mechanism must exist which enables an adaptation in clock gene expression over varying temperatures to maintain a stable near 24 h circadian period. This property of circadian clocks is pervasive across the eukaryotic kingdoms and is known as temperature compensation (Pittendrigh, 1954). Natural allelic variations in *Arabidopsis* accessions have been analysed for their contribution to measurable polygenic traits such as oscillation period and amplitude at different temperatures, based on Quantitative Trait Loci (QTL) analysis (Edwards *et al.*, 2005). QTL analysis for period and amplitude of leaf movement rhythms identified the flowering-time gene *GI*, the F-box protein *ZTL* and the transcripion factor *FLC* as candidates for temperature-responsive QTL (Edwards *et al.*, 2005). A follow-up study identified *flc* mutants to have significant circadian period phenotypes at 27°C, but not at other temperatures, indicating a role for *FLC* in temperature compensation (Edwards *et al.*, 2006). A Bayesian clustering method identified the expression of *LUX* to coincide

with temperature-dependent circadian period, and mathematical simulations suggest that the change in *LUX* mRNA levels are sufficient to cause the period phenotype of *flc* mutants (Edwards *et al.*, 2006). Further mathematical modelling has indicated that the balance between the expression of *LHY/CCA1* and evening-expressed genes such as *GI* and *LUX* can largely account for the temperature-specific phenotypes observed in *gi* loss of function mutants (Gould *et al.*, 2006).

1.2 Calcium Signalling

Ca^{2+} is a ubiquitous second messenger, which transduces both intercellular and intracellular signals in plants and mammals (Sanders *et al.*, 2002; Berridge *et al.*, 2003). Changes in the concentration of cytosolic-free Ca^{2+} ($[Ca^{2+}]_{cyt}$) are thought to encode information, which are perceived by downstream targets, or Ca^{2+}-binding proteins (CaBP). Stimulus-induced Ca^{2+} signalling generally results in transient elevations or short-period oscillations (Berridge *et al.*, 2003; Hetherington & Brownlee, 2004). Resting levels of $[Ca^{2+}]_{cyt}$ also oscillate with a circadian rhythm in *Arabidopsis*, *Nicotiana plumbaginifolia* and SCN neurons (Johnson *et al.*, 1995; Ikeda *et al.*, 2003). A proposed cytosolic feedback loop for the core circadian oscillator mechanism involving $[Ca^{2+}]_{cyt}$ is an emerging theme in the study of both mammal and plant cells, and demonstrates the temporal flexibility in addition to the already established spatial flexibility of Ca^{2+} as a second messenger (Dodd *et al.*, 2007; Harrisingh *et al.*, 2007; Harrisingh & Nitabach, 2008). While the position and physiological role of $[Ca^{2+}]_{cyt}$ in circadian networks remains largely unknown, due to the link with the transduction of environmental signals an appealing hypothesis is that $[Ca^{2+}]_{cyt}$ is involved in environmental sensing by circadian clocks through feedback regulation of clock gene expression.

1.2.1 Generation of $[Ca^{2+}]_{cyt}$ gradients

Ca^{2+} is maintained at low concentrations in the cytosol ($\sim$100 nM) relative to internal stores and the extracellular space ($\sim$10 mM) because Ca^{2+} is cytotoxic. The maintenance of a safe concentration is known as calcium homeostasis. Transient elevations in $[Ca^{2+}]_{cyt}$ result from the release of Ca^{2+} from internal organelles, such as the endoplasmic reticulum (ER), the vacuole (in plant cells) and the sarcoplasmic reticulum (SR; in mammalian muscle cells), or influx from the external medium (Berridge *et al.*, 2003), and result in an order of magnitude increase

in $[Ca^{2+}]_{cyt}$ before Ca^{2+} is pumped back out of the cytosol. A well-characterised Ca^{2+}-signalling system in plants is the control of stomatal closure in guard cells by ABA, which induces oscillations of $[Ca^{2+}]_{cyt}$, the frequency of which determine the stomatal aperture (Allen *et al.*, 2001; Hetherington & Brownlee, 2004). ABA induces production of secondary messengers which stimulate Ca^{2+} release from the ER and vacuole, or across the plasma membrane. Microinjection of the second messenger cyclic adenosine diphosphate ribose (cADPR) was shown to increases guard cell $[Ca^{2+}]_{cyt}$ (Leckie *et al.*, 1998), while the cADPR inhibitor nicotinamide interfered with ABA-induced stomatal closure (Leckie *et al.*, 1998), demonstrating a role for cADPR in mediating ABA signalling. Another important second messenger, inositol 1,4,5 triphosphate (IP_3), is generated by phosphatidyl inositol specific phospholipase C (PI-PLC), which is in turn inhibited by the pharmacological inhibitor U73122. Inhibition of the PI-PLC-IP_3 system with U73122 was shown to interfere with ABA-induced stomatal closure and $[Ca^{2+}]_{cyt}$ oscillations (Staxen *et al.*, 1999). Additionally, the amplitude and frequency of ABA-induced $[Ca^{2+}]_{cyt}$ oscillations in guard cells has been shown to depend on the concentration of ABA applied externally in *Commelina communis* (Staxen *et al.*, 1999) and *Arabidopsis* (Allen *et al.*, 1999; MacRobbie, 2000). In other cells, cADPR and IP_3 also induce Ca^{2+} release from vacuoles (Allen *et al.*, 1995) and inhibition of PI-PLC-IP_3 by U73122 interferes with Ca^{2+} signalling induced by drought and salinity (Knight *et al.*, 1997). Other Ca^{2+}-mobilising agents have been identified in plants, including inositol hexophosphate (IP_6), sphingosine 1-phosphate (S1P) and nicotinic acid adenine dinucleotide phosphate (NAADP; Hetherington & Brownlee, 2004; Sanders *et al.*, 2002).

The enzymes which synthesise Ca^{2+}-mobilising second messengers have been well characterised in mammals, though the corresponding enzymes in plants remain elusive. In mammalian cells, a multi-functional class of ADP-ribosyl cyclase (ADPRc) enzymes catalyse both the cyclisation of NAD^+ to produce cADPR and the hydrolysis of cADPR (Higashida *et al.*, 2001). Expression of an ADPR cyclase from the sea slug *Aplysia* in *Arabidopsis* resulted in increased ADPR cyclase and hydrolase activity, though no homologues of the *Aplysia* ADPRc or a form commonly found in mammalian vertebrates (CD38) could be identified within the *Arabidopsis* genome (Sánchez *et al.*, 2004). NAADP is also synthesised by ADPRc in mammals so its synthesis in plants remains uncharacterised equivalent to cADPR. In contrast, of the five known isoforms of mammal PI-PLC, there have been nine homologues identified in *Arabidopsis*, though specific functions of each isoform remain uncharacterised (Hunt *et al.*, 2004).

Stimulus-induced elevations in $[Ca^{2+}]_{cyt}$ have been described mathematically, both through the use of deterministic and stochastic formulations. An early model of IP_3-dependent Ca^{2+} release assumed the existence of two distinct internal Ca^{2+} stores, one sensitive to IP_3, and the other sensitive to Ca^{2+} (Goldbeter *et al.*, 1990). The aptly named *Two Pool model* is an excitable system dependent on the contribution from an input variable (representing the rate of IP_3 synthesis) which leads to oscillations (through a Hopf bifurcation) or a stable steady state (Goldbeter *et al.*, 1990; Keener & Sneyd, 2001). More detailed models of the IP_3 receptor have been proposed and incorporate its tetrameric structure, which has been shown to enable fast activation by Ca^{2+}, followed by inactivation by Ca^{2+} on a slower time scale (De Young & Keizer, 1992), as observed experimentally by Bezprozvanny *et al.* (1991). The role of ryanodine receptors has been associated primarily with Calcium-Induced Calcium Release (CICR), in which small increases in $[Ca^{2+}]_{cyt}$ are amplified via positive feedback as Ca^{2+} binds ryanodine receptors (Endo *et al.*, 1970; Keener & Sneyd, 2001). Again, models of varying complexity exist, from the simple CICR model in bullfrog sympathetic neurons by Friel (1995) to a detailed subunit-based description of the ryanodine receptor (Tang & Othmer, 1994; Keener & Sneyd, 2001). More recently, stochastic models have been proposed which account for the irregular spiking pattern of intracellular Ca^{2+} oscillations, and also incorporate spatial properties such as wave propagation (Falcke, 2003). The majority of mathematical modelling of intracellular Ca^{2+} dynamics is based on observations from mammalian cells, especially ventricular myocytes and skeletal smooth muscle cells, so the extent to which these models are applicable to studies in *Arabidopsis* remains uncertain. Furthermore, the short time-scale and single-cell nature of existing models contrasts with the whole-plant measurements of circadian $[Ca^{2+}]_{cyt}$ oscillations of interest in this thesis.

1.2.2 Circadian control of $[Ca^{2+}]_{cyt}$ in plants

Investigating the role and regulation of Ca^{2+} in the plant circadian signalling network is complicated by the observations that the mechanism driving oscillations of $[Ca^{2+}]_{cyt}$ is necessarily different from the mechanism controlling *CAB2* expression, as the oscillation period differs between $[Ca^{2+}]_{cyt}$ and *CAB2* expression in constant red light (RR; in *Nicotiana*; Sai & Johnson, 1999) and for *toc1*-1 mutants in constant R+B light (in *Arabidopsis*; Xu *et al.*, 2007). Circadian $[Ca^{2+}]_{cyt}$ oscillations have different circadian phases in different cell-types (Wood *et al.*, 2001),

so it is possible that the underlying mechanisms differ between cell types, providing an explanation for the desynchrony of $[Ca^{2+}]_{cyt}$ and *CAB2* expression rhythms in RR. Alternatively, there may be multiple circadian oscillators existing in each cell, as observed in the desynchrony of output rhythms (bioluminescence and aggregation) in the single-celled dinoflagellate alga *Gonyaulax polyedra* (Roenneberg & Morse, 1993).

Since the first observations of circadian oscillations of $[Ca^{2+}]_{cyt}$ in *Arabidopsis* and *Nicotiana*, progress has been made in elucidating their function, the pathways contributing to their regulation, and the cellular messengers which mediate the Ca^{2+} release events leading to oscillatory dynamics (Love *et al.*, 2004; Dodd *et al.*, 2006; Xu *et al.*, 2007; Tang *et al.*, 2007; Dodd *et al.*, 2007; Figure 1.3). $[Ca^{2+}]_{cyt}$ appears to encode photoperiodic information, because nyctohemeral[‖] oscillations of $[Ca^{2+}]_{cyt}$ are photoperiod-responsive, reaching peak levels at ZT6 in short days and ZT8 in long days, while light intensity further modulates the oscillation phase and amplitude (Love *et al.*, 2004). Interaction with the circadian clock also modulates short-term elevations of $[Ca^{2+}]_{cyt}$ resulting from low temperature (LT), as the amplitude of LT-induced Ca^{2+} transients correlates with the basal circadian $[Ca^{2+}]_{cyt}$ oscillation and the circadian variation of *RD29A* transcript abundance, a marker of LT-signalling (Dodd *et al.*, 2006). A reverse genetic screen has identified a number of circadian clock genes to be important in the regulation of $[Ca^{2+}]_{cyt}$, including central oscillator components *CCA1* and *ELF3*, for which loss-of-function mutants result in arrhythmia of $[Ca^{2+}]_{cyt}$ in LL (Xu *et al.*, 2007). The *cca1*-1 loss of function mutant has circadian oscillations of *CAB2*, *LHY*, *CATALASE 2* (*CAT2*) and *CCR2* in LL, though with a shortened period (Green & Tobin, 1999). As $[Ca^{2+}]_{cyt}$ is arrhythmic in *cca1*-1 mutants in LL, *CCA1* is a necessary component for the circadian control of $[Ca^{2+}]_{cyt}$ (Xu *et al.*, 2007). In contrast, *elf3*-1 mutants have no circadian oscillations of *CAB2* and *CCR2* expression in LL (Alabadí *et al.*, 2001; McWatters *et al.*, 2000). As no circadian rhythms can be observed in *elf3*-1 mutants, it is not possible to derive a functional role for *ELF3* in the regulation of basal $[Ca^{2+}]_{cyt}$ from the observation that $[Ca^{2+}]_{cyt}$ is also arrhythmic (Xu *et al.*, 2007). It was also shown that *phyB* mutants had no circadian oscillations of $[Ca^{2+}]_{cyt}$ in RR, *cry1* mutants had no circadian oscillations of $[Ca^{2+}]_{cyt}$ in constant blue light (BB), while both *phyB* and *cry1* mutants had reduced amplitude oscillations of $[Ca^{2+}]_{cyt}$ in LL (Xu *et al.*, 2007). Therefore, PHYB and CRY1 are important for the circadian control of $[Ca^{2+}]_{cyt}$ in both short and long wavelengths of light, though it is unknown whether

[‖] 'Nyctohemeral' is defined as "pertaining to both day and night", but is commonly confused with 'diurnal' (pertaining to day) which is an antonym for 'nocturnal' (pertaining to night).

they contribute to the circadian regulation of $[Ca^{2+}]_{cyt}$ upstream or downstream of *CCA1* (Figure 1.3). Characterising the phenotype of a *phyB cry1* double mutant for circadian $[Ca^{2+}]_{cyt}$ oscillations in LL is appealing, to establish whether PHYB and CRY1 alone are mediating clock regulation of $[Ca^{2+}]_{cyt}$. Another appealing possibility is that light and dark signals modulate circadian and nyctohemeral oscillations of $[Ca^{2+}]_{cyt}$ independently of the central oscillator, and that this effect is mediated by photoreceptors such as *PHYB* and *CRY1*.

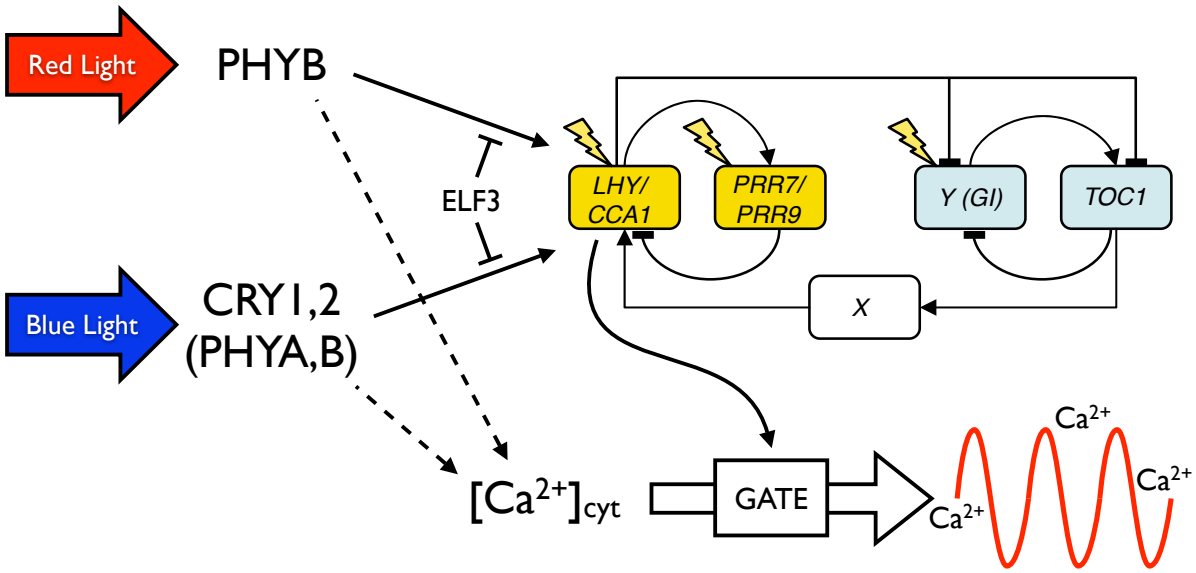

Figure 1.3: Model for the generation of circadian $[Ca^{2+}]_{cyt}$ oscillations.
Basal $[Ca^{2+}]_{cyt}$ is regulated by a circadian oscillator and a light signalling pathway. Light and dark signals appear to regulate $[Ca^{2+}]_{cyt}$ independently from the central oscillator mechanism. *CCA1* mediates the central oscillator regulation of $[Ca^{2+}]_{cyt}$, as *cca1* loss-of-function mutants have no circadian oscillations of $[Ca^{2+}]_{cyt}$ in LL. Modified from Xu *et al.* (2007), with the central oscillator represented by the diagram in Locke *et al.* (2006).

Two models have been proposed for the generation of circadian oscillations in $[Ca^{2+}]_{cyt}$. The first model proposes $[Ca^{2+}]_{cyt}$ oscillations to follow similar oscillations in $[Ca^{2+}]_{ext}$ via an IP_3-mediated pathway (Tang *et al.*, 2007). The oscillations of $[Ca^{2+}]_{ext}$ are thought to be driven by rhythmic water fluxes resulting from stomatal movements, and are interpreted at the plasma membrane by the Ca^{2+}-sensing CAS (Tang *et al.*, 2007; Webb, 2008). However, it has recently been shown that CAS localises to the chloroplast rather than the plasma membrane (Weinl *et al.*, 2008), and furthermore circadian rhythms in stomatal movements and $[Ca^{2+}]_{cyt}$ are not functionally linked because the circadian periods of $[Ca^{2+}]_{cyt}$ and stomatal movements are not consistent in *toc1*-1 and *ztl*-1 mutants (Webb, 2008). A second model for the generation of circadian $[Ca^{2+}]_{cyt}$ oscillations implicates cADPR to be the primary second messenger, as inhibition

of cADPR synthesis by nicotinamide abolishes circadian $[Ca^{2+}]_{cyt}$ oscillations, while the IP_3 inhibitor U73122 had no effect (Dodd *et al.*, 2007). In addition, cADPR was shown to form a feedback loop with the *Arabidopsis* circadian central oscillator mechanism, which might incorporate changes in $[Ca^{2+}]_{cyt}$ (Dodd *et al.*, 2007). The proposed cADPR-based feedback loop is investigated further in Chapter 5.

1.3 Mathematical Modelling of Biochemical Reaction Networks (BRNs)

Biological systems have traditionally been investigated through critical hypothesis testing, by performing experiments which distinguish two possible outcomes. The overall aim is to propose conceptual models which describe the inner workings of a system, on which further investigations may be based. Before the prevalence of powerful computing resources, mathematical descriptions of these models were severely restricted, as large systems of equations would need to be reduced to an approximation typically consisting of no more than three equations, to enable a closed-form solution. Now, we may define systems of seemingly infinite numbers of components (computational models), with the only restriction being the time it takes to simulate the underlying equations numerically. This has given rise to the derivation of many computational models of complex BRNs, such as circadian clocks (Leloup *et al.*, 1999; Ueda *et al.*, 2001; Leloup & Goldbeter, 2003; Forger & Peskin, 2003; Locke *et al.*, 2006).

1.3.1 Mass Action kinetics, Michaelis-menten and Hill equations

Classical approaches to modelling BRNs rely on mass action kinetics, which is that the rate of a reaction is proportional to the concentration of the reactants. The canonical example is to consider an enzymatic reaction, in which enzyme E catalyses the conversion of a substrate S to a product P via reversible formation of a complex SE, according to the following reaction system:

$$S + E \underset{k_-}{\overset{k_+}{\rightleftharpoons}} SE \xrightarrow{k} P + E \tag{1.1}$$

As S is consumed in the forward reaction forming the complex SE, the rate of change of $[S]$ (the concentration of S) has a negative term which is proportional to the product of $[S]$ and $[E]$,

with rate k_+. Also, the disassociation of the complex SE provides a positive term proportional to $[SE]$, with rate k_-. Extending this idea to equations for $[SE]$, $[P]$ and $[E]$, we form a nonlinear system of ordinary differential equations which represents the complete reaction:

$$\frac{ds}{dt} = -k_+se + k_-c \tag{1.2}$$
$$\frac{dc}{dt} = k_+se - k_-c - kc \tag{1.3}$$
$$\frac{de}{dt} = -k_+se + k_-c + kc \tag{1.4}$$
$$\frac{dp}{dt} = kc \tag{1.5}$$

where $s = [S]$, $e = [E]$, $c = [SE]$ and $p = [P]$. At this stage it is customary to invoke the equilibrium approximation or the quasi-steady state assumption (QSSA; Keener & Sneyd, 2001), which both lead to the same functional form for the rate of the reaction as a function of the concentration of the substrate.

The equilibrium approximation relies on the assumption that the substrate is in instantaneous equilibrium with the complex. Therefore,

$$k_+se = k_-c \tag{1.6}$$

Imposing a further assumption that the availability of the enzyme is approximately constant enables us to write $[E_0] = [E] + [SE]$. i.e. $e_0 = e + c$ or equivalently $e = e_0 - c$. Substituting this into Eqn. 1.6 and rearranging yields

$$c = \frac{se_0}{K_s + s} \tag{1.7}$$

where $K_s = k_-/k+$. The product P accumulates with rate kc (Eqn. 1.5), and so the total enzymatic reaction rate V is a function of the concentration of substrate, s. i.e.

$$V(s) = \frac{dp}{dt} = \frac{ke_0s}{K_s + s} = \frac{V_{\max}s}{K_s + s} \tag{1.8}$$

where $V_{\max} = ke_0$ is the maximum reaction rate.

Suppose instead we write the equations for s (Eqn. 1.2) and c (Eqn. 1.3) in the dimensionless

variables (see Keener & Sneyd (2001) for a complete description of this approach)

$$\sigma = \frac{s}{s_0}, \quad x = \frac{c}{e_0}, \quad \tau = k_1 e_0 t, \quad \kappa = \frac{k_{-1} + k_2}{k_1 s_0}, \quad \epsilon = \frac{e_0}{s_0}, \quad \alpha = \frac{k_{-1}}{k_1 s_0} \tag{1.9}$$

Then we obtain the following pair of differential equations

$$\frac{d\sigma}{d\tau} = -\sigma + x(\sigma + \alpha), \tag{1.10}$$

$$\epsilon \frac{dx}{d\tau} = \sigma - x(\sigma + \kappa) \tag{1.11}$$

The QSSA is to take $\epsilon \frac{dx}{d\tau} = 0$, which is valid providing ϵ is small, equivalent to $e_0 \ll s_0$. It follows that

$$x = \frac{\sigma}{\sigma + \kappa}, \tag{1.12}$$

$$\frac{d\sigma}{d\tau} = -\frac{q\sigma}{\sigma + \kappa}, \tag{1.13}$$

where $q = \kappa - \alpha = \frac{k_2}{k_1 s_0}$. In terms of the original variables, we obtain the Michaelis-Menten function

$$V = \frac{dp}{dt} = -\frac{ds}{dt} = \frac{k_2 e_0 s}{s + K_m} = \frac{V_{\max} s}{s + K_m}, \tag{1.14}$$

where $K_m = \frac{k_{-1} + k_2}{k_1}$ is the michaelis constant. This function has been shown to correspond well with a number of characterised enzymatic reactions, and is now considered a first approximation to describing the reactions in which the concentration of the substrate is much higher than that of the enzyme (Keener & Sneyd, 2001).

The law of mass action has also been used to derive a reaction rate when the enzyme has more than one binding site. This essentially leads to a chain of reactions with successive binding of substrate to complexes, eventually yielding the end-product. If the degree of cooperativity between binding sites is large, then it can be shown that the rate of the reaction can be described by a Hill equation (Keener & Sneyd, 2001)

$$\frac{dp}{dt} = \frac{V s^n}{s^n + \theta^n} \tag{1.15}$$

where n is the number of binding sites, V and θ are constants. The steepness of the sigmoidal Hill function is related to the number of binding sites n, becoming more switch-like as n is

increased.

Mathematical models of the *Arabidopsis* circadian clock have shown that a combination of Hill, Michaelis-menten and linear functions can accurately reproduce gene expression dynamics observed experimentally (Locke *et al.*, 2005a,b, 2006). In these models, the degradation of gene products is assumed to follow michaelis-menten kinetics and transcriptional activation/inhibition follows a Hill functional relationship, even though the enzymes responsible are mostly unknown. In addition to components which correspond to known network genes, hypothetical components were proposed as necessary for robust circadian rhythm generation (Locke *et al.*, 2005b). Each component gene comprises a fixed structure of three state variables representing mRNA, cytoplasmic protein and nuclear protein. The mRNA variable is an activator of cytoplasmic protein, which undergoes reversible translocation to the nucleus with a rate proportional to the concentration of the protein in the compartment (cytoplasm or nucleus) it came from. Upon prescribing a fixed structure of each component gene, identification of a candidate model is completed by arranging the component genes in a network, and then identifying the values of the kinetic parameters in each hill/michaelis-menten/linear functional representing the circadian clock BRN. As many of the molecular interactions have not been investigated experimentally, the values of the kinetic parameters are not available in the literature. Instead, parameter optimisation algorithms have been used which iteratively search through different parameter sets, assessing their performance by a cost function.

1.3.2 Linear and Nonlinear Dynamical Systems

The mathematical description of BRNs using functional approximations from mass action kinetics results in systems of nonlinear ordinary differential equations (ODEs). i.e.

$$\dot{x}(t) \quad = \quad f(x(t), u(t); p), \quad x \in \mathbb{R}^n, \quad p \in \mathbb{R}^m, \tag{1.16}$$

where $x(t)$ denotes the vector of state variables, e.g. concentrations of the biochemical components, $u(t)$ denotes the external inputs and p denotes the vector of kinetic rate parameters.

Any mathematical model of an autonomous oscillator must have solutions which tend towards a stable limit cycle. A limit cycle can be described as an isolated** periodic orbit (Khalil,

**Isolated means that the periodic orbit is contained within an open subset that contains no other periodic orbits. This requirement ensures that a periodic orbit resulting from the existence of a centre point - in which a planar system has two purely imaginary complex conjugate eigenvalues - is not defined as a limit cycle. i.e. $\dot{x} = Ax$ with

2002). i.e. $x(t+T) = x(t)$, where T is the oscillation period. More formally, a periodic solution to $\dot{x} = f(x)$, Γ, is a stable limit cycle if the ω-limit set of a solution with initial condition not on Γ has Γ as its limit set (Perko, 2001). The ω-limit set represents the set of limit points a solution to the ODE converges to as $t \to \infty$ and contrasts with the α-limit set which is when $t \to -\infty$. An unstable limit cycle is defined equivalently to the stable limit cycle but with the α-limit set.

The emergence of stable limit cycles in nonlinear systems is often dependent on the existence of a Hopf bifurcation. This is where a stable steady state loses stability as a pair of complex conjugate eigenvalues of the linearisation around the stable point cross the imaginary axis, in response to a parameter alteration. Proving global stability of a limit cycle in an arbitrary nonlinear system is not possible, though it is possible to analyse local stability using theory based on the Poincaré map (Khalil, 2002; Gonçalves & Yi, 2004). Through numerical simulation, it is possible to establish whether a particular solution to a nonlinear system (prescribed initial condition) converges to a limit cycle. The set of points in $\mathbb{R}^n$ from which the system trajectory does converges to the limit cycle is known as the basin of attraction (Khalil, 2002), and is another global property which is difficult to characterise. In a model of a circadian oscillator, the basin of attraction is an important concept, as it corresponds to the range of cellular conditions (under any chemical stimulus, in wild-type or transgenic lines) from which circadian oscillations may still continue. An alternative way of considering perturbations to limit cycles is by employing control theoretic notions of robustness. Period sensitivity analysis enables characterisation of robustness of oscillators to parameter perturbations, an approach which has been applied to circadian oscillator models (Ingalls, 2004; Stelling *et al.*, 2004). Structural perturbations may also be analysed by considering systems of the form (Trané, 2008)

$$\dot{x}(t) = f(x(t), p) + f_\Delta(x(t)), \quad x \in \mathbb{R}^n \tag{1.17}$$

where f_Δ is any function of the state variables x. Robustness may be analysed by finding the smallest $||f_\Delta||$ (for f_Δ belonging to some class of functions) such that the limit cycle loses stability or disappears (Trané, 2008).

Parameter selection for nonlinear ODE descriptions of BRNs can be extremely demanding when the number of parameters is large. When the kinetic rate parameters have not been mea-

$A = \begin{pmatrix} a & b \\ c & -a \end{pmatrix}$ and $a^2 + bc < 0$.

sured experimentally, parameters must be selected by solving an optimisation problem which penalises model deviations from a prior belief of the outputs. When there is a large quantity of experimental observations available, it may be possible to select parameters by optimising a cost function which fixes model simulations to measured data (Forger & Peskin, 2003). However, previous parameter identification of nonlinear ODE models for the *Arabidopsis* circadian clock used a cost function comprised of 'quantitative experimental features', which in the case of autonomous oscillators are properties such as oscillation period, phase and amplitude (Locke *et al.*, 2005a,b, 2006; Zeilinger *et al.*, 2006). Both approaches strongly favour the identification of models which can exhibit limit cycle oscillations.

The complexity arising from parameter identification of nonlinear systems provides the motivation for considering simpler model classes, such as linear time-invariant (LTI; Chen, 1998) or time-varying (Kim *et al.*, 2008a) models. In dynamical systems theory, a general LTI system is defined in terms of state variables, which may be observed or 'hidden'. Suppose $x \in \mathbb{R}^n$ is the vector of state variables, then we define a general multi-input multi-output (MIMO) linear system as:

$$\dot{x}(t) \quad = \quad Ax(t) + Bu(t), \quad y(t) = Cx(t) + Du(t) \tag{1.18}$$

where $y(t) \in \mathbb{R}^p$ is the vector of p measured outputs, $u(t) \in \mathbb{R}^m$ is the vector of m inputs, $A \in \mathbb{R}^{nxn}$ is the interconnectivity matrix, $B \in \mathbb{R}^{nxm}$ is the input matrix, $C \in \mathbb{R}^{pxn}$ is the output matrix and $D \in \mathbb{R}^{pxm}$ is the feedforward matrix.

Parameter identification for continuous-time LTI systems (Eqn. 1.18) is relatively straightforward compared with nonlinear systems, as the theory of Systems Idenfication enables fast and accurate computation and the inclusion of hidden (unmeasured) variables (Ljung, 1999). Systems identification may also be thought of as black-box modelling, as models are computed which relate input signals to output signals with no knowledge of the process transducing the signal. Algorithms to estimate continuous-time linear black-box models fall into two classes, known as direct methods and indirect methods (Sinha, 2000). For indirect methods, a discrete-time model is first computed from sampled input-output data, which is then converted to a continuous-time representation; direct methods compute continuous-time models directly, after first approximating the non-measurable time-derivatives of the (measured) state variables (Canty *et al.*, 2006). The Systems Identification Toolbox for MATLAB^{TM} (SID) has

built-in routines for estimating continuous-time state-space models of the form in Eqn. 1.18 using indirect methods (e.g. prediction-error based maximum likelihood with the *pem* command or subspace methods with *n4sid*; Ljung, 1999). A large variety of direct methods are available in the CONTinuous Time Systems IDentification MATLAB^{TM} toolbox (CONTSID; Garnier & Mensler, 2000). A number of comparisons of direct and indirect methods have been carried out, concluding that direct methods avoid unnatural nonminimum phase character, produce parameters which correspond with physical quantities and offer improved variance of parameter estimates (Unbehauen & Rao, 1998; Canty *et al.*, 2006). However, a major limitation of direct methods is the inability to incorporate hidden states (unmeasurable system components).

Systems Identification originates from the field of automatic control, and many examples can be found in the literature applied to industrial processes (Wang *et al.*, 2004; Canty *et al.*, 2006). However, there have been examples of LTI systems modelling in medicine and neurophysiology (Srikusalanukul *et al.*, 2000; Apkarian *et al.*, 1999), and more recently in signal transduction pathways (Mettetal *et al.*, 2008; Yildirim & Vidal, 2008). A drawback of using LTI systems for modelling biological phenomena is that molecular interactions are inherently nonlinear. Nevertheless, many experiments are designed to measure activity in a 'linear range', providing some justification to the approximation of the input-output behaviour with LTI systems. Irrespective of the model class used, construction of a computational model must follow a strong logical formalism, comprising data preprocessing, estimation, validation and prediction. Under this formalism, a successful model validation for an LTI system inherently incorporates the validation of a linearity assumption. To obtain a predictive model, many cycles of the iterative data processing-estimation-validation-prediction formalism may be necessary.

The philosophy undertaken in this thesis is to mathematically model interactions between the circadian clock and physiology beginning with the simplest possible model class, and to increase complexity as required. In particular, in Chapter 2 LTI systems are shown to be both relevant and informative for uncovering properties of a largely uncharacterised biological system from input-output data, though the input structure is shown to be multi-input after invalidation of a single-input formulation.

CHAPTER 2

Delay Linear Systems for the Circadian Regulation of $[Ca^{2+}]_{cyt}$

2.1 Introduction

In this chapter, we will attempt to increase the mechanistic understanding of the interactions between the circadian clock, the light signalling network and resting levels of cytosolic-free Ca^{2+} ($[Ca^{2+}]_{cyt}$). Light perception is vital in plants, for co-ordinating light-dependent processes such as photosynthesis and flowering. Periods of light and dark are anticipated by the circadian clock, which is known to in turn be regulated by light, both at transcriptional and post-translational levels (Xu *et al.*, 2007; Hotta *et al.*, 2007). In addition, $[Ca^{2+}]_{cyt}$ undergoes short-term elevations in response to pulses of blue light (Baum *et al.*, 1999; Harada *et al.*, 2003), and also mediates phytochrome phototransduction (Neuhaus *et al.*, 1993; Bowler *et al.*, 1994). $[Ca^{2+}]_{cyt}$ undergoes oscillations in constant light (LL) and light-dark (LD) cycles but tends to a steady state in constant dark conditions (DD; Figure 2.1), indicating that the circadian clock and the light signalling network are potent regulators of Ca^{2+}-release mechanisms (Johnson *et al.*, 1995; Love *et al.*, 2004; Xu *et al.*, 2007). Through construction of mathematical models, we have attempted to unravel some properties of the network which connects these three elements. In particular, we address whether light modulates $[Ca^{2+}]_{cyt}$ purely via changes in clock-

associated gene expression, or whether there are distinct clock- and light/dark-dependent pathways which regulate $[Ca^{2+}]_{cyt}$.

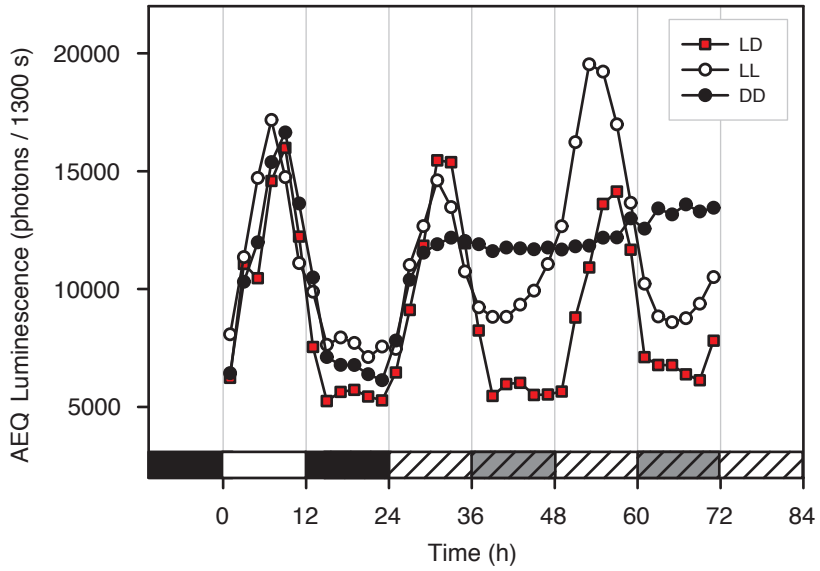

Figure 2.1: $[Ca^{2+}]_{cyt}$ oscillates in light-dark cycles and constant light but not in constant dark. $[Ca^{2+}]_{cyt}$ monitored by measuring luminescence from *Arabidopsis* seedlings transformed with *35S:aeq*. Seedlings were grown and entrained in 12 h light, 12 h dark (LD) cycles for 10 days before measurement in LD (red squares), LL (open circles) and DD (closed circles). White bars indicate light, black bars indicate dark. Light availability for hatched bars are conditional on each trace, whereby white hatched bars indicate subjective day, and grey hatched bars indicate subjective night. Modified from Xu *et al.*, 2007.

Ca^{2+} is an ubiquitous second messenger in eukaryotes, which signals information via changes in $[Ca^{2+}]_{cyt}$. In plants, elevations in $[Ca^{2+}]_{cyt}$ have been observed in response to touch, cold, light, fungal elicitors, abscisic acid (ABA), auxin and salt stress, occurring between 10 seconds and 60 minutes in duration (Hetherington & Brownlee, 2004). The longer time-scale circadian and nyctohemeral (cycles of light and dark) oscillations are thought to encode information concerning photoperiod and light intensity, via changes in oscillation amplitude and phase (Love *et al.*, 2004). Ca^{2+} ions are released from internal stores such as the endoplasmic reticulum (ER) and the vacuole upon ligand binding to receptor channels. Inositol triphosphate (IP_3), cyclic adenosine diphosphate ribose (cADPR) and nicotinic acid adenine dinucleotide phosphate (NAADP) have all been shown to mobilise Ca^{2+} from internal stores (Lee, 1997). Nyctohemeral oscillations of $[Ca^{2+}]_{cyt}$ are thought to depend on the Ca^{2+}-sensing receptor CAS, which regulates concentrations of IP_3 (Tang *et al.*, 2007), while circadian oscillations of $[Ca^{2+}]_{cyt}$ are absent in plants treated with 50 mM nicotinamide, an inhibitor of cADPR

synthesis (see Chapter 5; Dodd *et al.*, 2007). This suggests that there are multiple pathways which contribute to the regulation of basal $[Ca^{2+}]_{cyt}$. A genetic study conducted concurrently with the work presented in this chapter has revealed that both circadian-clock dependent and light/dark-dependent pathways are able to modulate $[Ca^{2+}]_{cyt}$ (Xu *et al.*, 2007).

Light is interpreted in plant cells by photoreceptors, of which there are three known families: the red/far-red light sensing PHYTOCHROMES (PHY) and the blue/UV-A light sensing CRYPTOCHROMES (CRY) and PHOTOTROPINS (PHOT). There are five known genes belonging to the PHYTOCHROME family, the major forms being the photo-labile PHYA and the photo-stable PHYB, and the less abundant PHYC, PHYD and PHYE. PHY are involved in the regulation of flowering time, entrainment of the circadian clock, seed germination, shade avoidance, transition to reproductive growth and de-etiolation (Somers *et al.*, 1998a; Chen *et al.*, 2004; Franklin & Whitelam, 2005). There are three known CRY photoreceptors in *Arabidopsis* (CRY1–3). CRY1 and CRY2 are also involved in the transition to reproductive-growth, de-etiolation and entrainment of the circadian clock (Franklin *et al.*, 2005), while the functions of the mitochondria and chloroplast targeted CRY3 remain uncharacterised (Li & Yang, 2007) . PHOT are associated with light-directed plant growth, chloroplast translocation and promote stomatal opening (Franklin *et al.*, 2005; Harada & Shimazaki, 2007).

Ca^{2+} is involved in red and blue light signalling in a number of pathways. The red-light photoreceptor PHYA induces *CHLOROPHYLL A/B BINDING PROTEIN* (*CAB2*) expression and photosystem I genes via Ca^{2+}-dependent pathways (Bowler *et al.*, 1994), while blue-light dependent PHOT1 and PHOT2 evoke $[Ca^{2+}]_{cyt}$ increases in response to blue light pulses, which are unaffected by a *cry1*-304 *cry2*-1 double mutation (Baum *et al.*, 1999; Harada *et al.*, 2003). In contrast, mutations in PHOT1 and PHOT2 have no effect on circadian and nycothemeral oscillations of $[Ca^{2+}]_{cyt}$ (Hotta, 2007). In constant red light (RR), there are no circadian $[Ca^{2+}]_{cyt}$ oscillations in *phyB*-1 mutants, and in constant blue light (BB), oscillations of $[Ca^{2+}]_{cyt}$ are absent in *cry1*-1 *cry2*-1 double mutants (Hotta, 2007).

The circadian clock is comprised of multiple interlocking feedback loops, which serve to co-ordinate physiology with a 24 hour periodic environment. The first feedback loop identified involves *CIRCADIAN CLOCK ASSOCIATED 1* (*CCA1*), *LATE ELONGATED HYPOCOTYL* (*LHY*) and *TIMING OF CAB EXPRESSION 1* (*TOC1*; Alabadí *et al.*, 2001). *CCA1* and *LHY* are partially redundant myb-like transcription factors (Schaffer *et al.*, 1998; Mizoguchi *et al.*, 2002)

which bind as a dimer to the conserved 'evening element' motif (EE; AAAATATCT), present in a significant proportion of circadian-regulated transcripts (Harmer *et al.*, 2000). Constitutive over-expression of *CCA1* saturates all genes containing the EE, subsequently suppressing circadian rhythm generation and resulting in arrhythmicity in several clock outputs (Wang & Tobin, 1998), including $[Ca^{2+}]_{cyt}$ (Xu *et al.*, 2007). *cca1*-1 mutants have short-period oscillations (Green & Tobin, 1999), indicating that *CCA1/LHY-TOC1* loop was not the only feedback loop capable of generating oscillations. However, *cca1* mutants have no circadian oscillations of $[Ca^{2+}]_{cyt}$ in LL (Xu *et al.*, 2007), which implies that *CCA1* is a necessary component for the control of $[Ca^{2+}]_{cyt}$ in LL, an observation that is critical for construction of a mathematical model for the regulation of basal $[Ca^{2+}]_{cyt}$. Furthermore, although arrhythmia is observed in *cca1*-1, *CCA1*-OX and *LHY*-OX in LL, there are still oscillations of $[Ca^{2+}]_{cyt}$ in LD cycles, which appear to anticipate dawn (Xu *et al.*, 2007).

In this chapter, mathematical models are considered which have circadian clock associated and light/dark associated inputs, seeking to describe measurements of $[Ca^{2+}]_{cyt}$. $[Ca^{2+}]_{cyt}$ tends towards a steady state in DD (Figure 2.1), implying that the central oscillator is either arrhythmic or does not contribute to the control of $[Ca^{2+}]_{cyt}$ in the absence of light. To distinguish these options, we tested whether the expression of circadian-regulated genes is oscillatory in DD in the growth conditions used for measuring $[Ca^{2+}]_{cyt}$. We found that the availability of exogenous sucrose enabled the plant circadian clock to sustain oscillations in DD (see Chapter 3); circadian oscillations quickly disappear in the absence of exogenous sucrose and the system tends to a steady state. How sucrose promotes oscillations in DD is unknown, and so this previously unreported finding is investigated further in Chapters 3 & 4. In building a mathematical model of the regulation of $[Ca^{2+}]_{cyt}$, data from plants grown in the absence of exogenous sucrose were used. This had the slight drawback that it prevented use of previously published mathematical models of the central oscillator as an input for $[Ca^{2+}]_{cyt}$, as they were all derived using data from plant grown in the presence of exogenous sucrose, and correspondingly exhibit stable oscillations in DD (Locke *et al.*, 2005a,b, 2006; Zeilinger *et al.*, 2006).

Ca^{2+} signalling is a topic well studied mathematically, as interest derives from the limit cycle oscillations generated in response to various stimuli (Keener & Sneyd, 2001). Typically, these models reflect specific receptor-binding activity, and often include spatial as well as temporal dynamics, but at the single-cell level. Building a mathematical model of circadian $[Ca^{2+}]_{cyt}$ sig-

nalling of this sort is not possible because measurements have been conducted for large populations of cells (clusters of seedlings), the specific influx and efflux Ca^{2+} channels are not known and the differences between cell types cannot be rectified (Love *et al.*, 2004; Dodd *et al.*, 2005a; Xu *et al.*, 2007). The model sought is therefore a single-output black-box model, which must incorporate a *CCA1*-dependent and possibly distinct light/dark-dependent pathway (Figure 2.2). Through estimation and cross-validation of a basic model class, we demonstrate a strong logical model definition, tuning parameters from 1 dataset, and validating with 3 contrasting sets. Comparisons of AEQUORIN luminescence data from wild-type and mutant backgrounds with corresponding mathematical simulations have enabled predictions of the time-scales and genetic components which comprise the biochemical connections between *CCA1*, the light signalling network and $[Ca^{2+}]_{cyt}$. A simple mathematical model describes a temporal separation of light and Ca^{2+} signalling to control phase in a circadian system.

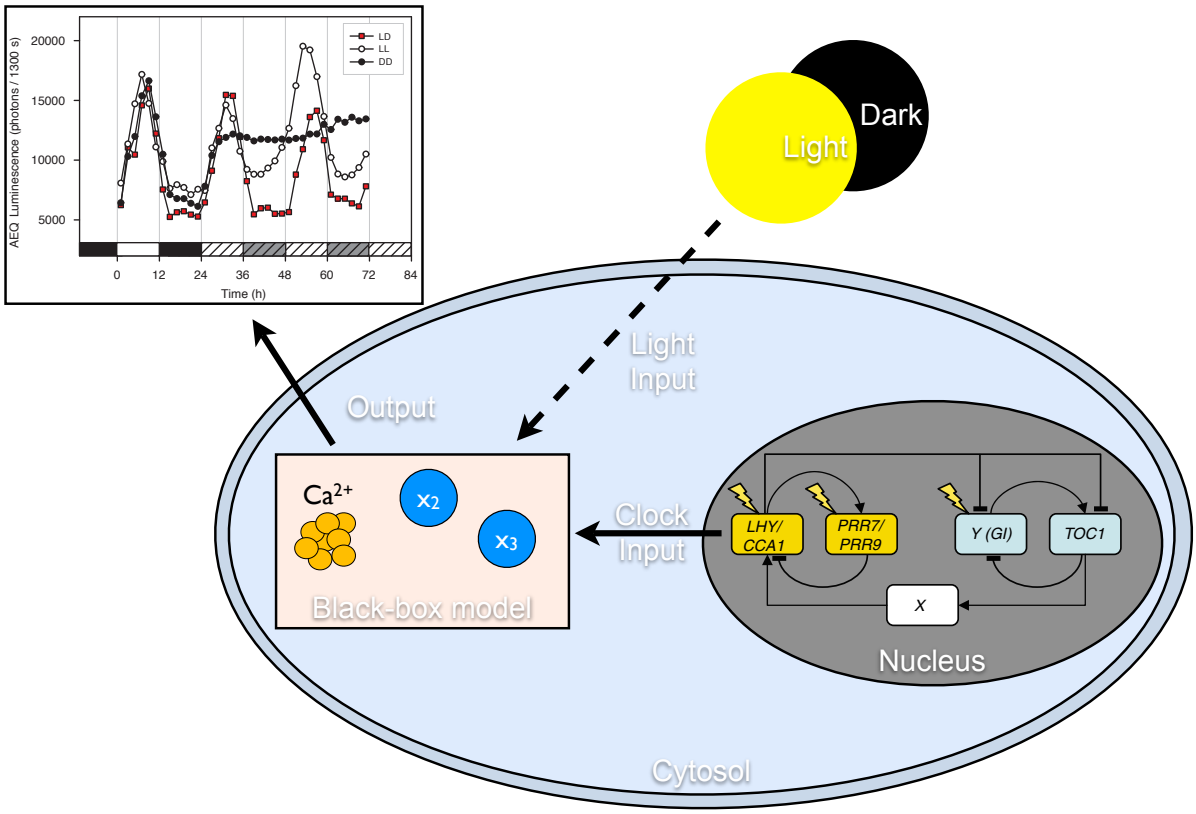

Figure 2.2: Schematic for a mathematical model of circadian and light/dark regulation of $[Ca^{2+}]_{cyt}$. The central oscillator network inside the nucleus reflects the *Three Loop Model* of the central oscillator (Diagram from Locke *et al.*, 2006). A black-box model incorporates signals (inputs) from the circadian clock (measurements of *CCA1* promoter activity via *CCA1:luc* luminescence) and a possibly distinct light/dark pathway signified by a dashed arrow. The black-box can contain hidden variables (x_2, x_3, ... *etc.*) which correspond to unknown components regulating $[Ca^{2+}]_{cyt}$. The desired model outputs are the measured AEQUORIN luminescence data.

2.2 Materials and Methods

2.2.1 Plant material and growth conditions

Arabidopsis thaliana seedlings (Col-0) transformed with the cDNA of the *LUCIFERASE* (*LUC*) coding sequence under the *CCA1* promoter (*CCA1:luc*) were obtained from Nottingham Arabidopsis Stock Centre (NASC). Experimental data from Col-0 *Arabidopsis* seedlings obtained from members of the Signal Transduction Laboratory (Department of Plant Sciences, University of Cambridge) have been used for mathematical modelling. Seeds were surface sterilised by washing sequentially in 96% w/v ethanol (EtOH; Fisher Scientific, UK) for 1 min, in 50% w/v sodium hypochlorite (NaClO; BDH Laboratories Supplies, UK) for 5 to 10 min and twice in sterile deionised water. The seeds were resuspended in 0.1% w/v agar (Bactoagar; Difco, UK) and plated on 90 mm round dishes (Sarstedt, Germany) containing sterile solid half strength Murashige and Skoog media (MS media; Duchefa, Netherlands; pH 7.0) and 0.8% agar. The plates were sealed with surgical micropore tape (3M, USA), stored in darkness at 4 °C for 2–3 days for seed stratification and transferred to a Sanyo MLR-35T growth cabinet set to 20 °C and a 24 h periodic cycle of light and dark (L12/D12, L16/D8 or L8/D16; 60 μmol photons m^{-2} s^{-1}).

2.2.2 Luminescence imaging

Arabidopsis seeds expressing *CCA1:luc* or *35S:aeq* were surface sterilized as above, and sown in clusters of 10-12 seeds inside rings made from 7.5 mm x 9 mm PVC tubes cut transversally every 0.5 cm. After stratification, the plates were transferred to a growth cabinet set to LD conditions for entrainment (20 °C; 60 μmol photons m^{-2} s^{-1}). The AEQUORIN was reconstituted by addition of 50 μl of 20 μM coelenterazine to each ring cluster once per day, two days prior to measurement. 50 μl of 5 mM luciferin was added to seedlings expressing *luc* once per day, 2 days prior to measurement.

Before each experiment, a bright-field image was taken of the plate. Photon-counting was conducted in a light-tight box using a Photek ICCD225 photon-counting camera system (Photek, UK) mounted above the plate in complete darkness. The camera was controlled by Photek IFS32 software, which programmed timing of all measurements automatically. Luminescence was measured for 1500 s every 2 h for *35S:aeq* lines, and 800 s every 1 h for *CCA1:luc*. The control box turned off the two arrays of blue and red light emitting diodes (LEDs) used

as light sources inside the box (100 μmol photons m^{-2} s^{-1}; equal amounts of red light, 630 nm, and blue light 475 nm) before starting the measurements. The software then saved the data, and turned on the lights again after the measurements before starting a delay between measurements. An additional control could be programmed to turn the LED arrays on and off independently of the camera control to allow light/dark experiments.

Images saved by the automated camera system were analysed using the Photek IFS32 software. The first 200 s of each measurement were discarded due to delayed chlorophyll fluorescence and 8-bit images were generated and pseudocoloured. Based on the bright-field image, regions of interest were demarcated around each ring cluster and the total photon counts (luminescence) were quantified.

2.2.3 Data for estimation and validation of mathematical models

We use the fact that *CCA1* is necessary for circadian oscillations of $[Ca^{2+}]_{cyt}$ in LL (Xu *et al.*, 2007) to define a proxy for the circadian clock as an input to a black-box model which describes basal $[Ca^{2+}]_{cyt}$. The short-period loss-of-function *cca1*-1 mutant (Green & Tobin, 1999) has no circadian oscillations of $[Ca^{2+}]_{cyt}$ in LL (Xu *et al.*, 2007), indicating that *CCA1* mediates the circadian control of $[Ca^{2+}]_{cyt}$. The *CCA1:luc* data obtained in Figure 2.3A was collected under equivalent growth conditions to the measurements of $[Ca^{2+}]_{cyt}$ in Figure 2.3A, which together form an input-output pair. The dynamics monitored in this experiment include three important elements for a mathematical description of $[Ca^{2+}]_{cyt}$: the oscillations of the circadian clock, light/dark forcing, and tendency to steady state in DD. Therefore, this experiment represents a good choice as a model training set. Both the input and output data are scale-free, as calibration of the signals to concentrations of mRNA or cytosolic-free Ca^{2+} is inaccurate*. To achieve a suitable comparability of different experiments with different signal strengths, the *CCA1:luc* luminescence data was normalised by dividing the whole data set by the maximum value in the LD cycles.

A series of cross-validation tests were also applied to each model estimated. Plants express-

*For stimulus-induced elevations in $[Ca^{2+}]_{cyt}$, AEQUORIN luminescence signals have been calibrated by using an empirically derived calibration equation which relates $[Ca^{2+}]_{cyt}$ to the ratio between the luminescence counts and the size of the AEQUORIN pool at the end of an experiment, L_t (Knight *et al.*, 1996). The equation used was $-\log[Ca^{2+}]_{cyt} = a\left[-\log\left(\frac{L_c}{L_t}\right)\right] + b$, where a and b are constants. For calibration of low $[Ca^{2+}]_{cyt}$, this equation has a very low gradient, which means that a large change in luminescence corresponds to a small change in $[Ca^{2+}]_{cyt}$. At low luminescence levels, stochastic variation becomes more significant and as a result, our calibrations of $[Ca^{2+}]_{cyt}$ have been wide-ranging.

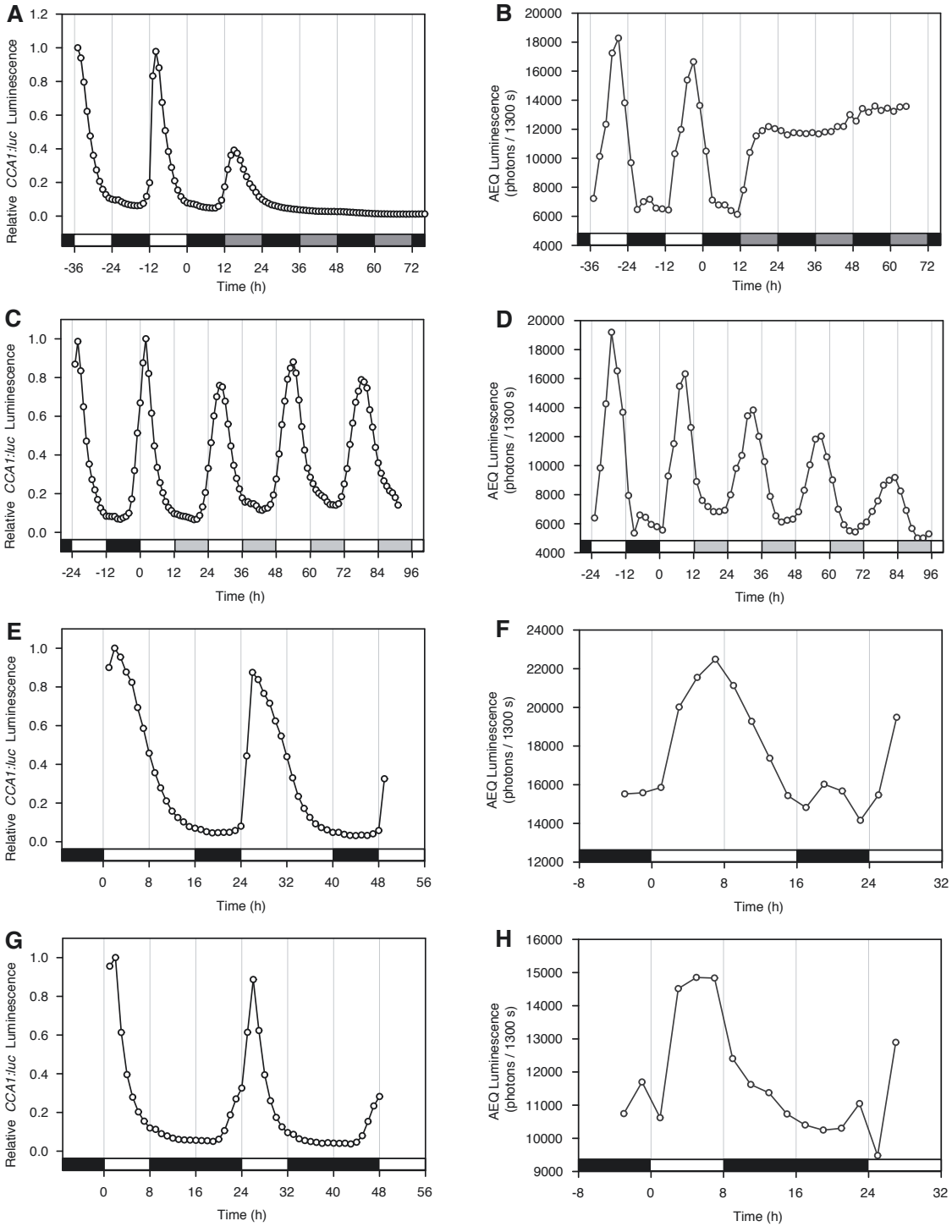

Figure 2.3: *CCA1:luc* and AEQUORIN luminescence data provide input and output signals for generation of linear state-space time-delay models.
(A,C,E,G) Relative *CCA1:luc* luminescence quantified for 10 day old *Arabidopsis* seedlings, where open red circles represent mean average of clusters of seedlings integrated for 800 s. (B,D,F,H) AEQUORIN luminescence quantified for 10 day old *Arabidopsis* seedlings, where open blue circles represent mean average of clusters of seedlings integrated for 1500 s. Seedlings were grown in entrained light-dark cycles prior to measurement in various conditions. Entrainment in L12/D12 photoperiod before transfer to constant (A,B) dark or (C,D) light. Entrainment and measurement is in cycles of (E,F) L16/D8 or (G,H) L8/D16. Bars on abscissa represent light regime in each experiment. White indicates light, black indicates dark, light grey is light in the subjective night and dark grey is dark in subjective daytime. Data collected by (A,E,G) Myself, (B,D) Dr. Carlos Hotta, University of Cambridge, UK, and (F,H) Dr. Katharine Hubbard, University of Cambridge, UK.

ing *CCA1:luc* or *35S:aeq* were exposed to three alternative photoperiodic regimes and luminescence quantified in each transgenic line. In addition to the DD estimation datasets (Figures 2.3A–B), this provided a total of four wild-type input-output datasets to assess model performance (Figure 2.3):

1. L12/D12 cycles before transfer to DD (L12/D12–DD)
2. L12/D12 cycles before transfer to LL (L12/D12–LL)
3. Entrained L16/D8 cycles (long day conditions)
4. Entrained L8/D16 cycles (short day conditions)

2.2.4 State-space time-delay systems

Mathematical models were constructed to describe experimental observations of $[Ca^{2+}]_{cyt}$ in 10 day old *Arabidopsis* seedlings (Figure 2.1), based on the expression of central oscillator genes and the availability of light. The extent to which the *CCA1*-dependent and light/dark-dependent pathways interact is not known, so their contribution is assumed independent throughout. The potential for light to regulate $[Ca^{2+}]_{cyt}$ via the clock is trivially covered by considering a single-input model. The underlying pathways which transduce circadian and light signalling events upstream of Ca^{2+} release have not been characterised, so these uncharacterised pathways are represented by delay parameters τ_i, as done previously (Herz *et al.*, 1996; Srividhya & Gopinathan, 2006; Sriram & Gopinathan, 2004). To model unknown pathways as explicit hidden variables could give rise to large numbers of state variables, increasing the complexity of parameter identification. Representing these pathways with delays reduces this complexity to a single parameter (per input pathway). Furthermore, identification of suitable delay steps may offer insight into the timing of $[Ca^{2+}]_{cyt}$ regulation. Due to the black-box nature of the problem, the simple model class of linear time-invariant (LTI) systems was chosen, as estimation of hidden states is possible through indirect systems identification (see Section 1.3.2). A continuous-time formulation was used as the underlying process is inherently continuous in time. Therefore, a single-output continuous-time state-space delay linear system with single or multiple inputs was chosen as the basis for mathematical modelling the regulation of basal $[Ca^{2+}]_{cyt}$ in *Arabidopsis*.

The proposed use of linear systems to describe biological systems is controversial, as molecular interactions are known to be both highly stochastic and nonlinear. We rationalise this decision by virtue of the many analytical tools available for linear systems that are not possible with nonlinear systems. These tools are utilised in this chapter to identify important properties of the biochemical network that regulates basal $[Ca^{2+}]_{cyt}$, including the identification of hidden variables (Sections 2.3.1 and 2.3.3), similarity transformations (Sections 2.3.6 and 2.3.7) and frequency response (Section 2.3.8). The sufficiency of linear systems in describing whole-plant dynamics is also demonstrated as models can be successfully cross-validated.

Let $x \in \mathbb{R}^n$ be the vector of state variables, comprising a state which represents $[Ca^{2+}]_{cyt}$ in the 1st entry, and a further $n-1$ unconstrained ('hidden') variables. Let $u \in \mathbb{R}^m$ be the vector of inputs. We define the state-space time-delay system as follows.

$$\begin{aligned} \frac{dx}{dt}(t) &= Ax(t) + Bu(t-\tau) \\ y(t) &= Cx(t) \end{aligned} \tag{2.1}$$

where $A \in \mathbb{R}^{nxn}$ is the matrix of interconnections, and $B \in \mathbb{R}^{nxm}$ is the input matrix.

Remarks

1. The transfer function representation of a delay linear system is related to the transfer function of a standard linear system, and may be found in terms of A, B and C by taking the Laplace transform of Eqn. 2.1. Let $X(s)$ be the Laplace transform of $x(t)$, $U(s)$ of $u(t)$ etc., then

$$\begin{aligned} sX(s) &= AX(s) + Be^{-s\tau}U(s) \\ \Rightarrow X(s) &= (sI - A)^{-1}Be^{-s\tau}U(s) \\ \Rightarrow Y(s) &= C(sI - A)^{-1}BU_\tau(s) = G(s)e^{-s\tau}U(s) \end{aligned}$$

   where $G(s) = C(sI - A)^{-1}B$ is the matrix of transfer functions $\mathscr{T}_{u\to y}$ for systems with zero delay. The additional term $e^{-s\tau}$ is not linear but may be thought of as an infinite-dimensional linear system, so might be well-approximated by additional state variables.

2. The internal structure of state variables in (delay) linear systems is not fixed. This is especially important when there are more state variables than measured outputs (i.e. there are

hidden variables), and it is not possible to set each state variable to be a measured variable (i.e. C as the identity matrix). A further consequence is that the dynamics of each hidden variable are not fixed. This notion is well understood in Control Theory, though we present a proof for completeness.

Proof. Suppose we have a general linear system (zero delay, without loss of generality) with m inputs, p outputs, and n state variables given by:

$$\begin{aligned} \frac{dx}{dt}(t) &= Ax(t) + Bu(t) \\ y(t) &= Cx(t) \end{aligned} \tag{2.2}$$

where $A \in \mathbb{R}^{nxn}$, $B \in \mathbb{R}^{nxm}$ and $C \in \mathbb{R}^{pxn}$. Consider a similarity transformation T such that $x = Tz$. Substituting into Eqn. 2.2 and taking the Laplace transforms leads to

$$\begin{aligned} sTZ(s) &= ATZ(s) + BU(s) \\ \Rightarrow Z(s) &= T^{-1}(sI - A)^{-1}BU(s) \\ \Rightarrow Y(s) &= CTT^{-1}(sI - A)^{-1}BU(s) \\ &= (C(sI - A)^{-1}B)U(s) \\ &= G(s)U(s) \end{aligned}$$

as before, and therefore co-ordinate transformations do not affect input-output dynamics.

□

3. The elements of u may have different delays, and so in general is defined as

$$u(t - \tau) = \begin{bmatrix} u_1(t - \tau_1) & u_2(t - \tau_2) & \dots & u_m(t - \tau_m) \end{bmatrix}^T \tag{2.3}$$

Definition of the model classes

Models are proposed either in which light is assumed to regulate $[Ca^{2+}]_{cyt}$ via changes in *CCA1* expression, or via an independent pathway. Let y be the model output corresponding to measured AEQUORIN luminescence, u_{CCA1} the measured *CCA1:luc* luminescence signal and u_{light} the light/dark input pathway. We first define the single input single-output (SISO) state-space time delay system.

SISO Model.

$$\begin{aligned} \frac{dx}{dt}(t) &= Ax(t) + bu_{CCA1}(t - \tau_{CCA1}) \\ y(t) &= \begin{pmatrix} 1 & 0 & \dots & 0 \end{pmatrix} x(t) \end{aligned} \tag{2.4}$$

where $A \in \mathbb{R}^{nxn}$ and $b \in \mathbb{R}^n$ are constant, and $x \in \mathbb{R}^n$ is the vector of state variables.

In the dual-input formulation, the light input pathway is considered to be a boolean variable. This gives rise to two further model classes, L_1 and L_0, which are described as follows:

L_1 and L_0 Models.

$$\begin{aligned} \frac{dx}{dt}(t) &= Ax(t) + B \begin{pmatrix} u_{CCA1}(t - \tau_{CCA1}) \\ u_{\text{light}}(t - \tau_{\text{light}}) \end{pmatrix} \\ y(t) &= \begin{pmatrix} 1 & 0 & \dots & 0 \end{pmatrix} x(t) \end{aligned} \tag{2.5}$$

where $A \in \mathbb{R}^{nxn}$ and $B \in \mathbb{R}^{nx2}$ are constant, and $x \in \mathbb{R}^n$ is the vector of state variables. The boolean value of u_{light} differs for L_1 and L_0 as:

Model	Light	Dark
L_1	1	0
L_0	0	1

2.2.5 Parameter estimation of delay linear systems

There currently exists no published method of estimating the delay parameters explicitly, so instead delay linear systems are estimated for a pre-specified generous range of delay values. For two input systems, delay value pairs on an evenly-spaced grid are considered. While this appears far from elegant, we are at least forced to cover all plausible combinations of delays, obtaining a performance measure across the pre-specified range. Upon prescribing the delay vector τ, the problem reduces to a standard systems identification problem and we are required only to generate the input-output data pairs with the appropriate time-spacing. Therefore the identification procedure consists of a data pre-processing stage in which the input-output data pairs are defined, followed by the parameter estimation of A and B in Eqn. 2.1 using PEM.

For pre-processing of the input-output data, consider the output observations $y^{(k)} = y(t = t_k)$ for $t_k \in T_y$ where T_y is the set of time-points corresponding to the observations. Let $u_i^{(l)} =$

$u_i(t = t_l)$ be the observations of the i^{th} input for $t_l \in T_{u_i}$ where T_{u_i} is the set of time-points corresponding to the observations of u_i. Denote the input-output dataset subject to delays τ by (u_τ, y). We form (u_τ, y) by finding values $u_1(t_k - \tau_1), u_2(t_k - \tau_2), \ldots$ for each $t_k \in T_y$ using linear interpolation, which enables non-integer values of τ. We assume that the measured signal does not deviate too far from the interpolated values. Finally, the dataset (u_τ, y) is restricted to the intersection of the existing data $T_y \cap T_{u_\tau}$, so data outside this range are not considered.

Each linear system parameter set was estimated using the prediction-error method (PEM), implemented in the Systems Identification Toolbox of MATLAB$^{\text{TM}}$ (*pem* function; Ljung, 1999). PEM falls under the class of indirect methods for continuous-time linear systems identification, in which a discrete time system is estimated and converted back to continuous time. Suppose we know x at $t = t_k$, then x can be computed for any $t = t_{k+1} > t_k$ as

$$x(t_{k+1}) = e^{A(t_{k+1}-t_k)}x(t_k) + \int_{t_k}^{t_{k+1}} e^{A(t_{k+1}-\lambda)}Bu(\lambda)d\lambda \tag{2.6}$$

If the observations obtained are uniformly spaced in time with sampling interval T and we assume that the input $u = u_k$ is constant for $t_k < t < t_{k+1}$ (i.e. zero-order hold, ZOH), then we obtain the discretisation of Eqn. 2.2:

$$x_{k+1} = Fx_k + Gu_k \tag{2.7}$$

where $t_k = t(kT)$, $u_k = u(kT)$, $x_k = x(kT)$, $F = e^{AT}$, $G = \int_0^T e^{A\tau}d\tau B$. It now remains to estimate the entries in F and G and then convert back to A and B. The prediction-error method seeks to minimise the squared differences between each measured point and the model prediction generated from the previous point (Ljung, 1999).

The output estimation data were further pre-processed so that the sample interval T was consistent between the input dataset (*CCA1:luc* luminescence; Figure 2.3A) and the AEQUORIN luminescence output estimation data (Figure 2.3B). This also enabled suitable values of u_{light} to be assigned across a dark to light transition. The implementation of the iterative prediction-error minimization (PEM) algorithm in MATLAB$^{\text{TM}}$ (*pem* function) only enables a zero-order hold (ZOH) intersample behaviour. As AEQUORIN luminescence has been measured at odd-numbered hours relative to dawn, transitions between light and dark cannot be accounted for, as a constant value of u_{light} 1 hour before a dark to light transition would not

switch until 1 hour after the switch *in planta*. Ignoring these considerations and applying the same analysis as for single-input models would only enable estimation of models with light input delays of 1 h, 3 h, 5 h etc. Otherwise, there are a number of options:

1. Re-measure AEQUORIN luminescence at even hours rather than odd hours. However, when quantifying luminescence with a photon counting camera, there must be no external light, so it would not be possible to measure a transition from dark to light.

2. Extra points could be appended to the output estimation dataset using the *misdata* function from the Systems Identification Toolbox in MATLAB^{TM}, which may be used for estimating missing data points.

3. A crude estimation of the missing points y_k could also be achieved by simply interpolating between the values y_{k-1} and y_{k+1} for each k.

To avoid potentially unhelpful additional experimentation, option 1 was rejected. Estimating 'missing data' treats missing points as extra parameters, vastly increasing the size of the parameter space. Since the number of 'missing points' is an order of magnitude larger than the number of model parameters in the linear system, this method is highly undesirable and leads to spurious results (simulation not shown). The third approach was simplest, and therefore most appropriate. Therefore, all models were estimated using the output estimation data with interpolated mid-points at even-valued times through the circadian cycle.

We sought to obtain the simplest model which accounted for the available data, and therefore assumed that the state-space realisations estimated are minimal. That is, the input-output behaviour (transfer function) may be described by the minimum number of state variables. Since our state-space realization is minimal, it is both controllable and observable (Chen, 1998). The state-space realisation was fixed in controller canonical form, to guarantee controllability of the resulting system (Chen, 1998). The *pem* command in MATLAB^{TM} has an option to return state-space models in a variant of the controller canonical form, defined as follows:

$$\frac{dx}{dt} = \begin{pmatrix} 0 & 1 & 0 & \dots & 0 \\ 0 & 0 & 1 & \dots & 0 \\ \vdots & & & \ddots & \vdots \\ 0 & 0 & \dots & 0 & 1 \\ a_1 & a_2 & a_3 & \dots & a_n \end{pmatrix} x + \begin{pmatrix} b_{11} & \dots & b_{1m} \\ \vdots & & \vdots \\ b_{n1} & \dots & b_{nm} \end{pmatrix} u \tag{2.8}$$

$$y = \begin{pmatrix} 1 & 0 & \dots & 0 \end{pmatrix} x \tag{2.9}$$

Further options of the *pem* function were set, to achieve the desired linear state-space model. Continuous-time models are estimated by setting the sample interval equal to 0, achieved by setting the options `'Ts',0`. We assumed the input signals were noise-free, as this both improved the resulting model performances (data not shown) and reflected the knowledge that the *CCA1:luc* luminescence signal is an order of magnitude brighter than AEQUORIN luminescence and as such has a more desirable signal-to-noise ratio. To implement this assumption, we enforced the Kalman matrix to be 0 by including `'Disturbance','None'` in the *pem* function call. In summary, models were estimated throughout by issuing the following command:

```
MODEL = pem(data,n,'Ts',0,'SSParameterization','Canonical', ...
        'DisturbanceModel','None')
```

where `n` is the model order sought.

2.2.6 Model selection - Akaike's Information Criterion (AIC)

Selection of the optimal delays is achieved by selecting the model with the best performance. The Akaike Information Criterion (AIC; Akaike, 1974) offers a method for assessing performance, relative to the number of estimated parameters. This criterion incorporates two penalty terms: a measure of the distances between experimental data and simulated output, and a term proportional to the number of parameters. A normalisation of the AIC is implemented in MATLAB™ as

$$\mathrm{AIC} = \frac{2(k - \log L)}{N} \tag{2.10}$$

where L is the maximised value of the likelihood function, k is the number of estimated parameters (including the initial conditions) and N is the number of data-points. Assuming Gaussian noise with covariance matrix Λ, the logarithm of the likelihood function is given by

$$l(\theta, \Lambda) = \log L(\theta, \Lambda) = -\frac{1}{2} \sum_{i=1}^{N} \epsilon_i(\theta) - \frac{N}{2} \log(\det \Lambda) \tag{2.11}$$

where ϵ_i is the difference between the measured value y_i and simulated output $\hat{y}_i$. Maximising the log-likelihood with respect to θ and Λ gives (Ljung, 1999)

$$l_{\max}(\hat{\theta}, \hat{\Lambda}) = \frac{N}{2}(1 + \log V) \tag{2.12}$$

where V is the loss function given by

$$V = \det\left(\frac{1}{N}\sum_{i=1}^{N}\epsilon_i(\hat{\theta})\epsilon_i(\hat{\theta})^T\right) \tag{2.13}$$

The AIC offers a method for comparing models of the same order with different delays, and also models of varying order. In our analysis, we use the small sample (second-order bias correction) version of the AIC, AIC_c (Hurvich & Tsai, 1989). The normalised AIC_c can be evaluated as

$$\text{AIC}_\text{c} = \text{AIC} + \frac{2k(k+1)}{N(N-k-1)} \tag{2.14}$$

with N,k as above.

2.2.7 Simulation of delay linear systems for comparison with input-output data

The estimation of continuous-time linear systems implicitly solves the model equations in a discretised form, forcing a zero-order hold (ZOH) intersample behaviour for the input signal u. For cross-validation purposes, the performance of each estimated model is evaluated using a first-order hold (FOH, linear interpolation) intersample behaviour, to better approximate the continuous-time nature of the *CCA1:luc* luminescence input signal. These simulations were conducted for each of the four *CCA1:luc* luminescence datasets available (Figure 2.3). The model equations were solved numerically using the *ode23* solver in MATLAB$^{\text{TM}}$ (Shampine & Reichelt, 1997) and simulated outputs were obtained every 0.2 h for analysis of oscillation phase.

To quantify the performance during cross-validation, Pearson's product-moment sample correlation coefficient (r) was computed between AEQUORIN luminescence data and corresponding simulated output using MATLAB$^{\text{TM}}$'s *corr* function. The sample correlation coeffi-

cient between vectors x and y is defined as

$$r(x,y) := \sum_{i=1}^{N} \left(\frac{x_i - \bar{x}}{||x_i - \bar{x}||_2} \cdot \frac{y_i - \bar{y}}{||y_i - \bar{y}||_2} \right) \tag{2.15}$$

where $\bar{x}$ and $\bar{y}$ are the sample means of x and y respectively and N is the number of entries in x and y. For each of the wild-type datasets available for estimation and cross-validation, r_D (L12/D12–DD), r_L (L12/D12–LL), r_{LD} (L16/D8) and r_{SD} (L8/D16) are defined accordingly.

For graphical display of each models performance, the simulated outputs are rescaled so they overlap with the measured data according to the linear map $y \mapsto ay + b$ which solves the minimisation problem

$$\min_{a,b} \sum_{i=1}^{N} (y^{(i)} - a\hat{y}^{(i)} - b)^2 \tag{2.16}$$

where $y^{(i)}$ is the i^{th} AEQUORIN luminescence sample, and $\hat{y}^{(i)}$ the corresponding simulated output. Note that the calculation of the sample correlation r is invariant to linear rescalings of this type. The minimisation problem (Eqn. 2.16) is solved using the *polyfit* function in MATLAB$^{\text{TM}}$.

2.3 Results

2.3.1 Regulation of $[Ca^{2+}]_{cyt}$ by a *CCA1*-dependent pathway: Estimation of single-input models

In this section, models are presented in which $[Ca^{2+}]_{cyt}$ is regulated by a single pathway, which is dependent on the expression of *CCA1*. The *SISO* model class Eqn. 2.4 was used to test the hypothesis that light regulates basal $[Ca^{2+}]_{cyt}$ via changes in the expression of *CCA1*. Preprocessing the input-output data is necessary for estimation of the *SISO* model. As the input signal tends towards zero in DD, we must ensure that the output approaches zero also. To enforce this, the average of the output signal between $t = 19$ h and $t = 63$ h (equal to 12457 photons / 1300 s) was subtracted from the output estimation vector and Eqn. 2.1 was changed

to

$$\begin{aligned} \frac{dx}{dt}(t) &= Ax(t) + Bu(t - \tau_{CCA1}) \\ y(t) &= Cx(t) + d \end{aligned} \tag{2.17}$$

where d is the steady value of the output signal y.

The system matrices A and B were estimated for τ_{CCA1} ranging between 0 h and 10 h in 0.1 h increments (Figure 2.4). For estimation of 1st and 2nd order models, AIC_c was a reasonably smooth function of the delay parameter τ_{CCA1} (Figure 2.4A). However, numerical instabilities could be observed in the estimation of 3rd and 4th order systems. The AIC_c of the best delay choice decreased as the model order was increased (Table 2.1), though inspection of the simulated output with respect to the estimation dataset revealed a lack of improvement beyond 2nd order (Figure 2.4B). In keeping with the philosophy that the lowest order should be selected for equivalent performance, these results suggest that AIC_c may not be penalising extra parameters sufficiently.

2.3.2 Cross-validation of the single-input model: Selection of optimal order and delay steps

Cross-validation tests were carried out to see whether the models estimated were applicable to alternative conditions (Section 2.2.3). The sample correlation coefficients (r_D, r_L, r_{LD} and r_{SD}; Eqn. 2.15) were computed between model simulated output and AEQUORIN luminescence data (Figure 2.5) using a first-order hold (FOH, linear interpolation) intersample definition. The sample correlation coefficient values for 1st order models were very low for large ranges in τ_{CCA1}, indicating a poor validation. However, performance improved for r_D (Figure 2.5A) and r_L (Figure 2.5B) when τ_{CCA1} was greater than 10 h. 2nd–4th order models showed greater homogeneity across this range of τ_{CCA1}, achieving higher performance than 1st order models in all datasets compared for nearly all τ_{CCA1} (Figure 2.5). However, it was difficult to distinguish the performance of higher order systems with only the sample correlation coefficients r_D, r_L, r_{LD} and r_{SD}.

For each model order, an optimal delay was chosen that maximised a weighted sum of the

Table 2.1: Optimal choice of τ_{CCA1} for each order of *SISO* models after parameter estimation. Entries correspond to the minimum AIC_c value observed over the range of τ_{CCA1} for each model order up to 4.

Order	τ_{CCA1}	AIC_c
1	10.0	15.12
2	9.1	13.59
3	8.5	13.19
4	0.5	13.12

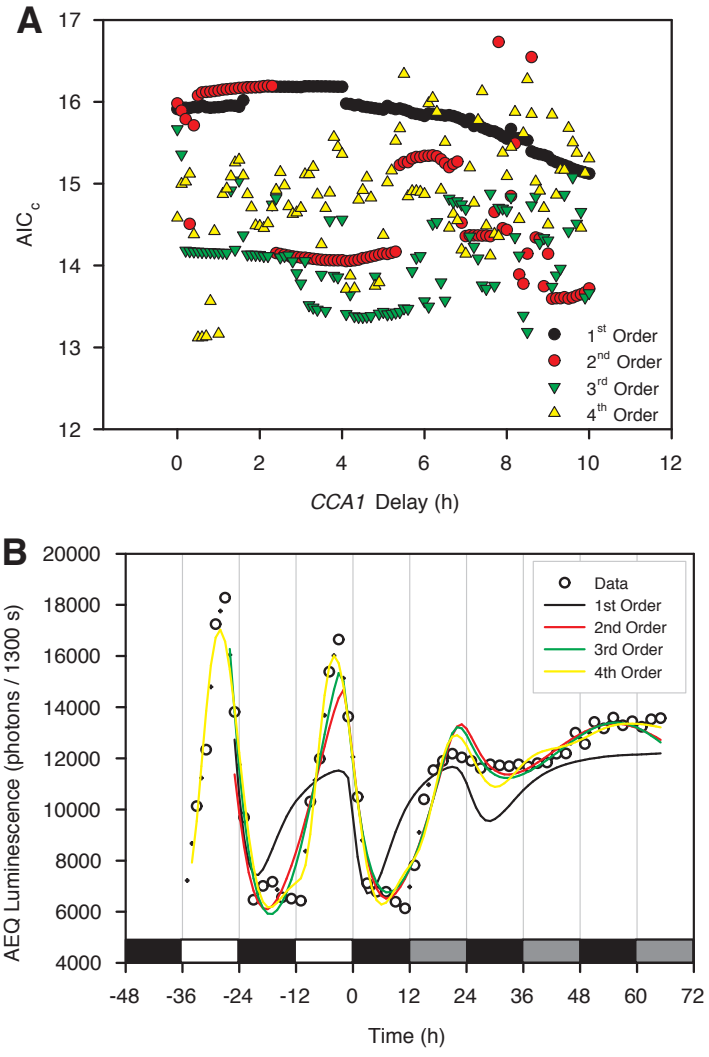

Figure 2.4: Estimation of *SISO* models for the regulation of $[Ca^{2+}]_{cyt}$ by a *CCA1*-dependent pathway. Relative *CCA1:luc* and AEQUORIN luminescence data from *Arabidopsis* seedlings entrained to L12/D12 cycles before transfer to DD (Figure 2.3) were pre-processed to reflect each value of τ_{CCA1} between 0 h and 15 h in 0.1 h increments. Continuous-time linear state-space models of orders 1 to 4 were computed with the *pem* function in the Systems Identification Toolbox for MATLAB^{TM}(Ljung, 1999). (A) AIC_c was computed for each model estimated by adding the output of the *aic* function in MATLAB^{TM} (Ljung, 1999) to the second-order bias correction as in Eqn. 2.14. (B) Simulated output for models with τ_{CCA1} corresponding to the lowest AIC_c for each order 1 to 4 (see Table 2.1 for values). Simulated output values obtained from the *compare* function in MATLAB^{TM}. Bars on abscissa represent light availability, white indicates light, black indicates dark, and dark grey indicates darkness during subjective daytime.

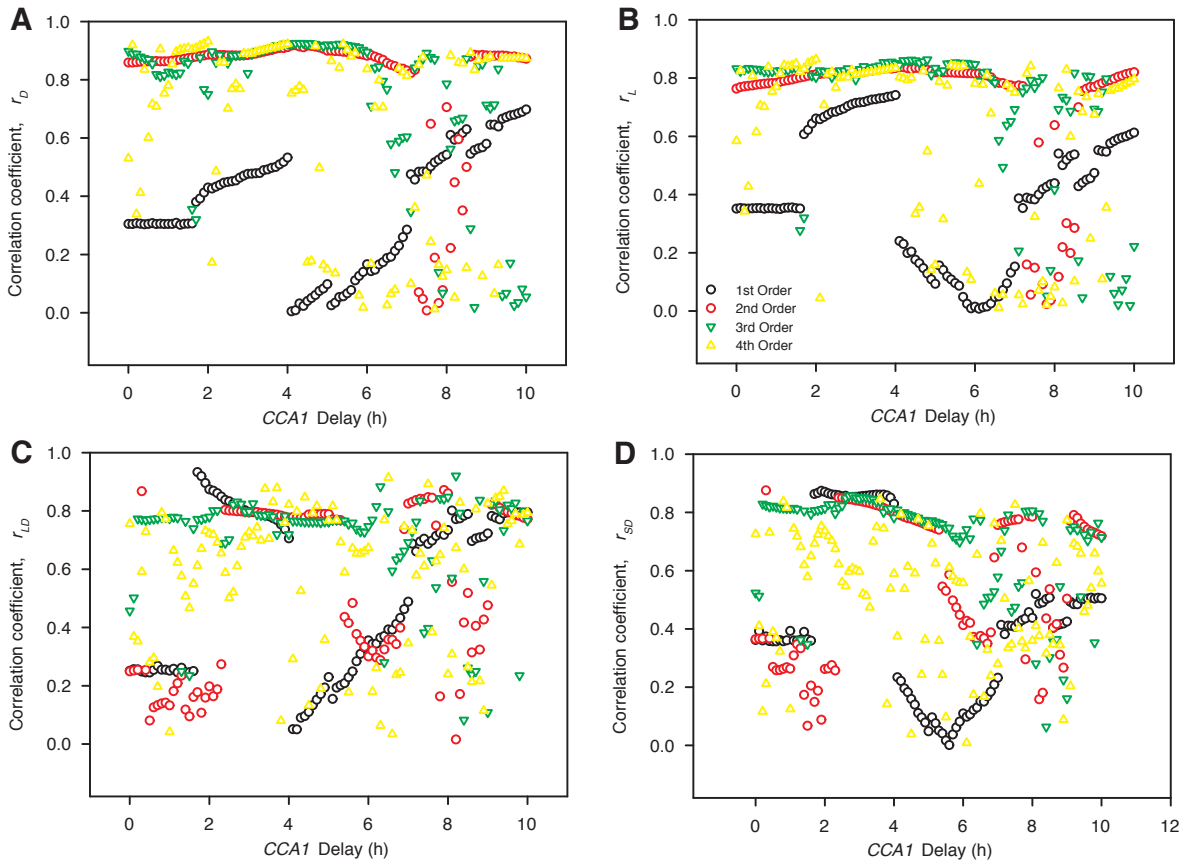

Figure 2.5: Correlation of single input model simulations to AEQUORIN luminescence data. Model equations were solved numerically with MATLAB™'s *ode23* solver (Shampine & Reichelt, 1997) to provide simulations of experimental conditions. Each linear model estimated was stimulated by the first 24 h of relative *CCA1:luc* luminescence data in light-dark cycles until transients disappeared. Then the appropriate full input dataset was fed into the model and outputs taken at time-points corresponding to measured AEQUORIN luminescence. The sample correlation coefficient between simulated model output and AEQUORIN luminescence data was computed using the *corr* function in MATLAB™. Simulations reflect (A) entrainment to L12/D12 cycles before transfer to DD, (B) entrainment to L12/D12 cycles before transfer to LL, (C) entrainment to L16/D8 cycles and (D) entrainment to L8/D16 cycles.

Table 2.2: Optimal choice of τ_{CCA1} for each order of single-input models after cross-validation. Entries correspond to the minimum value of $r_w = n_D r_D + n_L r_L + n_{LD} r_{LD} + n_{SD} r_{SD}$ for each model order. r_D, r_L, r_{LD} and r_{SD} are the sample correlation coefficient values between simulated model output and AEQUORIN luminescence data from seedlings in experimental conditions L12/D12–DD, L12/D12–LL, L16/D8 and L8/D16 respectively. n_D, n_L, n_{LD} and n_{SD} are the corresponding numbers of observations in each dataset.

Order	τ_{CCA1}	r_w
1	4.0	101.12
2	3.9	132.66
3	4.2	134.56
4	4.2	133.12

sample correlation coefficients, defined as

$$r_w := n_D r_D + n_L r_L + n_{LD} r_{LD} + n_{SD} r_{SD} \tag{2.18}$$

where the n_d are the number of observations in dataset d (see Table 2.2 for optimal locations). This enabled us to analyse complexity with respect to the estimation and validation datasets. The simulated outputs in each condition are plotted for optimal-delay choices for each order (1–4) in Figure 2.6. As observed during the estimation of each model, 1st order models per-

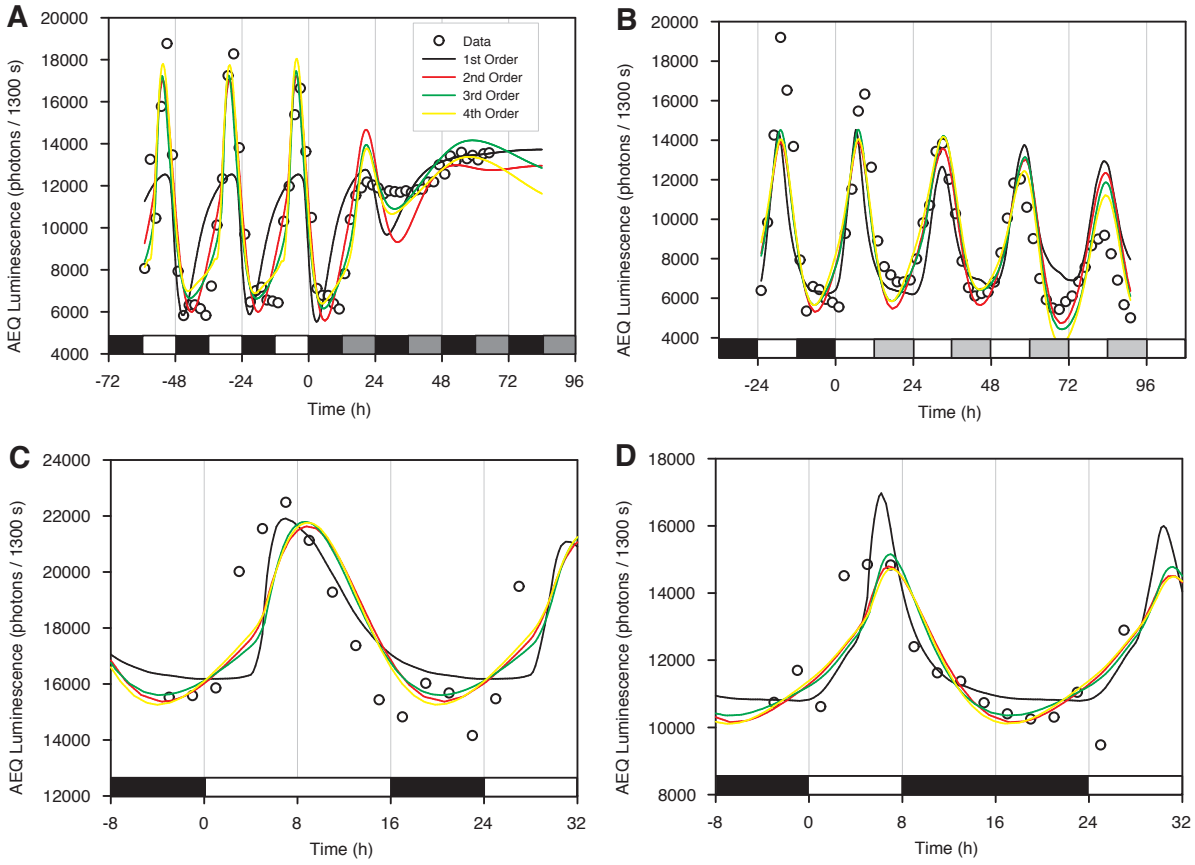

Figure 2.6: Cross-validation of optimal-τ_{CCA1} linear models for different orders with AEQUORIN luminescence data.
Linear state-space model equations solved numerically with MATLAB^{TM}'s *ode23* solver (solid lines; Shampine & Reichelt, 1997). For each order, models were simulated for the optimal choice of τ_{CCA1}, defined as the minimum of the weighted sum of sample correlation coefficients, r_w (Eqn. 2.18; see Table 2.2 for values). AEQUORIN luminescence data from Figure 2.3 (open circles), with interpolated mid-points at even-valued time-points also used for model estimation (crosshairs). Simulated outputs scaled to overlap with AEQUORIN luminescence data by finding the best linear scaling of the form $a\hat{y} + b$, where $\hat{y}$ is the simulated output. a and b are the solutions to $\min_{a,b} \sum_i^{N_d} (y^{(i)} - a\hat{y}^{(i)} - b)^2$ where $y^{(i)}$ are the measured AEQUORIN luminescence values and N_d is the number of data values. Solution found using the *polyfit* function in MATLAB^{TM}. Bars on abscissa represent light regime in each experiment/simulation. White indicates light, black indicates dark, light grey (B) is light in the subjective night and dark grey (A) is dark in subjective daytime.

formed poorly and no improvement could be seen above 2nd order, indicating that the most suitable number of state variables is 2 in this model class. Optimal-τ_{CCA1} 2nd–4th order models were unable to reproduce a non-oscillatory tendency towards steady state in DD (Figure 2.6A), though they produced oscillations in LL with the appropriate phase (Figure 2.6B). The phase of the oscillation peaks in entrained L16/D8 (Figure 2.6C) and L8/D16 (Figure 2.6D) cycles were also accurate to within 1 hour. However, for all model orders, simulated outputs did not well characterise the tendency towards a constant steady state in DD (Figure 2.6A), nor were they able to distinguish amplitude between L12/D12 cycles and LL (Figure 2.6B). Furthermore, the rapid increase in $[Ca^{2+}]_{cyt}$ following dark to light transitions in L16/D8 and L8/D16 was not predicted by the *SISO* models (Figures 2.6C,D).

2.3.3 Dual regulation of $[Ca^{2+}]_{cyt}$ by *CCA1* and light: Estimation of dual-input model classes

To investigate the possibility that $[Ca^{2+}]_{cyt}$ is independently regulated by the central oscillator (*CCA1*) and light/dark, two-input continuous-time linear systems with delays (τ_i, distinct) at each input were estimated. For the L_1 model class ($u_{light} = 1$, light; $u_{light} = 0$, dark), the same output translation (Eqn. 2.17) as for the *SISO* model was used, as both inputs approach zero in DD. However, for the L_0 model ($u_{light} = 0$, light; $u_{light} = 1$, dark), the DD steady state becomes $x_2 + b_{12} + d$ ($x_2 \neq 0$), providing some choice in the assignment of d. The minimum level of AEQUORIN luminescence across the estimation dataset ($d = 5818.6$) was taken in an effort to reproduce the locally constant basal level in the dark phase of L12/D12 cycles (Figure 2.3B), during which both *CCA1:luc* luminescence and light input values are near 0.

Two-input linear state-space models were computed using PEM for $\tau_{CCA1} = 0, 0.1, \ldots, 10$ and $\tau_{light} = 0, 1, \ldots, 5$, similarly to the method in Section 2.3.1. Each combination of delay parameter pairs, models up to 4th order, and both model classes (L_1 and L_0) were considered. As the model order increased, the variability between neighbouring values of τ_{CCA1} increased, presumably as a result of the numerical instabilities of the PEM algorithm (Figure 2.7). 1st order models performed better for larger τ_{light} in both the L_1 (Figure 2.7B) and L_0 (Figure 2.7A) light input classes, with AIC_c being a smooth function of τ_{CCA1} throughout. The 2nd order models were optimised by τ_{CCA1} near 8 h for L_1 (Figure 2.7D) and 4 h for L_0 (Figure 2.7C), though the distinction between different choices of τ_{light} was very small. Due to the high variability be-

tween neighbouring values of τ_{CCA1}, it was not possible to conclude about the optimal pathway delays for 3rd (Figures 2.7E,F) and 4th (Figures 2.7G,H) order models.

The AIC_c performance was analysed for the best choice of τ_{CCA1} over different orders, τ_{light} and light input scheme (see Table 2.3 for values). Optimal-τ_{CCA1} model performance showed some similarity between light schemes L_1 and L_0 for each order (Figure 2.8A,B). Increasing from 1 to 2 internal states represented the largest improvement in the AIC_c. However, in both cases 4 states was optimal. We suspected that AIC_c did not penalise extra parameters sufficiently for deciding the most suitable model order. Also plotted are the AIC_c performances for models for no delays (τ_{CCA1}= 0, τ_{light}= 0), which demonstrate that the provision of a nonzero τ_{CCA1} in 2nd order models may be accounted for by an additional state variable (Figure 2.8A). Despite obtaining similar AIC_c scores, the simulated output of 2nd order models (with optimal choice of τ_{CCA1}) using the L_0 scheme described the AEQUORIN luminescence data with more accuracy than the optimal-τ_{CCA1} L_1 models; L_0 models gave similar outputs irrespective of τ_{light} and reflected the rapid loss of oscillations seen after a period of extended dark (Figure 2.8C), while 2nd order L_1 models had undesirable damped oscillations in DD (Figure 2.8D). Optimal-τ_{CCA1} 4th order L_0 models obtained a near-perfect fit to the estimation data for all τ_{light} investigated (Figure 2.8E), and again were more representative of the AEQUORIN luminescence data than L_1 models, which appeared to exhibit some higher-frequency modes (Figure 2.8F). These results indicated a clear preference towards the L_0 light scheme.

Table 2.3: Optimal τ_{CCA1} for each τ_{light} in 2nd and 4th order L_0 and L_1 models.
Entries correspond to the values of τ_{CCA1} which minimise the AIC_c for each choice of τ_{light} for 2nd and 4th order models in both L_0 and L_1 light regimes. AIC_c was computed for each model estimated by adding the output of the *aic* function in MATLAB™ (Ljung, 1999) to the second-order bias correction as in Eqn. 2.14.

	L_0				L_1			
Order	2		4		2		4	
τ_{light}	τ_{CCA1}	AIC_c	τ_{CCA1}	AIC_c	τ_{CCA1}	AIC_c	τ_{CCA1}	AIC_c
0	3.8	13.17	0.0	11.77	7.4	13.23	8.5	12.13
1	4.5	13.12	0.5	11.95	8.1	13.17	9.1	12.18
2	5.5	13.41	0.4	11.95	8.1	13.26	5.4	12.77
3	3.5	13.33	0.3	11.66	8.3	13.35	8.6	12.26
4	4.2	13.36	0.1	11.66	9.0	13.48	9.6	12.45
5	4.4	13.29	0.1	11.68	9.0	13.47	2.6	12.60

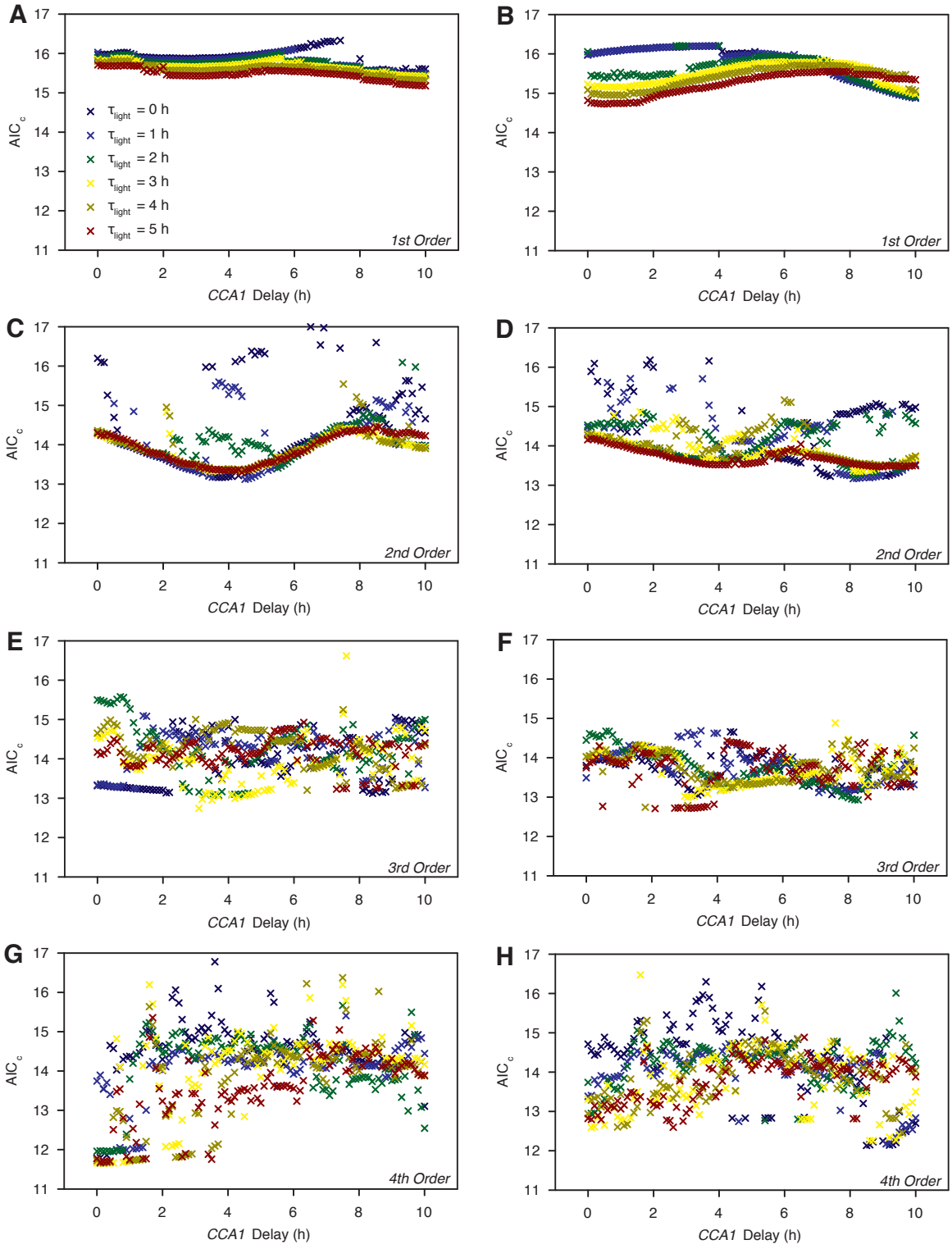

Figure 2.7: AIC_c performance of dual-input linear state-space time-delay systems for the regulation of $[Ca^{2+}]_{cyt}$.
Relative *CCA1:luc* and AEQUORIN luminescence data from *Arabidopsis* seedlings entrained to L12/D12 cycles before transfer to DD were pre-processed to reflect each value of τ_{CCA1} in between 0 h and 10 h in 0.1 h increments and τ_{light} between 0 h and 5 h in 1 h increments. The light input was defined to be (A,C,E,G) 0 during light, and 1 during dark, or (B,D,F,H) 1 during light, and 0 during dark. Continuous-time linear state-space models were then computed with the *pem* function in the Systems Identification Toolbox for MATLAB^{TM}(Ljung, 1999). AIC_c was computed for each model estimated by adding the output of the *aic* function in MATLAB^{TM} (Ljung, 1999) to the second-order bias correction as in Eqn. 2.14. The number of state variables in each model was (A,B) 1, (C,D) 2, (E,F) 3, and (G,H) 4.

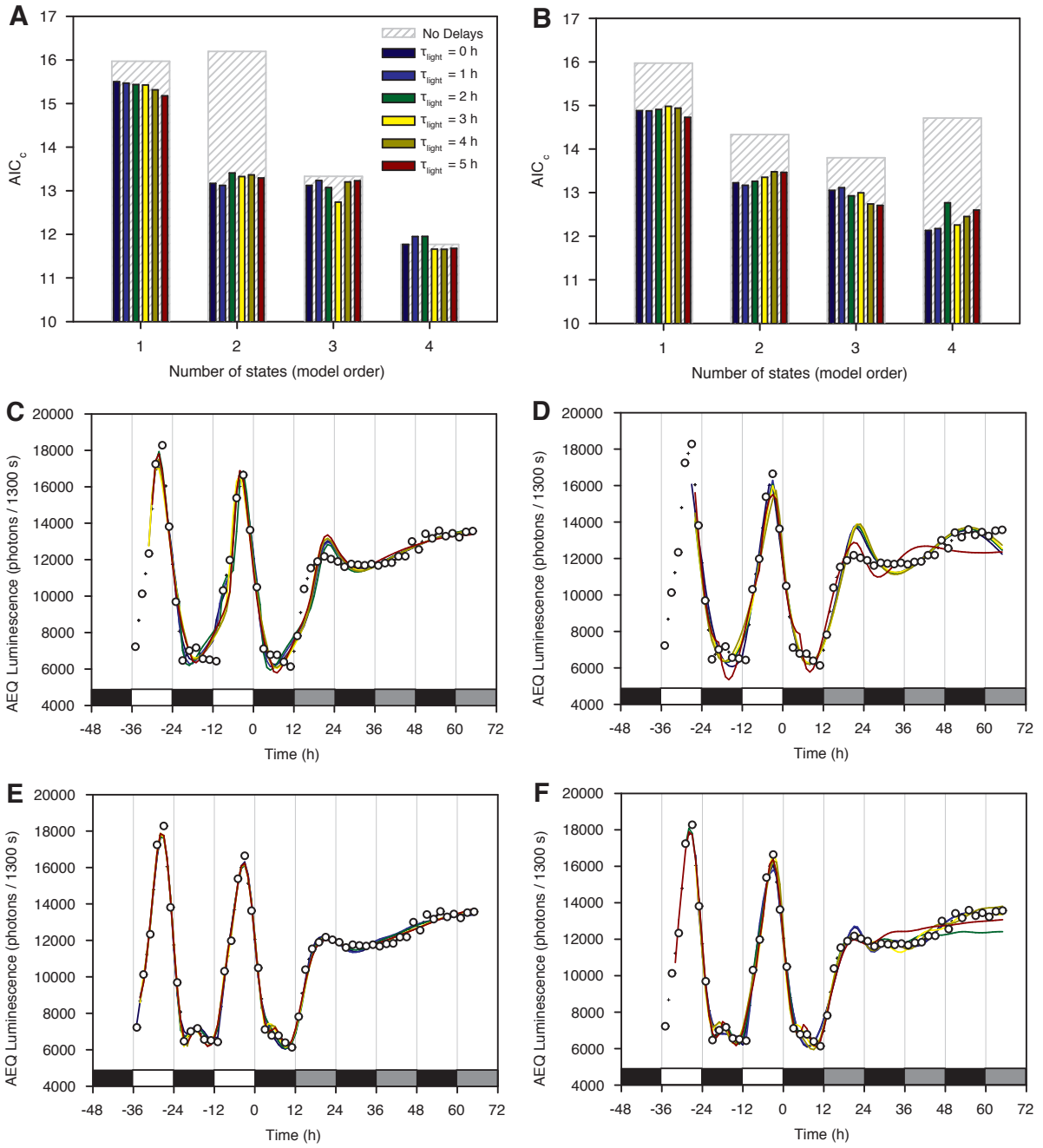

Figure 2.8: L_0 models are more accurate than L_1 models during estimation.
Estimation of the dual-input model classes comparing (A,C,E) L_0 and (B,D,F) L_1 light regimes. (A,B) AIC_c for the optimal τ_{CCA1} for each order and choice of τ_{light} (for values, see Table 2.3). Grey hatched underlays are the AIC_c values for models with $\tau_{CCA1}= 0$ and $\tau_{light}= 0$ and different n. AIC_c was computed for each model estimated by adding the output of the *aic* function in MATLAB^{TM} (Ljung, 1999) to the second-order bias correction as in Eqn. 2.14. (C–F) Linear state-space model equations solved numerically with MATLAB^{TM}'s *ode23* solver (solid lines; Shampine & Reichelt, 1997). Simulated outputs (solid lines) of optimal-τ_{CCA1} models, for each choice of τ_{light}, are compared against measured AEQUORIN luminescence data (black circles) and interpolated midpoints (crosshairs) used during estimation process (see text for further details). Shown are (C,D) 2nd order and (E, F) 4th order models. Measured data and simulations reflect $[Ca^{2+}]_{cyt}$ in *Arabidopsis* seedlings entrained to L12/D12 cycles before transferred to DD. Bars on abscissa represent light availability, white indicates light, black indicates dark, and dark grey indicates darkness during subjective daytime.

2.3.4 Cross-validation of the dual-input model classes

Estimation of the dual-input model class revealed that the way in which we define the light input, and in turn the system steady state, had a profound effect on the resulting performance and optimal delay-parameter choices. Defining light to be 0, and dark to be 1 (L_0) enabled a much closer fit to the estimation data for all orders (Figure 2.8). Depending on the value of τ_{light}, the optimal choice of τ_{CCA1} was between 3.5 h and 5.5 h for 2$^{\text{nd}}$ systems, and between 0 h and 0.5 h for 4$^{\text{th}}$ order systems (Table 2.3). This provided evidence that additional state variables can account for the delay between *CCA1* expression and the regulation of $[Ca^{2+}]_{\text{cyt}}$. Almost no difference could be observed in the simulated outputs between the different lengths of τ_{light} tested. This indicated that the linear state-space description was insensitive to this delay, and able to account for it implicitly in the choice of system matrices A and B. In order to select the most appropriate mathematical description of the regulation of $[Ca^{2+}]_{\text{cyt}}$, we needed to better distinguish between different choices of the light delay τ_{light}.

Cross-validation was performed for the L_0 models with the AEQUORIN luminescence data from Figure 2.3, as done for the single-input models in Section 2.3.2, computing the correlations r_D, r_L, r_{LD} and r_{SD} for each 2$^{\text{nd}}$ and 4$^{\text{th}}$ order L_0 model estimated (Figure 2.9). The sample correlation coefficients were a smooth function of τ_{CCA1} for each choice of τ_{light} in the 2$^{\text{nd}}$ order model class (Figure 2.9). With respect to the dataset used for estimation (L12/D12–DD), the best choice of τ_{CCA1} was between 4.5 h and 5.6 h, for all τ_{light} (Figure 2.9A). The optimal choice of τ_{CCA1} was shorter for validation sets L12/D12–LL (2.5–4.5 h; Figure 2.9C) and L8/D16 (0.8–1.1 h; Figure 2.9G). For L16/D8 cycles, the optimal choice of τ_{CCA1} was very high when $\tau_{\text{light}} \leq$ 1 h ($\tau_{CCA1} >$ 9 h) and very low when $\tau_{\text{light}} \geq$ 2 h ($\tau_{CCA1} <$ 0.2 h; Figure 2.9E). The performance of 4$^{\text{th}}$ order models with respect to sample correlation at optimised choices of τ_{CCA1} was generally no better than for 2$^{\text{nd}}$ order models, though showed less dependence on the value of τ_{CCA1} (Figures 2.9B,D,F,H). A marked improvement was seen in 4$^{\text{th}}$ order models when comparing L16/D8 cycles (Figure 2.9F), though they performed poorly in L8/D16 cycles (Figure 2.9H). In conclusion, the additional 2 state variables offered a very minor improvement to a given model's ability to match the shape of the AEQUORIN luminescence data, though were able to shorten the delay steps required between input and output signals. However, no further progress was made in selecting the most appropriate choice of τ_{light} by considering the sample correlation coefficients.

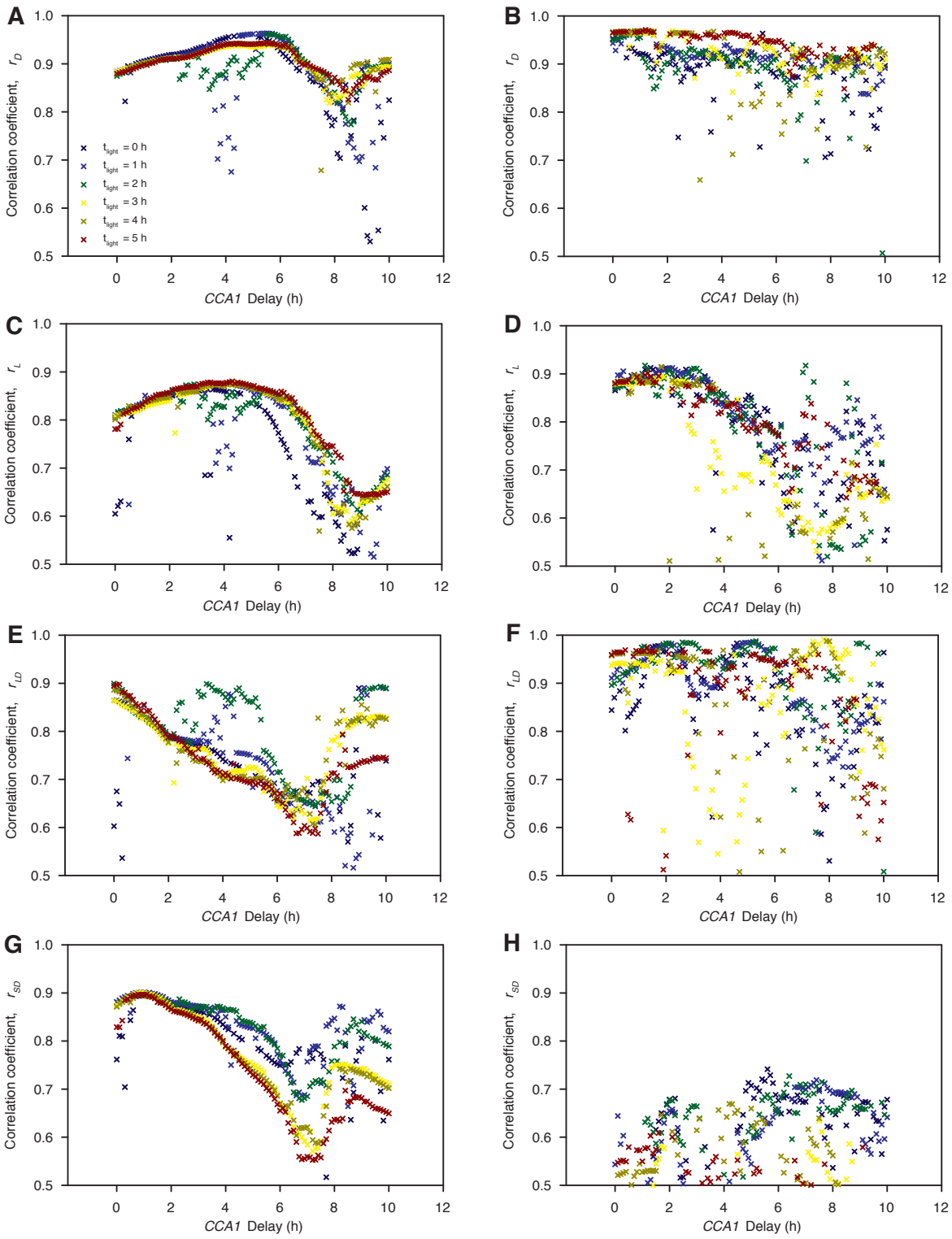

Figure 2.9: Correlation of L_0 dual-input model simulations to $[Ca^{2+}]_{cyt}$ data
Model equations were solved numerically with MATLAB^{TM}'s *ode23* solver (Shampine & Reichelt, 1997) to provide simulations of experimental conditions. Each linear model estimated was stimulated by the first 24 h of relative *CCA1:luc* luminescence data and corresponding light input (L_0) values in light-dark cycles until transients disappeared. Then the appropriate full input dataset was fed into the model and outputs taken at time-points corresponding to measured AEQUORIN luminescence. The sample correlation coefficient between simulated model output and AEQUORIN luminescence data computed using the *corr* function in MATLAB^{TM} for (A,C,E,G) 2nd order, and (B,D,F,H) 4th order models. (A,B) Entrainment to L12/D12 cycles before transfer to DD. (C,D) Entrainment to L12/D12 cycles before transfer to LL. (E,F) Entrainment to L16/D8 cycles. (G,H) Entrainment to L8/D16 cycles.

Table 2.4: Optimal choice of τ_{CCA1} for each τ_{light} of dual-input L_0 models after cross-validation. Entries correspond to the minimum value of $r_w = n_D r_D + n_L r_L + n_{LD} r_{LD} + n_{SD} r_{SD}$ for each value of τ_{light} for 2nd order models. r_D, r_L, r_{LD} and r_{SD} are the sample correlation coefficients between simulated model output and AEQUORIN luminescence data from seedlings in experimental conditions L12/D12–DD, L12/D12–LL, L16/8D and L8/16D respectively. n_D, n_L, n_{LD} and n_{SD} are the corresponding numbers of observations in each dataset.

τ_{light}	τ_{CCA1}	r_w
0	3.7	135.45
1	4.5	136.41
2	5.5	135.68
3	3.4	134.42
4	3.6	134.38
5	3.1	134.54

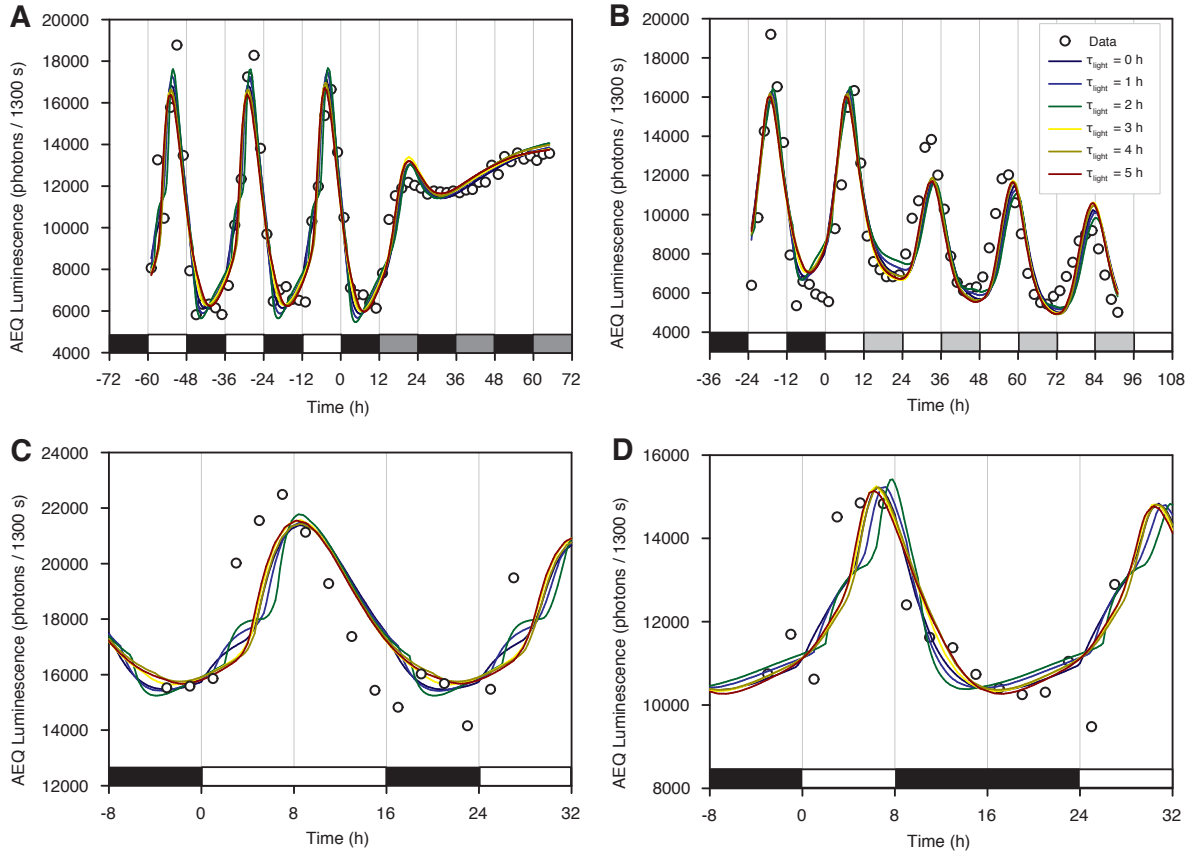

Figure 2.10: Cross-validation of 2nd order L_0 models with AEQUORIN luminescence data. Linear state-space model equations solved numerically with MATLAB™'s *ode23* solver (solid lines; Shampine & Reichelt, 1997). For each $\tau_{\text{light}} = 0, 1, \ldots, 5$, models simulated for the optimal choice of τ_{CCA1}, defined as the minimum of the weighted sum of AIC_c, r_w (Eqn. 2.18; see Table 2.4 for values). Simulated outputs scaled to overlap with AEQUORIN luminescence data from Figure 2.3 (open circles) by finding the best linear scaling of the form $a\hat{y} + b$, where $\hat{y}$ is the simulated output. The *polyfit* function in MATLAB™ was used to evaluate a and b as minimisers of $\sum_i^{N_d} (y^{(i)} - a\hat{y}^{(i)} - b)^2$ where $y^{(i)}$ are the measured AEQUORIN luminescence values and N_d is the number of data values. Bars on abscissa represent light regime in each experiment/simulation. White indicates light, black indicates dark, light grey (B) is light in the subjective night and dark grey (A) is dark in subjective daytime.

Table 2.5: Optimal choice of τ_{CCA1} for each τ_{light} of dual-input L_0 models after cross-validation. Entries correspond to the minimum value of $r_w = n_D r_D + n_L r_L + n_{LD} r_{LD} + n_{SD} r_{SD}$ for each value of τ_{light} for 4$^{\text{th}}$ order models. r_D, r_L, r_{LD} and r_{SD} are the sample correlation coefficients between simulated model output and AEQUORIN luminescence data from seedlings in experimental conditions L12/D12–DD, L12/D12–LL, L16/8D and L8/16D respectively. n_D, n_L, n_{LD} and n_{SD} are the corresponding numbers of observations in each dataset.

τ_{light}	τ_{CCA1}	r_w
0	5.5	133.10
1	0.1	134.49
2	7.0	135.77
3	0.3	131.32
4	3.1	133.39
5	1.2	133.39

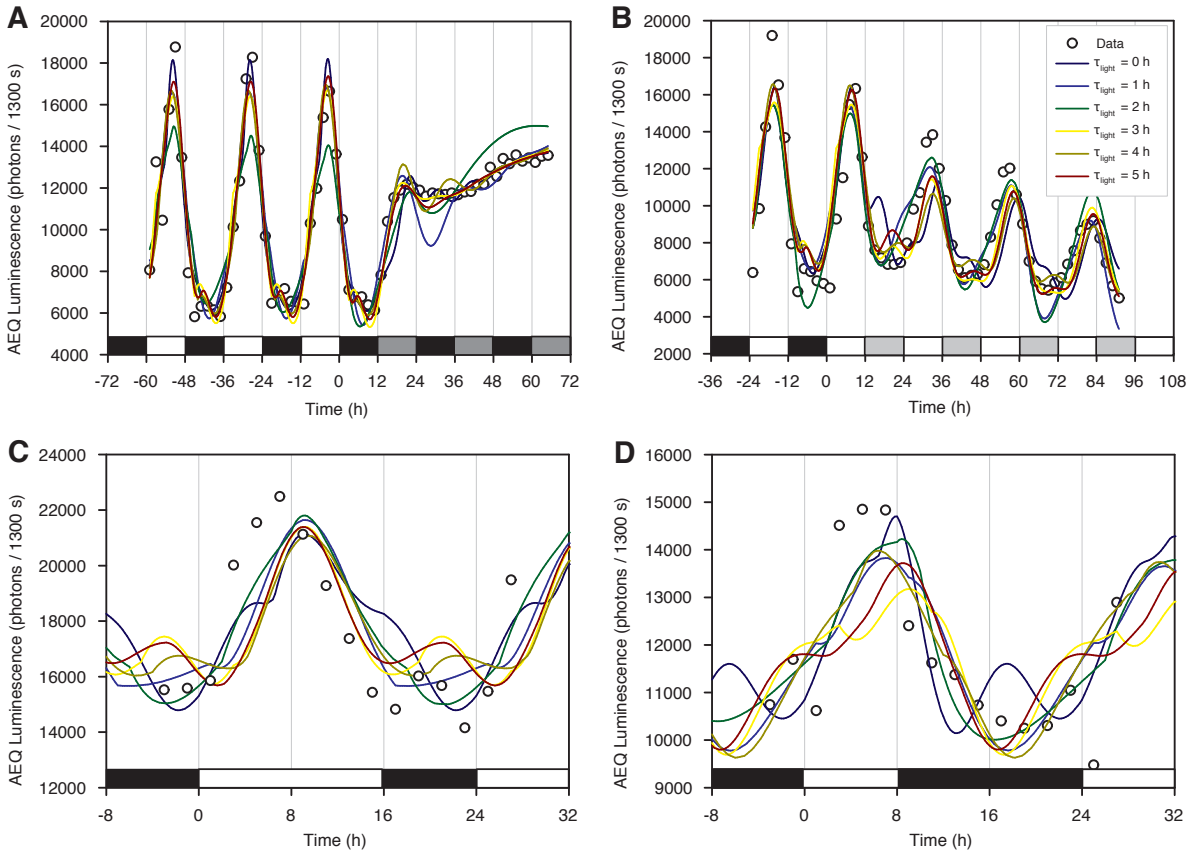

Figure 2.11: Cross-validation of 4$^{\text{th}}$ order L_0 models with AEQUORIN luminescence data. Linear state-space model equations solved numerically with MATLAB$^{\text{TM}}$'s *ode23* solver (solid lines; Shampine & Reichelt, 1997). For each $\tau_{\text{light}} = 0, 1, \ldots, 5$, models simulated for the optimal choice of τ_{CCA1}, defined as the minimum of the weighted sum of AIC_c, r_w (Eqn. 2.18; see Table 2.5 for values). Simulated outputs scaled to overlap with AEQUORIN luminescence data from Figure 2.3 (open circles) by finding the best linear scaling of the form $a\hat{y} + b$, where $\hat{y}$ is the simulated output. The *polyfit* function in MATLAB$^{\text{TM}}$ was used to evaluate a and b as minimisers of $\sum_i^{N_d} (y^{(i)} - a\hat{y}^{(i)} - b)^2$ where $y^{(i)}$ are the measured AEQUORIN luminescence values and N_d is the number of data values. Bars on abscissa represent light regime in each experiment/simulation. White indicates light, black indicates dark, light grey (B) is light in the subjective night and dark grey (A) is dark in subjective daytime.

Candidate models for each choice of τ_{light} were selected by maximising the weighted sum of sample correlation coefficients r_w (Eqn. 2.18) over τ_{CCA1} (Tables 2.4, 2.5). The simulated outputs of these optimal-τ_{CCA1} models were then compared with the measured AEQUORIN luminescence data. Almost no difference was observed between different choices of τ_{light} when considering the simulated outputs of 2$^{\text{nd}}$ order models in L12/D12–DD conditions (Figure 2.10A). All were able to match the oscillation phase in L12/D12 cycles but failed to maintain a stable level during the dark phase of these cycles. This gave the effect of an early anticipation of dawn, which was not observed experimentally. The tending behaviour towards steady state in DD was well represented in all cases. 4$^{\text{th}}$ order models had some dissimilarity across the range of τ_{light} (Figure 2.11A). In L12/D12 cycles, only the optimal-τ_{CCA1} models corresponding to τ_{light}= 1 h and τ_{light}= 2 h had smooth oscillations, while a very small second oscillation could be seen in the dark phase of the other τ_{light} models. This slightly biphasic oscillation was observed in the measured AEQUORIN luminescence signal, but it is not clear whether the 4$^{\text{th}}$ order delay linear systems models accurately accounted for this behaviour. There was also a range of troughs observed around 28 h into DD. The best model in this regard was the optimal-τ_{CCA1} model corresponding to τ_{light}= 5 h, which did not 'dip' far below the measured AEQUORIN luminescence signal. This residual oscillation in DD was also seen in the 2$^{\text{nd}}$ order models (Figure 2.10A), representing a shortfall of the model class.

The predictive capabilities of each optimal-τ_{CCA1} model were then analysed through comparison with AEQUORIN luminescence data from L12/D12–LL conditions, entrained L16/8D cycles and entrained L8/D16 cycles (Figures 2.10B–D & 2.11B–D). 4$^{\text{th}}$ order models continued to exhibit biphasic behaviour in LL, representing a major shortfall. $[Ca^{2+}]_{cyt}$ undergoes smooth oscillations in LL (Johnson *et al.*, 1995; Love *et al.*, 2004; Xu *et al.*, 2007), and this must be a strict criterion for a mathematical description to honour. Furthermore, similar erroneous biphasism is predicted in long-day conditions (Figure 2.11C) and short-day conditions (Figure 2.11D). In this respect, 4$^{\text{th}}$ order models should be rejected at this stage, as they have been over-fitted to exhibit the small oscillation observed in L12/D12 cycles.

The 2$^{\text{nd}}$ order models were unable to match the estimation data as accurately as the higher order systems, but their predictive capabilities were much greater. Smooth oscillations were observed in LL, which had a lower amplitude than the oscillations in L12/D12 cycles (Figure 2.10B). For some choices of τ_{light} (1, 2, and 3 h), a raised baseline was also observed be-

tween L12/D12 and LL. For all 2nd order models, simulated output peaked between 8.6–8.8 h after dawn (to the nearest 0.2 h) in entrained L16/D8 cycles, while the measured AEQUORIN luminescence signal peaked 7 h after dawn (Figure 2.10C). In entrained L8/D16 cycles, the 2nd order models peaked 6.4–7.8 h after dawn, while the measured signal peaked 5 h after dawn (Figure 2.10D). Therefore, the model simulations predict a slightly later phase of $[Ca^{2+}]_{cyt}$ compared to the data presented. The equivalent AEQUORIN luminescence data published in Love *et al.* (2004) have a later phase (9 h after dawn in L16/D8 cycles; 7 h after dawn in L8/D16 cycles), which agrees more closely with the model predictions. The trough values of the 2nd order models in L16/D8 cycles agreed with the measured AEQUORIN luminescence data (Figure 2.10C), though were earlier than measured data in L8/D16 cycles (Figure 2.10D). The difference between the broadness of the $[Ca^{2+}]_{cyt}$ oscillation in L16/D8 cycles and L8/D16 cycles in Love *et al.* (2004) was also predicted by the 2nd order models, despite not being clearly visible in the AEQUORIN luminescence data used for cross-validation.

2.3.5 Isolation of the pathways regulating $[Ca^{2+}]_{cyt}$ through simulated mutation

L_0 models of 2nd order have been demonstrated to represent a good description of the regulation of basal $[Ca^{2+}]_{cyt}$ in wild-type plants, though it has proved difficult to distinguish models resulting from different assignments of τ_{light}. This motivated us to isolate each input pathway for further investigation. Simulations were carried out in which either the *CCA1*-dependent pathway or the light/dark-dependent pathway was impaired. By comparison with experimental data, this enabled parallels to be drawn between mathematical predictions and mutant phenotypes.

Predicted $[Ca^{2+}]_{cyt}$ phenotypes of a null mutation in *CCA1*

To predict possible effects of a mutation in *CCA1*, optimal-τ_{CCA1} 2nd order L_0 models (Table 2.4) were simulated in the same range of photoperiodic conditions investigated previously (Figure 2.3), defining the *CCA1* input to be constantly zero (Figure 2.12). In DD, simulated output continued to rise to a high steady state value, larger than any value seen during L12/D12 cycles (Figure 2.12A). In LL, simulated output continued to fall instead, eventually reaching the steady state of the system corresponding to zero input ($x = 0, y = d$; Eqn. 2.17; Figure 2.12B). The model simulated outputs oscillated with a piecewise triangular waveform in L12/D12,

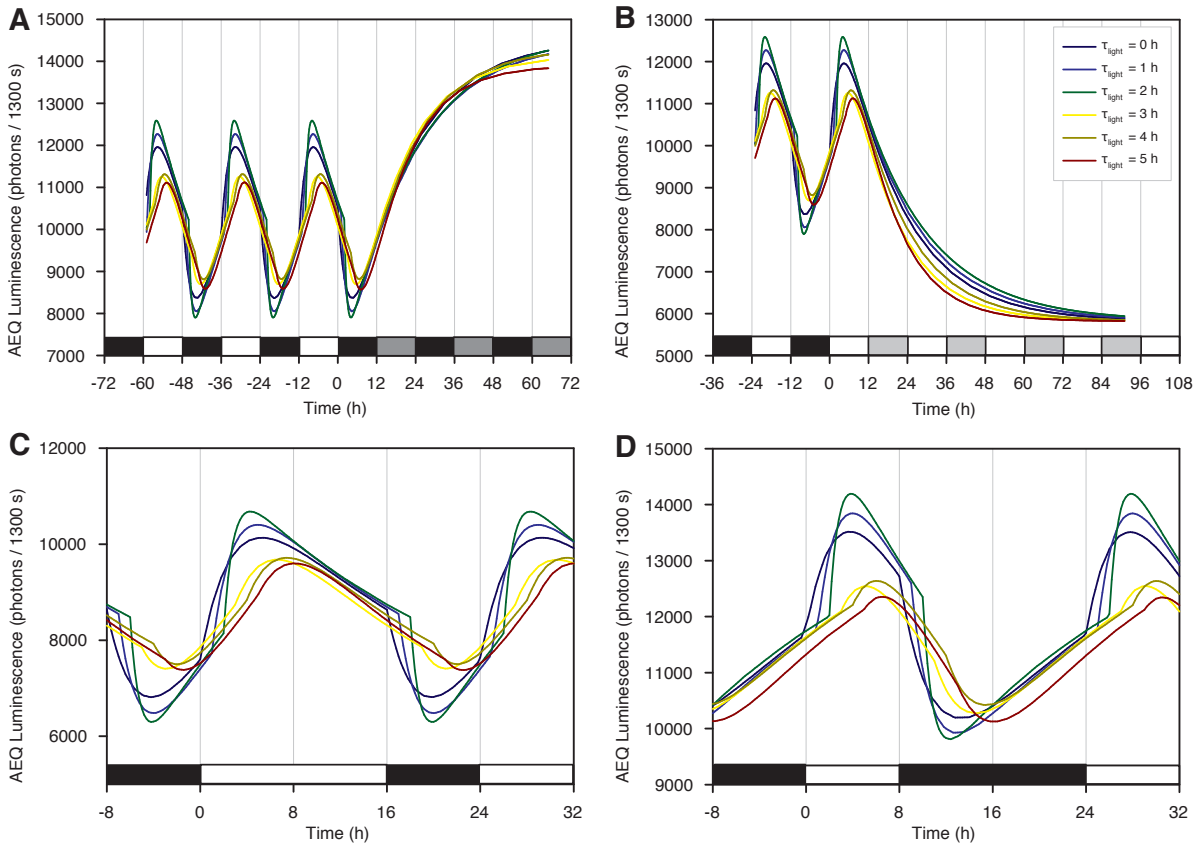

Figure 2.12: Simulation of the response of $[Ca^{2+}]_{cyt}$ to a mutation in *CCA1*.
Simulations (solid lines) reflect removal of the *CCA1*-dependent pathway, by setting the input pathway equal to zero throughout. Linear state-space model equations solved numerically with MATLAB^{TM}'s *ode23* solver (Shampine & Reichelt, 1997). For each $\tau_{\text{light}} = 0, 1, \ldots, 5$, models simulated for the optimal choice of τ_{CCA1}, defined as the minimum of the weighted sum of correlations with cross-validation test data, r_w (Eqn. 2.18; see Table 2.4 for values). Bars on abscissa represent light regime in each simulation. White indicates light, black indicates dark, light grey (B) is light in the subjective night and dark grey (A) is dark in subjective daytime.

L16/D8 and L8/D16 cycles for all τ_{light}, as a result of u_{light} switching between 0 and 1 (Figures 2.12A,C,D). When the light input was equal to 1 (darkness), the simulated output increased with a gradient which was inversely proportional to the length of the dark period (Table 2.6). An equal and opposite effect was observed when the light input was 0 (light), as the simulated output declined at a rate inversely proportional to the length of the light period. The timing of these transitions depended on the light delay parameter τ_{light}, with the transitions occurring later as a result of a longer delay (Table 2.6).

Simulations of a *CCA1* mutant were compared with measured AEQUORIN luminescence from the *cca1*-1 null mutant allele in an entrained L12/D12 cycle (Xu *et al.*, 2007). In *cca1*-1, $[Ca^{2+}]_{cyt}$ peaked 3.6 h after dawn, 4 h earlier than wild-type (Xu *et al.*, 2007). We found that the models with low τ_{light} offered the closest agreement to this observation (Figure 2.13; see

Table 2.6: Peak $[Ca^{2+}]_{cyt}$ in simulated nyctohemeral cycles of a *cca1* mutant.
2^{nd} order L_0 models simulated with $u_{CCA1} \equiv 0$ in entrained light-dark cycles, and peak time calculated to the nearest 0.2 h. Models selected for the optimal choice of τ_{CCA1} for each τ_{light}, defined as the minimum of the weighted sum of correlations with cross-validation test data, ρ_w (Eqn. 2.18). Linear state-space model equations solved numerically with MATLAB^{TM}'s *ode23* solver (Shampine & Reichelt, 1997).

τ_{light}	τ_{CCA1}	L12/D12	L16/D8	L8/D16
0	3.7	4.4	5.4	3.6
1	4.5	4.4	4.8	4.0
2	5.5	4.0	4.2	3.8
3	3.4	5.6	6.4	5.0
4	3.6	6.6	7.4	6.0
5	3.1	7.0	8.0	6.4

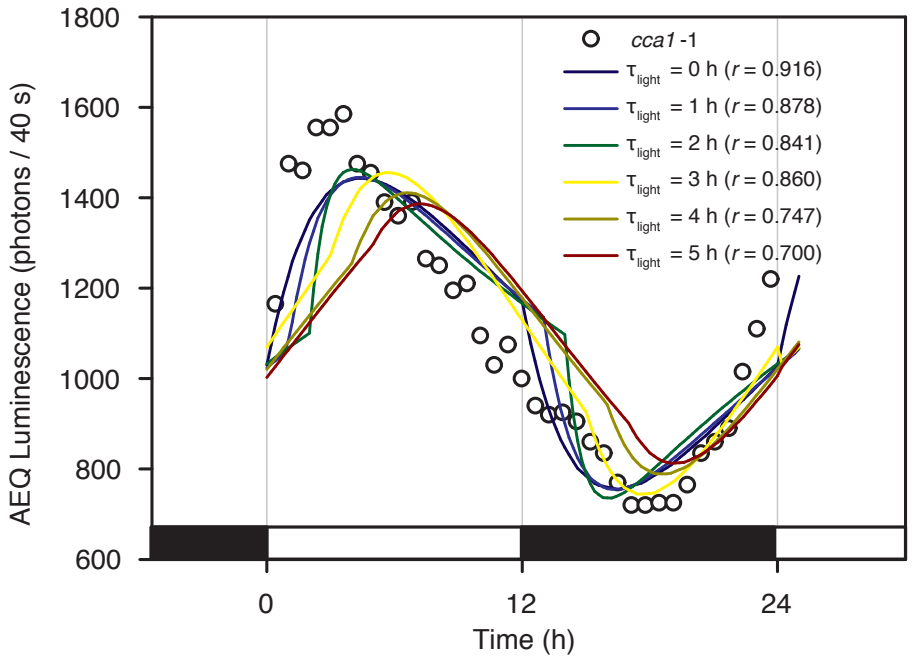

Figure 2.13: Comparing the $[Ca^{2+}]_{cyt}$ oscillation phase of a simulated *CCA1* mutant with *cca1*-1 distinguishes τ_{light}.
AEQUORIN luminescence measured in 10 day old *Arabidopsis* seedlings entrained to L12/D12 cycles by photon counting luminometry (red circles). Equivalent simulations of AEQUORIN luminescence from optimal-τ_{CCA1} 2^{nd} order L_0 models for different choices of τ_{light} (solid lines; see Table 2.6 for values of τ_{CCA1} corresponding to each τ_{light}, and times of peak $[Ca^{2+}]_{cyt}$). Linear state-space model equations solved numerically with MATLAB^{TM}'s *ode23* solver (Shampine & Reichelt, 1997). Values of r in the legend are the sample correlation coefficient between measured AEQUORIN luminescence and model simulation at the corresponding time-points. Bars on abscissa are white for light, and black for dark. AEQUORIN luminescence data reproduced from Xu *et al.* (2007).

Table 2.6 for peak times), indicating that τ_{light} should be no larger than 2 h. Therefore, the light regulation of $[Ca^{2+}]_{\text{cyt}}$ operates on a faster timescale than the *CCA1*-dependent regulation of $[Ca^{2+}]_{\text{cyt}}$, which appeared to occur after a delay 3.5–5.5 hours (see Table 2.3).

Predicted $[Ca^{2+}]_{\text{cyt}}$ phenotypes of a null mutation in the light/dark-input pathway

To establish the effect of a mutation in the light/dark input pathway regulating $[Ca^{2+}]_{\text{cyt}}$, candidate L_0 models (Table 2.4) were simulated under the cross-validation photoperiodic conditions, defining the light input to be equal to 1 throughout (Figure 2.14). Note that the choice of light input value is arbitrary, as a constant applied at the input represents only a change in the output translation d of Eqn. 2.17. Under the simulated light mutant scheme, we predict $[Ca^{2+}]_{\text{cyt}}$ to essentially follow the dynamics of the *CCA1:luc* luminescence signal used as the model input, subject to the relevant delay τ_{CCA1} (Figure 2.14). Simulated output increased after a period of extended darkness, but in contrast to the wild-type simulation, declined again before steadily increasing to the steady state (Figure 2.14A). In LL, simulated output continued to oscillate with the shape of the response closely matching the *CCA1:luc* luminescence signal (Figure 2.14B). In L16/D8 cycles, simulated output peaked 8–9 h after dawn, which was similar to the wild-type simulations, but the accumulation started later and was sharper (Figure 2.14C). There was a lag between the transition from dark to light and the following increase in simulated output, indicating that the light input pathway is required for the increase in $[Ca^{2+}]_{\text{cyt}}$ following a dark to light transition. The decline of simulated output in L16/D8 was also similar to wild-type data, undertaking a steady fall to a trough value around dawn. In entrained L8/D16 cycles, there was also some similarity between simulated light mutants and wild-type observations (Figure 2.14D), whereby simulated $[Ca^{2+}]_{\text{cyt}}$ peaked 7–8 h before dusk, declined quickly, and remained low during the last 8 hours of darkness before dawn.

2.3.6 Predicted $[Ca^{2+}]_{\text{cyt}}$ phenotypes of a null mutation in the hidden state variable

A limitation of using linear systems with hidden states is that structural and quantitative information is lost due to the invariance of input-output relationships to similarity transformations (see Section 2.2.4). Single-output linear state-space models were estimated in a fixed realisation similar to the controller canonical form (Eqn. 2.8; Chen, 1998), whereby one state variable is the measured signal and the other state variables are hidden (unconstrained). By comparing

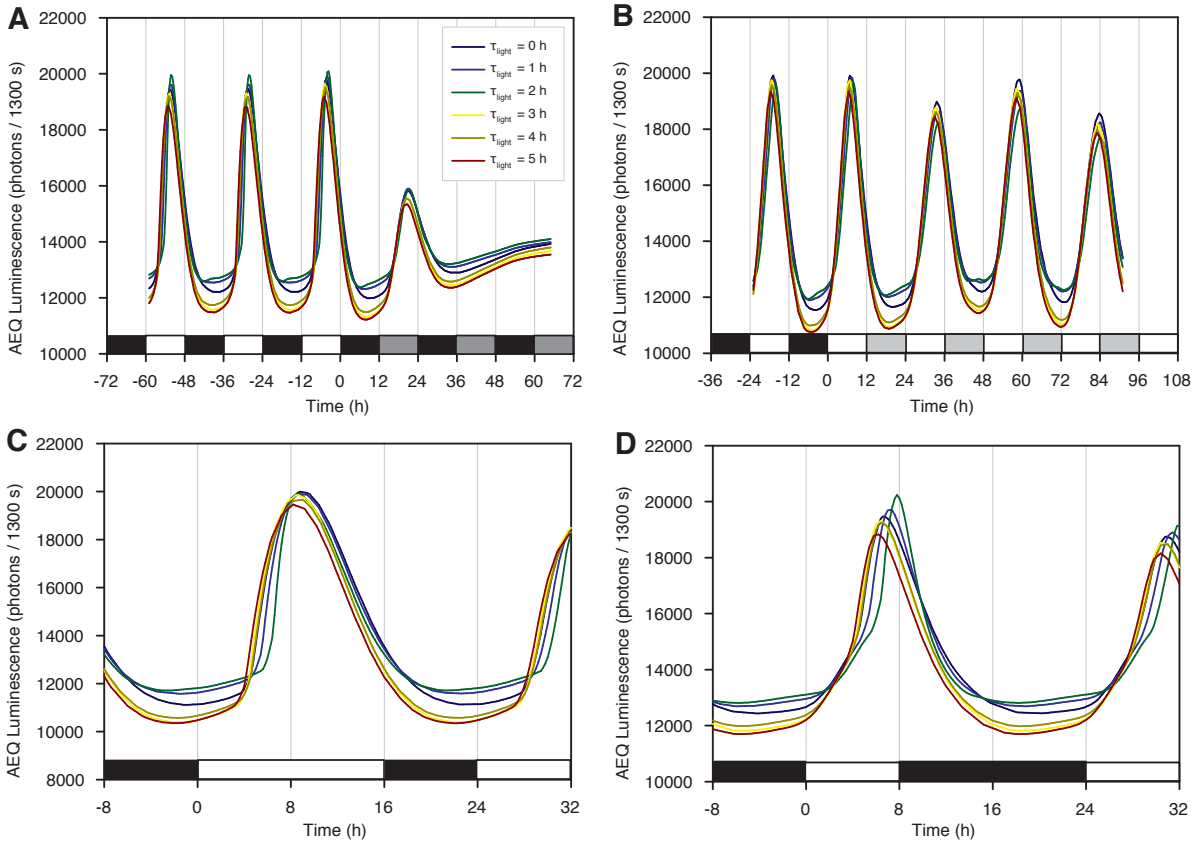

Figure 2.14: Simulation of $[Ca^{2+}]_{cyt}$ with a null mutation in the light/dark-dependent pathway. Simulations (solid lines) reflect removal of the light/dark-dependent pathway, by setting the light input pathway equal to one throughout. The *CCA1*-dependent pathway is assumed to be unaffected, and the wild-type data (Figure 2.3) is used for these simulations. Linear state-space model equations solved numerically with MATLAB^{TM}'s *ode23* solver (Shampine & Reichelt, 1997). For each $\tau_{\text{light}} = 0, 1, \ldots, 5$, models simulated for the optimal choice of τ_{CCA1}, defined as the minimum of the weighted sum of AIC r_w (Eqn. 2.18; see Table 2.4 for values). Bars on abscissa represent light regime in each simulation. White indicates light, black indicates dark, light grey (B) is light in the subjective night and dark grey (A) is dark in subjective daytime.

AEQUORIN luminescence data from wild-type and mutant backgrounds with corresponding model simulations we found that a 2$^{\text{nd}}$ order system offered the most suitable level of complexity, implying the existence of one hidden state variable (namely $X2$). Without structural or quantitative information, it is not possible to predict the dynamics of $X2$, though the potential effects of a mutation in $X2$ were classified by considering a family of co-ordinate transformations.

Consider a candidate model given by Eqn. 2.1. Applying a similarity transformation T such that $Tz = x$ yields:

$$T\dot{z}(t) = ATz(t) + Bu(t - \tau) \tag{2.19}$$

$$\text{i.e.} \qquad \dot{z}(t) = T^{-1}ATz(t) + T^{-1}Bu(t-\tau) = \hat{A}z(t) + \hat{B}u(t-\tau) \tag{2.20}$$

$$y = CTz = \hat{C}z \tag{2.21}$$

We therefore define the generalised system matrices $\hat{A}$, $\hat{B}$ and $\hat{C}$ as

$$\hat{A} = T^{-1}AT \tag{2.22}$$

$$\hat{B} = T^{-1}B \tag{2.23}$$

$$\hat{C} = CT \tag{2.24}$$

As the A matrix is estimated in controller canonical form and the similarity transformation must preserve the measured variable x_1 (i.e. $\hat{C} = C$) we obtain the following forms for A, B and T:

$$A = \begin{pmatrix} 0 & 1 \\ a_1 & a_2 \end{pmatrix}, \quad B = \begin{pmatrix} b_{11} & b_{12} \\ b_{21} & b_{22} \end{pmatrix}, \quad T = \begin{pmatrix} 1 & 0 \\ t_1 & t_2 \end{pmatrix} \tag{2.25}$$

Substitution into the generalised system matrices yields

$$\hat{A} = T^{-1}AT = \begin{pmatrix} t_1 & t_2 \\ \dfrac{-t_1^2 + a_2t_1 + a_1}{t_2} & -t_2 + a_2 \end{pmatrix} \tag{2.26}$$

$$\hat{B} = T^{-1}B = \begin{pmatrix} b_{11} & b_{12} \\ \dfrac{-b_{11}t_1 + b_{21}}{t_2} & \dfrac{-b_{12}t_1 + b_{22}}{t_2} \end{pmatrix} \tag{2.27}$$

While there is uncertainty about the true dynamics of the hidden variable $X2$, it is straightforward to classify the set of dynamics which correspond to a simulated mutation in the hidden variable. i.e. $X2 \equiv 0$. In this case, the generalised system reduces to a first order ODE given by:

$$\frac{dx_1}{dt}(t) = t_1x_1(t) + \begin{pmatrix} b_{11} & b_{12} \end{pmatrix} u(t-\tau) \tag{2.28}$$

where t_1 becomes a free parameter. If $t_1 \geq 0$, then the system is unstable, and x_1 will grow in magnitude unboundedly. Even if the real underlying system does go unstable in the absence of a functional $X2$, $[Ca^{2+}]_{cyt}$ will either saturate, or lead to cell death since Ca^{2+} is cytotoxic. This means we may not observe prolonged increases/decreases in $[Ca^{2+}]_{cyt}$. If $t_1 < 0$, the mutated

system is stable, and the dynamical behaviour of $[Ca^{2+}]_{cyt}$ can be described by one of the family of first-order systems in Eqn. 2.28.

The optimal-τ_{CCA1} 2nd order model corresponding to $\tau_{light} = 0$ h was used to simulate possible effects of a mutation in *X2* (Figure 2.15). The traces plotted relate to $t_1 = -0.01, -0.1, -0.25, -0.5$ and -1. Optimal-τ_{CCA1} models for $\tau_{light} = 1, 2, \ldots, 5$ were also tested, and similar results were observed (but not shown). As t_1 was decreased, the amplitude of the oscillations decreased in all photoperiods (Figure 2.15)[†]. In DD, simulated output increased

[†]For this 1st order system, t_1 is also the eigenvalue of the interconnectivity matrix A. Therefore, the tendency towards steady state is fast for large negative values of t_1.

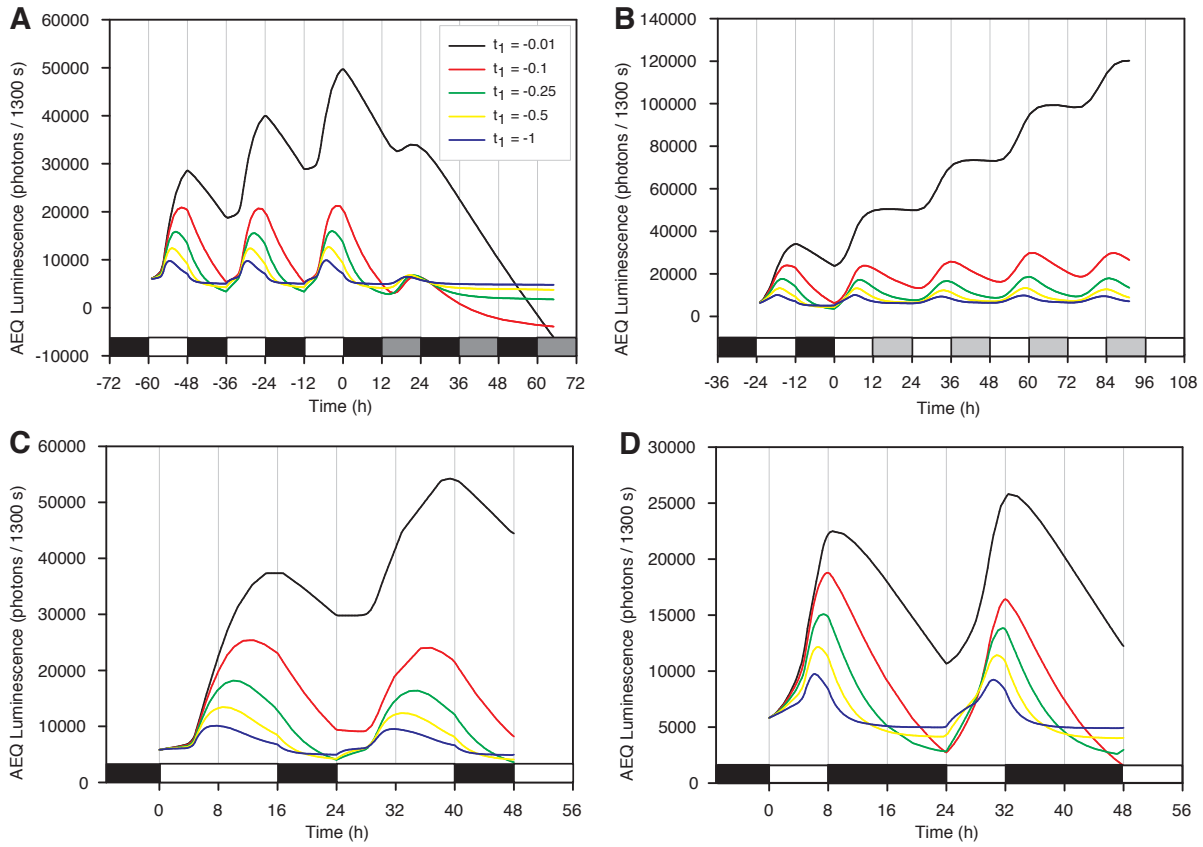

Figure 2.15: Simulations of the response of $[Ca^{2+}]_{cyt}$ to a mutation in the hidden variable *X2*. Simulations (solid lines) reflect removal of the hidden variable *X2*, by solving the first order equation $\dot{x} = t_1 x + b_{11} u_{CCA1} + b_{12} u_{light}$. t_1 is the free parameter from a similarity transformation which defines the family of mutant responses. b_{11} and b_{12} are the entries in the first row of the B matrix, estimated from wild-type data using the *pem* prediction-error minimization function in MATLAB^{TM} (Systems Identification Toolbox; Ljung, 1999). The estimated model corresponds to the case where $\tau_{light} = 0$ h, and $\tau_{CCA1} = 3.6$ h. The *CCA1*-dependent pathway is assumed to be unaffected by the mutation, and the wild-type data (Figure 2.3) is used for these simulations. The first 24 hours of input data is cycled through 5 times to remove transitory behaviours. Linear state-space model equations solved numerically with MATLAB^{TM}'s *ode23* solver (Shampine & Reichelt, 1997). Bars on abscissa represent light regime in each simulation. White indicates light, black indicates dark, light grey (B) is light in the subjective night and dark grey (A) is dark in subjective daytime.

to an intermediate value but decreased again to low levels, irrespective of t_1 (Figure 2.15A). This prediction contrasted with the wild-type simulation, providing a criterion for identifying genes/components corresponding to the hidden variable *X2*. In LL, the oscillation troughs were higher, and amplitude lower than in L12/D12 cycles for all t_1, as observed in the wild-type simulation (Figure 2.15B). Furthermore, for t_1 near 0, the simulated output increased in steps corresponding to the times when *CCA1:luc* was high (Figure 2.15B), illustrating how both *X2* and the light input pathway are responsible for decreasing the simulated ouput in the dark phase following a period of light, as well as elevating the simulated output in prolonged darkness. Simulations of entrained L16/D8 cycles led to a similar behaviour to that observed in simulated light mutants (Figure 2.14C), whereby there was a lag between the onset of light, and a corresponding increase in $[Ca^{2+}]_{cyt}$ (Figure 2.15C). However, the oscillation phase varied over a large range, from 7.6 h ($t_1 = -1$) to 16 h ($t_1 = -0.01$) after dawn, being progressively later for values of t_1 approaching 0. For entrained L8/D16 cycles, the oscillation phase was between 6.2 h ($t_1 = -1$) and 8.8 h ($t_1 = -0.01$) after dawn. In conclusion, there was an overlap between predictions for $[Ca^{2+}]_{cyt}$ in simulated light input mutations and *x2* mutants, which suggested that an as-yet unidentified molecular component (*X2*) was critical for transducing light information to $[Ca^{2+}]_{cyt}$. For example, *X2* may represent components of the light signalling network, which transduce wavelength-specific light availability and are also regulated by the circadian clock.

As *X2* is required for the increase in $[Ca^{2+}]_{cyt}$ following a dark to light transition, it is possible that *X2* incorporates one or a subset of the photoreceptors. Many photoreceptors undergo increased promoter activity in DD (Tóth *et al.*, 2001). *PHYA:luc* and *PHYB:luc* luminescence increases sharply 12 h after transition from light to continual darkness (Tóth *et al.*, 2001), which coincides with the observed $[Ca^{2+}]_{cyt}$ increase. PHYA and PHYB protein levels are also high in 7-day old dark-grown seedlings, but arrhythmic in light-dark cycles (Sharrock & Clack, 2002). It would be interesting to see if these proteins accumulate in extended darkness after entrained L12/D12 cycles. We compared our model predictions with the available AEQUORIN luminescence data for mutant lines in L16/D8 and L8/D16 conditions. We found that the *phyA*-201 mutant allele led to a delayed increase in $[Ca^{2+}]_{cyt}$ at the dark to light transition, and also a later phase of oscillation (11.3 h after dawn; Figure 2.16A; Hubbard, 2008). This experimental observation coincided well with the prediction of a mutation in *X2* when $t_1 \gtrsim -0.5$ (see Figure 2.16B

for comparison), implicating PHYA to be one or all of the hidden variable $X2$.

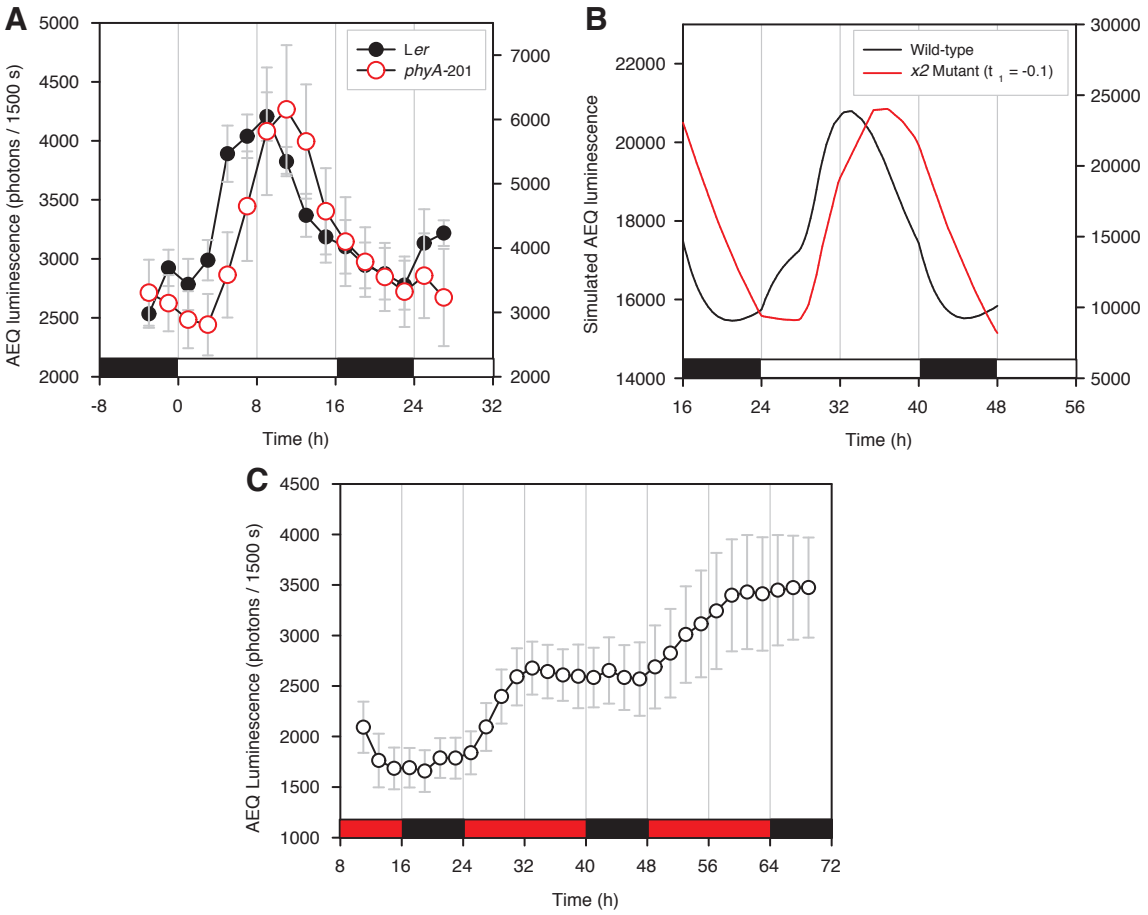

Figure 2.16: Red- and blue-light photoreception by $[Ca^{2+}]_{cyt}$.
Seedlings were grown for approximately 12 days in entrained cycles of 16 h light, 8 h dark (100 μmol m^{-2} s^{-1}). (A) Seedlings imaged under mixed red and blue light (80 μmol m^{-2} s^{-1}), with traces representative of the $[Ca^{2+}]_{cyt}$ oscillation in wild-type (*Ler*; black circles) and *phyA*-201 mutant (red open circles) seedlings. (B) Simulation of candidate L_0 model (τ_{CCA1}=3.7 h, τ_{light}=0 h) in L16/D8 cycles, comparing wild-type (black line) and *x2* mutant with $t_1 = -0.1$ (red line) backgrounds. (C) Seedlings imaged under single wavelengths of R light (60 - 80 μmol m^{-2} s^{-1}). White bars indicate mixed R + B light and red bars indicate R (black bars represent darkness). Data in (A) and (C) collected by Dr. Katharine Hubbard, University of Cambridge, UK. Modified from Hubbard (2008).

The assumption that t_1 is negative may not be correct, in which case the simulated *x2* mutant will lead to an unstable system, resulting in unbounded increases in $[Ca^{2+}]_{cyt}$. In fact, for $t_1 \gtrsim -0.01$, the model still predicts $[Ca^{2+}]_{cyt}$ to increase persistently in LL (Figure 2.15B), and attains progressively higher levels in LD cycles which increase faster for longer photoperiods (Figure 2.15C–D). In searching through the available AEQUORIN luminescence data, we found this behaviour occurred in seedlings entrained to 16 h monochromatic red light, 8 h dark cycles (Figure 2.16C, Hubbard, 2008). Xu *et al.* (2007) observed similar unbounded increases in $[Ca^{2+}]_{cyt}$ in wild-type *Arabidopsis* under constant blue light (BB), indicating that both blue and

red light are required for the decrease in $[Ca^{2+}]_{cyt}$ following the elevation after dawn. Transgenic manipulations in CRY1, CRY2 and PHYB all reduced both the accumulation in BB and the amplitude in LL (Xu *et al.*, 2007). It was also observed that $[Ca^{2+}]_{cyt}$ undergoes stable oscillations in RR in wild-type plants, but accumulates unboundedly in RR in the *phyB-5* mutant allele. When viewed together with the model predictions of a mutation in *X2*, there is evidence which suggests *X2* incorporates many elements of the light signalling network, both red- and blue-light dependent.

2.3.7 Determination of internal structure for the *CCA1*–Light/Dark–$[Ca^{2+}]_{cyt}$-*X2* network

Each linear model estimated was fixed into controller canonical form (Eqn. 2.8). The internal structure of these systems with hidden states is not fixed, as similarity transformations can re-structure the state variables while preserving the input-output behaviour. Therefore, we considered the second-order generalised system (Equations 2.26–2.27) to establish whether particular entries in A and B could be zero, and thus determining some structural information. The generalised A matrix is given by

$$\hat{A} = T^{-1}AT = \begin{pmatrix} t_1 & t_2 \\ \dfrac{-t_1^2 + a_2 t_1 + a_1}{t_2} & -t_2 + a_2 \end{pmatrix} \tag{2.29}$$

To assess the possibility that $[Ca^{2+}]_{cyt}$ does not influence the hidden variable *X2*, we need only consider the entries in A from the estimated models. Assuming $t_2 \neq 0$ (as otherwise the system would decouple into two first order equations), we derive a condition for the (2,1) position of $\hat{A}$ ($\hat{a}_{21}$) to be zero:

$$\begin{aligned} \hat{a}_{21} &= 0 \\ \Leftrightarrow \quad -t_1^2 + a_2 t_1 + a_1 &= 0 \\ \Leftrightarrow \quad t_1 &= \frac{a_2}{2} \pm \frac{\sqrt{a_2^2 + 4a_1}}{2} \end{aligned}$$

This value of t_1 exists provided the discriminant of the quadratic equation is non-negative. i.e $a_2^2 + 4a_1 \geq 0$. The values of $a_2^2 + 4a_1$ corresponding to the optimal-τ_{CCA1} 2^{nd} order models from Table 2.4 were all positive, implying that it is possible that *X2* does not depend on $[Ca^{2+}]_{cyt}$ in

these model formulations (see Table 2.7).

Table 2.7: Entries of A determine potential for $X2$ to not be regulated by $[Ca^{2+}]_{cyt}$.
Each row represents a 2nd order linear state-space model, based on the delay between the light input and the system (τ_{light}). In each case, the optimal τ_{CCA1} is selected based on cross-validation tests. The a_i are the entries from the A matrix estimated (see Eqn. 2.25). $a_2^2 + 4a_1$ is the discriminant of the quadratic equation which is the solution to the (2,1) entry of $\hat{A}$ being zero.

τ_{light}	τ_{CCA1}	a_1	a_2	$a_2^2 + 4a_1$
0	3.6	-0.0187	-0.3879	0.0757
1	4.5	-0.0290	-0.6240	0.2734
2	5.5	-0.0580	-1.2901	1.4323
3	4.3	-0.0303	-0.5936	0.2310
4	3.6	-0.0230	-0.4244	0.0880
5	3.7	-0.0242	-0.4291	0.0874

The generalised form of B can also be considered to investigate potential missing links in the input structure regulating $X2$. In particular, is $X2$ regulated by both the circadian clock and light, or just one of these pathways? The (2,1) entry of $\hat{B}$ is zero if and only if $t_1 = \dfrac{b_{21}}{b_{11}}$, while the (2,2) entry is zero if and only if $t_1 = \dfrac{b_{22}}{b_{12}}$. We found that for the same optimal-τ_{CCA1} models investigated above, t_1 must be chosen between -0.4 and -1.5 (depending on which model used) for any entries in B to be zero (Table 2.8). As the values of t_1 which correspond to $\hat{b}_{21} = 0$ and $\hat{b}_{22} = 0$ are distinct, it is not possible for both $\hat{b}_{21}$ and $\hat{b}_{22}$ to be zero. Therefore, it is not possible to say with any certainty whether there are direct causal relationships between the input pathways and $X2$.

Table 2.8: Entries of B determine potential for missing links in the input regulation of the hidden variable.
Each row represents a 2nd order linear state-space model, based on the delay between the light input and the system (τ_{light}). In each case, the optimal τ_{CCA1} is selected based on cross-validation tests. The b_{ij} are the entries from the B matrix estimated (see Eqn. 2.25). b_{21}/b_{11} is the value of t_1 (from similarity transformation T defined in Eqn. 2.25) which must be chosen for the (2,1) entry of B to be 0. b_{22}/b_{12} is the corresponding value of t_1 which results in the (2,2) entry being 0.

τ_{light}	τ_{CCA1}	b_{11}	b_{21}	b_{21}/b_{11}	b_{12}	b_{22}	b_{22}/b_{12}
0	3.6	4857.9	-2017.3	-0.41526	-1155	647.95	-0.561
1	4.5	6295	-3942.1	-0.62623	-1795.7	1372.4	-0.76426
2	5.5	11414	-14823	-1.2986	-3538.7	5079.3	-1.4354
3	4.3	6111.6	-3671.7	-0.60078	-1082.6	902.43	-0.83358
4	3.6	5055.6	-2181.8	-0.43156	-362.9	349.91	-0.96419
5	3.7	5101.7	-2224.4	-0.43602	-194.61	287.19	-1.4757

2.3.8 Frequency response of $[Ca^{2+}]_{cyt}$ to *CCA1* and Light/Dark

The frequency response of each pathway regulating $[Ca^{2+}]_{cyt}$ was computed for the candidate L_0 model with τ_{CCA1}= 3.7 h and τ_{light}= 0 h. A transfer function representation of the transfer functions from each input to the output was first computed by finding the Laplace transform of each side of the state-space linear system of ODEs (Eqn. 2.1), which reduces to

$$Y(s) = \begin{pmatrix} G_1(s) & G_2(s) \end{pmatrix} \begin{pmatrix} U_1(s) \\ U_2(s) \end{pmatrix} = G(s)U_\tau(s) \tag{2.30}$$

where $G(s) := C(sI - A)^{-1}B$ is partitioned into $G_1 := \mathcal{T}_{u_{CCA1} \to y}$ and $G_2 := \mathcal{T}_{u_{light} \to y}$ by the columns of B, $U_1(s) := \mathcal{L}(u_{CCA1}(t - \tau_{CCA1}))$ and $U_2(s) := \mathcal{L}(u_{light}(t - \tau_{light}))$. The resulting transfer functions were

$$G_1(s) = \frac{4804.1101(s - 0.001965)}{(s + 0.3454)(s + 0.05543)} \tag{2.31}$$

$$G_2(s) = \frac{-1099.4179(s - 0.1513)}{(s + 0.3454)(s + 0.05543)} \tag{2.32}$$

The magnitude and phase were then computed for G_1 and G_2 in the frequency range $\omega \in [10^{-4}, 1]$ rad/h using the *bode* function in MATLAB^{TM} (Laub, 1981), with the magnitude $|G(j\omega)|$ converted to decibel units as $20 \log |G(j\omega)|$. G_1 was found to be a band-pass filter with peak magnitude at $\omega = 0.140023$ rad/h, which corresponds to a frequency of $2\pi/\omega = 44.87$ h (Figure 2.17). In particular, G_1 dominates the system response over circadian periods (between 12 h and 48 h) and has a phase angle near 0 in this range. At lower frequencies (oscillations with larger periods), G_2 dominates the system response with a phase angle near 0 (Figure 2.17). The frequency response analysis demonstrates the requirement for two independent regulators of $[Ca^{2+}]_{cyt}$, and suggests that the regulation by the circadian clock is specifically enhanced over circadian timescales (periods near 24 h) and suppressed at lower or higher frequencies (Figure 2.17).

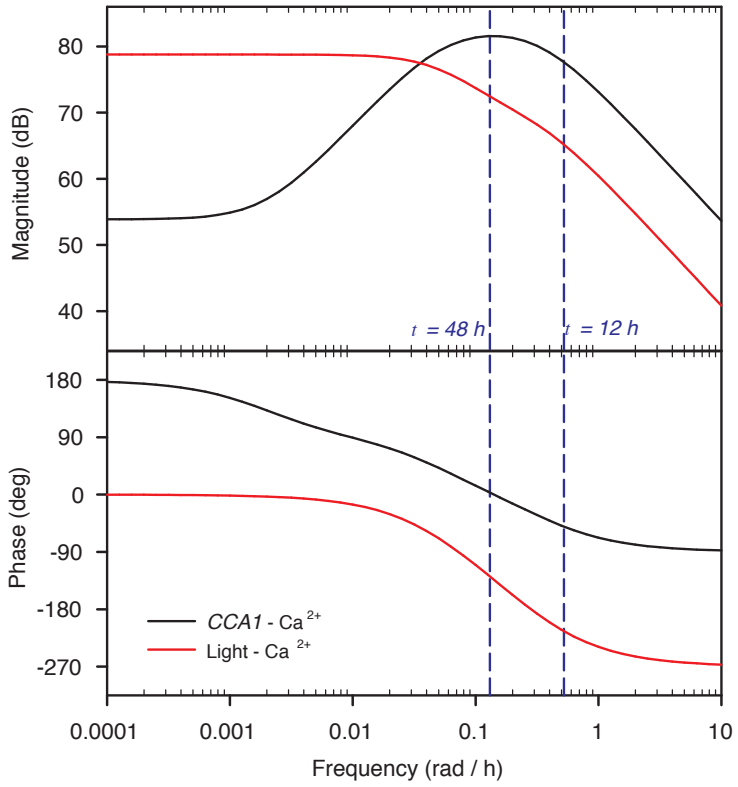

Figure 2.17: The regulation of $[Ca^{2+}]_{cyt}$ by *CCA1* is a band-pass filter.
The bode magnitude (top) and phase (bottom) plots are shown for the candidate L_0 model with τ_{CCA1}= 3.7 h and τ_{light}= 0 h. The magnitude plot displays the amplitude of the response of the transfer function G to a frequency ω in decibel units (i.e. $20\log|G(j\omega)|$) and the phase plot shows the phase angle $\angle G(j\omega)$. For each input pathway (*CCA1*–$[Ca^{2+}]_{cyt}$, black lines, and Light/Dark–$[Ca^{2+}]_{cyt}$, red lines) transfer function representations were obtained as $G(s) = C(sI - A^{-1})B$ to enable computation of $|G(jw)|$ and $\angle G(j\omega)$ with the *bode* function in MATLAB^{TM} (Laub, 1981). Blue dashed lines indicate the frequencies corresponding to periods (τ) between 48 h and 12 h.

2.4 Discussion

Mathematical models were derived to increase understanding of the regulation of basal $[Ca^{2+}]_{cyt}$ by the circadian clock and the light signalling network. Three model classes were investigated: a single-input single-output system which maps *CCA1:luc* luminescence data to AEQUORIN luminescence data (*SISO* model; Eqn. 2.4) and two dual-input systems which additionally track the availability of light and dark, switching between 1 and 0 (L_1) or 0 and 1 (L_0) respectively (Eqn. 2.5). In all cases, the uncharacterised but assumed present pathway intermediates were modelled as delay parameters τ_{CCA1} and τ_{light}. The black-box nature of the problem suggested that the underlying model should be as simple as possible, attempting to describe the fundamental dynamics of the system. Therefore, we have started by using continuous-time

linear state-space systems, subject to delays on the input signals (Eqn. 2.1). While there were drawbacks of using simple models, it was still possible to successfully validate a model, and in doing so learn properties of the network, including timescales and novel components.

2.4.1 $[Ca^{2+}]_{cyt}$ is regulated by a light/dark-dependent pathway and a hidden variable

Estimation of models which considered $[Ca^{2+}]_{cyt}$ to be regulated by a *CCA1*-dependent pathway alone were unable to reproduce the observed transition to DD. In L12/D12, $[Ca^{2+}]_{cyt}$ is low during the night, and after a prolonged period of darkness increases to an intermediate level, and undergoes very low amplitude (if any) oscillations (Figure 2.3B). Optimal prediction-error single-input models continued to oscillate, irrespective of the model order (number of state variables; Figure 2.4B), which indicated that the single-input model class used was not sufficient to describe the available AEQUORIN luminescence data. The optimal choice of τ_{CCA1} decreased as the model order was increased, which suggested that the additional state variables were accounting for the delay in the system (Table 2.1). Inspection of the model performance in the cross-validation conditions revealed that the models were generally able to track the correct phase and amplitude of oscillation in L12/D12 cycles, but were unable to distinguish the reduced amplitude in LL (Figure 2.6). Furthermore, in the absence of a functional *CCA1*, this model class predicts a constant level of $[Ca^{2+}]_{cyt}$ in LD cycles. However, recent published data has shown that the *cca1*-1 mutant still undergoes oscillations in LD, albeit with a significantly altered waveform (Xu *et al.*, 2007).

The dual-input model class enabled simulated $[Ca^{2+}]_{cyt}$ to cycle in nyctohemeral cycles when the *CCA1*-dependent pathway was removed (Figure 2.12). The two dual-input model classes L_0 (light = 0, dark = 1) and L_1 (light = 1, dark = 0) were compared for their performance with respect to the wild-type estimation data (L12/D12–DD; Figure 2.7). While both dual-input models offered improvement in AIC_c over the single-input class during estimation, models which responded to light as a nonzero input (L_1) did not perform as well as those which responded to dark in simulation (L_0; Figure 2.8), and through comparison of AIC_c (Table 2.3). The optimal choice of τ_{CCA1} during estimation was much lower for L_0 models, with L_1 yielding unrealistically high τ_{CCA1} (Table 2.3), further pointing to a dark-dependent activation of $[Ca^{2+}]_{cyt}$. We interpret this as $[Ca^{2+}]_{cyt}$ being regulated by a light-labile photoreceptor

(i.e. PHYA). 2nd order models were optimised by τ_{CCA1} ranging between 3.5 h and 4.5 h, while 4th order models preferred τ_{CCA1} near 0, again suggesting that the additional state variables were accounting for the delay between *CCA1* expression and Ca^{2+}-release. However, neither estimation nor cross-validation simulations were able to distinguish between varying τ_{light}, as simulated outputs were very similar (Figures 2.10, 2.11). Cross-validation suggested 2nd order models represented a more accurate description of the available measured data than 4th order models, which were prone to over-fitting due to the number of estimated parameters. We conclude that $[Ca^{2+}]_{\text{cyt}}$ is regulated by a *CCA1*-dependent pathway approximately 4 h in duration, a light/dark-dependent pathway of unknown timescale and a hidden variable *X2*.

2.4.2 Simulated *CCA1* mutant analysis reveals temporal information for the regulation of $[Ca^{2+}]_{\text{cyt}}$ by transitions between light and dark

To distinguish different delay lengths between the light/dark-input pathway and $[Ca^{2+}]_{\text{cyt}}$ (τ_{light}), simulations of a null mutation in *CCA1* were carried out in which the *CCA1* input was considered to be 0 throughout (Figure 2.12). In light-dark cycles, simulated $[Ca^{2+}]_{\text{cyt}}$ peaked at times which positively correlated with τ_{light} (see Table 2.6). This provided the first distinction between alternative choices of τ_{light}, and by comparing simulations with AEQUORIN luminescence data in the *cca1*-1 null allele, this indicated that τ_{light} should be no longer than 2 hours in duration. Simulation of the candidate models revealed that $[Ca^{2+}]_{\text{cyt}}$ can still oscillate in light-dark cycles and anticipate dawn in the absence of a circadian regulator (Figure 2.12), though the phase of the oscillation is shifted with respect to the dual-control (wild-type) system. To provide further validation and to hypothesise potential roles of other clock components, we compared these simulations with AEQUORIN luminescence measured in a variety of clock gene mutant backgrounds under LL (Figure 2.18) and L12/D12 (Figure 2.19).

In LL, $[Ca^{2+}]_{\text{cyt}}$ does not oscillate in the *cca1*-1 mutant background, though it is not possible to distinguish the level of $[Ca^{2+}]_{\text{cyt}}$ relative to the wild-type (Figure 2.18A; Xu *et al.*, 2007). In *CCA1*-ox, there is a clear peak of $[Ca^{2+}]_{\text{cyt}}$ 5.2 h after the transition from dark at $t = 0$ which coincides (in value) with the wild-type (Figure 2.18B; Xu *et al.*, 2007), before $[Ca^{2+}]_{\text{cyt}}$ undergoes a steady decline to low levels relative to the wild-type oscillation. The tendency towards the low steady state was equivalent to the behaviour predicted by candidate models for $[Ca^{2+}]_{\text{cyt}}$ under LL when the *CCA1* input pathway was suppressed (Figure 2.12B), further supporting

the dual-input delay linear systems representation for the regulation of basal $[Ca^{2+}]_{cyt}$. The *LHY*-ox trace shows a similar phenotype, whereby $[Ca^{2+}]_{cyt}$ peaks 3.9 h after the transition from dark to light, before stabilising at a relatively low level. The similarity might be attributed to the functional similarity between *CCA1* and *LHY* (Schaffer *et al.*, 1998; Wang & Tobin, 1998; Mizoguchi *et al.*, 2002), with over-expression of both proteins leading to similar effects on gene expression downstream of *CCA1* but upstream of $[Ca^{2+}]_{cyt}$. For *elf3*-1, $[Ca^{2+}]_{cyt}$ stabilises at a high level in LL, relative to the levels after transfer from dark to light (Figure 2.18D). The shape of this response agrees most closely with simulated $[Ca^{2+}]_{cyt}$ in DD (both simulated wild-type and *CCA1* mutant; see Figures 2.10A & 2.12A), indicating that *ELF3* can regulate the light-input pathway. *ELF3* has already been observed to regulate the circadian control of light input to the central oscillator (McWatters *et al.*, 2000; Covington *et al.*, 2001), and so the $[Ca^{2+}]_{cyt}$ phenotype in LL appeared to suggest a similar mechanism, whereby *ELF3* mediates the light control of $[Ca^{2+}]_{cyt}$ (Xu *et al.*, 2007).

In entrained L12/D12 cycles, each of these four mutant backgrounds (*cca1*-1, *CCA1*-OX, *LHY*-OX and *elf3*-1) still produce oscillations $[Ca^{2+}]_{cyt}$. In *cca1*-1, $[Ca^{2+}]_{cyt}$ peaks 3.6 h after dawn in response to the light/dark input pathway, undergoes a steady decline before increasing in anticipation of dawn. In the absence of a circadian regulator, it is surprising that $[Ca^{2+}]_{cyt}$ increases in anticipation of dawn. However, our candidate models have also predicted this behaviour in the absence of a circadian input (Figure 2.13). Therefore, we can attribute this behaviour to second-order dynamics (in response to step inputs), which we have shown are required for a suitable description of the system. In contrast to measurements of $[Ca^{2+}]_{cyt}$ in LL, *CCA1*-OX and *LHY*-OX lead to different phenotypes in LD (Figures 2.19B,C). Overexpression of *CCA1* has almost no effect on L12/D12 oscillations of $[Ca^{2+}]_{cyt}$ relative to wild-type, which peak 7 h after dawn and remain low during the dark phase (Figure 2.19B). However, overexpression of *LHY* causes $[Ca^{2+}]_{cyt}$ to peak later (11 h after dawn), then decline throughout the dark, reaching the lowest level at 1 h before dawn (Figure 2.19C). The *elf3*-1 mutation affects the L12/D12 $[Ca^{2+}]_{cyt}$ oscillation only in the first 3 hours after dawn, resulting in peaks both 3 h and 7 h after dawn. The initial increase in $[Ca^{2+}]_{cyt}$ after transition from dark to light is controlled by the light/dark input pathway, while the *CCA1*-input pathway comes into effect after a delay of $\approx$ 4 h. Therefore, mutation in *ELF3* affects the light/dark input pathway, agreeing with the observed effects in LL described in the previous paragraph (Figure 2.18D).

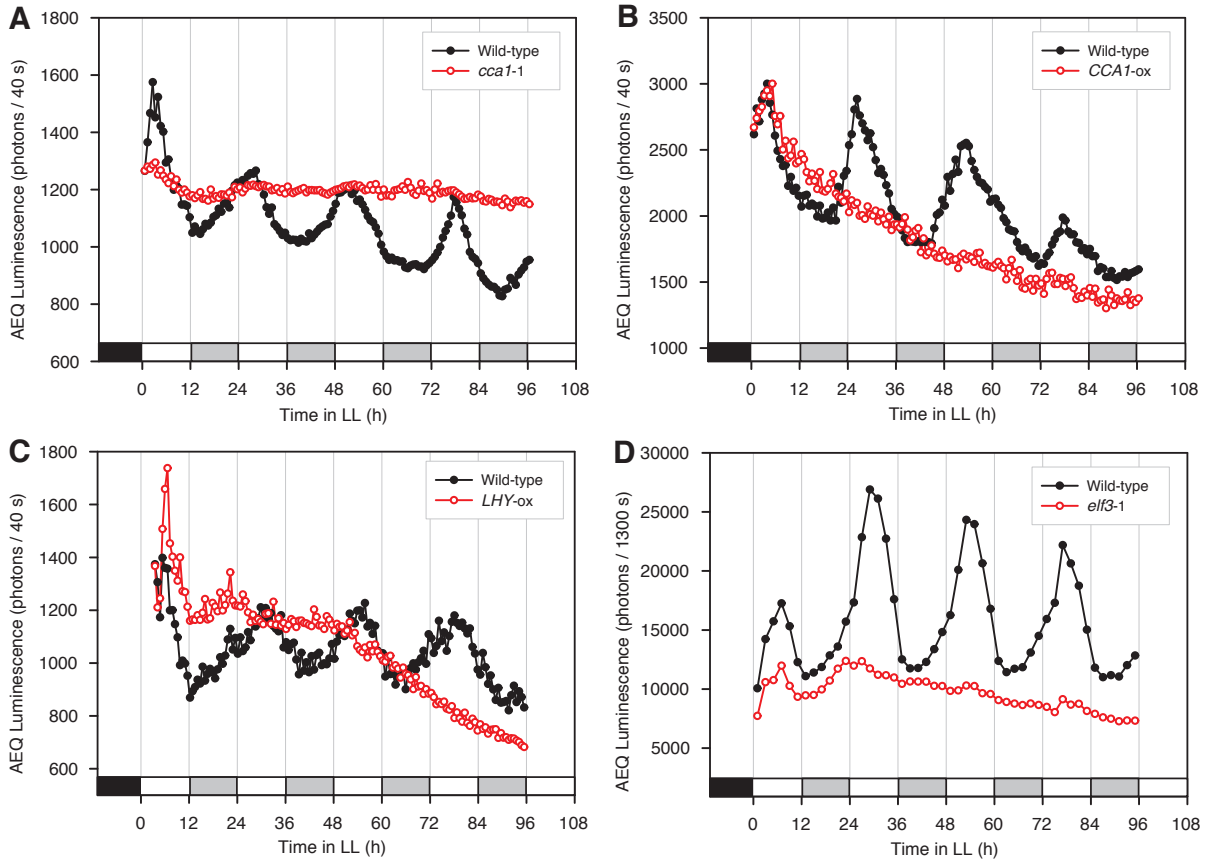

Figure 2.18: Mutations in core clock genes can lead to arrhythmic $[Ca^{2+}]_{cyt}$ in LL.
AEQUORIN luminescence in *cca1*-1 (A), *CCA1*-OX (B), *LHY*-OX (C), and *elf3*-1 (D) under LL (100 μmol m^{-2} s^{-1}) measured using photon-counting luminescence (A–C) or photon-counting imaging (D). Seedlings entrained under L12/D12 for 7 d before transfer to LL. Grey boxes indicate subjective night in LL. Data collected by (A–C) Dr. Xiaodong Xu, Vanderbilt University, USA, and (D) Dr. Carlos Hotta, University of Cambridge, UK. Modified from Xu *et al.* (2007).

2.4.3 The unconstrained internal structure of the 2nd order model complicates the identification of *X2*

The structure of the candidate 2nd order L_0 model (τ_{CCA1}= 3.7 h, τ_{light}= 0 h) was investigated because the causal relationships between the hidden state (*X2*) and the inputs and output of the model are not fixed (see Section 2.2.4, Remark 2). By considering generalised interconnectivity ($\hat{A}$; Eqn. 2.26) and input ($\hat{B}$; Eqn. 2.27) matrices defined in terms of a suitable similarity transformation, it was found that *X2* is at least regulated by a *CCA1*-dependent or light/dark-dependent pathway or both (Table 2.8), though nothing could be established regarding the interconnectivity of $[Ca^{2+}]_{cyt}$ and *X2* (Table 2.7). Therefore, the identification of biochemical components which constitute the role of *X2* is not straightforward from considering the effect of mutations in *X2* on the dynamics of $[Ca^{2+}]_{cyt}$, because a mutation in the hidden state *X2* may

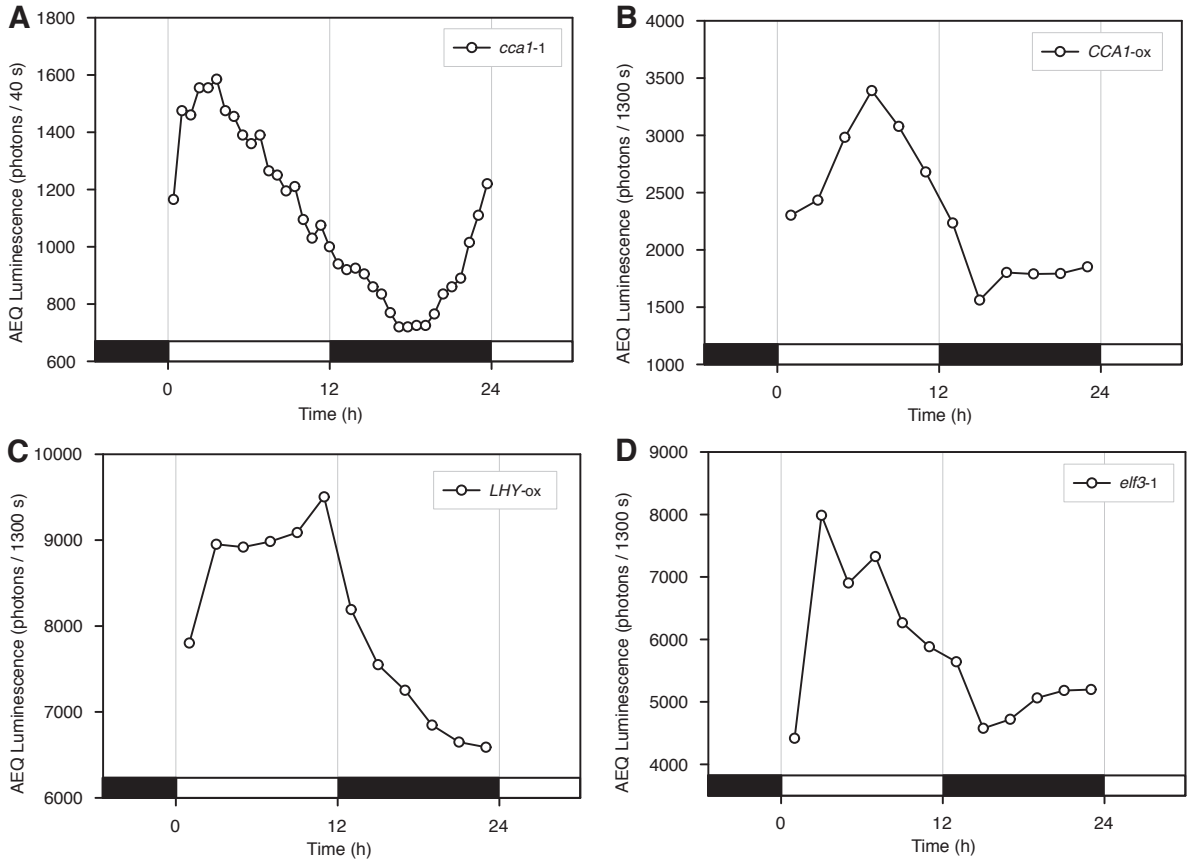

Figure 2.19: Mutations in core clock genes disrupt but do not remove $[Ca^{2+}]_{cyt}$ oscillations in light-dark cycles.
AEQUORIN luminescence in *cca1*-1 (A), *CCA1*-OX (B), *LHY*-OX (C), and *elf3*-1 (D) under 12 h light, 12 h dark cycles (100 μmol m^{-2} s^{-1}) measured using photon-counting luminescence (A) or photon-counting imaging (B–D). Seedlings entrained under L12/D12 for 7 d before the start of the experiment. Black boxes indicate night and white boxes indicate day. Data collected by (A) Dr. Xiaodong Xu, Vanderbilt University, USA, and (B,C,D) Dr. Carlos Hotta, University of Cambridge, UK. Modified from Xu *et al.* (2007).

not remove the complete light/dark dependency of $[Ca^{2+}]_{cyt}$, nor may it remove the circadian regulation by a *CCA1*-dependent pathway.

2.4.4 Simulations of a mutation in the light/dark input pathway or the hidden state variable

The optimal-τ_{CCA1} 2nd order L_0 models were simulated under the cross-validation photoperiodic regimes with the light/dark input set to a constant throughout, in order to predict potential effects of a mutation in the light/dark input pathway which regulates $[Ca^{2+}]_{cyt}$ (Figure 2.14). In light-dark cycles, there were only subtle differences between simulated wild-type and simulated mutations in the light/dark input pathway. The oscillations in L12/D12 had a

broader trough in the simulated mutations in the light/dark input pathway, compared with the nominal model configuration (Figure 2.14A). After transfer from L12/D12 to DD, the output of the simulated mutant increased to an intermediate level similar to wild-type data and simulation, but it was followed by a decline back to a relative low level before steadily increasing again (Figure 2.12A). Constant light oscillations of $[Ca^{2+}]_{cyt}$ in the simulated mutations in the light/dark input pathway had a similar amplitude to the light-dark cycles (Figure 2.12B). In entrained L16/D8 cycles, there was a lag between dark to light transition and the daytime $[Ca^{2+}]_{cyt}$ increase, indicating that the light/dark input pathway is required to elevate $[Ca^{2+}]_{cyt}$ in the early part of the day. However, this did not lead to a significantly delayed oscillation phase in light-dark cycles.

The candidate 2nd order model with τ_{light} equal to 0 h was investigated for the effect of a mutation in the hidden state variable *X2*. This led to a family of 1st order systems given by $\dot{x} = t_1 x + b_{11} u_{CCA1} + b_{12} u_{light}$, where t_1 is a free parameter. We found that for $t_1 < 0$, $[Ca^{2+}]_{cyt}$ did not stabilise at an intermediate level in DD, as observed in wild-type traces (Figure 2.15A). In addition, there was a clear lag between the onset of light and a corresponding increase in $[Ca^{2+}]_{cyt}$ under entrained L16/D8 cycles (Figure 2.15C). An identical prediction resulted from simulations of a mutation in the light/dark input pathway (Figure 2.14C), indicating that *X2* is required for the light-induced elevation in $[Ca^{2+}]_{cyt}$ at the transition from dark to light in entrained cycles. In fact, the dark to light transitory behaviours resulting from simulations of *X2* and light/dark input pathway mutants corresponded well in all entrained cycles investigated (L12/D12, Figures 2.14A, 2.15A; L8/D16, Figures 2.14D, 2.15D). However, in contrast to the simulated mutations in the light/dark input pathway, we found a broad range of oscillation phase in L16/D8 cycles (between 7.6 h and 16 h after dawn), which differed from the corresponding wild-type phase.

Despite the difficulties of obtaining structural information from delay linear systems models, from these simulated mutant analyses it was possible to predict specific light/dark-associated components to function in a light/dark – *X2* pathway which regulates $[Ca^{2+}]_{cyt}$. By comparing experimental measurements of $[Ca^{2+}]_{cyt}$ in photoreceptor mutants with the dynamics of simulated *x2* mutants, PHYA was found to be a candidate regulator of $[Ca^{2+}]_{cyt}$. The *phyA*-201 mutant had impaired LD oscillations of $[Ca^{2+}]_{cyt}$ similar to simulated *x2* mutants with $t_1 = -0.1$ (Figures 2.16A,B). Since the delayed increase at the dark to light transition was

also seen in simulations of a mutation in the light/dark input pathway, it is likely that PHYA mediates the light/dark – *X2* regulation of $[Ca^{2+}]_{cyt}$. Further experiments with wavelength-specific light sources indicated that a blue-light dependent component is required to decrease $[Ca^{2+}]_{cyt}$ during the latter part of the day (Figure 2.16C). Simulated *x2* mutants with $t_1 \gtrsim -0.01$ also had this behaviour, with model output progressively increasing during each LD cycle (Figure 2.15C). Therefore, it is possible that blue light photoreception is also encoded in the hidden component *X2*.

2.4.5 Summary

Experimental studies have used reverse genetic techniques to elucidate some conceptual understanding of how $[Ca^{2+}]_{cyt}$ is regulated by the circadian clock and light/dark (Xu *et al.*, 2007; Hotta, 2007; Hubbard, 2008). In this chapter, these observations were used to construct mathematical descriptions of the interactions between $[Ca^{2+}]_{cyt}$, light/dark signals and the central oscillator gene *CCA1* based on AEQUORIN and *CCA1:luc* luminescence data. We found that the regulation of $[Ca^{2+}]_{cyt}$ by *CCA1* occurs through a pathway of approximately 4 h in duration and operates as a band-pass filter for frequencies corresponding to circadian periods (between 12 h and 48 h). $[Ca^{2+}]_{cyt}$ is regulated by light/dark signals immediately ($\tau_{light} = 0$) whereby the absence of light (dark) contributes a nonzero signal, though this pathway dominates the system response at low frequencies. The most appropriate systems descriptions were 2^{nd} order, while an additional 2 hidden states could account for the *CCA1* delay but resulted in models which could not be successfully cross-validated. Comparing simulations of the 2^{nd} order models with the available experimental data enabled us to attribute phenotypes to removal of model components. The hidden variable appears to represent the action of the red-light sensitive phytochromes, and also the blue-light sensitive cryptochromes, despite the model not incorporating explicit dependencies on red and blue light signals. Contained within this chapter are many more simulations of mutant behaviours which have not been observed experimentally thus far, but provide specific behaviours which may be attributed to model components if and when they are observed. These behaviours have provided a bank of predictions which can be used to identify currently unknown components in the network of dual-regulation of $[Ca^{2+}]_{cyt}$.

CHAPTER 3

A Three Loop Model of the *Arabidopsis* Circadian Clock in the Absence of Exogenous Sucrose

3.1 Introduction

Sucrose is a major output of photosynthesis and is vital as an energy source for plants (Buchanan *et al.*, 2002). Until recently, the role of metabolic sugars in the plant circadian central oscillator had not been studied (Knight *et al.*, 2008). However, in LL oscillations in the concentration of cytosolic-free Ca^{2+} ($[Ca^{2+}]_{cyt}$) are absent in *Arabidopsis* seedlings grown on agar media containing 3% sucrose (Johnson *et al.*, 1995), indicating a role for sugars in regulating at least one circadian output. In this chapter, mathematical modelling has been used to study sugar availability as an input to the circadian central oscillator, and to predict target mechanisms. Furthermore, these predictions have been validated experimentally.

Sucrose accounts for the majority of fixed carbon during photosynthesis and serves as the principal long-distance transporter in many plants (Buchanan *et al.*, 2002). Sucrose is a nonreducing sugar because there is a stable glycosidic bond between the potentially reactive carbonyl carbons glucose and fructose, providing protection from oxidation (Buchanan *et al.*, 2002). Su-

crose synthesis occurs in the cytosol through a pathway of two enzymes. Sucrose-phosphate synthase (SPS) catalyses the synthesis of sucrose-6-phosphate (Suc6P), which is then hydrolysed by sucrose-phosphate phosphatase (SPP) into sucrose (Lunn & MacRae, 2003). This sequence of reactions associates a large negative free energy change and is therefore essentially irreversible (Buchanan *et al.*, 2002). Sucrose may also be synthesised by sucrose synthase (SUS), though this enzyme is more commonly associated with degradation of sucrose, yielding fructose and uridine diphosphate glucose (UDP-glucose; Baud *et al.*, 2004). Invertase (β–D-fructofuranosidase) also breaks down sucrose, yielding glucose and fructose (Tymowska-Lalanne & Kreis, 1998). In *Arabidopsis*, there are six known genes encoding sucrose synthase enzymes (*AtSus1-6*; Baud *et al.*, 2004; Barratt *et al.*, 2001), four encoding SPPs (Lunn *et al.*, 2000), four encoding SPSs (Lunn & MacRae, 2003), and four encoding invertases (*Atβfruct1-4*; Tymowska-Lalanne & Kreis, 1998).

When the synthesis and subsequent export of sucrose cannot keep pace with photosynthesis, fixed carbon enters the hexose phosphate pool, and is stored in the chloroplast as starch (Buchanan *et al.*, 2002). At night, the reserve of starch is broken down and converted to sucrose. The timing of these events might benefit from control by the circadian clock, though while sucrose and starch accumulate during the day and decline at night, their concentrations do not oscillate in LL or DD (Bläsing *et al.*, 2005; Lu *et al.*, 2005). However, transcript abundance of genes encoding starch-degradation enzymes follow the light-dark profiles almost exactly, remain low in DD, but continue to oscillate in LL (Lu *et al.*, 2005). In tomato, SPS activity oscillates in LL and light-dark cycles, though SPS protein levels remain constant (Jones & Ort, 1997). In addition to the synthesis of carbohydrates being regulated by the circadian clock, there is also evidence which suggests sucrose in turn regulates the oscillator mechanism. Sucrose represses PHYA signal transduction pathways (Dijkwel *et al.*, 1997); PHYA mediates light input to the circadian clock, and is also under circadian control (Hall *et al.*, 2001). Kurepa *et al.* (1998) studied the effect of exogenous sucrose supply on *Arabidopsis* seedlings, and found that *gi*-3 mutants contained higher endogenous $[\text{Suc}]_i$ than wild-type for all exogenous supply concentrations tested and flowering time in the dark was influenced by exogenous sucrose in *gi*-3. A recent article published after the work in this chapter was conducted, established *SENSITIVE TO FREEZING 6* (*SFR6*) to be important in sucrose modulation of transcript abundance of *CCA1*, *TOC1* and *GI* (Knight *et al.*, 2008). *sfr6* mutants had diminished responses to sucrose treatment,

including its effect on flowering time (Knight *et al.*, 2008).

The majority of circadian research in *Arabidopsis* is conducted with plants grown on agar media containing 3% sucrose (Millar *et al.*, 1995; Alabadí *et al.*, 2001; Mizoguchi *et al.*, 2005), and as such the mathematical models correspond to these growth conditions (Locke *et al.*, 2005a,b, 2006; Zeilinger *et al.*, 2006). Our measurements of $[Ca^{2+}]_{cyt}$ are from plants grown in the absence of exogenous sucrose, as exogenous supply of 3% sucrose inhibits oscillations in LL (Johnson *et al.*, 1995). In DD, $[Ca^{2+}]_{cyt}$ does not have circadian oscillations in the absence of sucrose (Xu *et al.*, 2007), though plants grown with 3% exogenous sucrose have circadian oscillations of *CCA1*, *LHY*, *TOC1*, *GI*, *ELF3*, *ELF4* and *CCR2* expression (Alabadí *et al.*, 2002; Ding *et al.*, 2007). As mathematical *Arabidopsis* circadian clock models have oscillations in DD, we were prevented from using them as an input to a mathematical model for the circadian regulation of $[Ca^{2+}]_{cyt}$ (Locke *et al.*, 2005b, 2006; Zeilinger *et al.*, 2006; see Chapter 2 for mathematical models of $[Ca^{2+}]_{cyt}$ regulation). Furthermore, the fact that there are circadian oscillations in DD with 3% exogenous sucrose and a tendency towards a steady state in the absence of exogenous sucrose (which is also noted by Oguchi *et al.*, 2004) motivated us to investigate the interactions between sucrose and the circadian network in *Arabidopsis*.

In this chapter, we have attempted to re-design the *Three Loop Model* of the central oscillator (Locke *et al.*, 2006) to account for our data measuring central oscillator gene expression in *Arabidopsis* seedlings grown without exogenous sucrose. The data in Figure 3.1 forms the training set to achieve such a model, and further experimentation has been carried out to both validate new models and test predictions of the target(s) of sucrose in the circadian network.

3.2 Materials and Methods

3.2.1 Measuring the effect of cold of *CCA1* promoter activity with a microplate luminometer

Cold-induced *CCA1* promoter activity was measured for plants grown on 0.8% (w/v) agar media containing 90 mM sucrose (Fisher Scientific, UK), 90 mM mannitol (BDH Laboratory Supplies, UK) or no added sugars. Transgenic *Arabidopsis* seedlings expressing *CCA1:luc* were grown in L12/D12 cycles for 10 days at constant 19°C, then transferred to DD for 48 h. Individual seedlings were then incubated overnight in luminometer cuvettes containing 1 ml of 1 mM

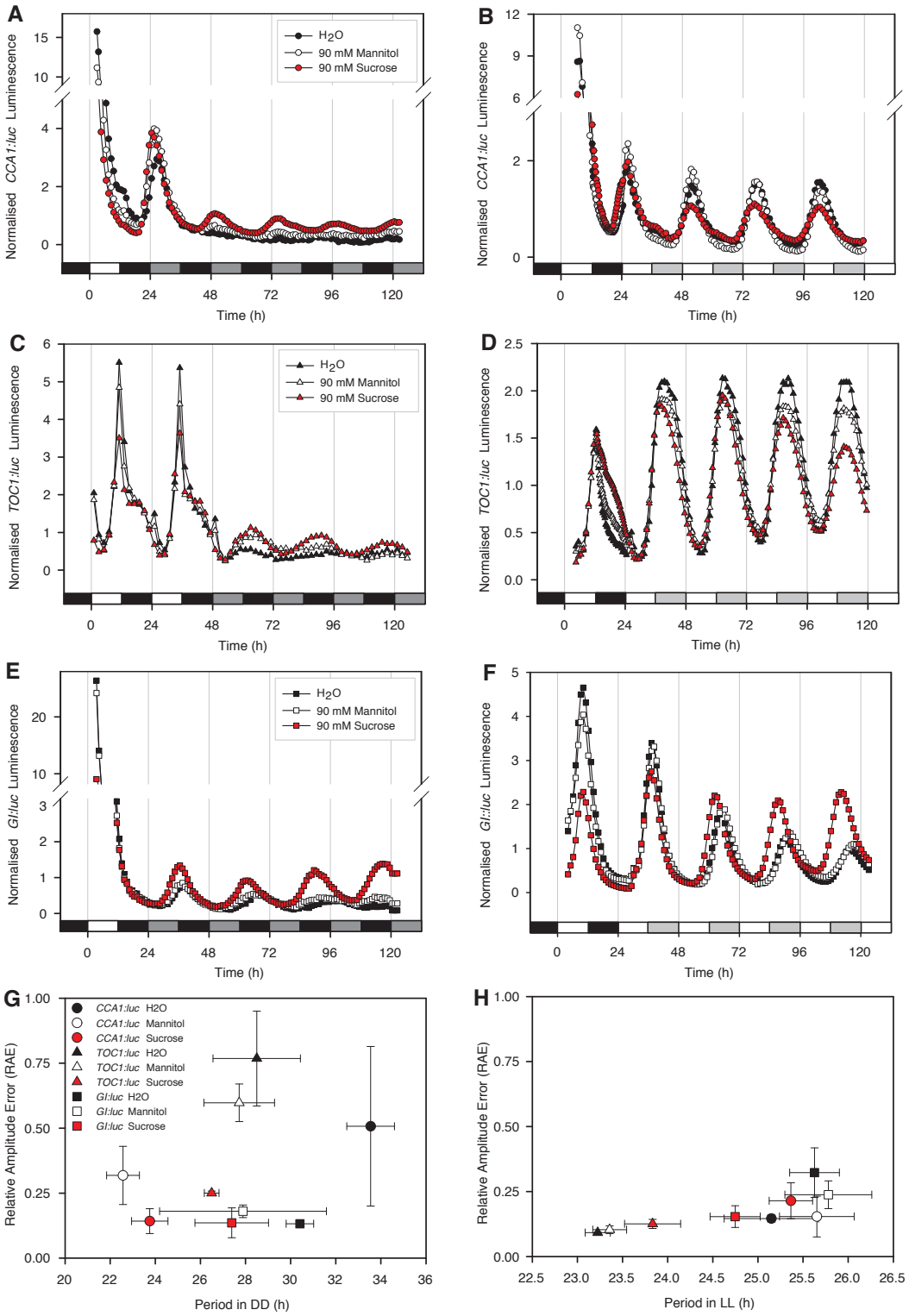

Figure 3.1: Exogenous sucrose modulates circadian central oscillator gene expression in LL and DD. 10 day-old *Arabidopsis* seedlings grown on agar media containing 90 mM sucrose (red symbols), 90 mM mannitol (open symbols), or no additional sugars (closed symbols), were entrained to L12/D12 cycles before transfer to constant (A,C,E,G) dark, or (B,D,F,H) light. Luminescence emitted from seedlings expressing (A,B) *CCA1:luc*, (C,D) *TOC1:luc*, or (E,F) *GI:luc* was quantified for 800 s for each datapoint using an automated photon counting camera. (G,H) Summary plot showing the mean estimated period plus standard deviation was calculated by FFT-NLLS analysis and plotted against the relative amplitude error (RAE) of the rhythms plus standard deviation. All data obtained from Seong Jin Baek (*personal communication*). Bars in abscissa are white during light, black during darkness, light grey for light during subjective night, and dark grey for dark during subjective day.

luciferin. Luminescence emitted from each cuvette was measured with a photon-counting luminometer (Electron Tubes, Ruislip, UK) for 60 s to obtain a reference signal, then placed in a frozen cuvette rack (IsoPack; Eppendorf, Germany) to maintain the temperature of the cuvettes at approximately 0°C for 2, 3, or 6 h. Following cold treatment, cuvettes were left at room temperature for 15 min to activate the temperature-dependent *luciferase* enzyme activity, then luminescence was measured for 240 s.

3.2.2 Numerical solution of the *Three Loop Model* equations

Throughout this chapter, the *Three Loop Model* (Locke *et al.*, 2006) has been used to investigate potential roles of sucrose in the circadian signalling network of *Arabidopsis*. Both the standard form of the equations (A.14–A.29), and a non-dimensionalised form (see Section 3.2.5) were solved numerically with MATLAB^{TM}'s *ode15s* stiff equation solver (Shampine & Reichelt, 1997) throughout. In general, the equations were solved for 600 h to remove transients before obtaining the desired time-points, initialising the solution as a vector of 1's*. To obtain specific time-points from the solution matrices (which will not be available explicitly in general), linear interpolation was used between the points lying either side of the desired time.

3.2.3 Period and amplitude plots for associating exogenous sucrose availability with single model parameter alterations

The *Three Loop Model* of the central oscillator (Equations A.14–A.29; Locke *et al.*, 2006) was used to investigate whether single parameter alterations could explain dynamical differences dependent on the exogenous supply of sucrose. For each parameter p, we associate a relative parameter value p^r, which is equal to 1 at it's nominal value (Table A.2). Oscillation period and amplitude in LL and DD were computed for $p^r = 10^{-2}, 10^{-1.99}, 10^{-1.98}, \ldots, 10^2$ corresponding to each model parameter considered. The light activating q_i's and the light protein parameters p_5, m_{15} and k_{13} (Eqn. A.26) were not considered, as they do not influence the state trajectory in constant conditions. The model equations (A.14–A.29) were simulated as in Section 3.2.2 for 600 h in both LL and DD, with the *refine* option in the *odeset* defined as 10†. In each case, the

*The initial condition was defined as a point on the limit cycle for the nominal equations and parameter values in Locke *et al.* (2006), though the limit cycle solution for (parametrically) perturbed systems is not known in advance. An arbitrary initial condition checks the existence of an attractive periodic orbit and a long solution time enables convergence close to the limit cycle.

†The *refine* option set to a value n simply generates n times as many points, independently of the solver tolerances. Refining the solution vectors enables a more accurate prediction of the time and value of peak and trough

state vector was initialised as a vector of 1's. The peak and trough values of [*LHY* mRNA]‡ were then located and used to evaluate period and amplitude. Period was taken as the difference in time of the final two peak values, while the amplitude was expressed as the fold ratio between the last peak and trough values in the simulation.

3.2.4 K-means clustering of simulated outputs

Simulated outputs from single-parameter alterations (Section 3.3.2) were classified into 8 categories using a K-means clustering algorithm (Macqueen, 1967). The *kmeans* function in MATLAB^{TM} (Statistics Toolbox; Seber, 2004) was used to implement the algorithm, setting the distance measure to be $1 - \rho$, where ρ is the sample correlation coefficient (Eqn. 2.15). The correlation distance measure enabled scale-free clustering with respect to the shape of the simulated outputs, which was important for comparison with data from bioluminescent reporters. Numerical solutions for [*LHY* mRNA] were obtained for 2 cycles (48 h) of L12/D12 followed by 120 h of DD according to the method of Section 3.2.2. The solution values corresponding to experimentally determined *CCA1:luc* luminescence were then used for K-means clustering.

3.2.5 Fine-tuning the *Three Loop Model* parameters for no exogenous sucrose supply

The *Three Loop Model* of the *Arabidopsis* clock (Equations A.14–A.29; Locke *et al.*, 2006) was again used to investigate potential roles for sugar signalling in the circadian network, this time allowing all model parameters to vary (see Section 3.3.3 for results). *Luciferase* luminescence data from plants grown without exogenous sucrose in the growth media was used to re-estimate the model parameters. At the time of undertaking this work, only the *CCA1:luc* and *TOC1:luc* experiments in L12/D12–LL and L12/D12–DD of Figure 3.1 were available, while *GI:luc* experiments were conducted later. In contrast to the single-parameter method (Section 3.2.3), the light-activation terms involving q_1, q_2 and q_4 were included (as dark to light transitions were present in the training datasets), but not the parameters which define the light input protein (p_5, m_{15}, k_{13} and q_3). Therefore, we were required to design an optimisation scheme which minimised the difference between measured data and simulation over the 73 model parameters.

values in an oscillation, of particular importance when computing period and amplitude from a numerical solution of differential equations.

‡The choice of state variable is arbitrary for computation of period, though [*LHY* mRNA] was selected as our earliest observations which motivated this work came from measurements of *CCA1:luc* luminescence.

Non-dimensionalisation of the *Three Loop Model* equations

As the dimension of a search space is increased, the quantity of experimental observations required for selection also increases. Each unknown parameter introduces uncertainty into the dynamical model's representation of the underlying biological system. There is also structural uncertainty, as the equations may not correctly represent the true underlying molecular interactions. In this chapter, we assume that the *Three Loop model* represents a sufficient structural representation of the molecular interactions between the gene products it defines, in order to distinguish the effects of exogenous sucrose supply. Therefore, dynamical differences resulting from altered sucrose levels may be represented by changes in the kinetic rate parameters which define the underlying molecular interactions. To reduce the size of the optimisation search space, we non-dimensionalised the model equations by re-scaling the state variables to the michaelis degradation constants k_i, resulting in a reduction in the size of the parameter space to 63 variables. This was permissible as the target data were scale-free, and would require us to rescale the simulated outputs for a suitable comparison with these data in any case.

Let $c_L^{(m)} = k_1 \hat{c}_L^{(m)}$, $c_L^{(c)} = k_2 \hat{c}_L^{(c)}$, etc. By defining ρ_i (i = L,T,X,Y,A) as the ratio between the cytoplasmic and nuclear protein scales (i.e. k_2/k_3 for LHY), and applying some parameter rescalings (Table 3.1), we define the *Non-Dimensionalised Three Loop* (*NDTL*) *Model*:

$$\frac{d\hat{c}_L^{(m)}}{dt} = \left(\frac{\hat{g}_0^{\alpha}}{\hat{g}_0^{\alpha} + \hat{c}_A^{(n)^{\alpha}}}\right)\left(\Theta_{\text{light}}(t)\left(\hat{q}_1\hat{c}_P^{(n)} + \hat{n}_0\right) + \frac{\hat{n}_1\hat{c}_X^{(n)^a}}{\hat{g}_1^a + \hat{c}_X^{(n)^a}}\right) - \frac{\hat{m}_1\hat{c}_L^{(m)}}{1+\hat{c}_L^{(m)}} \tag{3.1}$$

$$\frac{d\hat{c}_L^{(c)}}{dt} = \hat{p}_1\hat{c}_L^{(m)} - r_1\hat{c}_L^{(c)} + \hat{r}_2\hat{c}_L^{(n)} - \frac{\hat{m}_2\hat{c}_L^{(c)}}{1+\hat{c}_L^{(c)}} \tag{3.2}$$

$$\frac{d\hat{c}_L^{(n)}}{dt} = \rho_L(r_1\hat{c}_L^{(c)} - \hat{r}_2\hat{c}_L^{(n)}) - \frac{\hat{m}_3\hat{c}_L^{(n)}}{1+\hat{c}_L^{(n)}} \tag{3.3}$$

$$\frac{d\hat{c}_T^{(m)}}{dt} = \left(\frac{\hat{n}_2\hat{c}_Y^{(n)^b}}{\hat{g}_2^b + \hat{c}_Y^{(n)^b}}\right)\left(\frac{\hat{g}_3^c}{\hat{g}_3^c + \hat{c}_L^{(n)^c}}\right) - \frac{\hat{m}_4\hat{c}_T^{(m)}}{1+\hat{c}_T^{(m)}} \tag{3.4}$$

$$\frac{d\hat{c}_T^{(c)}}{dt} = \hat{p}_2\hat{c}_T^{(m)} - r_3\hat{c}_T^{(c)} + \hat{r}_4\hat{c}_T^{(n)} - ((1-\Theta_{\text{light}}(t))\hat{m}_5 + \hat{m}_6)\frac{\hat{c}_T^{(c)}}{1+\hat{c}_T^{(c)}} \tag{3.5}$$

$$\frac{d\hat{c}_T^{(n)}}{dt} = \rho_T(r_3\hat{c}_T^{(c)} - \hat{r}_4\hat{c}_T^{(n)}) - ((1-\Theta_{\text{light}}(t))\hat{m}_7 + \hat{m}_8)\frac{\hat{c}_T^{(n)}}{1+\hat{c}_T^{(n)}} \tag{3.6}$$

$$\frac{d\hat{c}_X^{(m)}}{dt} = \frac{\hat{n}_3\hat{c}_T^{(n)^d}}{\hat{g}_4^d + \hat{c}_T^{(n)^d}} - \frac{\hat{m}_9\hat{c}_X^{(m)}}{1+\hat{c}_X^{(m)}} \tag{3.7}$$

$$\frac{d\hat{c}_X^{(c)}}{dt} = \hat{p}_3\hat{c}_X^{(m)} - r_5\hat{c}_X^{(c)} + \hat{r}_6\hat{c}_X^{(n)} - \frac{\hat{m}_{10}\hat{c}_X^{(c)}}{1+\hat{c}_X^{(c)}} \tag{3.8}$$

$$\frac{d\hat{c}_X^{(n)}}{dt} = \rho_X(r_5\hat{c}_X^{(c)} - \hat{r}_6\hat{c}_X^{(n)}) - \frac{\hat{m}_{11}\hat{c}_X^{(n)}}{1+\hat{c}_X^{(n)}} \tag{3.9}$$

$$\frac{d\hat{c}_Y^{(m)}}{dt} = \left(\Theta_{\text{light}}(t)\hat{q}_2\hat{c}_P^{(n)} + \frac{(\Theta_{\text{light}}(t)\hat{n}_4 + \hat{n}_5)\hat{g}_5^e}{\hat{g}_5^e + \hat{c}_T^{(n)^e}}\right)\left(\frac{\hat{g}_6^f}{\hat{g}_6^f + \hat{c}_L^{(n)^f}}\right) - \frac{\hat{m}_{12}\hat{c}_Y^{(m)}}{1+\hat{c}_Y^{(m)}} \tag{3.10}$$

$$\frac{d\hat{c}_Y^{(c)}}{dt} = \hat{p}_4\hat{c}_Y^{(m)} - r_7\hat{c}_Y^{(c)} + \hat{r}_8\hat{c}_Y^{(n)} - \frac{\hat{m}_{13}\hat{c}_Y^{(c)}}{1+\hat{c}_Y^{(c)}} \tag{3.11}$$

$$\frac{d\hat{c}_Y^{(n)}}{dt} = \rho_Y(r_7\hat{c}_Y^{(c)} - \hat{r}_8\hat{c}_Y^{(n)}) - \frac{\hat{m}_{14}\hat{c}_Y^{(n)}}{1+\hat{c}_Y^{(n)}} \tag{3.12}$$

$$\frac{dc_P^{(n)}}{dt} = (1-\Theta_{\text{light}}(t))p_5 - \frac{m_{15}\hat{c}_P^{(n)}}{k_{13}+\hat{c}_P^{(n)}} - q_3\Theta_{\text{light}}(t)\hat{c}_P^{(n)} \tag{3.13}$$

$$\frac{d\hat{c}_A^{(m)}}{dt} = \Theta_{\text{light}}(t)\hat{q}_4\hat{c}_P^{(n)} + \frac{\hat{n}_6\hat{c}_L^{(n)^g}}{\hat{g}_7^g + \hat{c}_L^{(n)^g}} - \frac{\hat{m}_{16}\hat{c}_A^{(m)}}{1+\hat{c}_A^{(m)}} \tag{3.14}$$

$$\frac{d\hat{c}_A^{(c)}}{dt} = \hat{p}_6\hat{c}_A^{(m)} - r_9\hat{c}_A^{(c)} + \hat{r}_{10}\hat{c}_A^{(n)} - \frac{\hat{m}_{17}\hat{c}_A^{(c)}}{1+\hat{c}_A^{(c)}} \tag{3.15}$$

$$\frac{d\hat{c}_A^{(n)}}{dt} = \rho_A(r_9\hat{c}_A^{(c)} - \hat{r}_{10}\hat{c}_A^{(n)}) - \frac{\hat{m}_{18}\hat{c}_A^{(n)}}{1+\hat{c}_A^{(n)}} \tag{3.16}$$

Table 3.1: Rescaled parameters for the *NDTL Model*.

Three Loop Model equations (A.14–A.29) non-dimensionalised by rescaling each state variable by its associated michaelis constant of degradation (k_i, $i = 1,\ldots,12,14,15,16$). Rescaling the model parameters as defined in this table leads to the *NDTL Model* equations (3.1–3.16). The values given correspond to the nominal parameter values defined by Locke *et al.* (2006).

Name	Definition	Value	Name	Definition	Value
$\hat{q}_1$	q_1/k_1	1.7539	$\hat{p}_3$	p_3k_7/k_8	21.2321
$\hat{n}_0$	n_0/k_1	0.0209	$\hat{r}_6$	r_6k_9/k_8	85.1865
$\hat{g}_0$	g_0/k_{16}	1.6383	$\hat{m}_{10}$	m_{10}/k_8	0.3286
$\hat{n}_1$	n_1/k_1	3.2668	ρ_X	k_8/k_9	0.0388
$\hat{g}_1$	g_1/k_9	0.1834	$\hat{m}_{11}$	m_{11}/k_9	0.1954
$\hat{m}_1$	m_1/k_1	0.8357	$\hat{q}_2$	q_2/k_{10}	1.388
$\hat{p}_1$	p_1k_1/k_2	1.2683	$\hat{n}_4$	n_4/k_{10}	0.0495
$\hat{r}_2$	r_2k_3/k_2	0.1377	$\hat{n}_5$	n_5/k_{10}	0.0953

Continued on next page

Table 3.1: *Continued from previous page*

Name	Definition	Value	Name	Definition	Value
$\hat{m}_2$	m_2/k_2	13.0657	$\hat{g}_5$	g_5/k_6	2.9209
ρ_L	k_2/k_3	1.2255	$\hat{g}_6$	g_6/k_3	0.0505
$\hat{m}_3$	m_3/k_3	2.8898	$\hat{m}_{12}$	m_{12}/k_{10}	2.4834
$\hat{n}_2$	n_2/k_4	1.1692	$\hat{p}_4$	p_4k_{10}/k_{11}	0.2355
$\hat{g}_2$	g_2/k_{12}	0.0204	$\hat{r}_8$	r_8k_{12}/k_{11}	0.1981
$\hat{g}_3$	g_3/k_3	0.2082	$\hat{m}_{13}$	m_{13}/k_{11}	0.0738
$\hat{m}_4$	m_4/k_4	1.4856	ρ_Y	k_{11}/k_{12}	1.0106
$\hat{p}_2$	p_2k_4/k_5	4.0531	$\hat{m}_{14}$	m_{14}/k_{12}	0.3384
$\hat{r}_4$	r_4k_6/k_5	0.316	$\hat{q}_4$	q_4/k_{14}	0.2366
$\hat{m}_5$	m_5/k_5	0.0005	$\hat{n}_6$	n_6/k_{14}	0.7789
ρ_T	k_5/k_6	6.8073	$\hat{g}_7$	g_7/k_3	0.0003
$\hat{m}_6$	m_6/k_5	1.1562	$\hat{m}_{16}$	m_{16}/k_{14}	1.1813
$\hat{m}_7$	m_7/k_6	0.122	$\hat{p}_6$	p_6k_{14}/k_{15}	42.847
$\hat{m}_8$	m_8/k_6	10.0233	$\hat{r}_{10}$	$r_{10}k_{16}/k_{15}$	1.9206
$\hat{n}_3$	n_3/k_7	0.2431	$\hat{m}_{17}$	m_{17}/k_{15}	63.3073
$\hat{g}_4$	g_4/k_6	1.336	ρ_A	k_{15}/k_{16}	0.1152
$\hat{m}_9$	m_9/k_7	1.542	$\hat{m}_{18}$	m_{18}/k_{16}	0.0256

Simulated annealing algorithm for fine-tuning model parameters

The large number of parameters in the *NDTL Model* almost certainly leads to a large number of local minima of any cost function which penalises deviations between simulated outputs and measured data. Therefore, algorithms which move in the direction of local minima automatically (i.e. gradient descent methods) are not desirable as they can 'get stuck' at poor local minima (Robert & Casella, 2004). Simulated Annealing (SA) is a class of algorithms which employ random search directions to approximate global minima, designed to solve optimisation problems with large search spaces (Metropolis *et al.*, 1953; Robert & Casella, 2004). SA was also used for parameter selection of most plant central oscillator models (Locke *et al.*, 2005a,b, 2006). We used an SA algorithm to refine the parameters of the *NDTL Model* (Eqns. 3.1–3.16), in order to investigate the role of sucrose in the circadian clock.

Consider the following nonlinear system:

$$\dot{x} = f(x, p) \tag{3.17}$$

where $x \in \mathcal{R}^n$ is the state vector comprising concentrations of mRNA and protein in the cytoplasm and nucleus of the 5 model components *LHY* (*LHY/CCA1*), *TOC1*, *X*, *Y* (*GI*) and *A* (*PRR7/9*), and $p \in \mathcal{R}^m$ is the vector of m model parameters. We seek p which minimizes the 'difference' between model simulation and *luc* luminescence data for seedlings grown without exogenous sucrose. We took the standard LSQ (least squares) approach, minimising the 2-norm of the residuals between data and simulated output.

$$\Delta(p) := \sum_{d \in \mathcal{D}} \sum_{i=1}^{N_d} e(p)/N_d \tag{3.18}$$

where $\mathcal{D}$ is the set of *luc* luminescence data, N_d the number of observations in experiment $d \in \mathcal{D}$ and $e(p)$ the residual between data and simulated model output with parameters p. The denominator N_d ensures an equal contribution from each experiment, irrespective of the number of observations. There have been no previous attempts to calibrate luminescence data to actual concentrations of mRNA, so we assumed that the measured luminescence is a linear function of [mRNA]. Therefore, we define the residual norm e by solving a linear regression problem.

$$e(p) := \min_{a,b} ||ax_d(p) + b - y_d||_2 \tag{3.19}$$

where y_d is the vector of *luciferase* luminescence measurements from dataset d, and x_d the associated simulated output. This scheme ensures that the dynamics of the optimised model are not constrained by the signal strength of the *luc* reporter system.

The cost function in Eqn. 3.18 was evaluated by obtaining solutions for simulated [*LHY* mRNA] and [*TOC1* mRNA] at the time-points corresponding to the LL and DD *luc* luminescence data as in Section 3.2.2. The *polyfit* function in MATLAB^{TM} was then used to find the minimisers a and b in Eqn. 3.19 to compute $e(p)$ for each dataset, which were then substituted into Eqn. 3.18 to find $\Delta(p)$. The dynamics of [*Y* (*GI*) mRNA] were not incorporated into the cost function as the corresponding measurements of *GI:luc* only became available shortly before

writing this thesis. Instead, *GI* expression is compared during cross-validation (Section 3.3.3).

SA algorithms generate a Markov chain of proposal solutions p which converge on a local minimum of the cost function $\Delta(p)$. At each iteration, a new proposal p_1 is generated which is based on the current state p. Then, we move to the new state according to some acceptance probability $a(p, p_1, T)$. Here, T is the 'cooling' parameter, which is a decreasing function (of the iteration) designed to reduce the acceptance probability of non-improvement states later in the chain. The most commonly used acceptance function corresponds to the Metropolis-Hastings (MH) algorithm (Kirkpatrick *et al.*, 1983) defined as

$$a(p, p_1, T) := \min\left\{1 \quad , \quad \exp\left(\frac{\Delta(p) - \Delta(p_1)}{T}\right)\right\} \tag{3.20}$$

Due to the large number of parameters and the additional uncertainty that the model equations are a sufficient description of the underlying system, we ran the algorithm many times, obtaining many local minima. The MH formulation defined the acceptance of proposal parameter sets (Eqn. 3.20), where the cooling parameter was taken to be a normalised linear function of the iteration number. In addition, an adaptive cooling method was used on the search direction. At each iteration, we propose a random search direction in an N-dimensional projection $\mathcal{P}^N$ comprised of N randomly chosen parameters, where $N := \lceil \alpha\Delta \rceil$ and α is a constant. Each of these N parameters (p_i) are moved to $\hat{p}_i$ which is gaussian-distributed with mean p_i and variance σ^2, where $\sigma := \beta\Delta$ and β is another constant. This adaptive scheme enabled us to fine-tune the parameters more efficiently, as the parameters are perturbed less at each iteration as we approach local minima of the cost function.

Initial approximate minimisers of Eqn. 3.18 often had an undesirable behaviour in entrained light-dark (L16/D8 or L8/D16) cycles. The system trajectory did not converge to a limit cycle oscillation, but instead had autonomous oscillatory behaviour with a period near to but not exactly 24 h occurred in addition to periodic behaviour from 24 h periodic light-dark forcing. This could be seen most clearly in simulated [*TOC1* mRNA], which could be described as a biphasic 24 h oscillation in which the phase difference between the two peaks was changing each cycle (increasing progressively by ≈ 1 h. To eradicate solutions with this behaviour, a second term was added to the cost function (Eqn. 3.18) to penalise systems which generated trajectories with multiple periods in these alternative photoperiods. The model equations (3.1–3.16) were simulated under L16/D8 and L8/D16 conditions for 840 h, and the first 600 h discarded as transitory

in each case. The times of local maxima and minima of simulated [*TOC1* mRNA] were then computed for $t \in [600 \quad 840]$, as $t^{(1)}_{\max}, t^{(2)}_{\max}, \ldots, t^{(p)}_{\max}$ and $t^{(1)}_{\min}, t^{(2)}_{\min}, \ldots, t^{(q)}_{\min}$ respectively. Then, allowing for biphasic oscillations, we defined the entrainment cost term as

$$\Delta^{\mathrm{LD}}_{\mathrm{ent}} := \left\| \begin{pmatrix} t^{(5)}_{\max} \\ t^{(6)}_{\max} \\ \vdots \\ t^{(p)}_{\max} \end{pmatrix} - \begin{pmatrix} t^{(1)}_{\max} \\ t^{(2)}_{\max} \\ \vdots \\ t^{(p-4)}_{\max} \end{pmatrix} \right\|_2 + \left\| \begin{pmatrix} t^{(5)}_{\min} \\ t^{(6)}_{\min} \\ \vdots \\ t^{(q)}_{\min} \end{pmatrix} - \begin{pmatrix} t^{(1)}_{\min} \\ t^{(2)}_{\min} \\ \vdots \\ t^{(q-4)}_{\min} \end{pmatrix} \right\|_2 \tag{3.21}$$

for LD as L16/D8 and L8/D16. Therefore the complete cost function used in Section 3.3.3 was

$$\Delta(p) = e^{\mathrm{DD}}_{\mathrm{LHY}}(p) + e^{\mathrm{DD}}_{\mathrm{TOC1}}(p) + e^{\mathrm{LL}}_{\mathrm{LHY}}(p) + e^{\mathrm{LL}}_{\mathrm{TOC1}}(p) + \Delta^{\mathrm{L16/D8}}_{\mathrm{ent}}(p) + \Delta^{\mathrm{L8/D16}}_{\mathrm{ent}}(p) \tag{3.22}$$

3.3 Results

3.3.1 $[\mathrm{ATP}]_i$ does not limit *Luciferase* light emission after 60 hours of darkness

The measured luminescence signal from *CCA1:luc* expressing *Arabidopsis* seedlings grown in DD is lower in the absence of exogenous sucrose supply. During glycolysis, the metabolism of sucrose generates ATP (Buchanan *et al.*, 2002). Therefore, exogenous supply of sucrose might increase $[\mathrm{ATP}]_i$, leading to higher light emission from the *Luciferase* enzyme. To control for the possibility that reduced light emission in plants grown in the absence of exogenous sucrose prevents observation of circadian oscillations in *CCA1:luc*, *TOC1:luc* and *GI:luc* luminescence due to low $[\mathrm{ATP}]_i$, cold-induced promoter activity of *CCA1* was measured after a period of extended darkness. Plants were exposed to cold treatments of 2, 3 and 6 h in duration, and the activity of the cold-inducible *CCA1* promoter was monitored with photon-counting luminometry as described in Section 3.2.1. Irrespective of whether sucrose was available in the growth media, large increases in promoter activity were observed after each of the three cold shock durations tested (Figure 3.2). As growing plants in DD on sucrose-supplemented media did not increase the relative luminescence after a cold shock, we conclude that in DD ATP availability was not limiting the reaction which enables *luciferase* to emit light in the presence of it's substrate luciferin.

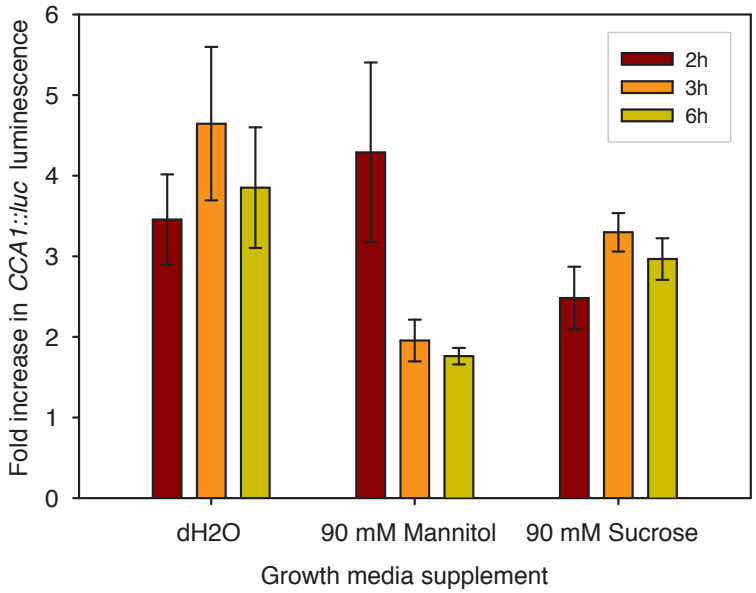

Figure 3.2: Cold induces *CCA1* promoter activity after 60 hours of darkness.
Arabidopsis seedlings were grown on agar media containing H_2O, 90 mM mannitol or 90 mM sucrose and entrained under L12/D12 cycles for 10 d before transfer to DD for 60 h. Luminescence was quantified for 60 s in a luminometer to obtain basal activity. Cold treatment was then administered for 2 h (dark red bars), 3 h (orange bars) or 6 h (green bars), left for 15 minutes at 19°C before quantifying luminescence for 240 s. Bars indicate average of cold-induced luminescence divided by basal luminescence for each condition ($n = 12$).

3.3.2 Accounting for no exogenous sucrose with single-parameter modifications to the *Three Loop Model*

Identifying single parameter alterations as potential sucrose targets

After prolonged darkness, circadian oscillations in promoter activity of central oscillator genes were present in plants grown with exogenous sucrose (90 mM), while *CCA1* and *TOC1* expression in plants without exogenous sucrose (H_2O or 90 mM mannitol controls) tended to a steady state (Figure 3.1). Oscillations in *GI:luc* were present in the absence of exogenous sucrose, though with a lower amplitude and longer period than in the presence of exogenous sucrose (Figures 3.1E,G). We sought single parameter alterations to the *Three Loop Model* of the *Arabidopsis* circadian clock (Locke *et al.*, 2006) which could predict a loss of oscillations in DD whilst retaining circadian rhythmicity in LL.

Period and amplitude of oscillation were computed as functions of each model parameter to assess rhythmicity of single-parameter alterations to the *Three Loop Model*. Parameters were identified in which increases and decreases in their relative value led to a loss of rhythmicity in DD, while retaining oscillations in LL. As examples, $n_3 \lesssim 0.2$ (Figure 3.3A) and $n_5 \lesssim 0.3$

(Figure 3.3B) had oscillation fold ratios near 1 in DD implying arrhythmicity, though > 10 in LL implying stable oscillations. Parameter alterations for values of p^r which produced LL periods between 20 h and 30 h and a DD oscillation fold ratio < 1.1 were shortlisted. This candidate set of parameter alterations included over one-third (26/70) of all parameters (Figure 3.3C).

Table 3.2: Candidate single-parameter modifications simulated for K-means clustering.
Shortlist of parameters which could be modified to achieve a loss of oscillations in DD (oscillation fold ratio no greater than 1.1), while retaining stable oscillations in LL (oscillation fold ratio greater than 1.1 and period between 20 and 30 h). The candidate parameter regions (increases or decreases) analysed for their median value are indicated in this table. Each candidate-region median value was used to simulate the model equations in L12/D12 before transfer to DD. Simulations were then classified into 8 clusters by K-means clustering (Macqueen, 1967), with $1 - \rho$ as the distance measure where ρ is the cross-correlation. Implementation was in MATLAB™ with the *kmeans* function (Stastistics Toolbox; Seber, 2004).

Decreases			Increases		
Parameter	Rel. Value	Cluster	Parameter	Rel. Value	Cluster
n_3	0.0692	5	g_2	19.5	5
n_5	0.0525	2	g_7	43.65	7
g	0.0617	7	m_3	51.29	4
α	0.02	8	m_6	20.89	5
g_5	0.0145	5	m_8	25.7	5
m_3	0.0115	1	m_9	13.8	5
k_1	0.0288	6	m_{12}	19.0546	5
k_3	0.0155	4	m_{13}	74.131	5
k_4	0.055	5	m_{14}	19.5	5
k_7	0.0692	5	m_{17}	11.749	7
k_{10}	0.0513	5	k_3	63.0957	3
k_{11}	0.0129	5			
k_{12}	0.0513	5			
k_{15}	0.0102	7			
p_2	0.055	5			
p_4	0.0513	5			
r_7	0.0129	5			

Comparing single-parameter alterations with *CCA1:luc* luminescence data

Candidate perturbations that best matched *CCA1:luc* luminescence measurements in DD in the absence of exogenous sucrose were identified by simulation of each candidate perturbation and comparison with the experimental data (Figure 3.1A). For each candidate parameter, the median value in the range of candidate decreases or increases (both if required) was selected for simulation (indicated by the red crosses in Figure 3.3C; Table 3.2). Simulations of *LHY* mRNA in entrained L12/D12 cycles before transfer to DD were categorized into 8 clusters using a K-means algorithm (Macqueen, 1967; see Section 3.2.4 for details; Table 3.2; Figure 3.4). Seven-

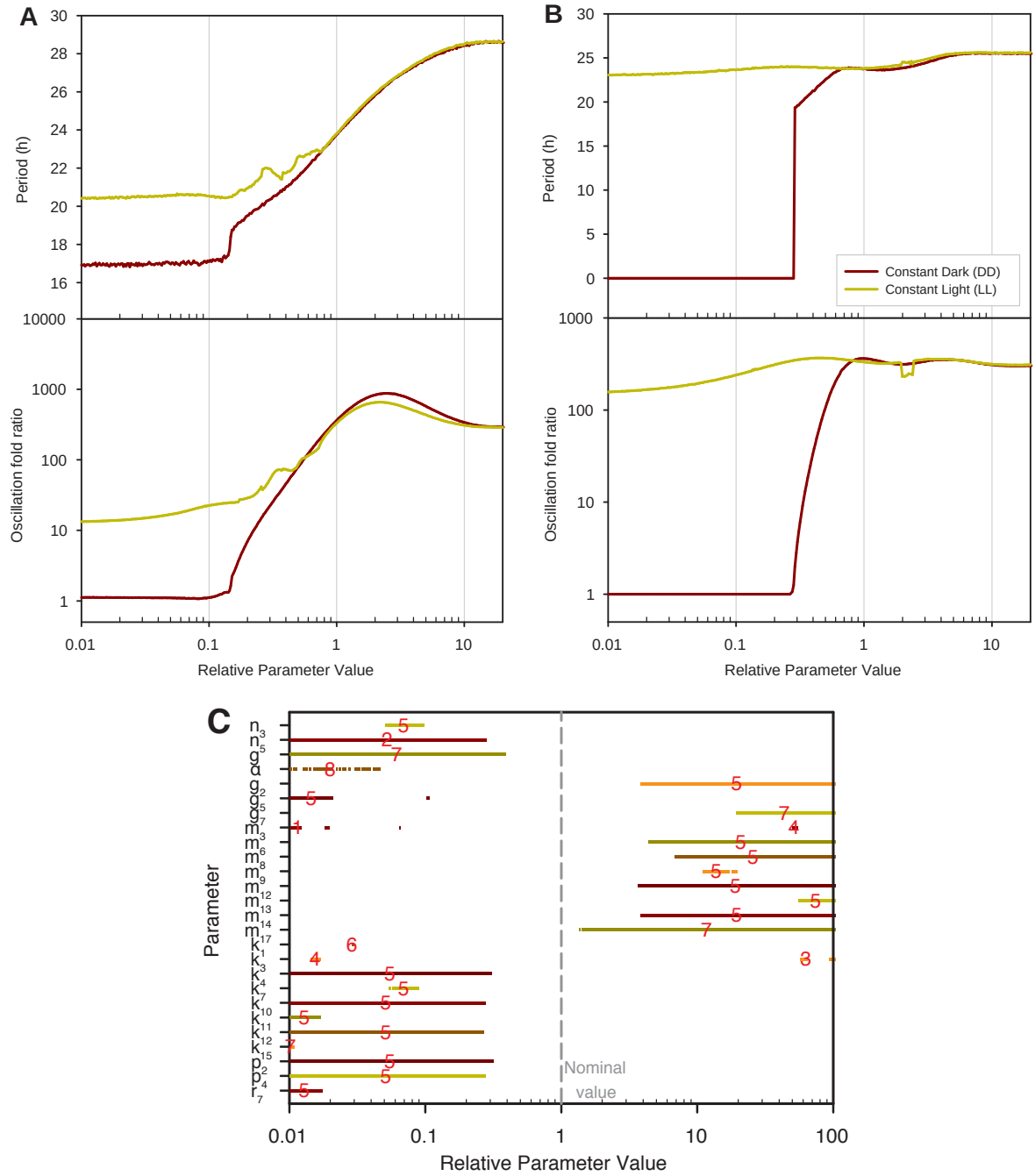

Figure 3.3: Single parameter modifications enable steady state in DD and stable oscillations in LL. The *Three Loop Model* (Locke *et al.*, 2006; Equations A.14–A.29) was simulated under LL and DD for 600 h to assess how the model can reproduce the behaviours seen when plants are grown in the absence of exogenous sucrose. Period and oscillation fold ratio plotted as functions of the relative values of (A) n_3 (maximum rate of X transcription, and (B) n_5 (maximum light-independent rate of Y (*GI*) transcription. A,B) Period was computed as the time difference between the last two peak values of simulated [*LHY* mRNA]. Oscillation fold ratio (amplitude) was computed by dividing the value of the last local maximum by the value of the last local minimum of [*LHY* mRNA]. (C) Points indicate regions of relative parameter value for which LL period is between 20 h and 30 h, and DD oscillations fold ratio is less than 1.1. Red numbers located at the relative parameter values used for K-means clustering of simulated output in DD, the number itself denoting which cluster the trajectory belongs to (see Figure 3.4, and Table 3.2 for values).

teen of the twenty-eight candidate parameter alterations led to sharp light-induced oscillations in LD cycles, before a fast suppression towards zero in DD (Figure 3.4E). Seven candidates achieved steady state in DD with a slowly decaying amplitude oscillation (Figures 3.4D,F,G), while another two candidates showed no distinction between L12/D12 cycles and DD (Figures 3.4A,C). The candidate corresponding to Figure 3.4B showed significant similarity to the measured *CCA1:luc* luminescence data (Figure 3.1A). In both measured data and simulation, the signal undergoes a medium-sized oscillation peaking approximately 12 h into DD, before settling at a constant low value (≈ 0). Further parameter inspection revealed that by taking n_5 to be 0.25 of its nominal value enabled the closest match to the target dynamics of *CCA1* expression. This was defined as the (candidate) *N5 Model*. Our candidate model therefore offered a prediction for the effect of supplementing growth media with 90 mM sucrose. The biological interpretation of this prediction is that sucrose up-regulates the light-independent transcription rate of Y, which is believed to be the *GIGANTEA* (*GI*) gene (Locke *et al.*, 2005b, 2006).

Cross-validation of the *N5 Model* with wild-type data

Simulations of the *N5 Model* were compared with measured *luc* luminescence data in the absence of exogenous sucrose, to assess the wider applicability of this candidate model. In DD, simulations of all model components converged quickly to a low steady state, as reflected by *CCA1:luc* and *TOC1:luc* luminescence data. However, the persistence of circadian oscillations of *GI:luc* luminescence in DD was not predicted by the *N5 Model* (Figure 3.5A). The timing of peak expression for simulated *LHY*, *TOC1* and *Y/GI* was accurate in the L12/D12 cycles before transfer to DD (Figure 3.5A). In LL, oscillations in simulated *LHY* and *TOC1* peaked earlier than the measured data, indicating that a lag occurs after transfer from L12/D12 cycles to LL which was not predicted by the *N5 Model* (Figure 3.5B). In contrast, simulated *Y/GI* peaked later than *GI:luc* luminescence in LL (Figure 3.5B). In light-dark cycles, the shape of the *N5 Model* oscillations contrasted with the corresponding *luc* luminescence data for each model component, though the oscillation phase was accurate (Figures 3.5C,D). In particular, the model accurately predicted the phase shifts of peak *TOC1* and *GI* expression when comparing L16/D8 cycles (Figure 3.5C) and L8/D16 cycles (Figure 3.5D).

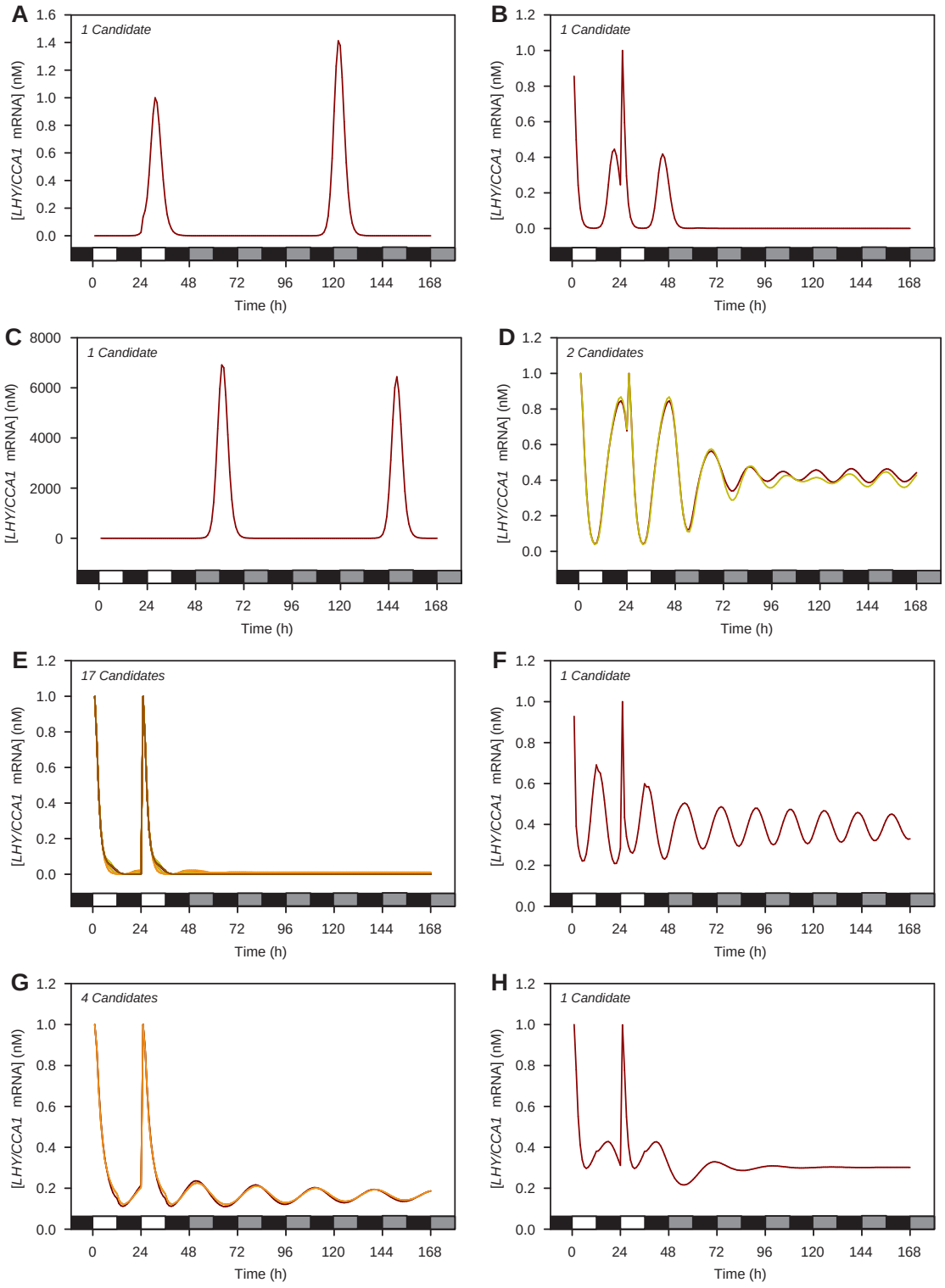

Figure 3.4: K-means clustering of DD simulations reveals prediction of sucrose target.
Simulations of single-parameter modifications to the *Three Loop Model* (Locke *et al.*, 2006; Equations A.14–A.29) assessed for similarity to effect of growing *Arabidopsis* without exogenous sucrose. Parameter modifications were chosen so LL period was between 20 h and 30 h, and DD oscillation fold ratio was no greater than 1.1 (Table 3.2). For each candidate parameter region (increase or decrease), the median value was selected. Model equations were solved numerically for 48 h in L12/D12 and 120 h in DD, with values of simulated [*LHY* mRNA] returned at 0.2 h intervals between t = 0 h and t = 168 h. Simulation vectors classified into 8 clusters using the *kmeans* function in MATLAB^{TM} (Stastistics Toolbox; Macqueen, 1967; Seber, 2004), with $1 - \rho$ as the distance measure (where ρ is the sample correlation coefficient). Panels A through H correspond to clusters 1 to 8 sequentially (see Table 3.2).

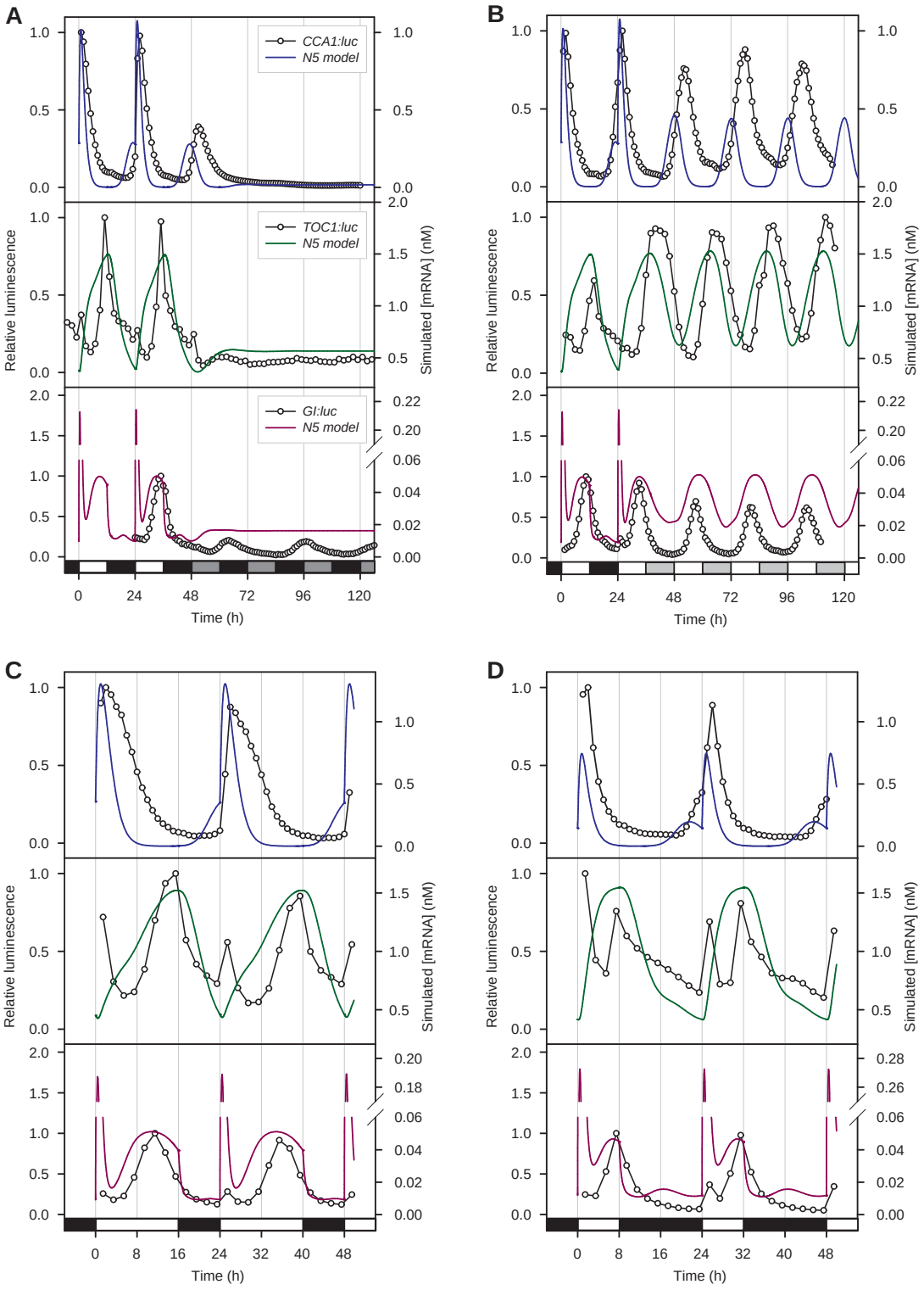

Figure 3.5: Cross-validation of the *N5 Model* to *luc* luminescence data in DD, LL, L16/D8 and L8/D16. Comparison of simulations of the *N5 Model* (blue lines) with corresponding (relative) measured luminescence data (open circles) for *LHY* (top panels), *TOC1* (middle panels) and *GI* (bottom panels). *Three Loop Model* equations with n_5 set to 0.25 of the nominal value were solved numerically using MATLAB^{TM}'s *ode15s* solver (Shampine & Reichelt, 1997). (A) Entrainment to L12/D12 cycles before transfer to DD, (B) entrainment to L12/D12 cycles before transfer to LL, (C) L16/D8 cycles, and (D) L8/D16 cycles. Data collected by Katharine Hubbard and Seong Jin Baek, (University of Cambridge, *personal communication*). In abscissa, white bars indicate light, black bars indicate dark, dark grey indicates dark in subjective daytime and light grey indicates light in subjective night-time.

3.3.3 Accounting for no exogenous sucrose with multiple-parameter modifications to the *Three Loop Model*

Fine-tuning of the *Three Loop Model* parameters

In this section, the possibility that sucrose modulation of the central oscillator can be described mathematically by a change in multiple parameters of the *Three Loop Model* is considered (Locke *et al.*, 2006). This contrasts to the previous section in which only single parameter modifications were considered. The system equations were first non-dimensionalised to reduce the size of the search space (*NDTL Model*, Equations 3.1–3.16), then the resulting system parameters (Table 3.1) were retuned based on experimental data from seedlings grown on agar media in the absence of exogenous sucrose (Figure 3.1). Parameters were selected through minimisation of a cost function which penalised deviation from experimental data or led to the onset of multiple periodic oscillations (see Section 3.2.5). The optimisation method was initialised at the non-dimensionalised parameter set corresponding to the nominal model configuration of equations A.14–A.29 (see Table 3.1 for corresponding parameter values).

The modified SA algorithm (Section 3.2.5) was able to produce many solutions, which matched the target datasets with accuracy. Four hundred independent trials were run for 1000 iterations each with $\alpha = 0.5$ and $\beta = \frac{100}{3}$, providing an array of trial-optimal solutions (defined as the parameter sets corresponding to the minimum cost function value attained over each trial). The cost function values corresponding to the trial-optimal solutions were distributed bimodally, indicating that in many cases the algorithm was unable to avoid poor local minima ($\Delta(p) \gtrsim 0.2$; Figure 3.6A). However, in some cases the algorithm reached parameter sets for which $\Delta(p) < 0.2$ within the first 200 iterations (Figure 3.6B). In Figures 3.6B–F two models are considered (see Table 3.3 for parameter values). *Model 1* corresponds to the trial-optimal solution with the lowest value of $\Delta(p)$ observed over the four hundred trials, while *Model 5* represents the 5^{th} lowest $\Delta(p)$, but the lowest for which there were no oscillations in DD for both simulated *LHY* (Figure 3.6C) and *TOC1* mRNA (Figure 3.6D). The four lowest scoring models (i.e. *Model 1*, *Model 2*, *Model 3* and *Model 4*) had damped oscillations in simulated [*LHY* mRNA] after transfer to DD (Figure 3.6C). The small amplitude of the oscillations seemingly did not increase the cost function enough to select away from these parameter sets. However, no oscillations were seen in *Model 1* or *Model 5* for simulated [*TOC1* mRNA] in DD, and both also accurately reproduced the oscillations of *CCA1:luc* and *TOC1:luc* luminescence observed

in L12/D12 (Figure 3.6D). Many parameter sets explored during the optimisation were able to distinguish between the lower amplitude oscillations of *CCA1:luc* luminescence in LL than in LD cycles; this was also true of *Model 1* and *Model 5* (Figure 3.6E). The candidate models were also capable of predicting the larger amplitude oscillations of *TOC1:luc* luminescence in LL over those observed in L12/D12 (Figure 3.6F).

Cross-validation of fine-tuned models with wild-type data

Validation tests were performed to assess the wider applicability of the models derived in this section. It was important to compare simulated dynamics of Y (*GI*) with measurements of *GI:luc*, as *GI* expression was not part of the selection criteria for fine-tuned models and additionally, *GI* transcription was implicated as a sucrose target in Section 3.3.2. In L12/D12 cycles, simulated [Y (*GI*) mRNA] from *Model 1* and *Model 5* increased transiently at dawn before increasing until dusk, then quickly decreased to a constant low level in the dark phase (Figures 3.7A–B). *GI:luc* luminescence did not show such a large transient increase at dawn but increased until dusk, then decreased similar to the simulations of the two candidate models. Upon transfer to DD, *GI:luc* luminescence emitted from plants grown both in the presence and absence of exogenous sucrose continued to oscillate with a low amplitude rhythm, whereas *Model 1* and *Model 5* both predicted constant low [Y (*GI*) mRNA] in DD (Figure 3.7A). In LL, *GI:luc* luminescence oscillated with slightly less amplitude than in L12/D12 cycles, peaking 2–3 hours before subjective dusk, while simulated [Y (*GI*) mRNA] of both models had oscillations that peaked 1–2 hours after subjective dusk (Figure 3.7B). In both *Model 1* and *Model 5*, LL oscillations of simulated [Y (*GI*) mRNA] had biphasic oscillations, as seen in the nominal model configuration (Locke *et al.*, 2006), though this was not seen in our measurements of *GI:luc* luminescence, both in the presence and absence of exogenous sucrose (Figure 3.7B).

Next, oscillations of *CCA1*, *TOC1* and *GI* expression in light-dark cycles of differing photoperiods were considered (Figures 3.7C–H). *CCA1:luc* luminescence oscillated in L16/D8 cycles with a peak 2 h after dawn, before declining to a constant low level reached at dusk (Figure 3.7C). In L8/D16 cycles, *CCA1:luc* luminescence oscillated with a peak 2 h after dawn, decreased to a constant low level by dusk, then increased 3 h before dawn (Figure 3.7D). *Model 1* and *Model 5* were both able to reproduce the change in width of oscillation between L16/D8 and L8/D16 cycles and anticipated dawn in L8/D16, though only *Model 1* anticipated dawn at

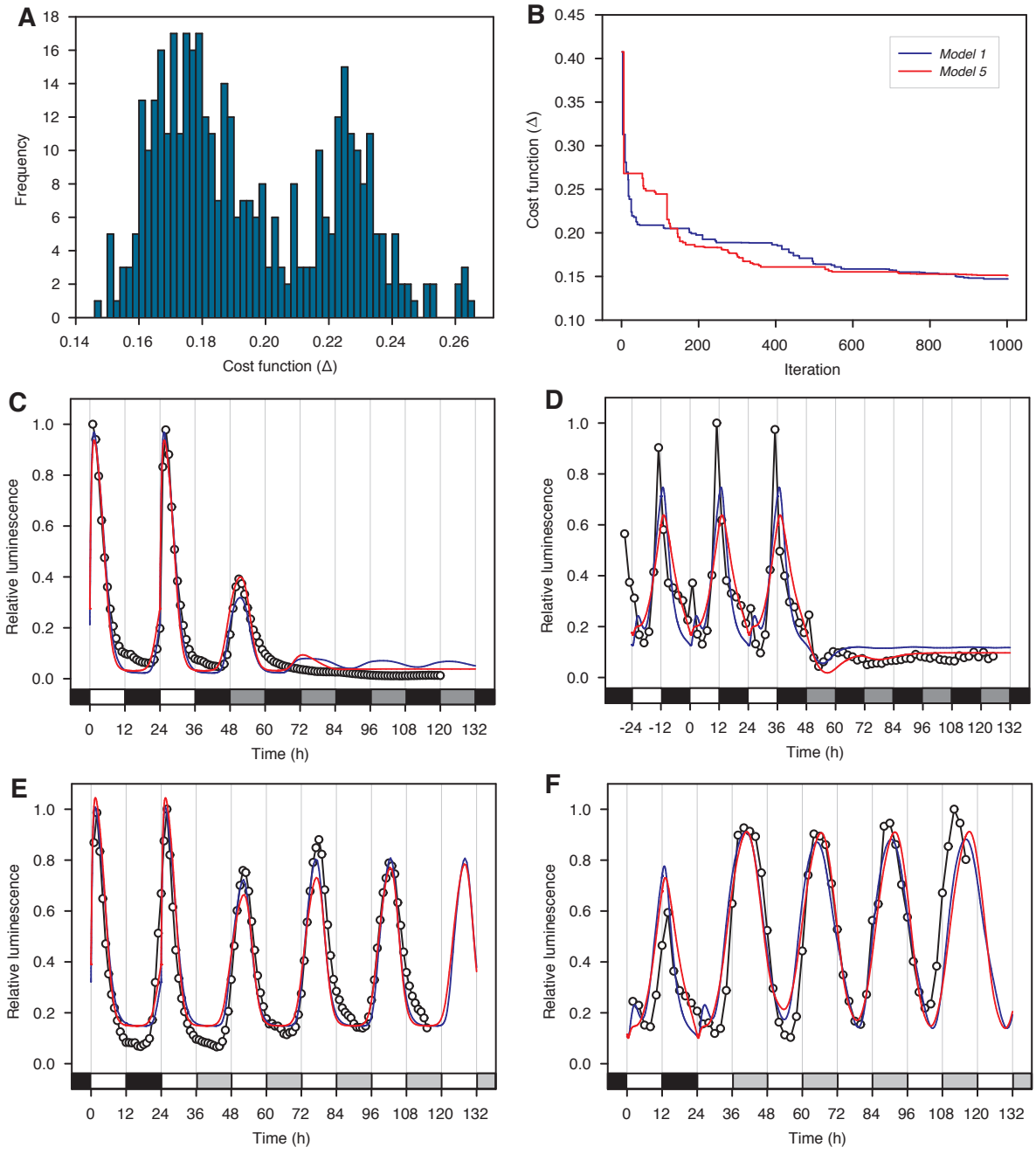

Figure 3.6: Parameter re-tuning of the *Three Loop Model* to account for no exogenous sucrose. Parameters from the *NDTL Model* (Eqns. 3.1–3.16) were optimised with respect to a cost function corresponding to the data in Figure 3.1 using a Simulated Annealing algorithm over 400 independent trials of 1000 iterations each. (A) Lowest costs of each trial displayed as a histogram. (B) The lowest cost function value achieved as a function of the iteration number is plotted for two models: *Model 1* (blue line) corresponds to the lowest cost attained over all 400 trials, while *Model 5* (red line) corresponds to the 5^{th} lowest score. (C – F) Comparison of measured luminescence data (open circles) with corresponding simulations of *Model 1* (blue line) and *Model 5* (red line). For each model, the simulated output ($\hat{y}$) was rescaled with values a and b which minimised $\min_{a,b} \sum_i (y_i - a\hat{y}_i - b)^2$ where the y_i are the measured luminescence values. (C) *CCA1:luc* luminescence measured in entrained L12/D12 cycles before transfer to DD at $t = 36$, and rescaled simulations of [*LHY* mRNA]. (D) *TOC1:luc* luminescence in entrained L12/D12 cycles before transfer to DD at $t = 36$, and rescaled simulations of [*TOC1* mRNA]. (E) *CCA1:luc* luminescence measured in entrained L12/D12 cycles before transfer to LL at $t = 24$, and rescaled simulations of [*LHY* mRNA]. (F) *TOC1:luc* luminescence in entrained L12/D12 cycles before transfer to LL at $t = 24$, and rescaled simulations of [*TOC1* mRNA]. Luminescence data in D, E and F were obtained from Seong-Jin Baek (*personal communication*).

Table 3.3: Candidate parameter sets from fine-tuning.
A Metropolis-hastings algorithm was used to refine the *NDTL Model* parameters, based on *CCA1:luc* and *TOC1:luc* luminescence data. *Model 1* corresponds to the parameter set with lowest cost function during optimisation, and *Model 5* the 5$^{\text{th}}$ lowest cost overall, but lowest of models which tend to steady state in DD. Tabulated values are the relative parameter sets based on the values in Table 3.1.

Parameter	*Model 1*	*Model 5*	Parameter	*Model 1*	*Model 5*
q_1	1.1620	1.8689	m_7	1.4205	0.3447
q_2	0.1930	0.6184	m_8	1.0212	1.0498
q_4	1.2855	1.5719	m_9	1.3556	0.7569
n_0	0.6599	0.9832	m_{10}	0.7353	0.9643
n_1	0.3931	0.6578	m_{11}	1.1935	0.9847
n_2	0.7852	0.8166	m_{12}	1.6672	1.3404
n_3	2.3971	2.6644	m_{13}	1.0295	0.8325
n_4	1.3212	2.0471	m_{14}	1.0243	0.5075
n_5	0.5990	0.3222	m_{16}	1.2139	0.9445
n_6	1.2228	0.9435	m_{17}	0.6810	1.1407
a	1.1040	0.6665	m_{18}	1.5128	1.4185
b	2.1621	1.6100	p_1	0.6290	0.4971
c	1.3502	1.6279	p_2	1.4066	1.1454
d	0.7824	1.6591	p_3	1.2930	0.5408
e	1.2389	1.4814	p_4	0.8127	1.0030
f	1.6439	1.0295	p_6	0.8485	1.1129
g	0.5568	0.7329	r_1	0.8686	0.6608
α	1.5077	1.4316	r_2	0.3801	0.5359
g_0	1.4030	1.4133	r_3	0.5565	1.1744
g_1	1.1038	1.0409	r_4	0.6094	1.1017
g_2	0.8166	1.1862	r_5	1.4205	0.7415
g_3	1.2856	0.7802	r_6	0.6103	1.7480
g_4	0.7379	0.3949	r_7	0.6581	2.2134
g_5	0.8031	0.6612	r_8	0.5266	1.1484
g_6	1.8767	0.7370	r_9	1.1112	1.0065
g_7	1.1953	0.4917	r_{10}	1.1925	0.7078
m_1	0.7560	1.0997	ρ_L	0.7413	0.7910
m_2	0.7207	0.9365	ρ_T	1.3384	1.0044
m_3	1.2693	1.5396	ρ_X	0.9911	0.7587
m_4	1.3819	1.3328	ρ_Y	0.9219	0.8465
m_5	1.5939	0.9055	ρ_A	0.9196	1.1095
m_6	0.1991	0.8877			

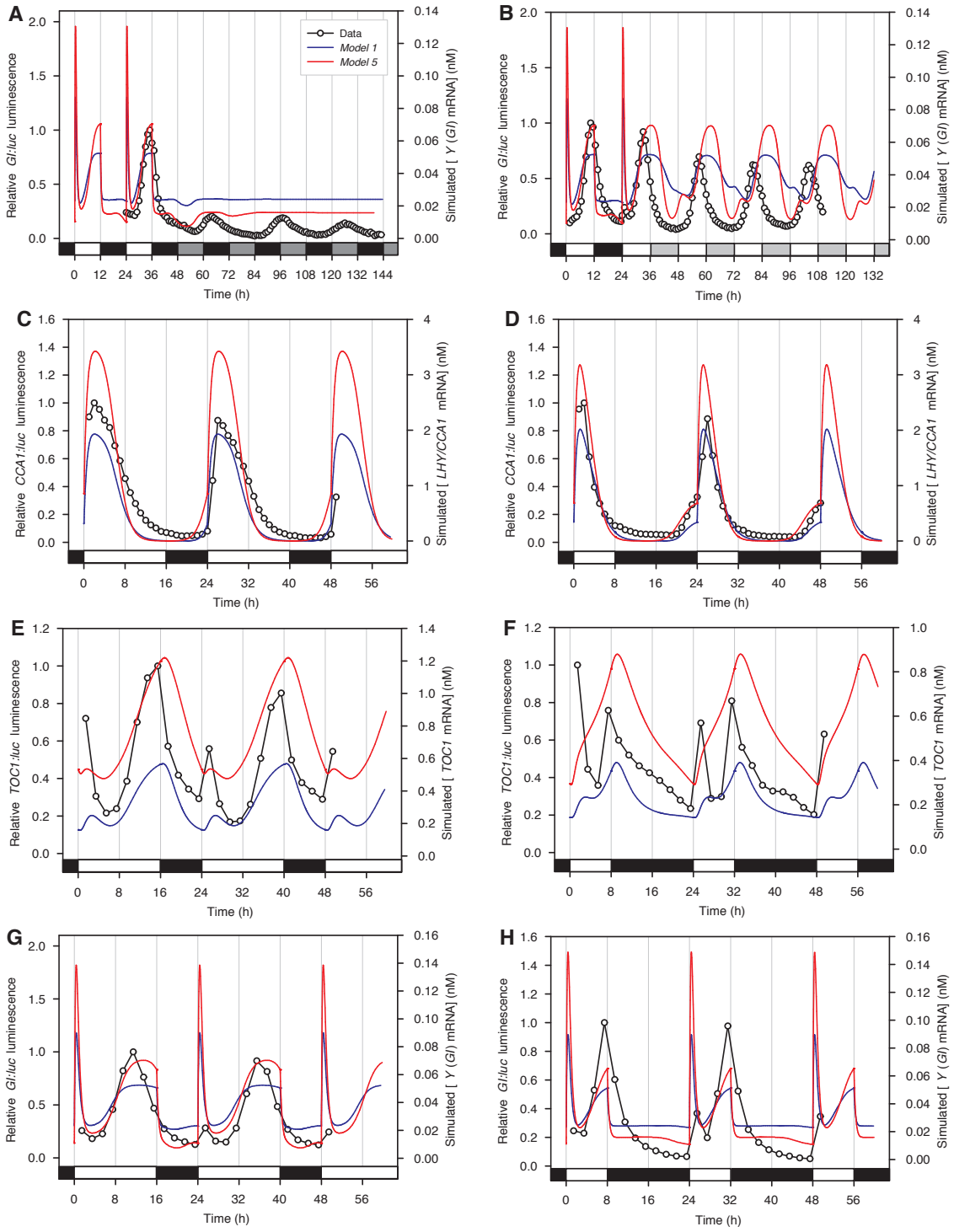

Figure 3.7: Cross-validation of re-tuned *Three Loop Models* to luminescence data in DD, LL, L16/D8 and L8/D16.
Comparison of (relative) measured luminescence data (open circles; left axes) with corresponding simulations of Models 1 (blue line; right axes) and 5 (red line; right axes). (A) *GI:luc* luminescence in L12/D12 cycles before transfer to DD at $t = 36$ (Seong Jin Baek, *personal communication*), versus corresponding simulations of [Y (*GI*) mRNA]. (B) *GI:luc* luminescence in L12/D12 cycles before transfer to LL at $t = 24$ (Seong Jin Baek, *personal communication*), versus corresponding simulations of [Y (*GI*) mRNA]. (C,E,G) L16/D8 cycles. (D,F,H) L8/D16 cycles. (C,D) Relative *CCA1:luc* luminescence compared with simulated [*LHY* mRNA]. (E,F) Relative *TOC1:luc* luminescence (Katharine Hubbard, *personal communication*) compared with simulated [*TOC1* mRNA]. (G,H) Relative *GI:luc* luminescence (Katharine Hubbard, *personal communication*) compared with simulated [Y (*GI*) mRNA]. In abscissa, white bars indicate light, black bars indicate dark, dark grey indicates dark in subjective daytime and light grey indicates light in subjective night-time.

the correct time in L16/D8 (Figures 3.7C,D). *TOC1:luc* luminescence had biphasic oscillations in L16/D8 and L8/D16, achieving peak levels 1 h after dawn and at dusk (Figures 3.7E,F). Both candidate models had biphasic oscillations of [*TOC1* mRNA] in L16/D8 cycles (Figure 3.7E), though the peak 1–2 hours after dawn was smaller than for *TOC1:luc* luminescence. Only *Model 1* had two distinguishable peaks of [*TOC1* mRNA] in L8/D16 cycles (Figure 3.7F). *GI:luc* luminescence also had biphasic oscillations in L16/D8 and L8/D16 cycles, though the light-induced peak at dawn was smaller than the peak just before dusk (Figures 3.7G,H). *Model 1* and *Model 5* both had exaggerated light-induced peaks relative to *GI:luc* luminescence, though timing of both peaks was accurate (Figures 3.7G,H). However, a very sharp decline in simulated [Y (*GI*) mRNA] was seen at the transition from light to dark in both candidate models.

Parameter analysis implicates *GI* as a sucrose-target

Parameters associated with Y (*GI*) mRNA were frequently altered when fine-tuning the *Three Loop Model* parameters to data collected in the absence of exogenous sucrose. The parameter alterations were considered on the following levels: the mean of all parameter sets visited during each of the 400 x 1000 iterations, the mean of the trial-optimal solutions (parameter sets corresponding to the lowest cost function scores in each trial), and the mean of the best (lowest $\Delta(p)$) 30 trial-optimal solutions (Table 3.4). On all three levels considered, $\hat{n}_5$ was reduced more on average than any other parameter, and further note that this was the same parameter identified in the single-parameter analysis of Section 3.3.2. In the best 30 trial optimal solutions, n_5 decreased by 56% while the second largest reduction (g, the hill coefficient of A activation by LHY) was only by 30%, providing further confidence that $\hat{n}_5$ should be reduced to account for an absence of exogenous sucrose (Table 3.4). The acute light activation of Y (*GI*; $\hat{q}_2$) was also reduced frequently during optimisation, though not to the same extent as $\hat{n}_5$ on average (Table 3.4). The largest parameter increase was seen for $\hat{n}_4$ (maximum light-dependent transcription rate of Y), increasing to at least double that of any other parameter on average, and 93% in the best 30 trial-optimal solutions. The maximum degradation rate of Y (*GI*) mRNA ($\hat{m}_{12}$) also increased frequently during the optimisation. Inspection of equation 3.10 reveals that the four parameters which changed the most ($\hat{n}_4$, $\hat{q}_2$, $\hat{n}_5$ and $\hat{m}_{12}$) are all associated with Y (*GI*) mRNA[§].

[§]Through non-dimensionalisation of the model equations, these parameters were all rescaled by dividing by k_{10} (see Table 3.1). However, changing our choice of scale would not influence our conclusions greatly, as both

Table 3.4: Averaged parameter alterations from re-tuning *Three Loop Model* for no exogenous sucrose. Parameters from the *NDTL Model* (Eqns. 3.1–3.16) were optimised with respect to a cost function corresponding to the data in Figure 3.1 using a Simulated Annealing algorithm over 400 independent trials of 1000 iterations each. Each of the three columns represents average parameter changes ordered by size, with top 5 decreases and top 5 increases displayed. The leftmost column is the average over the entire solution set, comprising 400 x 1000 parameter sets. The middle column represents the average of the trial-optimal solutions (parameter sets corresponding to the lowest cost function score in each trial), while the rightmost column considers the best 30 of these trial-optimal solutions. For a description of the parameters in this table, see Table A.2.

Whole solution set		Trial-optimal solutions		Best 30 trial-optimal solutions	
Parameter	Relative Value	Parameter	Relative Value	Parameter	Relative Value
n_5	0.8089	n_5	0.6962	n_5	0.4426
q_2	0.8926	q_2	0.8462	g	0.7025
m_1	0.8981	m_1	0.8775	m_6	0.7433
n_6	0.9094	p_1	0.8866	q_2	0.7474
n_1	0.9157	n_6	0.8923	ρ_L	0.7686
⋮	⋮	⋮	⋮	⋮	⋮
m_3	1.1139	q_1	1.1722	n_3	1.2605
m_4	1.1410	m_4	1.1779	p_2	1.2643
m_{16}	1.1675	m_{16}	1.2225	α	1.3947
m_{12}	1.1949	m_{12}	1.3764	m_{12}	1.4062
n_4	1.4093	n_4	1.7687	n_4	1.9363

Our parameter analysis suggested that sucrose acts to up-regulate the transcription of *GI*. In the *Three Loop Model*, transcription of *GI* is considered to be a decreasing function of the availability of LHY/CCA1 or TOC1 nuclear protein (Locke *et al.*, 2006). When there is light, transcription occurs with rate $n_4 + n_5$, and in the dark this rate reduces to n_5. Both the analysis in this section and in Section 3.3.2 indicated that n_5 should be set at least 50% lower without 90 mM exogenous sucrose. However, the fine-tuning method in this section predicts the change in $n_4 + n_5$ to be minor ($= 0.2506$ with 90 mM exogenous sucrose, nominal *Three Loop Model*; $= 0.2389$ without 90 mM exogenous sucrose, top 30 pareto-optimal parameter sets). Therefore, these mathematical analyses predict that addition of 90 mM sucrose increases the rate of *GI* transcription in the dark by over 100%, and in the light by only 5%. As $[\text{Suc}]_i$ undergoes a diurnal rhythm (Lu *et al.*, 2005), we interpret our analysis to mean that exogenous sucrose does not affect the central oscillator when $[\text{Suc}]_i$ is already high. This also explains why circadian oscillations in LL are not affected greatly by addition of 90 mM sucrose (see Figures 3.1B,D,F), and indicates the importance of studying the circadian network in LD cycles and DD.

parameter increases and parameter decreases are seen in the parameters comprising Equation 3.10.

3.3.4 Simulated mutant analysis

To further test the parameter-modified models, we performed a simulated mutant analysis, as done in a previous attempt to mathematically model the central oscillator (Zeilinger *et al.*, 2006). The *N5 Model*, *Model 1* and *Model 5* were investigated for the effect of mutations to central oscillator components (Table 3.5). The *N5 Model* predicted a period-shortening in LL for *toc1* null (3.6 h) and *gi* null (3.3 h) mutations (Table 3.5), agreeing with published experimental data (Millar *et al.*, 1995; Mizoguchi *et al.*, 2005). However, *Model 1* and *Model 5* predicted LL arrhythmia for *toc1* and *gi* null mutants (Table 3.5). Despite there being a relative lack of published *luc* luminescence data for seedlings grown without exogenous sucrose, *CAB2:luc* luminescence has short-period oscillations in *toc1*-1 mutants (Xu *et al.*, 2007) and $[Ca^{2+}]_{cyt}$ has short-period oscillations in *gi*-2 mutants (Dr. F. Robertson, *personal communication*). Therefore, the *N5 Model* is more capable of reproducing mutant phenotypes than the fine-tuned models.

Table 3.5: Simulated mutant analysis of *Three Loop Model* altered for no exogenous sucrose.
Simulated circadian period computed for the *Three Loop Model*, the *N5 Model*, *Model 1* and *Model 5* by finding the time difference between successive peaks of simulated [*LHY* mRNA] after 600 h in LL. Mutant periods are displayed as the deviation from the simulated wild-type period. Mutants were simulated as in Zeilinger *et al.* (2006). For *ztl*, the numbers in brackets corresponds to reducing all TOC1 degradation rates by one-half, rather than only the dark-dependent rates (unbracketed values; see Locke *et al.*, 2006). Asterisks indicate very low amplitude oscillations, which are unlikely to be detectable experimentally, and so can be considered arrhythmic.

Genotype	*Three Loop*	*N5*	*Model 1*	*Model 5*
Wild-type	23.8	24.0	25.5	25.6
cca1	-0.6	-0.6	-0.6	0.5
cca1 lhy	-6.0	arr.	arr.	-10.2*
toc1	-3.4	-3.6	arr.	arr.
gi	-1.2	-3.3	arr.	-5.3*
prr7 prr9	5.5	arr.	14.1	16.0*
ztl	0 (1.07)	0 (0.52)	0 (0.58)	0 (0.53)

In general, simulations of central oscillator gene knockout mutants with the *N5 Model* had similar phenotypes to the nominal *Three Loop Model*, i.e. the majority of LL period phenotypes are predicted to be unaffected by sucrose. However, a reduction in n_5 led to a loss of oscillations in LL in a simulated *cca1 lhy* double mutant (Figure 3.8, Table 3.5). This contrasts with the observation that LL oscillations persist with decaying amplitude in *cca1 lhy* double mutants in the presence of 90 mM exogenous sucrose (Locke *et al.*, 2006)¶. The simulations with the *N5 Model*

¶The majority of circadian research in *Arabidopsis* is conducted with seedlings grown in the presence of exogenous sucrose. A search of the literature found no experimental data for measurements of gene promoter activity in *cca1 lhy* double mutants.

therefore predict exogenous sucrose to increase the amplitude/persistence of LL oscillations in *cca1 lhy*. This prediction represents a good validation test for the *N5 Model*.

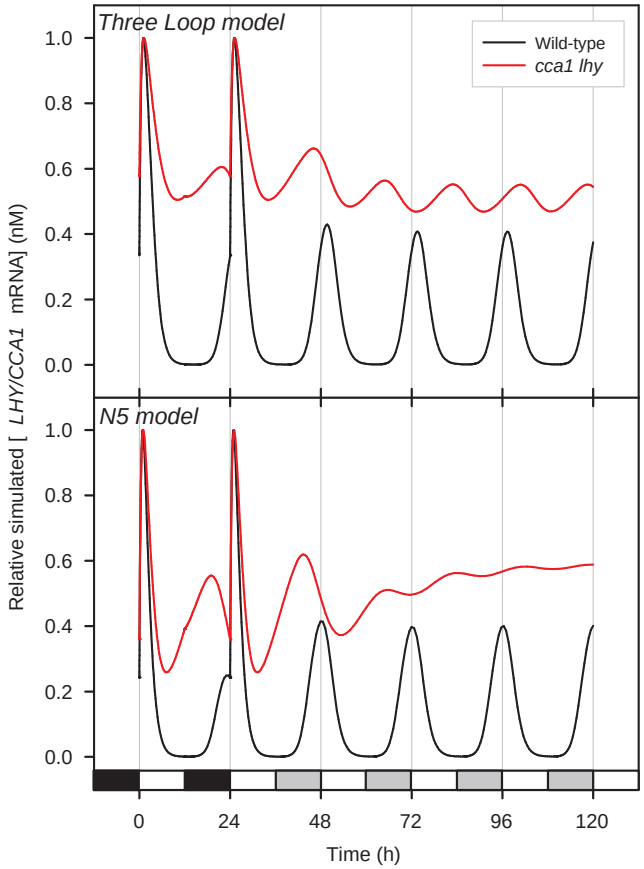

Figure 3.8: The simulated LL phenotype of *cca1 lhy* depends on sucrose availability.
Simulated [*LHY* mRNA] in LL comparing a *cca1 lhy* double mutant (red lines) with wild-type (black lines) for the nominal *Three Loop Model* (top panel; 3% exogenous sucrose) and the *N5 Model* (bottom panel; no exogenous sucrose). Model equations were solved numerically using MATLAB^{TM}'s *ode15s* stiff equation solver (Shampine & Reichelt, 1997). *cca1 lhy* mutant was simulated by setting p_1 (rate of *LHY* translation) equal to 1/1000 of the nominal value, as done in Locke *et al.* (2006).

3.4 Discussion

The effects of supplying exogenous sucrose to *Arabidopsis* seedlings include suppression of circadian oscillations of $[Ca^{2+}]_{cyt}$ in LL (Johnson *et al.*, 1995) and larger amplitude circadian oscillations of clock gene promoter activity in DD (Figure 3.1). Our measurements of $[Ca^{2+}]_{cyt}$ (Love *et al.*, 2004; Xu *et al.*, 2007; Chapter 2) were conducted in the absence of exogenous sucrose and demonstrate circadian oscillations in LL but no oscillations in DD. Published models of the central oscillator mechanism were derived using data from plants grown with 3% exogenous

sucrose (Locke *et al.*, 2005a,b, 2006; Zeilinger *et al.*, 2006), rendering them inappropriate as an input to a model for the circadian regulation of $[Ca^{2+}]_{cyt}$. Therefore, we sought to obtain a modification to the *Three Loop Model* which could account for the dynamical differences observed for *CCA1:luc* and *TOC1:luc* luminescence in LL and DD in the absence of exogenous sucrose.

3.4.1 The *N5 Model* outperforms fine-tuned models

The set of single-parameter alterations to the *Three Loop Model* were explored for potential sucrose targets. When the (light-independent) rate of *Y* (*GI*) transcription was reduced to one-quarter of the nominal value, simulated [*LHY* mRNA] accurately reproduced *CCA1:luc* luminescence data in DD in the absence of exogenous sucrose (Figures 3.4B, 3.1A). This candidate modification to the *Three Loop Model* was defined as the *N5 Model*. Enabling all parameters to vary led to a much wider range of possible dynamics in the model components. The parameters were constrained to match the measured *CCA1:luc* and *TOC1:luc* luminescence data with model simulations and a reduction in n_5 in addition to an increase in n_4 was required to account for no exogenous sucrose (Table 3.4). *Model 1* and *Model 5* were considered as further candidate models. Both the single-parameter (Section 3.3.2) and the fine-tuning (Section 3.3.3) approaches were based on observations of *CCA1:luc* and *TOC1:luc* luminescence, as *GI:luc* luminescence data had not been collected at the time of conducting the work. Therefore, it was assumed that all oscillator components were arrhythmic in DD, an assumption that is not valid given the observed oscillations of *GI:luc* in the absence of exogenous sucrose (Figure 3.1E). However, it would not be possible to modify parameters of the *Three Loop Model* to exhibit oscillations in *Y* (*GI*) but not *TOC1*, as *TOC1* is present in all feedback loops containing *Y* (*GI*), and feedback is required for oscillations. Consequently, our experimental observations in the absence of exogenous sucrose demonstrate that a structural element is incorrect in the *Three Loop Model* of the central oscillator.

Cross-validation of the three candidate models with wild-type data confirmed that experimentally observed dynamics were frequently predicted by the models. However, a simulated mutant analysis demonstrated that the fine-tuned models were not robust to simulated mutation. Only the *N5 Model* predicted LL oscillations to persist in *toc1* null and *gi* null mutants, as observed experimentally for $[Ca^{2+}]_{cyt}$ and *CAB2:luc*. One explanation for the failure of the fine-tuned models is that the 63 non-dimensionalised parameters were not constrained sufficiently

by the cost function (Eqn. 3.22) to produce models capable of accurately predicting mutant phenotypes. All of the analysis presented in this chapter suggests that the equation for [Y (*GI*) mRNA] (Eqn. A.23) should be modified to account for no exogenous sucrose. Therefore, the search space for fine-tuning might be reduced significantly by considering only the parameters appearing in this equation. Additionally, inclusion of mutant data in the cost function may guide the optimisation algorithm toward more representative parameter sets. However, it is important not to rule out the possibility that the model equations themselves may be insufficient to describe the differences resulting from the availability of exogenous sucrose.

Also resulting from our simulated mutant analysis of the *N5 Model* was the prediction that LL oscillations in *cca1 lhy* double mutants are less persistent in the absence of sucrose (Figure 3.8). We found no published data for oscillations of *cca1 lhy* double mutants in the absence of exogenous sucrose, so additional experimentation is required to validate the prediction. This prediction represents a stringent test of the *N5 Model* because it distinguishes the availability of sucrose, unlike simulations of other clock gene mutations when compared with the nominal *Three Loop Model* (Table 3.5).

3.4.2 GIGANTEA mediates sucrose modulation of the central oscillator in DD

Thus far, mathematical investigations have generated hypotheses that *GIGANTEA* mediates the sucrose sensing of the central oscillator. Both the *N5 Model* and fine-tuned models hypotheses suggest the (light-independent) rate of *GI* transcription is unaffected by exogenous sucrose in the light, when sucrose is being produced by the cell. The models predicted a null mutation in *GI* to remove the ability of the central oscillator to perceive sucrose. This leads to the expectation of no circadian oscillations in DD in *gi* null mutants, irrespective of the availability of exogenous sucrose. *CAB2:luc* luminescence was measured by a collaborator in the Webb Laboratory (Seong Jin Baek) in seedlings grown under L12/D12 cycles before transfer to DD in wild-type WS (Wassilewskija) plants and *gi*-11 null mutants (Figure 3.9; Ding *et al.*, 2007). Large amplitude oscillations in *CAB2:luc* luminescence were present in wild-type plants grown with 90 mM exogenous sucrose, while osmotic control lines (90 mM mannitol) had no oscillations after transfer from L12/D12 (Figure 3.9). However, the *gi*-11 mutant had no oscillations in sucrose-supplemented or mannitol-supplemented growth media, as predicted by the mathematical analysis. Therefore, *GI* at least mediates the sucrose modulation of the central

oscillator in DD.

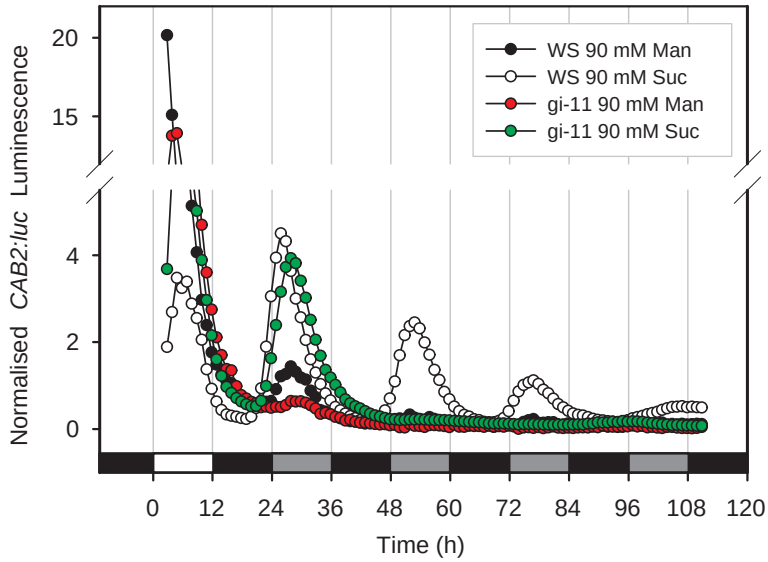

Figure 3.9: Sucrose-dependent DD oscillations of *CAB2:luc* luminescence absent in *gi*-11 null mutant. Luminescence measured in *Arabidopsis* seedlings expressing *CAB2:luc* entrained and measured in L12/D12 cycles, then transferred to DD. Compared are wild-type WS (closed and open circles), and *gi*-11 null mutants (red and green circles). Seedlings grown on agar media containing either 90 mM mannitol (closed and red circles) or 90 mM sucrose (open and green circles). Each point represents the normalised average luminescence of 4 clusters of 10–12 seedlings measured for 800 s every hour. Data normalised by dividing each data-point by the average over the whole trace. Raw data collected by Seong Jin Baek, Department of Plant Sciences, University of Cambridge.

A potential alternative explanation for the loss of circadian rhythms of *CAB2:luc* in *gi*-11 mutants is that *GI* forms a critical feedback loop with a sucrose sensing gene, and by breaking this loop, circadian oscillations cannot persist in DD. If this were the case, then a mutation in the sucrose-sensing gene with which *GI* interacts would have an identical effect on DD circadian oscillations. *GI* contributes to two feedback loops in the *Three Loop Model* of the *Arabidopsis* circadian clock, the *GI–TOC1* evening loop and also the connecting *LHY–GI–TOC1–X* loop. Therefore, it was important to establish the sensitivity of *toc1*, *cca1* and *lhy* mutants to exogenous sucrose supply. Circadian oscillations of *CCR2:luc* persist in DD in *cca1*-1 and *cca1*-1 *lhy* RNAi mutants grown in the presence of 90 mM exogenous sucrose, but are absent in *gi*-3 and *toc1* RNAi mutants (Alabadí *et al.*, 2002; Mizoguchi *et al.*, 2005). This suggests that sucrose targets the *GI–TOC1* loop. However, recent experimental work in our laboratory has shown that oscillations of *CAB2:luc* luminescence persist in DD in the *toc1*-2 null mutant (Seong Jin Baek, *personal communication*). As suppression of *TOC1* abolishes *CCR2* rhythms but not *CAB2* rhythms in DD, it is possible that different oscillator components are driving the expression of

these genes. For instance, rhythmic regulation of *TOC1* by *GI* (Locke *et al.*, 2006) might mediate *CCR2* expression in DD, with *CAB2* more directly associated with *GI*. Nevertheless, our observations indicate that *TOC1* is not a necessary oscillator component for rhythmic behaviour in DD. A mutation in *TIME FOR COFFEE* (*TIC*; *tic*-1) results in arrhythmia in DD and LL (Ding *et al.*, 2007), so it is unlikely that *TIC* is involved in sucrose-sensing. We found no other mutations which had arrhythmic phenotypes in DD in the presence of exogenous sucrose, accentuating the importance of the *gi*-3 and *gi*-11 mutations insensitivity to sucrose.

3.4.3 A novel sugar signalling pathway

In work recently published by Knight *et al.* (2008), *sfr6* mutants were shown to be insensitive to exogenous sucrose supply. The authors also speculated that *TOC1* or *GI* might be a target of a Suc–*SFR6* pathway. Taken together with the results of this chapter, this forms a plausible hypothesis for a novel sugar signalling pathway for circadian regulation (Figure 3.10). The potential interaction between *SFR6* and *GI* should be studied *in planta* to characterise this pathway.

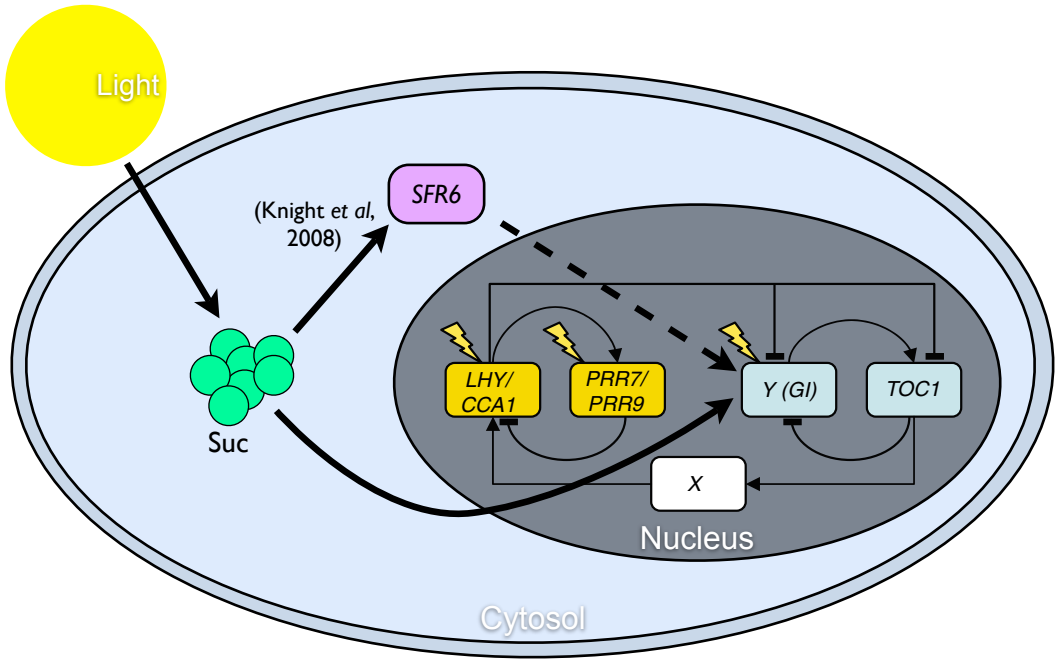

Figure 3.10: Schematic for possible sucrose-dependent pathways regulating *GI*.
Circadian clock network reflecting the *Three Loop Model* of the central oscillator (Locke *et al.*, 2006). Sucrose regulated by the availability of light, as a product of photosynthesis. Sucrose regulates *SFR6* (Knight *et al.*, 2008), and also regulates *GI* (Figure 3.9). Dashed line indicates potential interaction between *SFR6* and *GI*, as speculated by Knight *et al.* (2008).

3.4.4 Summary

The results presented in this chapter have shown that mathematical modelling can lead to predictions of biological function. Parameter analysis implicated *GI* to participate in sucrose-sensing within the circadian network and this prediction was validated experimentally (Figure 3.9). This work also demonstrates the importance of carefully selecting the conditions under which circadian research is conducted. Firstly, supplementing agar media with sucrose affects circadian function. Secondly, both light/dark cycles and constant dark conditions provide dynamical information absent in constant light conditions. This research provides results into an emerging area of circadian research, as interactions between the circadian network and cytosolic signalling and metabolic events are being explored (Dodd *et al.*, 2007; Yin *et al.*, 2007; Imaizumi *et al.*, 2007; O'Neill *et al.*, 2008; Harrisingh & Nitabach, 2008).

CHAPTER 4

GI-Mediated Sucrose Modulation of the *Arabidopsis* Circadian Clock

4.1 Introduction

In this chapter, the demonstration that *GIGANTEA* mediates sucrose modulation of the central oscillator (Chapter 3) is built upon. Using a combination of mathematical and experimental approaches, the mechanism of regulation of *GI* by sucrose is investigated. There is particular focus on the possibility that sucrose targets a post-translational mechanism which accelerates GI protein degradation (David *et al.*, 2006).

Dark-dependent GI degradation was demonstrated using transgenic *Arabidopsis* plants expressing functional, epitope-tagged GI proteins for monitoring GI protein levels in L12/D12 cycles (David *et al.*, 2006). The tandem affinity purification (TAP) system was used to monitor GI protein under the control of its endogenous promoter (*GI:GI-TAP*) or a constitutive 35S promoter (*35S:GI-TAP*) in a *gi*-2 mutant background. As *GI:GI-TAP* compensates for the misexpressed GI protein in a *gi*-2 mutant background, the resulting line has an essentially wild-type phenotype. Expression of *35S:GI-TAP* in the *gi*-2 mutant background corresponds to replacing the endogenous *GI* with promoter with a constitutive promoter, thereby removing the responsiveness of *GI* expression to its transcription factors. It was found that *35S:GI* plants had os-

cillations of GI in L12/D12 cycles, despite there being no rhythmic transcription of *GI* (David *et al.*, 2006). Therefore, GI protein is degraded at different rates, depending on the availability of light. Treating *gi*-2 *35S:GI* plants with (26S) proteasome inhibitors led to higher levels of GI protein in darkness, indicating that the 26S proteasome was involved in the dark-induced proteolysis of GI (David *et al.*, 2006).

All published models of the *Arabidopsis* circadian clock include a dark-dependent TOC1 protein degradation mechanism (Locke *et al.*, 2005a,b, 2006; Zeilinger *et al.*, 2006). This mechanism represents the targeted degradation of TOC1 by ZTL, as described by Más *et al.* (2003a). However, dark-induced proteolysis of GI protein by the 26S proteasome (David *et al.*, 2006) is not accounted for in any of the mathematical oscillator models, as GI degradation is deemed to be independent of the availability of light. In Chapter 3, it was established that *GI* is a necessary component for sucrose-sensing by the central oscillator in DD (Figure 3.9). Mathematical analyses indicated that *GI* is regulated transcriptionally by sucrose, though this was not tested experimentally. By incorporating a term for dark-dependent GI degradation into the equations of the *Three Loop Model*, the possibility that sucrose regulates GI proteolysis is investigated. Experimental methods are proposed to distinguish between the possibilities that sucrose regulates *GI* via transcriptional, post-translational or both transcriptional and post-translational control, and preliminary experimental data are presented.

4.2 Materials and Methods

4.2.1 Plant material and growth conditions

In this chapter, transgenic *Arabidopsis thaliana* seedlings transformed to express *LUCIFERASE* (*LUC*) under the control of the *GI* promoter have been used to investigate sucrose modulation of the central oscillator. The seed line was obtained from Dr. S. Davis (Ding *et al.*, 2007; Max Planck Institute for Plant Breeding Research, Germany).

4.2.2 Imaging of *luciferase* activity for topical sucrose treatment

Circadian rhythms of luciferase luminescence were measured before and after automated treatment of 90 mM sucrose or 90 mM mannitol. *Arabidopsis* WS seeds were surface-sterilized as described previously (Section 2.2.1), stratified at 4°C for 2 d in darkness, and germinated in

96-well plates, with each well containing 150 μl of half-strength Murashige and Skoog medium (Sigma) and 0.8 % (w/v) agar. Seedlings were grown in 12 h light/ 12 h dark (LD12/12) for 12 d at constant 19°C, then treated with 100 μl of 1 mM luciferin and placed in darkness for 36 h or 48 h.

Automated sucrose/mannitol treatment and photon counting was conducted using a microplate microfunctional plate reader (Fluostar OPTIMA, BMG Labtech, Germany). Luminescence was quantified in 30 min intervals for 12 s. Sucrose/mannitol treatment was administered after 24 h of measurement, before further measurement for 60-84 h.

4.2.3 Numerical approximation of peak and trough values of *luc* luminescence data

The timing of oscillation peaks and troughs were approximated using a computational algorithm based on *K-means* clustering (Macqueen, 1967). Experimental data was pre-processed by removing linear trends using the *detrend* function in MATLAB^{TM}. Turning points were then identified, defined as data-points lying between two higher values in the case of a local minimum, or two lower values in the case of a local maximum. Each of these extremal points were considered candidates if they were greater than the average of all data values (for local maxima; average is 0 for detrended data), or lower than the average data-value (for local minima). The candidate turning points were then clustered by the times of their occurrence using the *kmeans* function in MATLAB^{TM} (Seber, 2004), with the squared Euclidean distance as the algorithm distance measure. The number of clusters returned was selected as the number of peaks and troughs expected by visual inspection of the data. The averages of clustered times were then taken as the oscillation peaks and troughs accordingly.

4.2.4 Numerical solution of the *Three Loop Model* equations

The *Three Loop Model* equations and variants thereof have been solved numerically throughout this chapter as described in Section 3.2.2.

4.3 Results

4.3.1 Simulated post-translational modification of GIGANTEA enables sucrose-dependent oscillations in DD

The equations of the *Three Loop Model* were modified to include terms for dark-dependent degradation of *Y* (*GI*), using the same functional form as used to describe the *ZTL*-mediated degradation of TOC1 (Equations A.18–A.19; Locke *et al.*, 2005b, 2006). In doing so, we define the *PostGI Model* in which Eqn. A.24 and A.25 respectively become

$$\frac{dc_Y^{(c)}}{dt} = p_4 c_Y^{(m)} - r_7 c_Y^{(c)} + r_8 c_Y^{(n)} - ((1 - \Theta_{\text{light}}(t))\hat{m}_{13} + m_{13})\frac{c_Y^{(c)}}{k_{11} + c_Y^{(c)}} \tag{4.1}$$

$$\frac{dc_Y^{(n)}}{dt} = r_7 c_Y^{(c)} - r_8 c_Y^{(n)} - ((1 - \Theta_{\text{light}}(t))\hat{m}_{14} + m_{14})\frac{c_Y^{(n)}}{k_{12} + c_Y^{(n)}} \tag{4.2}$$

where $\hat{m}_{13}$ and $\hat{m}_{14}$ are the dark-dependent degradation rates of *Y* (*GI*) protein in the cytoplasm and nucleus respectively. Values of $\hat{m}_{13}$ and $\hat{m}_{14}$ were explored to evaluate whether this modification might describe the difference in gene expression between plants grown with and without exogenous sucrose. To achieve a suitable scaling of the new parameters, the values were based on the corresponding light/dark-independent counterparts m_{13} and m_{14} respectively by a scale factor d. i.e.

$$\begin{aligned} \hat{m}_{13} &:= d m_{13} \\ \hat{m}_{14} &:= d m_{14} \end{aligned} \tag{4.3}$$

An increase in d corresponds to an increase in the dark-dependent degradation of GI. Therefore, $d = 0$ implies the rate of GI proteolysis in is independent of the availability of light, while a high value of d indicates high dark-induced GI proteolysis. Increasing d led to simulated outcomes that were similar to measured data for *LHY/CCA1* and *TOC1* in the absence of exogenous sucrose (Figure 4.1). As d was increased, DD oscillations of simulated [*LHY/CCA1* mRNA] (Figure 4.1A) and [*TOC1* mRNA] (Figure 4.1B) decreased in amplitude, and for $d = 3$ and $d = 4.5$ overlapped well with corresponding *luc* luminescence data. In LL, oscillations were independent of d ($\hat{m}_{13}$ and $\hat{m}_{14}$) and so the period of simulated outputs were unaffected. When simulating the transfer from entrained L12/D12 cycles to LL, the oscillation phase depended on the value of d for both simulated [*LHY/CCA1* mRNA] (Figure 4.1C) and [*TOC1* mRNA] (Fig-

ure 4.1D). Dark-dependent GI degradation led to phase advances of 2.4 h ($d = 1.5$), 3 h ($d = 3$) or 4.5 h ($d = 4.5$) relative to the nominal limit cycle oscillation ($d = 0$; Figure 4.1E). As dark-induced proteolysis is absent in the light, the system dynamics are independent of d in LL and the limit cycle trajectory will be the same for each d, implying that simulated circadian period will be unaffected by d. However, a phase change resulted from the different dynamics present in L12/D12 cycles prior to transfer to LL, whereby there was a positive correlation between the value of d and the phase advance (Figure 4.1E). The mathematical analysis suggested that the availability of sucrose might decrease the rate of GI turnover in darkness. This provided an alternative predicted mechanism for GI-mediated sucrose-sensing by the central oscillator to the mechanism presented in Chapter 3.

4.3.2 Simulated effect of sucrose on GI protein levels in light-dark cycles

The *PostGI Model* was used to simulate the effect of exogenous sucrose supply on GI protein cycling in L12/D12 for wild-type (*gi*-2 *GI:GI-TAP*) and GI-overexpressing lines (*gi*-2 *35S:GI-TAP*) under the hypothesis that sucrose stabilises GI protein. An absence of exogenous sucrose was simulated using the *PostGI Model* equations with $d = 3$ (recall that d is the relative rate of dark-dependent GI degradation when compared with the dark-independent rate in Locke *et al.*, 2006). A presence of exogenous sucrose was investigated taking $d = 0$ which corresponds to the nominal *Three Loop Model* and also with $d = 0.5$ which reflects a contribution from the difference in endogenous sucrose levels resulting from photosynthesis, even when $[\text{Suc}]_i$ is buffered with exogenous sucrose. The *PostGI Model* with $d = 0.5$ therefore corresponds to the hypothesis that the rate of GI degradation is a function of sucrose rather than the availability of light.

Simulated GI protein cycling in wild-type *Arabidopsis*

Simulated L12/D12 cycles of [GI protein] in a wild-type background showed only minor differences between the three values of d investigated (Figure 4.2). For $d = 3$ (no exogenous sucrose), simulated [Y (GI) protein] (cytoplasmic plus nuclear) peaked earlier (ZT7.6) than for $d = 0$ (ZT11.4) and $d = 0.5$ (ZT10; Figure 4.2). The shape of the oscillation was skewed by increasing d, though large amplitude oscillations were still present in L12/D12 (Figure 4.2). Therefore, assuming that sucrose stabilises GI protein, it would be unexpected for exogenous

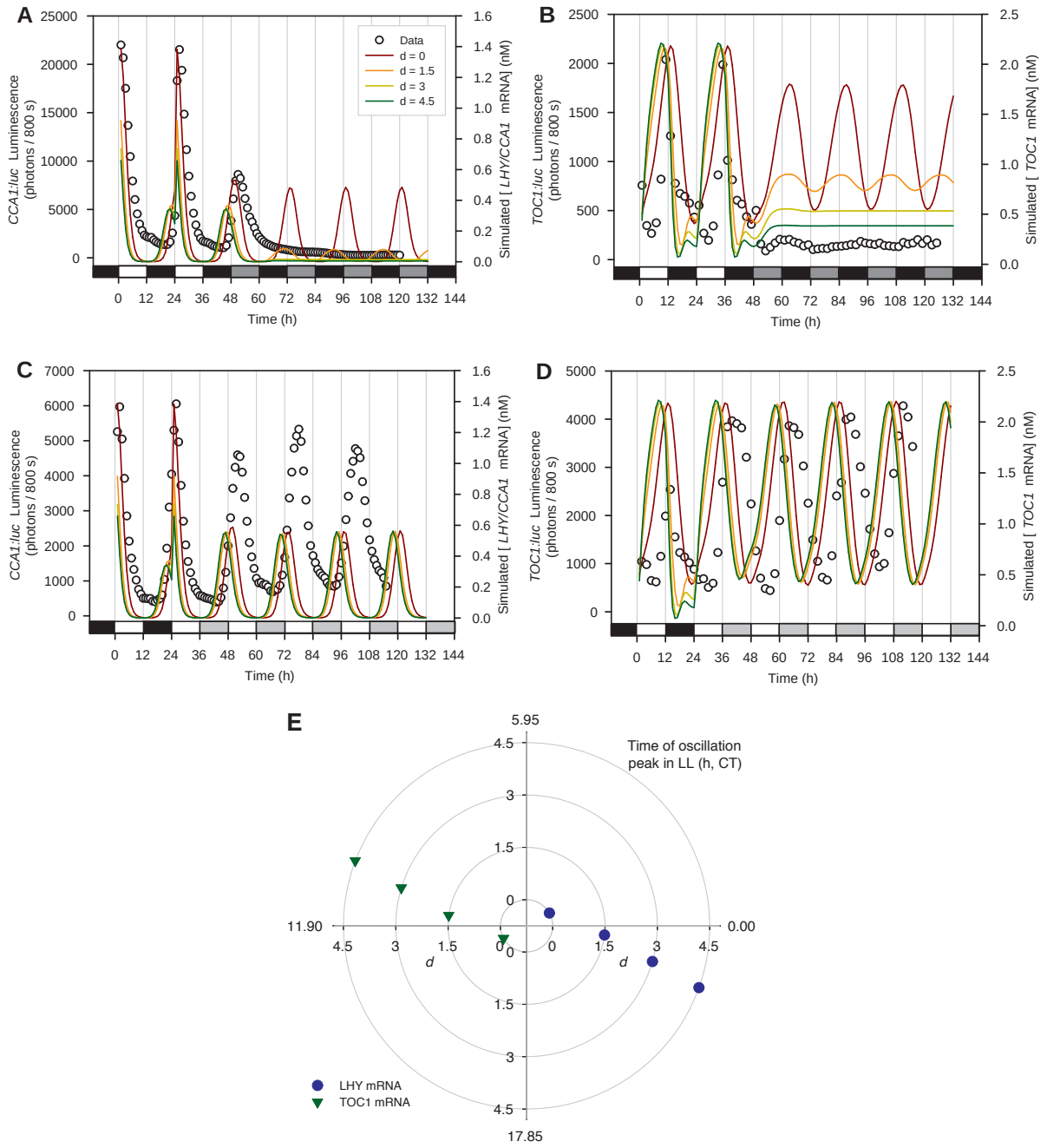

Figure 4.1: Dark-dependent degradation of *Y* (*GI*) enables sucrose-dependent oscillations in DD. *Three Loop Model* equations (A.14–A.29) modified to include dark-dependent degradation terms (Equations 4.1–4.2). Rate of dark-dependent degradation parameters $\hat{m}_{13}$ and $\hat{m}_{14}$ were defined in terms of corresponding dark-independent parameters as $\hat{m}_{13} = dm_{13}$ and $\hat{m}_{14} = dm_{14}$, for a constant d to be prescribed. Modified model equations were simulated for $d = 0, 1.5, 3, 4.5$ in (A,B) 48 h of L12/D12 followed by 96 h of DD, and (C,D) 48 h of L12/D12 followed by 96 h of LL. (A,C) Simulated [*LHY/CCA1* mRNA] (solid lines) compared with *CCA1:luc* luminescence (open circles). (B,D) Simulated [*TOC1* mRNA] (solid lines) compared with *TOC1:luc* luminescence (open circles). (E) Time of oscillation peak in the 5th cycle of LL after entrained L12/D12 cycles as a function of d (radial axis), expressed in modulo 23.8 (limit cycle period in LL) with 0 corresponding to the start of constant light ($t = 24$ in Figures 4.1C,D).

sucrose supply to abolish nyctohemeral oscillations of [GI protein] in wild-type *Arabidopsis*, as large amplitude oscillations result from the rhythmic transcriptional control of *GI*. It is important to note at this stage that in the presence of measurement and process noise, it may not be possible to distinguish the dynamics predicted by these simulations with the current methods for quantifying protein abundance.

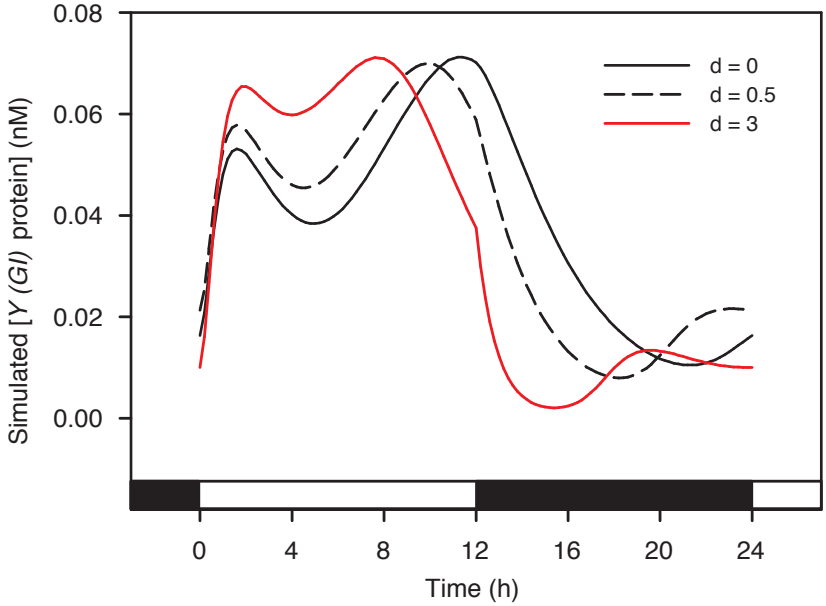

Figure 4.2: Simulated sucrose-dependency of *GI:GI-TAP* protein cycling in L12/D12.
The *PostGI* model was used to simulate [GI protein] in L12/D12 cycles, dependent upon the hypothesised sucrose-dependent GI protein degradation. The *PostGI* model is defined as the *Three Loop Model* (Locke *et al.*, 2006) with additional dark-dependent degradation of GI protein (nuclear and cytoplasmic), with rate equal to 3 times the rate of light/dark-independent GI degradation. Simulations correspond to *GI:GI-TAP* expressed in the *gi*-2 mutant background, as constructed by David *et al.* (2006). Simulated treatments are the presence of exogenous sucrose (black lines; solid, $d = 0$ or dashed, $d = 0.5$), and no exogenous sucrose (red lines, $d = 3$).

Incorporating constitutive GI expression from the *35S* promoter

Before simulating the *gi-2 35S:GI-TAP* lines, the influence of constitutive *35S:GI* expression in wild-type *Arabidopsis* was quantified. *35S:GI* expression was represented in the *PostGI Model* equations by the addition of a constant value n_{35S} to the rate of change of simulated [Y (GI) mRNA]. i.e. Eqn. A.23 was modified to

$$\frac{dc_Y^{(m)}}{dt} = \underbrace{\left(\Theta(t)q_2 c_P^{(n)} + \frac{(\Theta(t)n_4 + n_5)g_5^e}{g_5^e + c_T^{(n)^e}}\right)\left(\frac{g_6^f}{g_6^f + c_L^{(n)^f}}\right)}_{\text{Contribution from the endogenous } GI \text{ promoter}} - \frac{m_{12}c_Y^{(m)}}{k_{10} + c_Y^{(m)}} + \underbrace{n_{35S}}_{\substack{35S:GI \\ \text{expression}}} \tag{4.4}$$

where q_2, n_4, n_5, g_5, e, g_6, f, m_{12}, k_{10} are model parameters (see Table A.2), $c_T^{(n)}$ is the con-

centration of simulated nuclear TOC1 protein, $c_L^{(n)}$ is the concentration of simulated nuclear LHY/CCA1 protein, $\Theta(t)$ is the boolean light value, and $c_P^{(n)}$ is the concentration of a simulated light-labile protein in the nucleus (see Appendix A.2 for further details). n_{35S} was chosen so that simulated [Y (*GI*) mRNA] was higher than for simulated wild-type ($n_{35S} = 0$) at all times through entrained L10/D14 cycles (without exogenous sucrose), as observed by Mizoguchi *et al.* (2005)*. As these experiments were conducted in the absence of exogenous sucrose, the *PostGI Model* with $d = 3$ was used to investigate the effect of varying n_{35S}. We found that $n_{35S} = 0.2\ nM\ h^{-1}$ yielded sufficiently high levels of simulated GI expression (Figure 4.3).

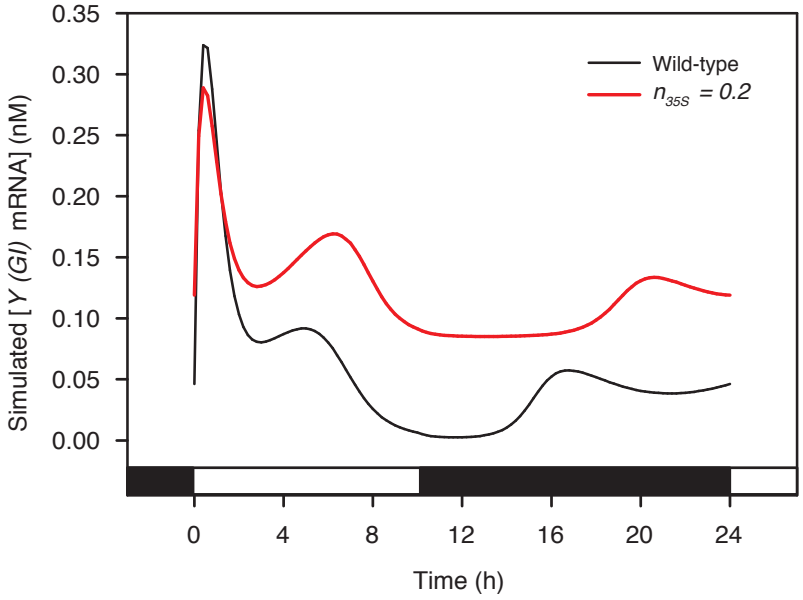

Figure 4.3: Calibration of the rate of constitutive *35S:GI* expression.
The *PostGI* model was used to calibrate the rate of constitutive *35S:GI* expression which agrees with RT-PCR measurements of *GI* mRNA by Mizoguchi *et al.* (2005). The *PostGI* model is defined as the *Three Loop Model* (Locke *et al.*, 2006) with additional dark-dependent degradation of GI protein (nuclear and cytoplasmic), with rate equal to 3 times the rate of light/dark-independent GI degradation. The equations were then modified to include a constant rate n_{35S} of Y (*GI*) mRNA synthesis. Model equations were solved numerically with MATLAB^{TM}'s *ode15s* stiff equation solver for 324 h in L10/D14 cycles, with the final 24 h displayed. Compared are simulated wild-type (black line; $n_{35S} = 0$) and simulated *35S:GI* (red line; $n_{35S} = 0.2$). Bars on abscissa are open indicating light, and closed indicating dark.

Simulated GI protein cycling in GI-overexpressing *Arabidopsis*

Having obtained an approximation for the rate of constant increase in simulated GI mRNA production resulting from *35S:GI* expression which corresponded with experimental data, it was possible to simulate the *gi*-2 *35S:GI-TAP* line by removing the contribution of the endogenous

*Note we did not consider the light-induced peak of expression shortly after dawn, as this was not observed by Mizoguchi *et al.* (2005), and was only slightly affected over a large range of n_{35S}.

GI promoter from Eqn. 4.4. i.e.

$$\frac{dc_Y^{(m)}}{dt} = n_{35S} - \frac{m_{12}c_Y^{(m)}}{k_{10} + c_Y^{(m)}} \tag{4.5}$$

The *PostGI Model* with this modified equation for simulated [*Y* (*GI*) mRNA] was used to simulate GI protein levels in L12/D12 cycles (Figure 4.4), as done for the *GI:GI-TAP* line in Figure 4.2. Significant differences could be seen between different values of d when simulating the *gi*-2 *35S:GI-TAP* line (Figure 4.4). The amplitude of L12/D12 oscillations of simulated [GI protein] (cytoplasmic plus nuclear) increased with the rate of dark-dependent GI protein degradation d, with no oscillations for $d = 0$ (Figure 4.4). It is likely that such a large difference in amplitude (between $d = 0.5$ and $d = 3$) could be observed experimentally and if shown would indicate that the rate of GI protein degradation is sensitive to the availability of sucrose.

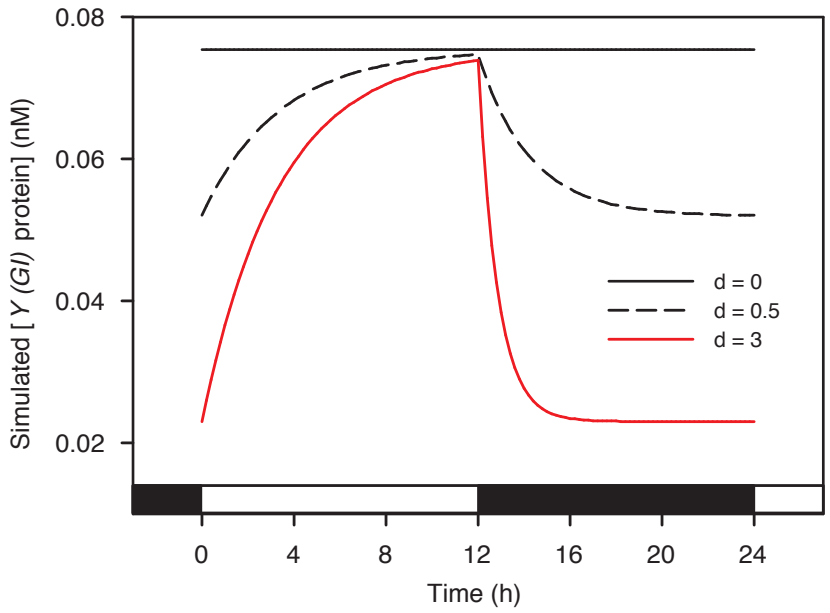

Figure 4.4: Simulated *35S:GI* protein cycling in L12/D12 with the *PostGI Model* comparing the availability of exogenous sucrose.
The *PostGI* model was used to simulate [GI protein] in L12/D12 cycles under the hypothesis that GI protein degradation is lower in the presence of exogenous sucrose. The *PostGI* model is defined as the *Three Loop Model* (Locke *et al.*, 2006) with additional dark-dependent degradation of GI protein (nuclear and cytoplasmic), with rate equal to three times the rate of light/dark-independent GI degradation. Simulations correspond to *35S:GI-TAP* expressed in the *gi*-2 mutant background (David *et al.*, 2006). The *PostGI* model equation for simulated [*Y* (*GI*) mRNA] was modified by replacing all positive terms with a constant value, $n_{35S} = 0.2$ nM h^{-1} (Eqn. 4.5). Simulated treatments are the presence of exogenous sucrose as for the nominal *Three Loop Model* (solid black line, $d = 0$) or under the assumption that the rate of GI degradation increases during darkness as a result of no endogenous sucrose production (dashed black line, $d = 0.5$), or the absence of exogenous sucrose (red line, $d = 3$).

4.3.3 Response of *GI* expression to topical sucrose treatment

The effect of topical sucrose treatment on central oscillator promoter activity was investigated, in an attempt to distinguish whether sucrose modulates *GI* expression via transcriptional or post-translational regulation. The mathematical models which were modified to account for an absence of exogenous sucrose were used to predict how gene expression responds to topical treatment of sucrose. Then, the corresponding *in vivo* experiments were conducted to test the contrasting hypothesised transcriptional (*N5*) and post-translational (*PostGI*) models for sucrose-sensing by *GI*.

Simulated response of *N5 Model* and *PostGI Model* to sucrose treatment

The *N5 Model* and the *PostGI Model* (with $d = 3$) were used to simulate [*LHY/CCA1* mRNA], [*TOC1* mRNA], *Y* (GI) mRNA], and [*PRR7/PRR9* mRNA] in the absence of exogenous sucrose in L12/D12 cycles before transfer to DD for 60 or 72 h (Figure 4.5). At these points, the modified model equations were switched with the nominal *Three Loop Model* configuration (Equations A.14–A.29) to simulate an immediate increase in exogenous sucrose corresponding to topical treatment of 90 mM sucrose. With no prior knowledge of the rate of uptake of sucrose into the cell, it was assumed that $[\text{Suc}]_i$ increases immediately following treatment. Furthermore, using the nominal *Three Loop Model* implicitly assumed that $[\text{Suc}]_i$ increases following topical addition to levels equivalent to seedlings grown on a 90 mM sucrose-supplemented growth media. *GI:luc* luminescence increased within the first 30 min (first data-point) following sucrose treatment *in vivo* (Figure 4.6), indicating that the assumption that $[\text{Suc}]_i$ increases immediately after addition of 90 mM sucrose might be justified.

Simulated sucrose treatment resulted in re-established circadian oscillations of all model components for both the *N5 Model* and the *PostGI Model* in DD (Figure 4.5). The time through the circadian cycle at which simulated sucrose treatment was applied (with respect to the last zeitgeber, a dark to light transition) did not affect simulated output because near-steady state levels were reached after 60 h in DD, and thus an identical stimulus (simulated sucrose treatment) was applied to a near-identical initial condition. After simulated sucrose treatment with both the *N5 Model* and *PostGI Model*, simulated [*LHY/CCA1* mRNA] had oscillations which increased in amplitude with the first peak occurring 11.2–11.4 h after simulated treatment (Figure 4.5). Oscillations continued with increasing amplitude slowly approaching the nominal

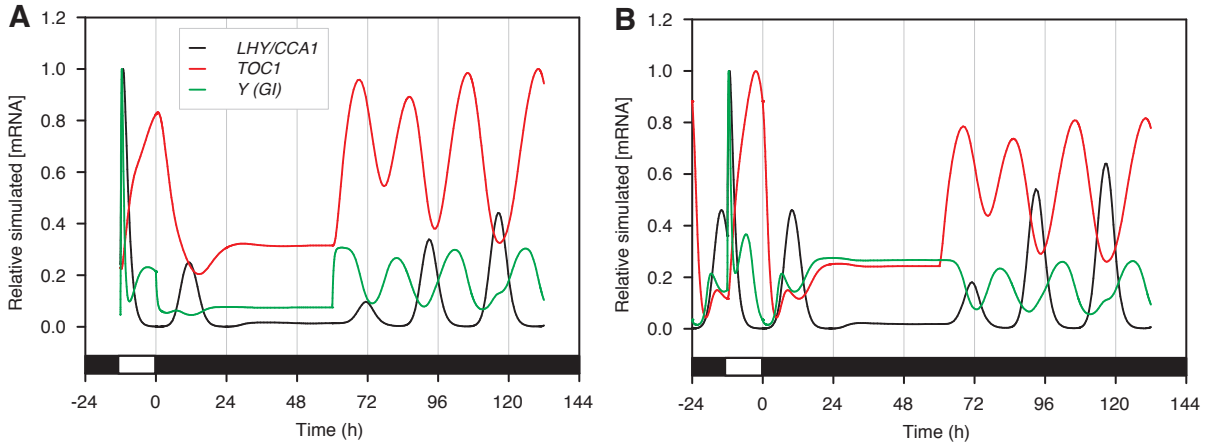

Figure 4.5: Simulated effects on oscillator transcript abundance of a sucrose dose after a period of extended darkness.
Three Loop Model (Equations A.14–A.29; Locke *et al.*, 2006) modified to reflect absence of exogenous sucrose, simulated in DD after entrainment to L12/D12 cycles. Simulated effect of dosing seedlings with 90 mM sucrose by switching from modified to nominal model configuration at $t = 60$. Modifications to the *Three Loop Model* are (A) a reduction in n_5 to 25 % of its nominal value, and (B), incorporating dark-dependent degradation of Y (GI) protein as in Equations 4.1–4.2 with $d = 3$.

Three Loop Model oscillation trajectory. The slow recovery to the nominal oscillation was also indicative of the other model component [mRNA] levels following simulated sucrose treatment (Figure 4.5A). As the nominal *Three Loop Model* equations corresponded to seedlings treated topically with 90 mM sucrose after simulating an absence of exogenous sucrose with both the *N5 Model* and the *PostGI Model*, both of the resulting trajectories will converge on the same limit cycle trajectory. However, the transient tending behaviour distinguished the two hypotheses generated by the models *in silico*. With the *N5 Model*, simulated [*Y* (*GI*) mRNA] increased sharply following simulated sucrose treatment because the rate of *Y* (*GI*) transcription was increased by a factor of 4 (Figure 4.5A). However, with the *PostGI Model* simulated [*Y* (*GI*) mRNA] remained constant for approximately 4 h following sucrose treatment and then decreased (Figure 4.5B). This was because GI protein levels were increased initially (degradation rate of Y/GI protein decreases by a factor of 4) which activates *TOC1* transcription; only after TOC1 protein has accumulated will *GI* transcription be inhibited leading to a decrease in simulated [*Y* (*GI*) mRNA].

Sucrose treatment *in vivo*

The *in vivo* analysis of topical sucrose treatment supported the hypothesis that sucrose modulates *GI* transcription. When seedlings were treated with 90 mM sucrose at CT0, *GI:luc* in-

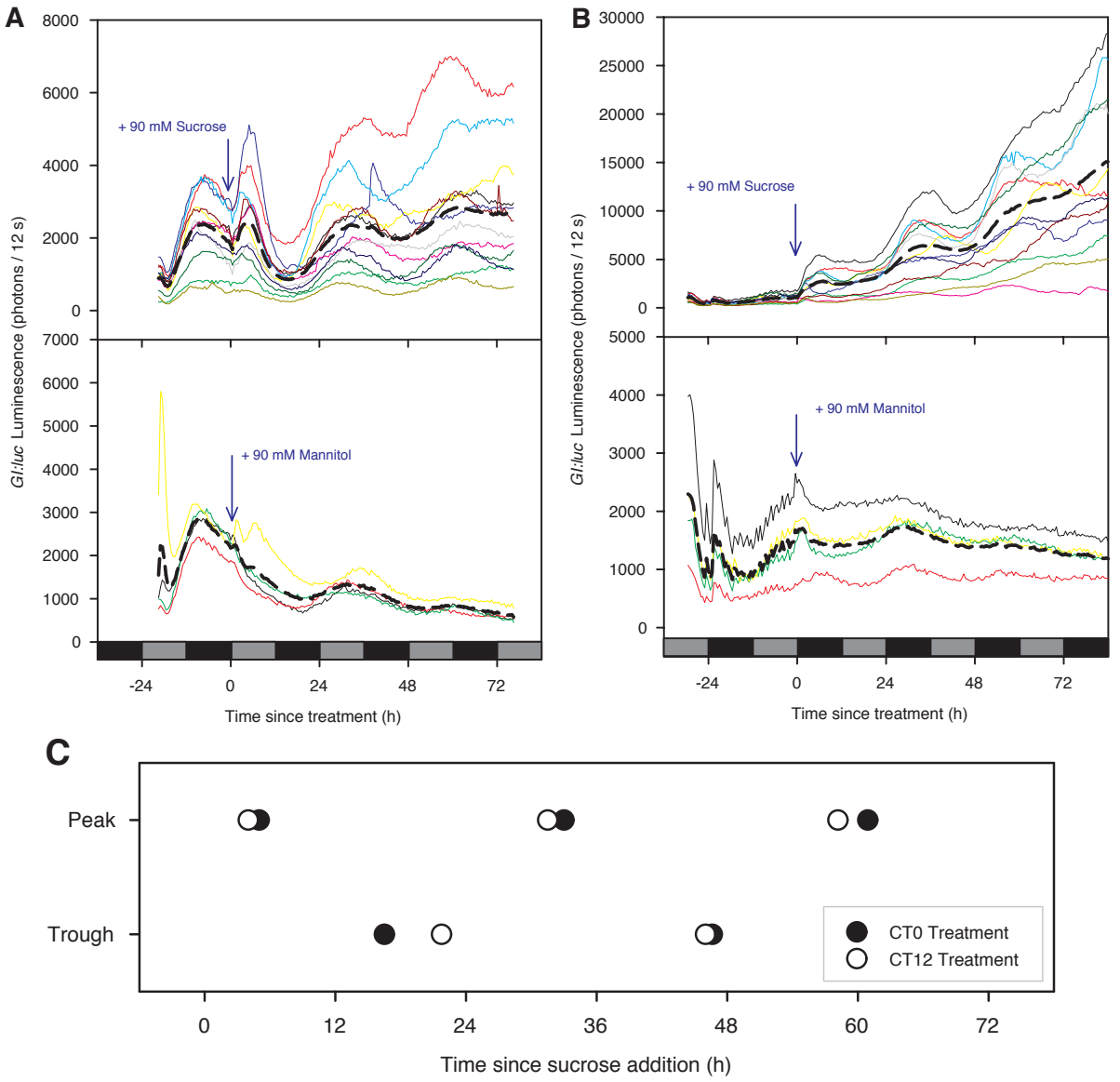

Figure 4.6: Sucrose amplifies circadian rhythms in DD and is a *zeitgeber* for *GI*.
Rhythms of *GI* promoter activity quantified for seedlings treated (at $t = 0$) with 100 μl of 90 mM sucrose (top panels) or 90 mM mannitol (bottom panels) after (A) 60 h (CT0), or (B) 72 h (CT12) darkness. (A,B) *GI:luc* luminescence quantified using a multi-functional 96 well plate reader for 12 s every 30 min. Traces are the total signal from a single well containing 2-3 seedlings (coloured thin lines), and the average signal (dashed thick line) for sucrose-treatment ($n = 12$) or mannitol-treatment ($n = 4$). Bars on abscissa are grey, subjective day; black, subjective night. (C) Oscillation peaks and troughs calculated for (A) and (B) by clustering turning points in the averaged datasets ($n = 12$; Section 4.2.3).

creased initially, and continued to oscillate with increasing signal (Figure 4.6A). An immediate increase in signal and oscillation amplitude of *GI:luc* luminescence also occurred in seedlings treated with 90 mM sucrose at CT12 (Figure 4.6B). The osmotic control of 90 mM mannitol did not increase *GI:luc* luminescence transiently and the decaying amplitude oscillations approached steady state.

The times of oscillation peaks and troughs of *GI:luc* luminescence were approximated using a simple clustering algorithm of turning points in the dataset (Section 4.2.3). The timing of these peaks and troughs remained approximately the same relative to the time of sucrose treatment comparing application at CT0 and CT12 (Figure 4.6C). Therefore, sucrose might be a *zeitgeber* for *GI* because it re-entrains circadian oscillations in *GI* expression. *GI* promoter activity increased in response to topical sucrose treatment, which coincided with the prediction of the *N5 Model* for simulated [*Y* (*GI*) mRNA], but contrasted with the corresponding simulation using the *PostGI* model (Figure 4.7). This provided evidence for the hypothesis that sucrose increases the basal rate of *GI* transcription.

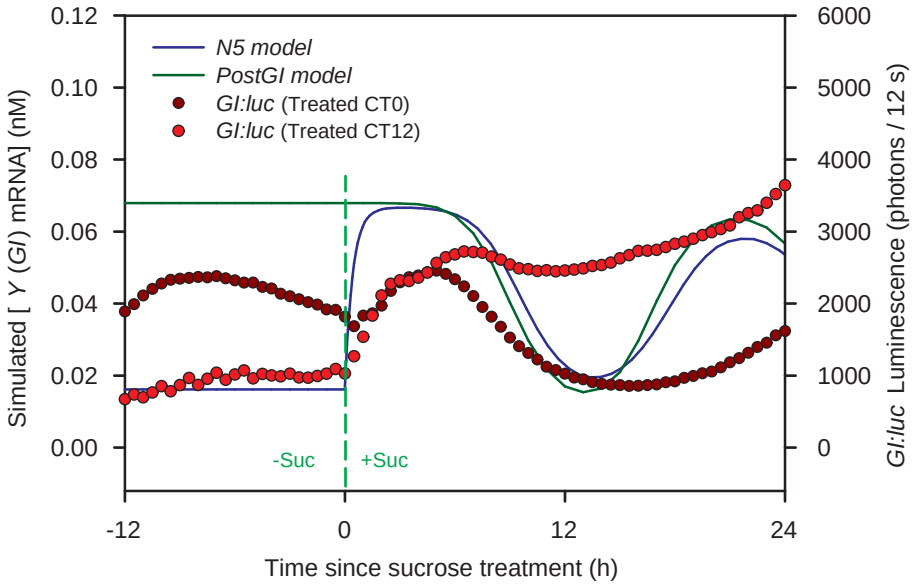

Figure 4.7: Sucrose activates *GI* transcription as predicted by the *N5 Model*.
Mathematical simulation of [*Y* (*GI*) mRNA] in constant dark after simulated sucrose treatment (solid lines) compared with corresponding *GI:luc* luminescence data (red circles). 14-day-old *Arabidopsis* seedlings expressing *GI:luc* were entrained in L12/D12 cycles before transfer to DD for 60 h (dark red circles, CT0) or 72 h (light red circles, CT12), then treated with 100 μl of 90 mM sucrose (data as in Figure 4.6). Corresponding simulations using the *N5 Model* (light blue line, Figure 4.5A) and the *PostGI Model* (dark blue line, Figure 4.5B) were conducted by numerical integration of the *Three Loop Model* equations with the *ode23s* stiff equation solver in MATLAB^{TM}.

4.4 Discussion

After demonstrating the necessity of a functional *GI* for sucrose modulation of the central oscillator in DD in Chapter 3, it was investigated whether *GI* was regulated at the transcriptional or post-translational level. The analysis in Chapter 3 also suggested that the rate of *GI* transcription was increased in the presence of exogenous sucrose. Here it was determined that a dark-dependent GI protein degradation mechanism might account for sucrose-dependent oscillations in DD. However, comparisons of the dynamics of *GI:luc* luminescence with model simulations following a step change in exogenous sucrose availability suggests transcriptional rather than post-translational regulation of *GI* confers responsiveness to sucrose.

4.4.1 The *PostGI Model*: GI protein stabilisation

The *PostGI Model* was defined to account for dark-induced proteolysis of GI by the 26S proteasome (David *et al.*, 2006). For simplicity, it was assumed that degradation occurred both in the cytosol and the nucleus and the dark-independent degradation rate was unaltered from the nominal *Three Loop Model* (Eqn. 4.3). Therefore, GI degradation increases in the dark in the absence of exogenous sucrose by rates $\hat{m}_{13}$ nM h^{-1} in the cytosol and $\hat{m}_{14}$ nM h^{-1} in the nucleus (Equations 4.1–4.2). All other *Three Loop Model* parameters were kept at their nominal rates, which is a potential shortfall of the *PostGI* model. In particular, the new mechanism affected the simulated light-dark cycles of [*TOC1* mRNA], forcing a biphasic oscillation (Figures 4.1B,D). However, the nominal *Three Loop Model* does not accurately describe light-dark oscillations of *TOC1* expression (compare Figures 3.1D and 4.1D).

As the relative rate of dark-dependent GI degradation ($d = \hat{m}_{13}/m_{13} = \hat{m}_{14}/m_{14}$) was increased, the amplitude of DD oscillations was suppressed. The first peak of simulated [*LHY/CCA1* mRNA] remained unaffected, similar to that observed for *CCA1:luc* luminescence in the absence of exogenous sucrose. Therefore, a high rate of dark-dependent degradation of GI corresponded to dynamical behaviours when there is no exogenous sucrose supply, and a lower rate corresponded to exogenous supply of sucrose. This is equivalent to saying that exogenous sucrose stabilises GI protein in the dark. Presumably, a high level of $[\mathrm{Suc}]_i$ during light (photosynthesis) would have the same (stabilising) effect, providing a possible explanation for the proposed dark-dependency of GI protein degradation (David *et al.*, 2006).

4.4.2 Distinction of transcriptional and post-translational mechanisms

Simulations of the *N5 Model* from Chapter 3 were compared with the *PostGI Model* to determine conflicting predictions that could be exploited to establish the most likely model of GI-mediated sucrose modulation of the circadian clock. To establish whether *GI* is regulated transcriptionally by sucrose, the effect of topical sucrose treatment on *GI* expression in DD was investigated both *in silico* and *in vivo*. The possibility that sucrose regulates *GI* at the post-translational was investigated by comparing L12/D12 oscillations of GI protein in the presence and absence of sucrose in both wild-type and GI-overexpressing backgrounds. In tandem, these experiments might distinguish between three possible hypotheses for the modes of *GI* regulation by sucrose: only transcriptional control, only post-translational contol, or dual transcriptional and post-translational control.

Sucrose regulates *GI* transcriptionally and is a *zeitgeber* for *GI* expression

The effect of topical sucrose treatment was measured in *GI:luc* expressing plants. By comparison with simulations of the *N5 Model* and the *PostGI Model*, evidence was found supporting the hypothesis that sucrose up-regulates *GI* transcription, as *GI* expression increased following topical sucrose treatment, a prediction of the *N5 Model* (Figures 4.5, 4.6, 4.7). It was also found that the oscillations in *GI:luc* luminescence resulting from sucrose treatment were not dependent on the circadian time of application, indicating that sucrose is a *zeitgeber* for *GI* in DD (Figure 4.6C). It would be interesting to measure the response of other circadian markers in response to a topical sucrose treatment. These can include promoter-*luc* fusions analogous to *GI:luc*, and also crossed into a range of mutant backgrounds. Of particular interest would be the *gi*-11 null mutant, to establish whether topical sucrose treatment is perceived by the *Arabidopsis* central oscillator only via *GI*, or through multiple pathways. It is clear that additional experimental characterisation of the effect of topical sucrose treatment would unravel further properties of the interactions between sugar signalling pathways and oscillator components, and also of the circadian central oscillator mechanism itself.

A protein assay for determining whether sucrose exerts post-translational control of *GI*

To establish whether sucrose regulates *GI* at the post-translational level, the *PostGI Model* was used to simulate L12/D12 cycles of [Y (*GI*) protein] in the presence ($d = 0$ or $d = 0.5$), no

dark-induced GI proteolysis) and absence ($d = 3$) of exogenous sucrose (Section 4.3.2). First, the experiments of David *et al.* (2006) which demonstrated the dark-dependent proteolysis of GI were simulated. This experiment offers a clear distinction between sucrose modulating *GI* transcript or protein by the following argument. If sucrose only regulates *GI* transcriptionally, as predicted by the *N5 Model*, then the *gi*-2 *35S:GI-TAP* line will be insensitive to sucrose, as the native *GI* promoter is dysfunctional. However, a sucrose-dependency in the *gi*-2 *GI:GI-TAP* line would be expected due to the presence of the native *GI* promoter. In contrast, if sucrose only regulates *GI* post-translationally (*PostGI Model*), then only a small sucrose-dependency might be seen for *gi*-2 *GI:GI-TAP* (Figure 4.2), but a significant sucrose-dependency would be seen in *gi*-2 *35S:GI-TAP* (Figure 4.4). Due to the limited potential to characterise quantifiable differences in protein abundance *in vivo*, only stark differences may be observed such as the strong suppression of L12/D12 GI protein cycles by sucrose hypothesised to exist in the *gi*-2 *35S:GI* background by the *PostGI Model*. Therefore, the proposed combination of experiments may only answer whether or not GI protein is regulated by sucrose, and not distinguish control of *GI* transcriptionally. However, combined with the evidence presented in Figure 4.7 which demonstrates *GI* expression is increased by topical sucrose treatment (as predicted by the *N5 Model*), we feel there would be sufficient evidence to discriminate whether sucrose regulates *GI* only transcriptionally, only post-translationally, or both at the transcriptional and post-translational levels. The proposed protein experiments are currently being conducted by a collaborating member of the Webb Laboratory (Seong Jin Baek).

4.4.3 Summary

The central oscillator perceives $[\text{Suc}]_i$ via changes in the abundance of GI. The results presented above provided preliminary evidence for a transcription-based, rather than post-translational mechanism. However, a critical test has been designed which will elucidate the true underlying mechanism, the possible outcomes of which have been simulated using the *N5 Model* and the *PostGI Model*. This work represents further progress towards a model integrating carbohydrate metabolism into the circadian signalling network in *Arabidopsis*.

CHAPTER 5

Modelling a cADPR-Dependent Feedback Loop of the Circadian Clock

5.1 Introduction

In this chapter, the position and function of cyclic adenosine diphosphate ribose (cADPR) in the circadian oscillator network in *Arabidopsis thaliana* is addressed *in silico*. Recent work has shown that cADPR mediates the circadian control of $[Ca^{2+}]_{cyt}$, whilst also regulating the central oscillator mechanism (Dodd *et al.*, 2007). However, it is not clear which central oscillator genes interpret the action of circadian cADPR signalling.

cADPR is a Ca^{2+} mobilising second messenger in animals and plants (Clapper *et al.*, 1987; Navazio *et al.*, 2001; Galione *et al.*, 1991). cADPR was first identified by Lee *et al.* (1989) in sea urchin eggs, and described as a cyclic metabolite of NAD+ with intracellular Ca^{2+}-mobilising activity. cADPR is synthesised from NAD+ by the membrane-bound ADP-ribosyl (ADPR) cyclase enzyme (Lee & Aarhus, 1991), and broken down by cADPR-hydrolase (Lee & Aarhus, 1993) in the presence of nicotinamide. At high concentrations, cADPR binds to ryanodine receptors (RyR), promoting calcium-induced calcium release (CICR; Galione *et al.*, 1991). There are no known homologs of ADPR cyclase (or hydrolase) in plants, though cADPR has been shown to promote Ca^{2+} release from the vacuoles of beet storage root (Allen *et al.*, 1995). cADPR

also mediates abscisic acid (ABA) induced gene expression in response to cold, drought and salt stress (Wu *et al.*, 1997), and stomatal closure (Leckie *et al.*, 1998).

In *Arabidopsis*, [cADPR] has circadian oscillations in constant light (LL) which achieve peak levels 8 hours after subjective dawn, while in *CCA1*-ox (constitutive overexpressor of *CCA1*), [cADPR] does not oscillate and remains at a constant low level (Figure 5.1A; Dodd *et al.*, 2007). cADPR synthesis is inhibited by nicotinamide, a by-product of the cyclisation of NAD^+ by *ADPR cyclase* (Sethi *et al.*, 1996). Treatment of 50 mM nicotinamide significantly reduces cADPR synthesis in *Arabidopsis*, and has the additional effect of abolishing circadian oscillations of $[Ca^{2+}]_{cyt}$ (Figure 5.1B; Dodd *et al.*, 2007). The Ca^{2+}-sensor CAS has been suggested to contribute to diurnal variations $[Ca^{2+}]_{cyt}$ via an IP_3-based pathway (Tang *et al.*, 2007). However, treating *Arabidopsis* seedlings with the IP_3 inhibitor U73122 or the plasma-membrane channel blocker $GdCl_3$ had no effect on circadian oscillations of $[Ca^{2+}]_{cyt}$ (Dodd *et al.*, 2007). Therefore, cADPR mediates the circadian control of $[Ca^{2+}]_{cyt}$.

In addition to being an output of the *Arabidopsis* circadian clock, there is evidence that cADPR forms a cytosolic feedback loop with the central oscillator (Dodd *et al.*, 2007). In a bioinformatic study comparing the set of circadian-regulated transcripts with sets of transcripts regulated by signalling molecules, cADPR was identified to be commonly associated with circadian regulation. The overlap between cADPR- and circadian-regulated transcripts was the most statistically significant overlap, and included central oscillator genes *LHY*, *CCA1*, *GI* and *PRR7* (Figure 5.1C; Dodd *et al.*, 2007). In *Arabidopsis* seedlings which express an ADP-ribosyl cyclase enzyme from *Aplysia kurodai* under the control of a β-estradiol-inducible promoter (*XVE:ADPRc*), changes in clock gene transcript abundance were measured 6 hours after application of β-estradiol (Sánchez *et al.*, 2004). Both *LHY* and *CCA1* transcripts abundance was decreased relative to wild-type plants, while expression of *GI*, *PRR5*, *PRR7* and *CRY1* was increased (Sánchez *et al.*, 2004). Therefore, transient increases in [cADPR] resulting from induced ADPR cyclase expression results in altered clock gene expression, implying that cADPR regulates the circadian clock. Further evidence for a cADPR-based feedback loop was identified as treatment with the cADPR inhibitor nicotinamide increased circadian period of *CAB2*, *CCA1*, *LHY* and *TOC1* transcript abundance (Figure 5.1E) and oscillations of leaf position in LL (Figures 5.1F,G; Dodd *et al.*, 2007). However, there was no circadian phenotype when measuring circadian oscillations of leaf movement in the *XVE:ADPRc* line (Figure 5.1H; Dodd *et al.*, 2007).

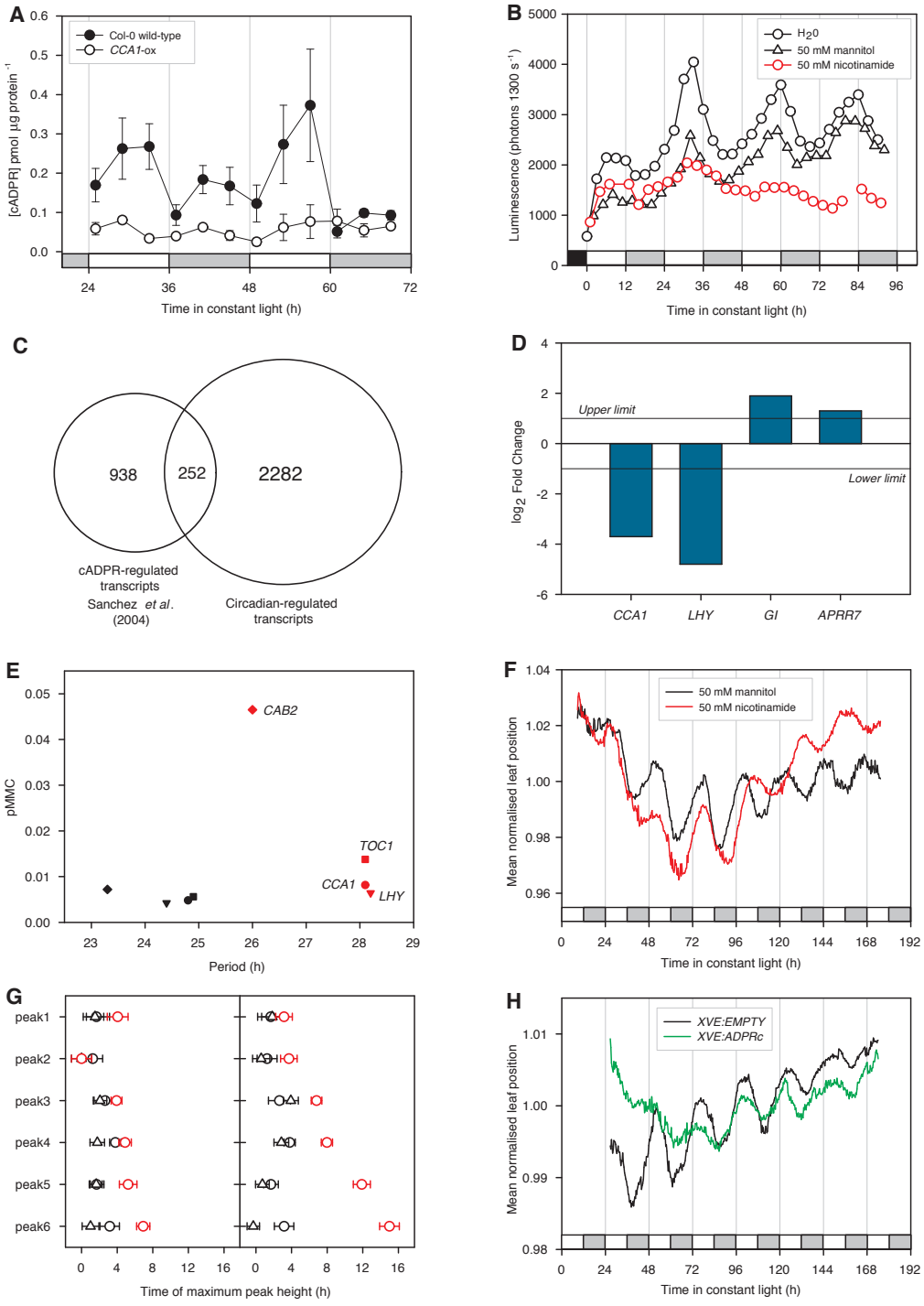

Figure 5.1: Modulation of the *Arabidopsis* circadian clock by a cADPR-based feedback loop.
(A) Circadian rhythm of [cADPR] in LL present in Col-0 wild-type and absent in *CCA1*-ox plants. (B) Circadian rhythm of $[Ca^{2+}]_{cyt}$ is abolished with 50 mM nicotinamide (red circles). Control lines are 50 mM mannitol (black triangles) or water (black circles). (C) There is a significant overlap between circadian- and cADPR-regulated transcripts (Sánchez *et al.*, 2004; Dodd *et al.*, 2007). (D) Log_2 fold change of transcript abundance 6 h after induction of *Aplysia* ADPR cyclase (Sánchez *et al.*, 2004). (E) Circadian period increases after treatment every 3 h with 50 mM nicotinamide (red) or water (black). Multiple-measures correction (pMMC) describes the goodness of fit. (F) Circadian rhythm of leaf position after treatment with 50 mM nicotinamide (red) or 50 mM mannitol (black). (G) Time of circadian peaks of leaf position in seedlings treated with 10 mM (left panel) or 50 mM (right panel) nicotinamide (red circles), mannitol (black triangles) or water (black circles). (H) Circadian rhythm of leaf position after induced expression of *XVE:ADPRc* (green line) or *XVE:EMPTY* control (black line). (A,B,F,H) Bars on x-axis indicate light during subjective daytime (white bars) and subjective night-time (grey bars), or dark (black bars). Modified from Dodd *et al.* (2007).

5.2 Mathematical methods

Mathematical models of the *Arabidopsis* circadian clock were used to investigate the effects of manipulating [cADPR] levels. All existing models of the central oscillator mechanism consider only gene-gene interactions and activation/degradation by light (Locke *et al.*, 2005a,b, 2006; Zeilinger *et al.*, 2006). There has so far been no attempt to incorporate the effect of small molecules, where knowledge of interactions with central oscillator genes is limited. Elevated [cADPR] has a pronounced effect on circadian-regulated genes (Sánchez *et al.*, 2004), though the mechanism responsible has not been characterised. In this chapter, we assume that the wild-type oscillating levels of cADPR are implicitly accounted for in mathematical descriptions of the central oscillator as the circadian period is approximately 24 h rather than the long period when cADPR synthesis is suppressed with nicotinamide (Figure 5.1F; Dodd *et al.*, 2007). We assume further that the effect of elevated [cADPR] can be described by perturbing the reactions defined by the model, through altering the parameters which define these reactions.

The motivation for investigating the role of cADPR of the circadian clock network derived from a set of experimental observations that were seemingly uncorrelated or contradictory. Induced expression of ADPR cyclase was shown to have a large effect on the transcript abundance of circadian clock genes in *Arabidopsis* (Sánchez *et al.*, 2004), without affecting circadian period or phase relative to wild-type plants (Figure 5.1H). Initially, we considered using sensitivity analysis to identify how the oscillation period varied as a function of each parameter value. However, existing methods are based on linear approximations and therefore correspond to small deviations from the nominal parameter values (Ingalls & Sauro, 2003; Ingalls, 2004). Due to the large deviations in gene expression being investigated, the 'local' approach was not suitable. Instead, simulation methods were designed to analyse the effect of large parameter perturbations to the kinetic parameters of the mathematical circadian clock models, considering the existing experimental data already available (Figure 5.1).

5.2.1 Simulating effects of high and low [cADPR] on clock gene expression with the *Interlocked Feedback Loop Model*

In general, we can describe the *Interlocked Feedback Loop Model* by a nonlinear system

$$\dot{x} = f(x, p) \tag{5.1}$$

where $x \in \mathcal{R}^n$ is a vector of concentrations of mRNA, protein in the nucleus and cytoplasm for each gene, and $p \in \mathcal{R}^m$ is the vector of m model parameters (see Appendix A.1 for a detailed description of the model). The simplest method for altering the parameters is to assume that the effect of elevated [cADPR] on the circadian clock is immediate and sustained at a constant level. Suppose that ADPR cyclase is induced at $t = \tau$, then we define the constant perturbation $p_C(t)$ as follows

$$p_C(t) := \begin{cases} p_0, & t \leq \tau \\ rp_0, & t > \tau \end{cases} \tag{5.2}$$

where p_0 is the nominal value of the parameter p, and $r > 0$ is the perturbation amplitude.

Induction of *XVE:ADPRc* by β-estradiol was shown to continually increase [cADPR] over 20 hours (Sánchez *et al.*, 2004). However, the effect on transcript abundance was most pronounced 6 hours after application of β-estradiol. The activity of the ADPR cyclase enzyme was also higher at 16 h than 6 h. This suggests that the effect on downstream gene expression of increased ADPR cyclase activity, presumably via cADPR, is transient. We supposed that the effect of elevated [cADPR] on the circadian clock increases initially after induction and then decreases back to the normal operating conditions. By assuming linear uptake and exponential decay of the inducer, we define the (additive) transient perturbation $p_T(t)$.

$$p_T(t) := \begin{cases} p_0, & t \leq \tau \\ p_0 + \frac{rte^{1-\frac{t}{t_{\max}}}}{t_{\max}}, & t > \tau \end{cases} \tag{5.3}$$

where r is the ratio between the perturbed and nominal parameter values at the peak time $t = t_{\max}$. Peak times were tested that related to the peak change in gene expression ($t_{\max} = 6$), peak ADPR cyclase activity ($t_{\max} = 16$) and peak [cADPR] ($t_{\max} = 20$; Figure 5.2.1). The most representative profile of the experiment used to find suitable parameter perturbations is the exponential profile which peaks 6 hours after simulated induction, as it is the downstream effect of cADPR which is being modified through parameter perturbation.

The performance of parameter perturbations was assessed by comparing simulated gene expression values with the data published in Sánchez *et al.* (2004) as follows. The model equations (Equations A.1–A.13) were simulated in L16/D8 cycles and at $t = \tau$ subjected to a parameter perturbation. To ease the computational burden, a series of initial conditions was

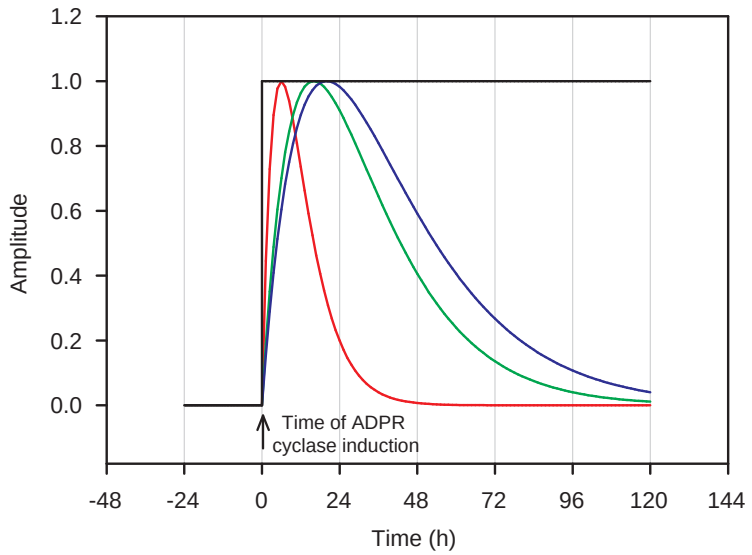

Figure 5.2: Perturbation profiles applied to the *Interlocked Feedback Loop Model*.
Graphical representation of each perturbation profile, applied at $t = 0$. Constant perturbation (Eqn. 5.2, black trace), and transient perturbations (Eqn. 5.3) with $t_{\max} = 6$ (red trace), $t_{\max} = 16$ (green trace) and $t_{\max} = 20$ (blue trace) are plotted for unit amplitude ($A = 1$). Modified from Figure S4A in Dodd *et al.* (2007).

computed as the numerical solution at different integer times along the limit cycle of the unperturbed *Interlocked Feedback Loop model*. The initial conditions therefore correspond to different values of the perturbation time τ. At $t = \tau + 6$, the fold change of *LHY* (f_{LHY}), *TOC1* (f_{TOC1}) and *Y* (f_{Y}) mRNA was computed relative to the equivalent unperturbed simulation. Therefore, only one quarter of the limit cycle was analysed for fold changes in simulated gene expression, meaning that obtaining numerical solutions was very fast. A cost function was defined to assess how close each perturbation was to the target values.

$$\|e\|_2 = \sqrt{(f_{\text{LHY}} - 0.056)^2 + (f_{\text{TOC1}} - 1)^2 + (f_{\text{Y}} - 3.732)^2)} \tag{5.4}$$

The target value for the LHY component, 0.056, was calculated as the arithmetic mean of the fold changes in *LHY* and *CCA1* expression. Similarly, the value for *Y* was taken to be the fold change in *GI*, as *GI* is considered to be the most likely identity of *Y* (Locke *et al.*, 2006). Since *TOC1* was not found to be significantly regulated by ADPR cyclase (Sánchez *et al.*, 2004), the target value was set as 1. No restriction was imposed on the change in *X* mRNA as it's identity remains unknown. Variants of the cost function were also investigated, in particular by normalising each squared bracket by the target value, or the square of the target value. However, this had the effect of rewarding perturbations for which f_{LHY} was very close to 0.056,

whilst only weakly penalising deviations of f_{TOC1} and f_{Y} from their target values (data not shown). Parameter perturbations were retained as candidates if they achieved a cost function score less than 2.

An algorithm was defined that systematically tested perturbations in the rate constants of the *Interlocked Feedback Loop Model* for their ability to match the observed fold changes in *LHY*, *CCA1*, *TOC1* and *GI* which resulted from transient induction of *XVE:ADPRc* (Sánchez *et al.*, 2004). Initially, parameters were perturbed singly as this gave the potential to establish predictions for cADPR targets in the central oscillator mechanism and reflected our prior assumption that cADPR targets few rather than all components. However, despite exploring a range of amplitudes for all perturbation profiles (Figure 5.2.1), we found no examples for which $\|e\| < 2$. Parameters were thus perturbed in pairs to cover as much of the parameter space as possible. Furthermore, this was in keeping with the philosophy that only very few components are directly regulated by the cADPR-mediated pathway. Each perturbation was conducted for a random linear combination of each parameter pair ($\binom{53}{2} = 1378$ choices) and a range of amplitudes r (between -1 and 1). An example of simulated output after imposing perturbations in this way can be seen in Figure 5.3.

Figure 5.3 illustrates how a transient perturbation (with $t_{\max} = 6$) to a (hill exponent of *LHY* activation by X) and p_1 (rate of *LHY* translation) can yield altered gene expression close to the target values ($f_{\mathrm{LHY}} = 0.002$, $f_{\mathrm{TOC1}} = 1.001$, $f_{\mathrm{Y}} = 3.719$, $\|e\|_2 = 0.054$). Note that in this example, parameters that directly affect Y mRNA have not been perturbed. The result of perturbations to oscillating systems is by no means intuitive.

5.2.2 Refinement of the pairwise parameter perturbation method and application to the *Three Loop Model*

Initially, the *Interlocked Feedback Loop Model* was used for investigating cADPR-mediated changes in clock gene expression. After publication of the results (Dodd *et al.*, 2007), the parameter perturbation method was refined and applied to the *Three Loop Model* in an attempt to find a coherent prediction for the target of a cADPR-based feedback loop for the central oscillator. The decision to switch models reflected increased confidence in the *Three Loop model*'s ability to match experimentally observed behaviours and was additionally motivated by the inclusion of the extra component A (*PRR7/9*). The transient perturbation (p_T) was redefined as

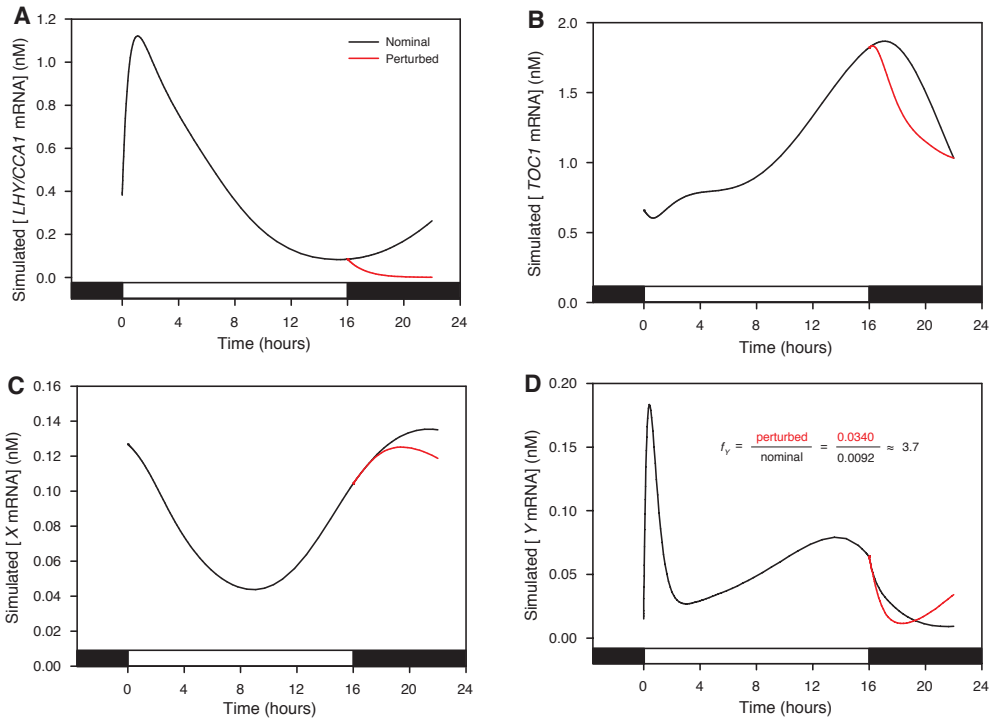

Figure 5.3: Parametric perturbations alter gene expression in the *Interlocked Feedback Loop Model*. Simulated induction of ADPR cyclase (red traces) is compared against wild-type expression (black traces) in the *Interlocked Feedback Loop Model* (Locke *et al.*, 2005b). Model equations (Equations A.1–A.13) were solved numerically with Θ_{light} set to reflect long-day (16 h light, 8 h dark) conditions. The concentrations of mRNA for the model components *LHY* (A), *TOC1* (B), *X* (C) and *Y* (D) are plotted against time. The transient perturbation (Eqn. 5.3) was imposed at $t = 16$ to parameters a and p_1. White and black bars indicate light and dark respectively.

a multiplicative perturbation to the nominal parameter set p_0

$$p_T(t) := \begin{cases} p_0, & t \leq \tau \\ (1 + \frac{r-1}{6} t e^{1-\frac{t}{6}}) p_0, & t > \tau \end{cases} \tag{5.5}$$

where r is relative parameter value at the peak time $t = 6$. For each pair of parameters, 100 trials were simulated for each perturbation in which random values were assigned for r (constant perturbation, Eqn. 5.2 or transient perturbation, Eqn. 5.5). In both cases, these values relate the largest relative deviation from the nominal value. So, we chose a distribution on the positive real line with mean 1, by assigning $r = 10^u$ where u is a uniformly distributed random number over the closed interval [-2,2]. In this section, a cost function was not used to assess how close a perturbation matched the data from Sánchez *et al.* (2004). Instead, perturbations were considered candidates when f_{LHY} (fold change in [*LHY* mRNA] 6 hours after simulated induction of ADPR cyclase) was less than 0.1, $0.5 < f_{\text{TOC1}} < 2$, and $f_{\text{Y}} > 2.5$. This avoided the issues of normalisation when using a cost function, as discussed in the previous section. For analysis of the

Three Loop Model, a further constraint of $f_A > 2$ was considered. A represents the influence of *PRR7* – which was significantly up-regulated by increased [cADPR] (Figure 5.1D) – and *PRR9* which did not appear in the dataset and thus not significantly regulated by cADPR. Candidate parameter perturbations were again removed if the state trajectory did not return to the limit cycle in simulated LL.

The 100 random perturbations were conducted for each pairwise combination of parameters from the *Interlocked Feedback Loop Model* (Locke *et al.*, 2005b) and the *Three Loop Model* (Locke *et al.*, 2006). Two perturbation profiles (transient and constant) were imposed at each hourly time over the 24 hour day. Since only a small dataset is available to guide our analysis, a more general look at possible effects of elevated [cADPR] is presented. Distributions are presented which illustrate properties of LL oscillations after simulated induction of ADPR cyclase. In addition, we attempted to characterise regions of the model which when perturbed, matched experimentally observed behaviours. The results of these analyses are presented in Section 5.3.2.

5.2.3 Calculation of period and phase in LL

The set of candidate perturbations was refined by removing cases where the perturbation led to a loss of rhythmicity in LL. This is reasonable since there is no arrhythmic phenotype after induction of ADPR cyclase (Figure 5.1H). The period and amplitude of oscillation in LL was computed to assess rhythmicity. The relevant model equations were solved numerically with MATLAB^{TM} as before, except that *ode23s* was used for certain perturbations that could not be resolved by *ode15s*. Θ_{light} was varied to reflect two cycles of diurnal conditions (12 h light, 12 h dark) followed by 196 hours of LL. The perturbations were imposed at the last dark to light transition, as per our experimental data. The time difference of the last two peak values of simulated [*LHY* mRNA] was used to estimate period $\hat{T}$. The ratio between the last local maxima and local minima provide an amplitude estimate $\hat{A}$. For the transient perturbations, the phase $\hat{\phi}$ was computed relative to the unperturbed period T as follows.

$$\hat{\phi} := (\hat{\tau} - \tau + \frac{T}{2}) \mod T - \frac{T}{2} \tag{5.6}$$

where τ is the time of the last peak value of [LHY mRNA] in the unperturbed case, $\hat{\tau}$ for the perturbed case. This definition ensures that the phase lies in the interval $[-\frac{T}{2}, \frac{T}{2}]$.

5.3 Results

5.3.1 Parameter perturbation analysis applied to the *Interlocked Feedback Loop Model*

Time of induction of candidate perturbations

The observed changes in gene expression after transient induction of *XVE:ADPRc* might vary depending on the time that the inducer chemical is applied. This is because non-stimulated expression of circadian clock-associated genes varies over the course of the day. Sánchez *et al.* (2004) did not report the time at which they applied the inducer chemical. We found that the number of random pairwise perturbations that could be considered candidates varied greatly depending on the time at which the perturbation was imposed (Figure 5.4). A bimodal distribution prevailed for the constant perturbation and the transient perturbation with $t_{\max}$ equal to 6 h and 16 h, with a broad peak centred at ZT15 (cluster B) and a smaller peak at ZT0 (cluster A; Figure 5.4A; Dodd *et al.*, 2007). For the transient perturbation with $t_{\max} = 20$, only cluster B was observed.

Frequency of individual parameters represented by candidate set of perturbations

The candidate parameter pairs were analysed for the frequency at which each individual parameter was represented to obtain a prediction of the point of entry of the proposed cADPR-dependent feedback loop into the *Arabidopsis* circadian clock network. In general, there was a reasonably uniform distribution over the parameters, indicating that there are many ways of perturbing the model to achieve the relevant fold changes in transcript abundance (Figure 5.5). The most frequently represented parameter in the set of candidate constant perturbations was g_2 (constant of *TOC1* activation by *Y*) occurring in 5.30% of the combined total of candidate parameter perturbations*, followed by r_3 (rate of TOC1 nuclear import; 4.15%) and g_5 (constant of *Y* inactivation by *TOC1*; 3.74%; Figure 5.5A). The same three parameters were also the most frequently occurring in the candidate set of transient perturbations with $t_{\max} = 6$ h (g_2 – 4.97%, g_5 – 4.59%, r_3 – 5.82%; Figure 5.5B) and $t_{\max} = 16$ h (g_2 – 5.17%, g_5 – 6.38%, r_3 – 10.29%; Figure 5.5C), while r_3 (12.72%) and g_5 (7.52%) were most frequently considered candidate tran-

*The occurrence of parameters in each candidate set is a percentage of the total of all parameter occurrences, which is precisely twice the number of candidate perturbations as each candidate perturbation involves two parameters. Therefore, if a parameter comprises 10% of a candidate set, then it must occur in 20% of all candidate pairwise parameter perturbations.

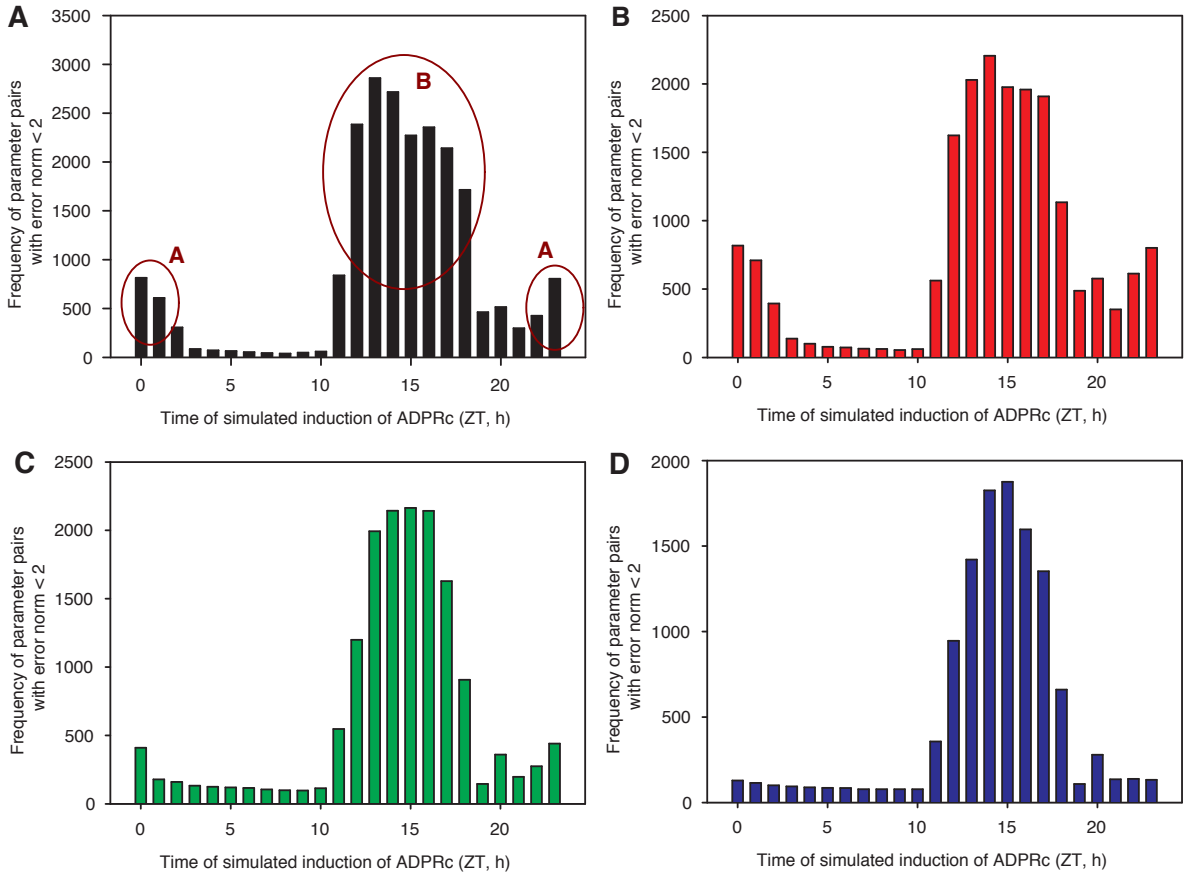

Figure 5.4: Time of simulated induction of ADPR cyclase affects differential gene expression. The number of pairwise parameter perturbations that altered clock transcript abundance with error norm < 2, depended on the time of simulated induction of ADPR cyclase. The distribution of candidate perturbations for the time of simulated induction of ADPR cyclase is plotted for (A) constant perturbations and transient perturbations with (B) $t_{\max} = 6$, (C) $t_{\max} = 16$ and (D) $t_{\max} = 20$. Bimodal distributions show two candidate clusters (A and B) indicated by the dark red ovals. Modified from Figure S4B in Dodd *et al.* (2007).

sient perturbations with $t_{20} = 20$ h (Figure 5.5D). Each of the frequently represented parameters identified appear in different equations of the reaction system suggesting they are unrelated. However, they all correspond to reactions which belong to the negative feedback loop between *TOC1* and *Y* (see Equations A.1–A.13). Therefore, this analysis suggests that cADPR targets the *TOC1–Y* negative feedback loop, which results in the fold changes in clock gene expression reported by Sánchez *et al.* (2004).

The state variables which correspond to the candidate parameter perturbations were next analysed to obtain a more general prediction for the point of entry of cADPR into the *Arabidopsis* circadian clock network. Figure 5.6 illustrates the frequency at which each mRNA or protein was directly affected by candidate perturbations. Additionally, these results are expressed as percentages of the total candidate state occurrences (Table 5.1). The most frequently repre-

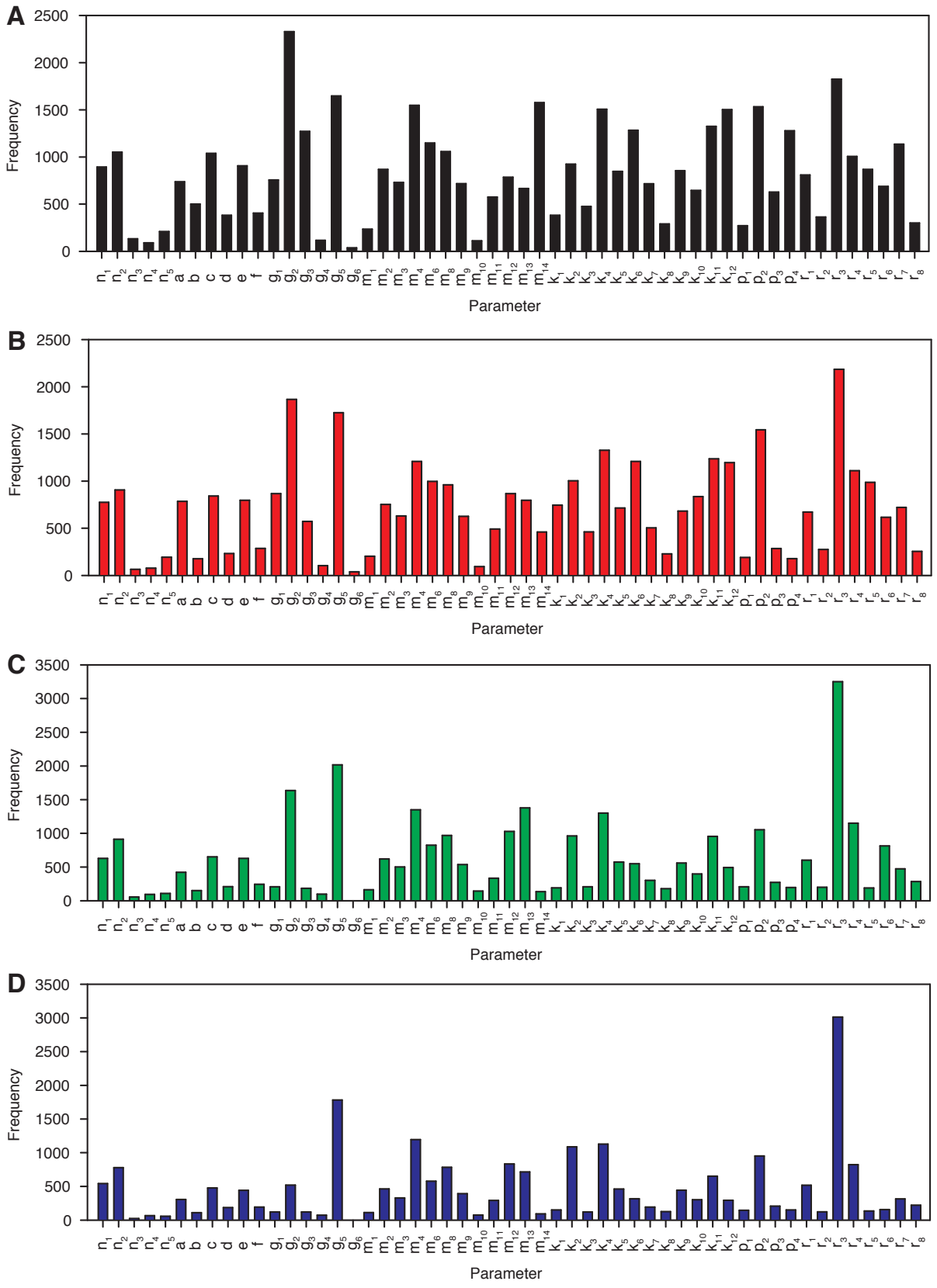

Figure 5.5: Frequency of candidate parameters in the *Interlocked Feedback Loop Model*.
Frequency of each model parameter occurring in the set of candidate perturbations ($\|e\| < 2$, Eqn. 5.4), for (A) constant perturbations, and transient perturbations with (B) $t_{\max} = 6$, (C) $t_{\max} = 16$ and (D) $t_{\max} = 20$.

sented model component in the set of candidate constant perturbations was *TOC1* mRNA, followed by *TOC1* protein and *Y* protein (see Table 5.1 for percentages; Figure 5.6A). *TOC1* protein was the most represented in all transient perturbations, followed by *TOC1* mRNA, providing evidence that *TOC1* mediates cADPR-feedback to the circadian clock mechanism (Figure 5.6). A prediction that *TOC1* mRNA is the point of entry for cADPR regulation in the circadian clock seems surprising, as *TOC1* expression was unchanged in *XVE:ADPRc* and constrained to be invariant in the perturbation analysis. Therefore, this prediction implies that large transient changes in the expression of other clock genes may be mediated by changes in *TOC1* transcript abundance, which itself returns to basal levels within 6 h. This prediction exemplifies the potential for mathematical analyses to generate non-intuitive hypotheses.

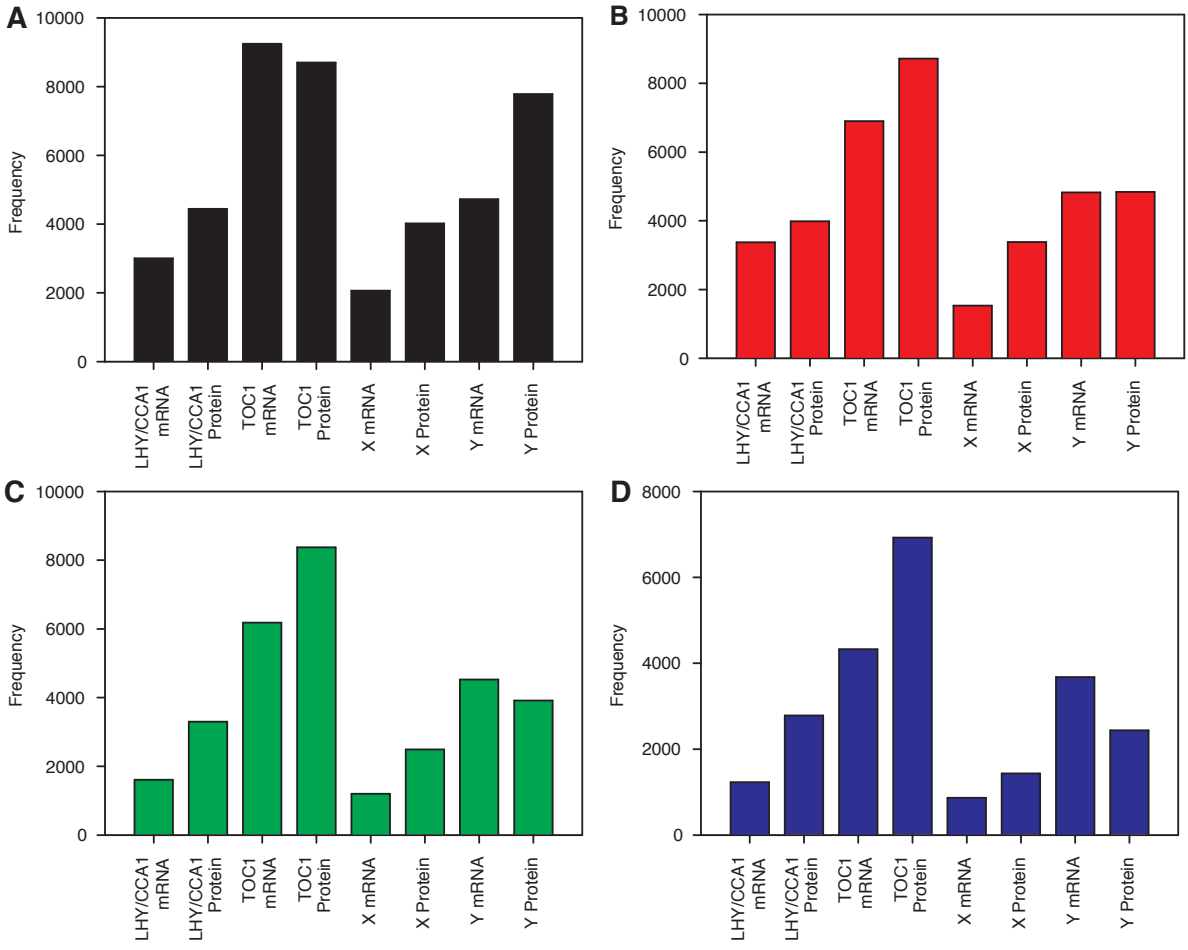

Figure 5.6: Frequency of component mRNA or protein affected by candidate perturbations to the *Interlocked Feedback Loop Model*.
Frequency of each component mRNA or protein occurring in the set of candidate perturbations ($\|e\| < 2$, Eqn. 5.4), for (A) constant perturbations, and transient perturbations with (B) $t_{\max} = 6$, (C) $t_{\max} = 16$ and (D) $t_{\max} = 20$. The parameter frequency data in Figure 5.5 is binned into the 8 model components according to the equations in which each model parameter appears (see Equations A.1–A.13). Each protein on the x-axis corresponds to the combination of cytoplasmic and nuclear protein for each model gene.

Table 5.1: Occurrence of component mRNA or protein affected by candidate perturbations to the *Interlocked Feedback Loop Model*.
Values represent the occurrence of component mRNA or protein corresponding to the parameters belonging to each candidate set of perturbations ($\|e\| < 2$, Eqn. 5.4). The data in Figure 5.6 is expressed for each component as the percentage of the total occurrences of all components in the set of candidate perturbations.

	Constant	Transient perturbations		
State variable	perturbation	$t_{max} = 6$ h	$t_{max} = 16$ h	$t_{max} = 20$ h
LHY mRNA	6.83	8.99	5.10	5.19
LHY protein	10.10	10.61	10.45	11.76
TOC1 mRNA	21.02	18.37	19.57	18.27
TOC1 protein	19.78	23.21	26.49	29.23
X mRNA	4.70	4.08	3.80	3.67
X protein	9.13	9.01	7.88	6.05
Y mRNA	10.74	12.84	14.33	15.52
Y protein	17.69	12.89	12.38	10.29

The circadian clock is robust to transient manipulations of the cADPR-based feedback loop

Transient perturbations to limit cycle oscillations do not affect the period of oscillation. As t tends towards ∞, the perturbation to the nominal parameter value decreases towards 0 (see Eqn. 5.3). Providing that the trajectory never leaves the region of attraction, then the trajectory will return to its nominal oscillation and the period remains unchanged. However, this excursion may incur some phase change.

The candidate perturbations were applied to simulations of LL after transfer from L12/D12 cycles (Figure 5.7). At $t = 0$, the perturbations were imposed (transient with $t_{max} = 6$ in this figure). Figure 5.7B illustrates the return to the nominal limit cycle (from $t = 12$ for clarity). The resulting phase change was calculated by comparing the difference between the final peak value of [*LHY* mRNA] relative to the unperturbed simulation (Figure 5.8), as explained in Section 5.2.3. Transient perturbations that peak after 6 hours do not incur a large phase change in general (Figures 5.8A and 5.8B). Nearly all perturbations from cluster A resulted in a phase change of less than 3 hours (Figure 5.8A). Most perturbations from cluster B also yielded no large phase change, however there were also a subset that resulted in anti-phase oscillations (Figure 5.8B). Candidate transient perturbations that peak after 16 or 20 hours and returned to the limit cycle had a reasonably uniform distribution of phase relative to the unperturbed trajectory (Figures 5.8C–F).

Constant perturbations (Eqn. 5.2) had large effects on the dynamical characteristics of the

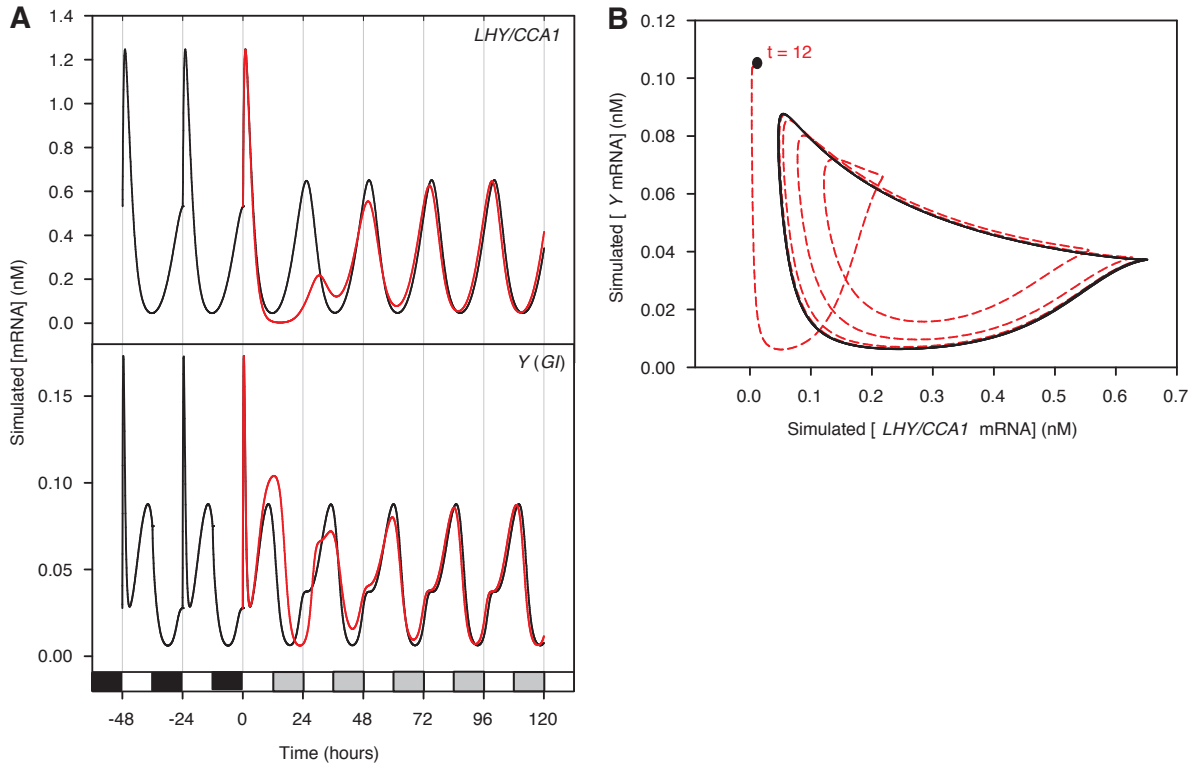

Figure 5.7: Transcript abundance returns to nominal oscillations after transient perturbations in LL. Transient perturbation (Eqn. 5.3, $t_{\max} = 6$) applied to parameters k_5 (michaelis constant of cytoplasmic *TOC1* protein degradation) and p_2 (translation rate of *TOC1*) of the *Interlocked Feedback Loop Model* (Locke *et al.*, 2005b). Perturbation imposed at the transition from light-dark cycles (12 hours light, 12 hours dark) to LL ($t = 0$, red traces). Black traces indicate corresponding unperturbed simulation. (A) [*LHY* mRNA] (top) and [*Y* mRNA] (bottom panel) plotted against time. (B) [*Y* mRNA] plotted against [*LHY* mRNA] from $t = 12$ (for clarity). Black bars on abscissa indicate darkness, white bars light and grey bars subjective dark under LL.

Interlocked Feedback Loop Model. A constant perturbation takes the assumption that elevated [cADPR] has a continual effect on downstream genes. While constantly high responses were not been observed experimentally in response to induced expression of ADPR cyclase (Sánchez *et al.*, 2004), the simulations may correspond to the overexpression of target genes of cADPR which alter clock function. Candidate constant perturbations were simulated as for the transient perturbations, solving the model equations (Equations A.1–A.13) in light-dark cycles before transfer to LL for 120 hours. The period of oscillation was computed as explained previously (Section 5.2.3) and plotted against the error norm score achieved by each candidate constant perturbation imposed at ZT0 (Figure 5.9A) and ZT15 (Figure 5.9B), which indicated that the time of simulated ADPR cyclase induction gave rise to contrasting behaviours. When induction commenced within cluster A (ZT23–ZT1), 69.41% of candidate constant perturbations had circadian periods < 24.5 h. In contrast, 70.36% of candidate perturbations from cluster B had circadian periods > 25.5 h, with the distribution centred near 28 h (Figure 5.9B).

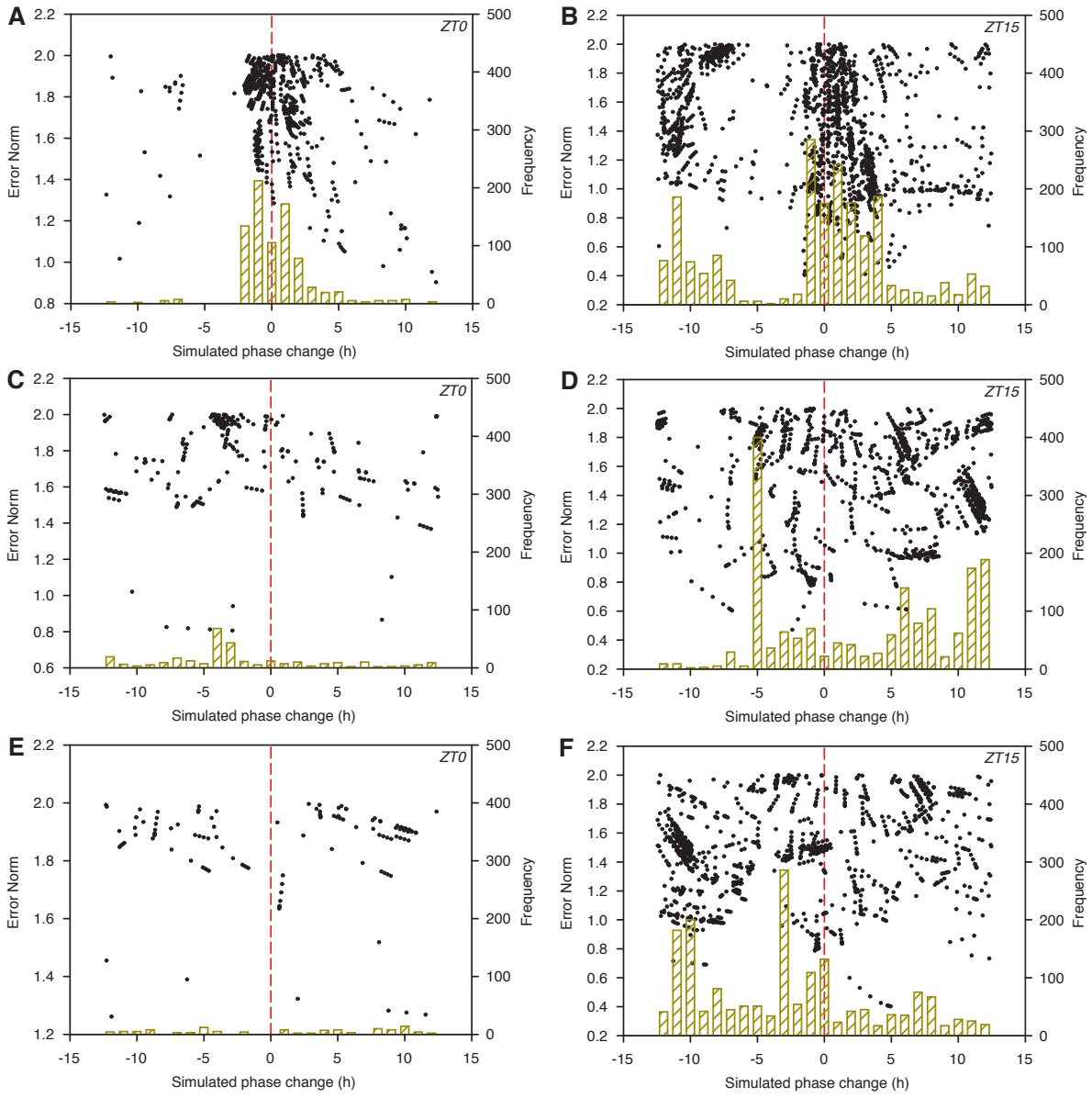

Figure 5.8: Simulated transient activation of cADPR-regulated genes.
Illustration of phase change in LL oscillations after transient perturbations (Eqn. 5.3). Equations A.1–A.13 were solved for 2 days of diurnal (12 h light, 12 h dark) cycles $t = 0$ to $t = 48$, followed by 196 h of LL, up to $t = 240$. Perturbation was imposed at $t = 48$, as per experimental protocol employed for data shown in Figure 5.1H. Phase change computed as $\hat{\phi} = (\hat{\tau} - \tau + \frac{T}{2}) \mod T - \frac{T}{2}$, where $\hat{\tau}, \tau$ are the times of the last peak values of simulated [*LHY* mRNA], and T the nominal period of oscillation in LL. Candidate perturbations that did not yield oscillations were removed from this analysis. Phase change is compared against error norm score (black dots, left axis), and displayed as a frequency of candidates at each hourly phase change (dark yellow bars, right axis). Plots relate candidate transient perturbations with (A,B) $t_{\max} = 6$, (C,D) $t_{\max} = 16$, (E,F) $t_{\max} = 20$, where the cyclase was induced at (A,C,E) ZT0 and (B, D, F) ZT15. Modified from Figure 3A in Dodd *et al.* (2007).

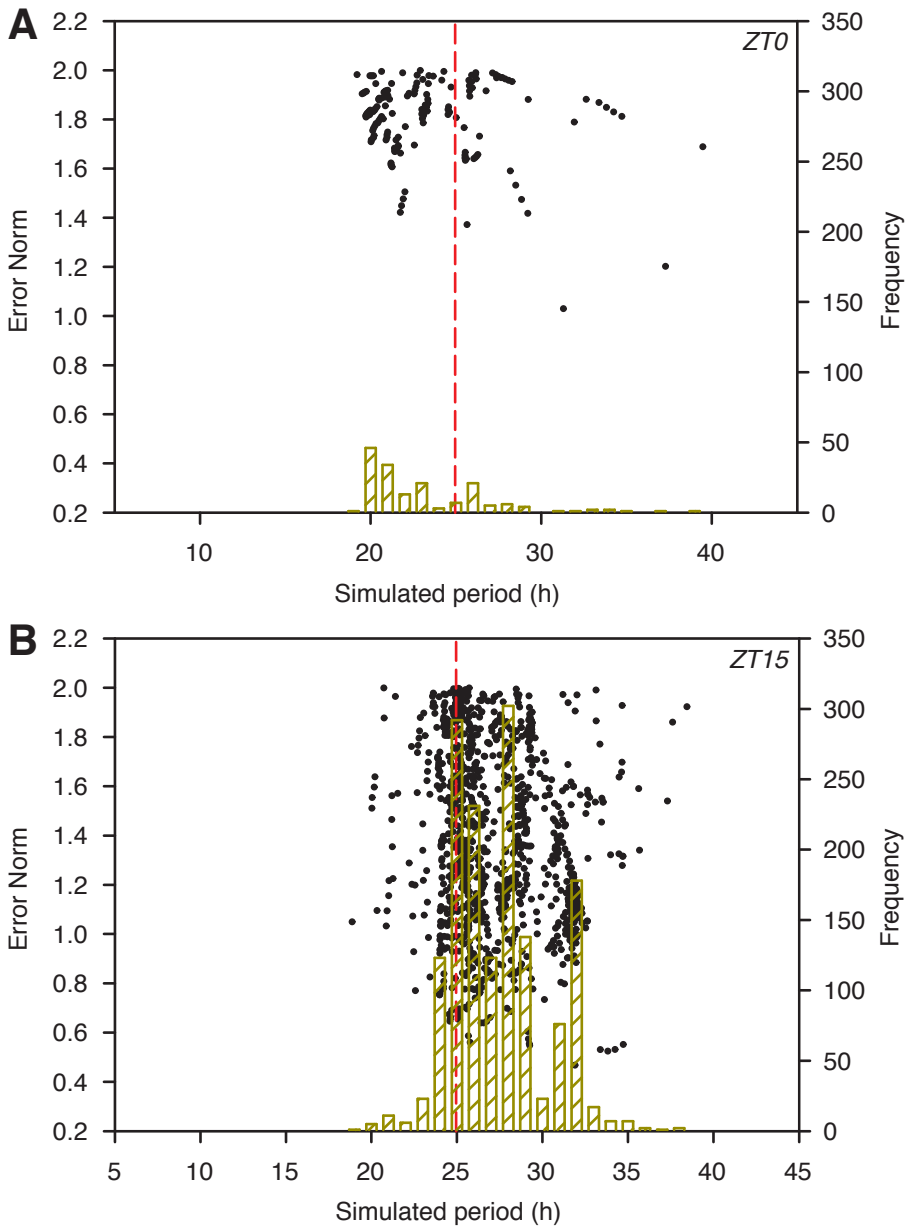

Figure 5.9: Simulated constant activation of cADPR-regulated genes.
Period is shown for candidate constant perturbations which had error norm score < 2 after induction at (B) ZT0 (cluster A) and (B) ZT15 (cluster B). Equations A.1–A.13 were solved numerically in LL for 300 h, and period computed as the time difference between the final two peak values of *LHY* mRNA. Periods lying between 10 and 40 hours are compared against error norm score (black dots, left axis), and displayed as frequency for each hourly period in the range (dark yellow bars, right axis). Modified from Figure 3B in Dodd *et al.* (2007).

After simulating constant activation of cADPR-regulated genes, we sought to find how suppression of cADPR targets might influence the central oscillator. This analysis corresponded to experimentally inhibiting cADPR synthesis, which can be achieved through constant addition of nicotinamide (Sethi *et al.*, 1996). Addition of nicotinamide yields a dose-dependent lengthening of circadian period in LL, by approximately 1 hour with 10 mM nicotinamide, and by

3 hours with 50 mM nicotinamide (Dodd *et al.*, 2007). Suppression of cADPR synthesis was simulated by reversing the sign of perturbation amplitude r of the candidate constant perturbations and computing the circadian period. It was found that candidate perturbations had longer periods than wild-type (unperturbed) for both clusters A (ZT0, 94.39% with period > 25.5 h) and B (ZT15, 55.09% with period > 25.5 h).

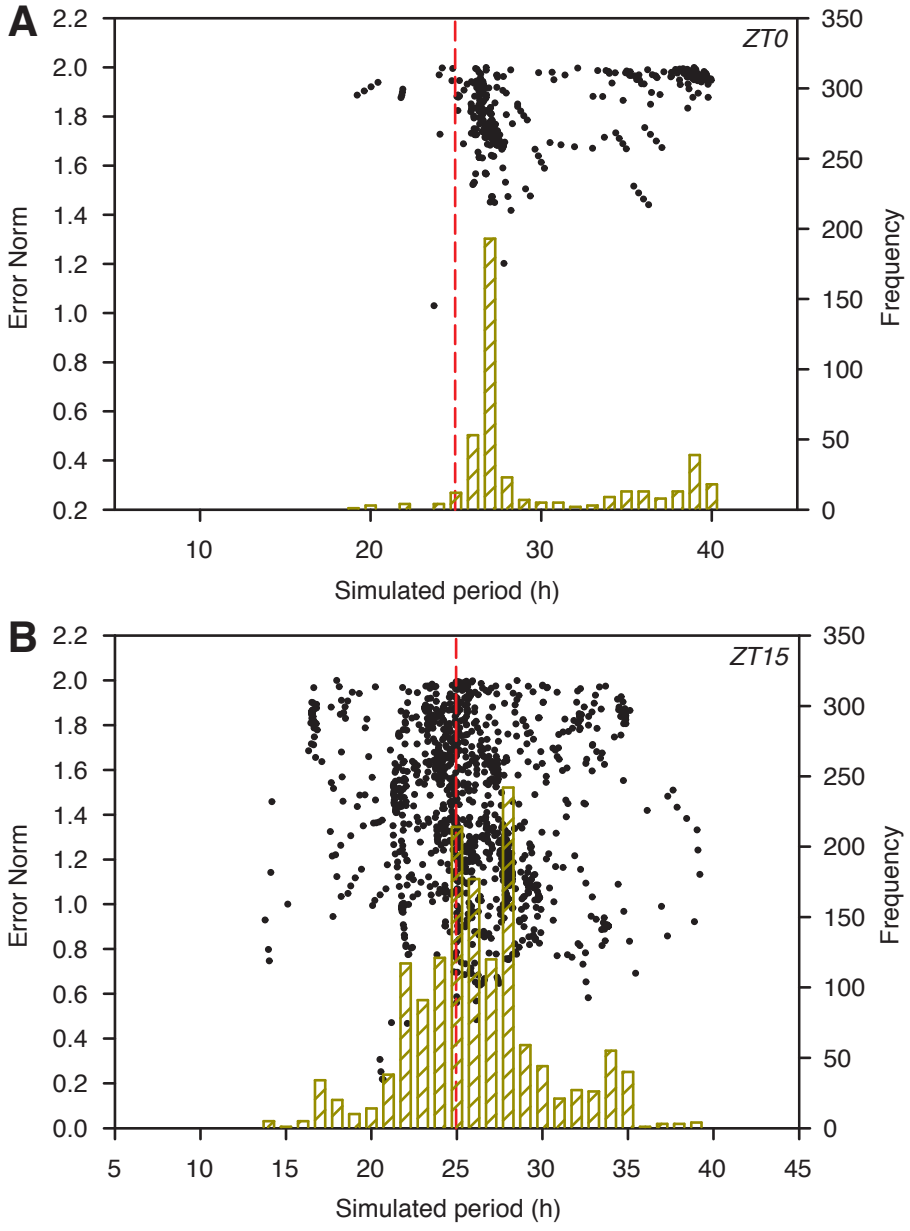

Figure 5.10: Simulated suppression of cADPR-regulated genes.
Period is computed for candidate constant perturbations with A set to have opposite sign. Candidates are those with error norm score < 2 after simulated induction at (A) ZT0 (cluster A) and (B) ZT15 (cluster B). Equations A.1–A.13 were solved numerically in LL for 300 h, and period computed as the time difference between the final two peak values of *LHY* mRNA. Resulting periods lying between 10 and 40 hours are compared against error norm score (black dots, left axis), and displayed as frequency for each hourly period in the range (dark yellow bars, right axis). Modified from Figure 3C in Dodd *et al.* (2007).

5.3.2 A refined pairwise parameter perturbation method applied to the *Interlocked Feedback* and *Three Loop Models*

In this section, a refined pairwise parameter perturbation method is applied to both the *Interlocked Feedback* and *Three Loop Models*. The new method treats alterations in cADPR-regulated gene expression as multiplicative, rather than additive perturbations to model parameters. Pairwise perturbations applied to the *Three Loop Model* were considered candidates according to whether or not the simulated fold change in *PRR7/9* (f_A) was greater than 2, as observed experimentally for *PRR7* (Sánchez *et al.*, 2004). It was important to consider $f_A > 2$ as an additional criterion to $f_{LHY} < 0.1$, $0.5 < f_{TOC1} < 2$ and $f_Y > 2.5$ as the effect of parameter perturbations on simulated *PRR7/9* expression may be informative. Conversely, not imposing $f_A > 2$ enabled comparison with the results for the *Interlocked Feedback Loop Model* and from the additive perturbation method in Section 5.3.1, and additionally covers the possibility that *PRR7* makes only a minor contribution to the combined *PRR7/9* component in the *Three Loop Model*.

Transient manipulations to the cADPR-based feedback loop may have no effect on simulated oscillation phase

The distribution of phase in LL after transient perturbations was centred near to the nominal unperturbed phase (Figure 5.11). The *Interlocked Feedback Loop Model* had a reasonably uniform distribution of phase in response to transient perturbations, though did indicate a possible phase advance of approximately 3 hours (Figure 5.11A). The same method applied to the *Three Loop Model* without imposing $f_A > 2$ had a slight tendency toward a phase change of zero (Figure 5.11B). In almost 30% of rhythmic trials, the phase change lies between -1.5 hours and 1.5 hours. Imposing $f_A > 2$ significantly reduced the number of candidate perturbations and led to a uniform distribution of phase in response to transient perturbations (Figure 5.11B).

Constant manipulations to the cADPR-based feedback loop affect simulated circadian period

Simulated constant activation of cADPR yielded a shortened period in LL (Figure 5.12). For analysing period, constant perturbation candidates were removed if the amplitude of oscillation (*LHY* mRNA) was less than one tenth of the value seen in the wild-type. Periods between

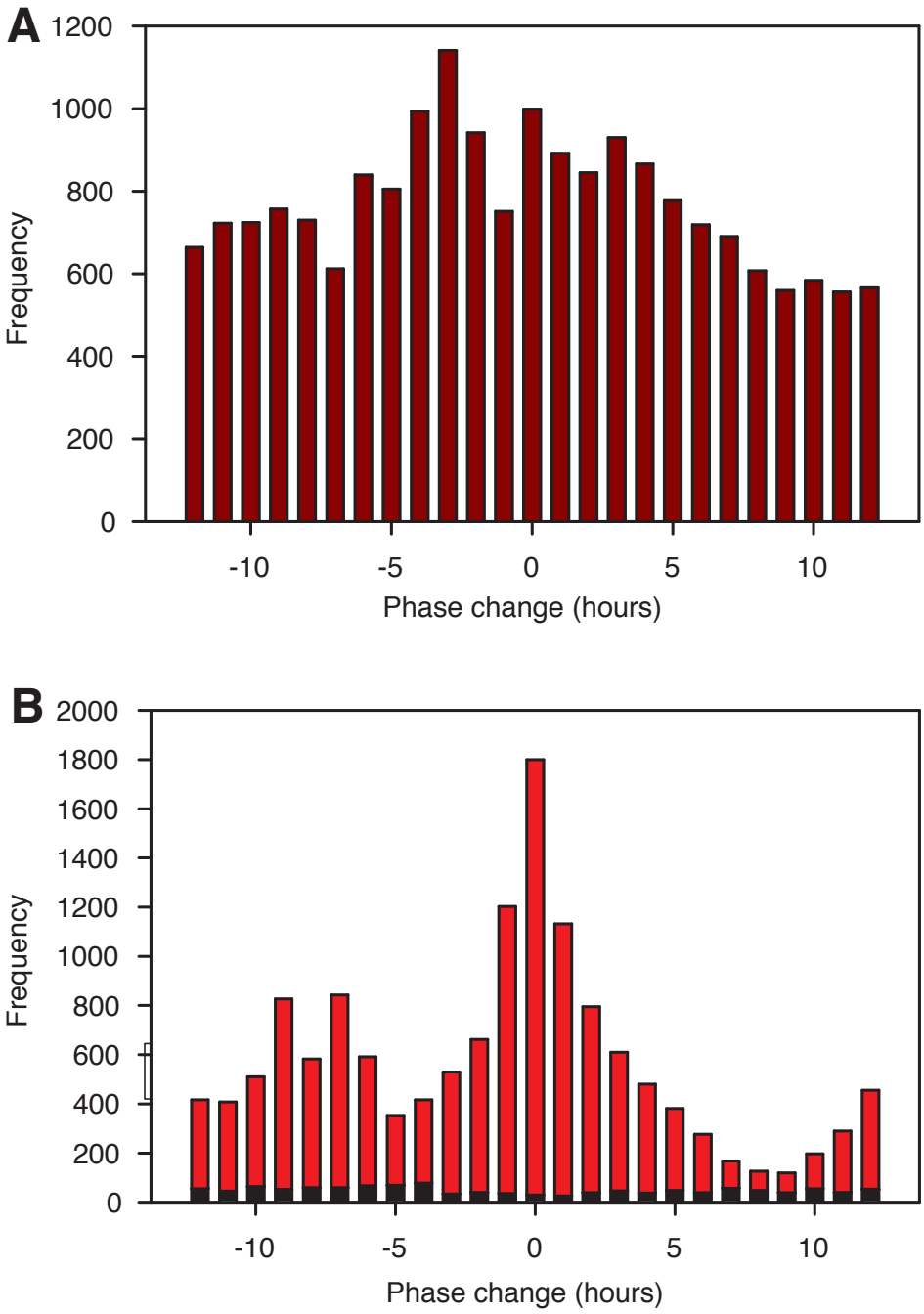

Figure 5.11: Effect of transient perturbations on oscillation phase.
Histogram plot of phase change of LL oscillations after transient perturbations (Eqn. 5.3). Equations A.1–A.13 (Interlocked) and A.14–A.29 (Three Loop) were solved numerically for 48 h of L12/D12 cycles (from $t = 0$ to $t = 48$), followed by 196 h of LL, (up to $t = 240$). Perturbation was imposed at $t = 24$, as per experimental protocol employed for data shown in Figure 5.1H. Phase change computed as $\hat{\phi} = (\hat{\tau} - \tau + \frac{T}{2}) \mod T - \frac{T}{2}$, where $\hat{\tau}, \tau$ are the times of the last peak values of simulated [*LHY* mRNA], and T the nominal period of oscillation in LL. Candidate perturbations that did not yield oscillations were removed from this analysis. Plots relate perturbations to (A) the *Interlocked Feedback Loop Model* (Locke *et al.*, 2005b) and (B) the *Three Loop Model* (Locke *et al.*, 2006). In (B), dark portions of the upright bars indicate the candidate parameter perturbations for which f_A (fold change in simulated [A mRNA] was > 2), while the whole bar represents no constraint on f_A.

10 and 40 hours were considered, as periods outside this range are not physiological and unlikely to be observed experimentally. The distribution of period of the *Interlocked Feedback Loop Model* equations in response to p_C (Eqn. 5.2) was bimodal, with means at 22 h and 15.5 h (Figure 5.12A). Approximately 77% of periods were less than the nominal period of 24.95 h. Distribution of period for candidate constant perturbations to the *Three Loop Model* were also bimodal in general (Figure 5.12B). Most perturbations for which $f_A < 2$ had periods near 20.5 h, while those with $f_A > 2$ oscillated with a period near 17.5 h. Approximately 79% of periods were less than the nominal period of 23.8 h.

Simulated constant suppression of cADPR yielded a longer period in LL (Figure 5.13). Suppression of cADPR was simulated by imposing the candidate perturbations with the reciprocal of their relative parameter value r in Eqn. 5.2. As for simulated activation of cADPR, periods between 10 and 40 h were considered that had an amplitude (*LHY* mRNA) greater than one-tenth of the unperturbed oscillation. 75% of candidate constant (reciprocal) perturbations to the Interlocked model predicted a period increase. The distribution of periods suggested an increase to around 30 h (Figure 5.13A). The period of reciprocal constant perturbations to the *Three Loop Model* was greater than the unperturbed oscillation in 91% of rhythmic trials. Periods in the range 27–29 h were most frequent (Figure 5.13B).

The cADPR-based feedback loop is sensitive to the time of simulated *XVE:ADPRc* induction

Time-dependent effects of elevated [cADPR] were evaluated for the refined method as done previously in Section 5.3.1. The shape of the distribution over the time of simulated *XVE:ADPRc* induction of candidate perturbations to the *Interlocked Feedback Loop Model* was almost identical between transient and constant perturbation profiles, and showed slight biphasism (Figures 5.14A–B). *XVE:ADPRc* induction times approaching the light to dark transition (CT13–16) comprised 59.2% of candidate transient perturbations and 57.3% (Figure 5.14A) of candidate constant perturbations (Figure 5.14B). There was also a cluster of candidate perturbations at the dark to light transition (CT23–0) comprising 6.8% of transient perturbations (Figure 5.14A) and 3.78% of constant perturbations (Figure 5.14B). The distribution over the time of simulated *XVE:ADPRc* induction of simulated candidate perturbations to the *Three Loop Model* was also bimodal, with peaks at approximately CT12 and CT19 (Figures 5.14C–D). The larger clusters at CT18–20 comprised 37.79% of the candidate set of transient perturbations

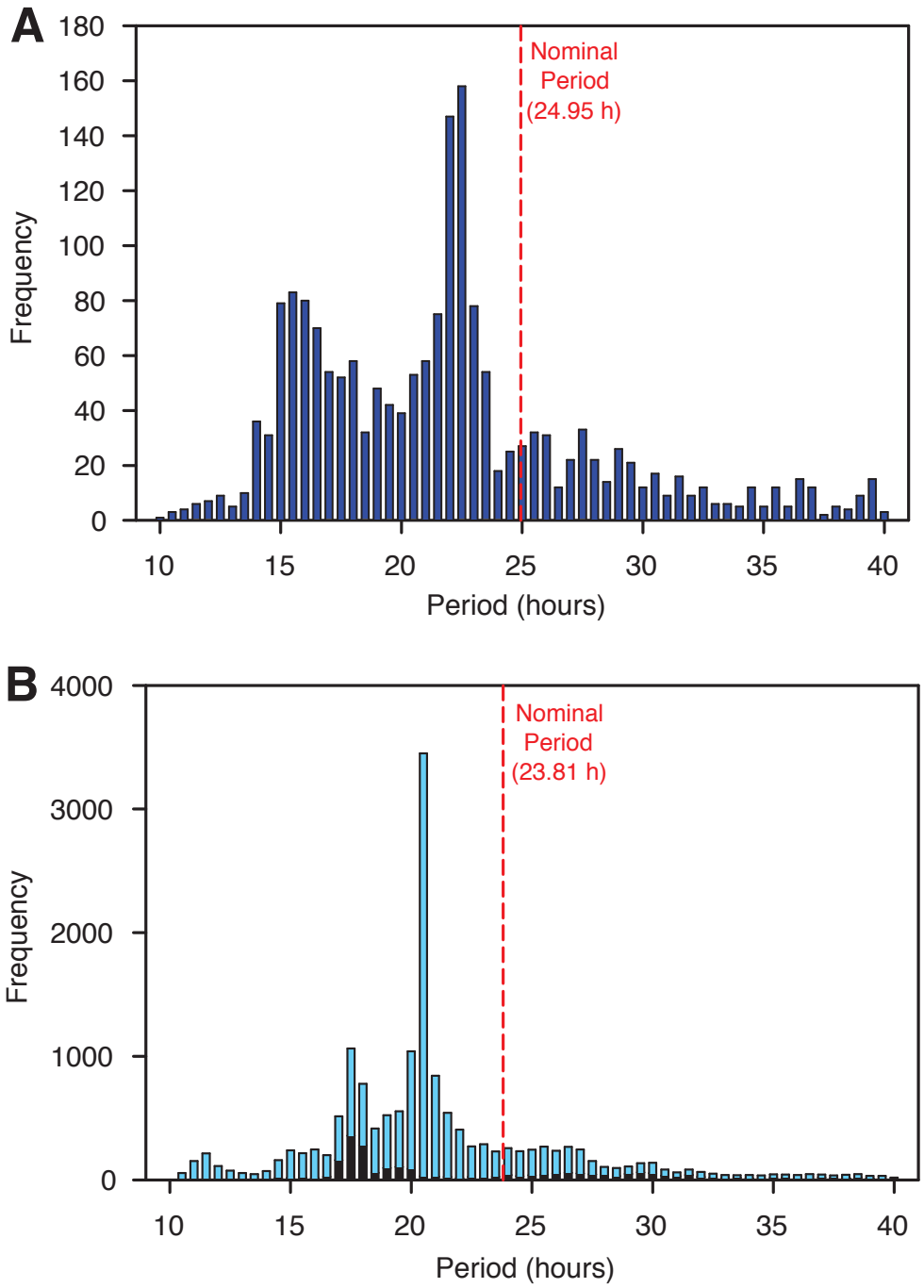

Figure 5.12: Constant perturbations yield short period oscillations in LL.
Histogram plot of the LL period after constant perturbations (Eqn. 5.2). Equations A.1–A.13 (Interlocked) and A.14–A.29 (Three Loop) were solved numerically for 2 days of diurnal (12 h light, 12 h dark) cycles $t = 0$ to $t = 48$, followed by 196 h of LL, up to $t = 240$. Perturbation was imposed at $t = 24$, as per experimental protocol employed for data shown in Figure 5.1H. Period was computed as the time difference between the last two peak values of simulated [*LHY* mRNA]. Candidate perturbations that did not yield oscillatory solutions or an amplitude at least one tenth of the wild-type were removed from this analysis. Periods outside the range [10,40] are not plotted, as they are deemed non-physiological. Plots relate perturbations to (A) the *Interlocked Feedback Loop Model* (Locke *et al.*, 2005b) and (B) the *Three Loop Model* (Locke *et al.*, 2006). In (B), dark portions of the upright bars indicate the candidate parameter perturbations for which f_A (fold change in simulated [A mRNA] was > 2), while the whole bar represents no constraint on f_A.

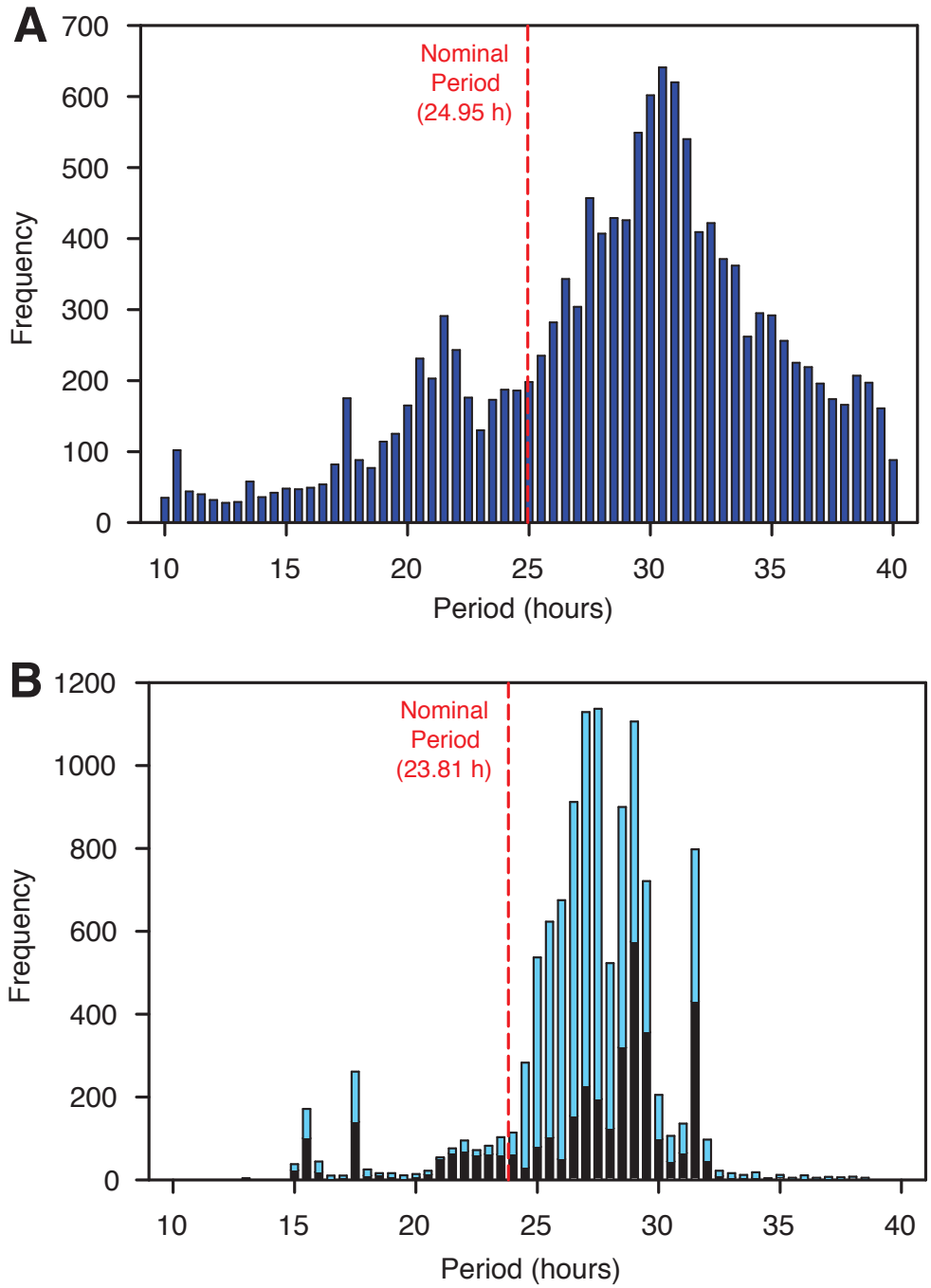

Figure 5.13: Simulated constant repression of cADPR yields a long period in LL.
Histogram plot of the LL period after constant perturbations (Eqn. 5.2) with maximal value r set to be the reciprocal of candidate values for simulated high [cADPR]. Equations A.1–A.13 (Interlocked) and A.14–A.29 (Three Loop) were solved numerically for 2 days of diurnal (12 h light, 12 h dark) cycles $t = 0$ to $t = 48$, followed by 196 h of LL, up to $t = 240$. Perturbation was imposed at $t = 24$, as per experimental protocol employed for data shown in Figure 5.1H. Period was computed as the time difference between the last two peak values of simulated [*LHY* mRNA]. Candidate perturbations that did not yield oscillatory solutions or an amplitude at least one tenth of the wild-type were removed from this analysis. Periods outside the range [10,40] are not plotted, as they are deemed non-physiological. Plots relate perturbations to (A) the *Interlocked Feedback Loop Model* (Locke *et al.*, 2005b) and (B) the *Three Loop Model* (Locke *et al.*, 2006). In (B), dark portions of the upright bars indicate the candidate parameter perturbations for which f_A (fold change in simulated [A mRNA] was > 2), while the whole bar represents no constraint on f_A.

(Figure 5.14C) and 39.13% of the candidate set of constant perturbations (Figure 5.14D) when imposing no constraint on f_A, with 57.98% of transient perturbations and 39.77% of constant perturbations for the candidate sets imposing $f_A > 2$. Candidate perturbations applied at CT11–13 comprised 21.38% of the transient set (Figure 5.14C) and 23.27% of the constant set (Figure 5.14D) when imposing no constraint on f_A, with 21.67% of transient perturbations and 30.65% constant perturbations for the candidate sets imposing $f_A > 2$.

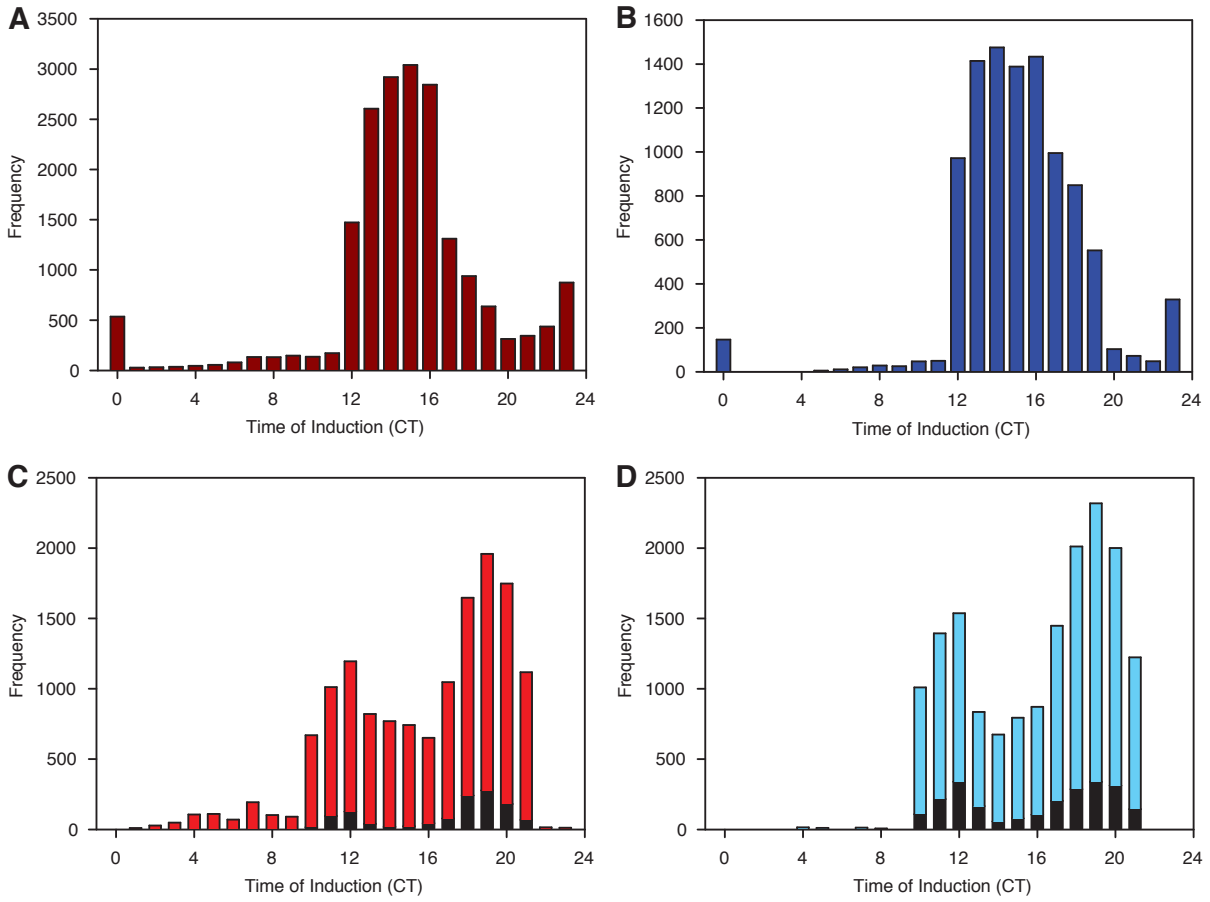

Figure 5.14: The cADPR-based feedback loop is sensitive to the time of simulated *XVE:ADPRc* induction.
Plot displays the number of random pairwise perturbations that matched the target fold changes in simulated gene expression, similar to the measured values in Sánchez *et al.* (2004). The fold change in simulated [*LHY* mRNA] (f_{LHY}) was required to be < 0.1, $0.5 < f_{TOC1} < 2$ and $f_Y > 2.5$. Perturbation profiles applied were (A,C) transient (Eqn. 5.3) or (B,D) constant (Eqn. 5.2). (A,B) Perturbations applied to the *Interlocked Feedback Loop Model* (Locke *et al.*, 2005b). (C,D) Perturbations applied to the *Three Loop Model* (Locke *et al.*, 2006), with the dark portion of the upright bars relating candidate perturbations with $f_A > 2$ (fold change in simulated [*PRR7/9* mRNA]) imposed.

Predicting oscillator gene targets of the cADPR-based feedback loop

The perturbations to the mathematical models of the *Arabidopsis* circadian clock which achieved fold changes in gene expression relative to the nominal oscillation which were equivalent to experimental observations (Sánchez *et al.*, 2004) were analysed for the identity of parameters in each candidate set. Figure 5.15 indicates the frequency at which each of the *Interlocked Feedback Loop Model* parameters were one of a candidate pair, and also with which model component the candidate parameters are associated. The most frequently represented parameter in the set of candidate transient perturbations was m_8 (maximum light-independent degradation rate of nuclear *TOC1* protein) occurring in 10.14% of the combined total of candidate parameter perturbations, followed by k_1 (michaelis constant of *LHY* mRNA degradation) comprising 6.98% and r_4 (rate of TOC1 transport out of the nucleus) comprising 6.03% of the candidate set (Figure 5.15A). On a model component level, parameters associated with *TOC1* protein were the most frequently represented in the candidate set of transient perturbations comprising 29.05% of the total set (Figure 5.15C). The set of candidate constant perturbations was more evenly distributed among the model parameters, as the most frequently occurring parameter (k_6, michaelis constant of cytoplasmic TOC1 degradation) accounted for only 5.58% of the total set (Figure 5.15B). At the model component level, parameters associated with the dynamics of *X* protein were most frequently represented in the candidate set of constant perturbations comprising 21.31% of the total set, while *TOC1* protein accounted for 17.74% of the candidate set (Figure 5.15D). The results from using multiplicative perturbations contrast with results in the previous section when additive perturbations were used (compare Figures 5.15C,D with Figure 5.6). This indicates that the predictions of cADPR targets are sensitive to the methods used in this chapter and are consequently untrustworthy.

The candidate parameter perturbations to the *Three Loop Model* were next analysed, first for the case where there is no restriction on the fold change in simulated [*PRR7/PRR9* mRNA] (f_A; indicated by the full bars in Figure 5.16). There were four parameters which accounted for more than 5% of the total set of candidate transient perturbations (g_0 – constant of *LHY* inactivation by A, m_{17} – maximum rate of cytoplasmic A protein degradation, k_1 – michaelis constant of *LHY* mRNA degradation and p_2 – rate of *TOC1* translation; Figure 5.16A). g_0, m_{17} and p_2 were also frequently represented in the candidate set of constant perturbations, in addition to c (hill exponent of *TOC1* inactivation by *LHY*; Figure 5.16B). Parameters which define the dynamics

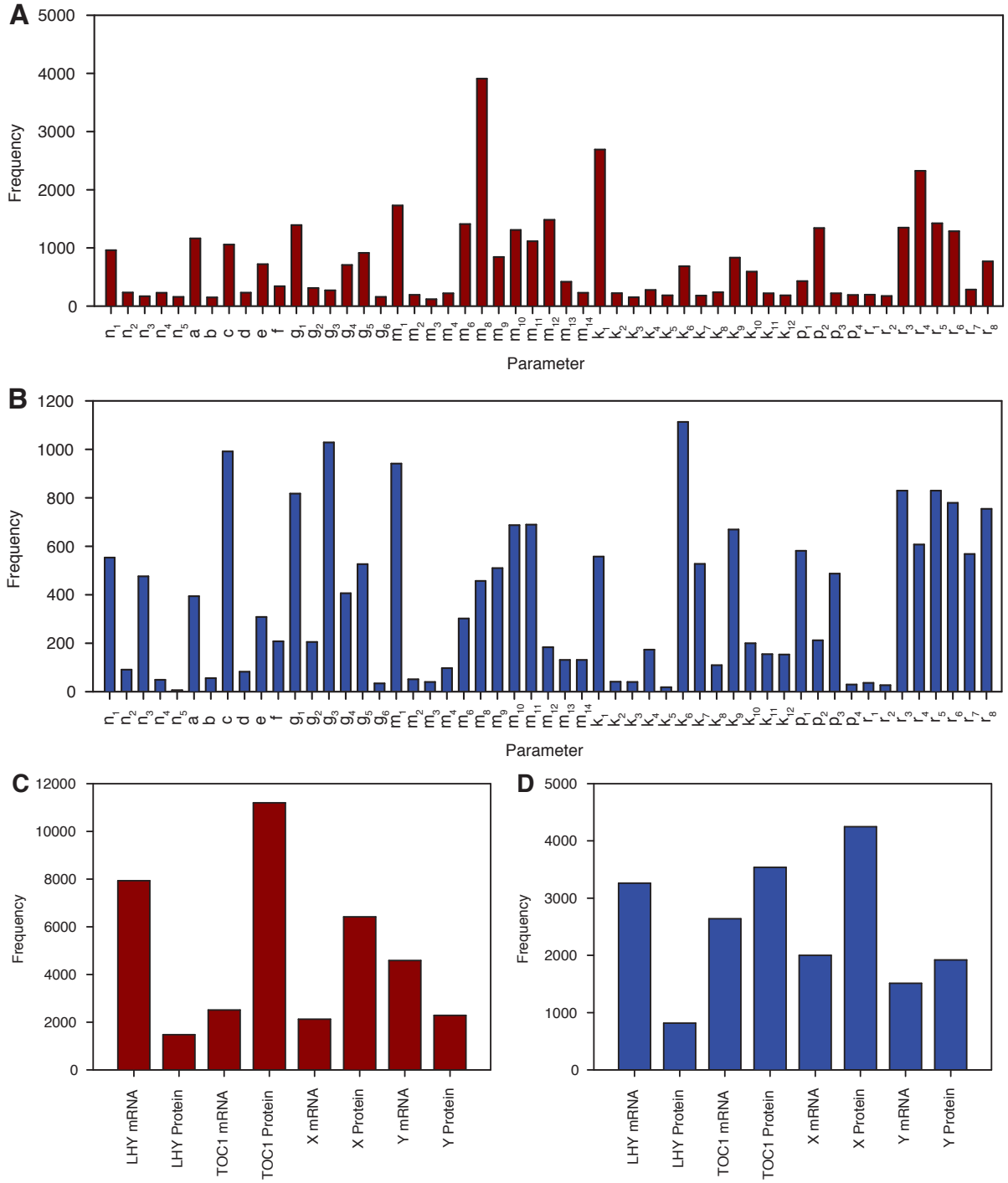

Figure 5.15: Distribution of candidate perturbations over the parameters and components of the *Interlocked Feedback Loop Model*.
Perturbations to the *Interlocked Feedback Loop Model* (Locke *et al.*, 2005b) analysed for the resulting change in gene expression 6 hours after simulated induction of ADPR cyclase. (A,C) Transient and (B,D) constant perturbations considered candidates if $f_{\mathrm{LHY}} < 0.1$, $f_{\mathrm{TOC1}} \in [0.5, 2]$ and $f_{\mathrm{Y}} > 2.5$, and remain rhythmic when simulated in LL (Figure 5.7). (A, B) Frequency of each model parameter considered candidate. (C, D) Frequency of each component mRNA or protein directly influenced by candidate parameter perturbation.

of *LHY* mRNA (23.73%) and *TOC1* protein (20.65%) were most frequently represented in the set of candidate transient perturbations (Figure 5.16C) and were also frequently represented in the set of candidate constant perturbations (*LHY* mRNA – 17.66%, *TOC1* protein – 14.91%) though *A* protein accounted for an additional 18.58% of this candidate set (Figure 5.16D).

Imposing the *PRR7/9* criterion of $f_A > 2$ leads to very different results in the parameter and component analysis for perturbations to the *Three Loop Model* (Figure 5.16). The most frequently occurring parameter in the set of candidate transient perturbations (k_{14} – michaelis constant of *A* mRNA degradation) accounted for 30.98% of the candidate set (Figure 5.16A), while parameters which define the dynamics of *A* mRNA comprise 47.02% of the candidate set (Figure 5.16C). In the candidate set of constant perturbations (imposing $f_{\mathrm{A}} > 2$), k_{14} accounts for 9.4% of the total set, while the related m_{16} (maximum rate of *A* mRNA degradation; 14.18% of total) and n_6 (maximum rate of *A* transcription; 15.81% of total) were also frequently one of a candidate pair of parameters (Figure 5.16B). Parameters which define the dynamics of *A* mRNA comprised 43.68% in the candidate set of constant perturbations (Figure 5.16D). These results indicate that direct control over *PRR7/9* mRNA is required for pairwise multiplicative parameter perturbations to yield the changes in expression of *LHY/CCA1*, *TOC1*, *GI* and *PRR7* (target fold changes include $f_{\mathrm{A}} > 2$) observed by Sánchez *et al.* (2004).

5.4 Discussion

cADPR levels were manipulated *in vivo* and *in silico* to assess how a cADPR-dependent pathway might act as a regulatory feedback loop in the *Arabidopsis* circadian clock. [cADPR] was increased *in vivo* using an *Aplysia kurodai* ADP-ribosyl cyclase fused to a 17-β-estradiol-inducible promoter (*XVE:ADP-ribosyl cyclase*; Sánchez *et al.*, 2004). [cADPR] increased continually over 20 h, to levels over 30-fold higher than in wild-type plants (Sánchez *et al.*, 2004). cADPR-regulated transcript abundance was affected more after 6 h than 20 h, suggesting that inducible over-expression of ADP-ribosyl cyclase has a transient effect on downstream gene expression. Simulations were performed to mimic potential effects of altered cADPR- and circadian-regulated transcript abundance on clock function. It was assumed that these effects could be approximated by varying model parameters in a time-dependent fashion, such that the most pronounced change occurred at 6 h (Sections 5.3.1 & 5.3.2), 16 h or 20 h (only Section 5.3.1), times which correspond to peak changes in gene expression, ADPR cyclase activity and

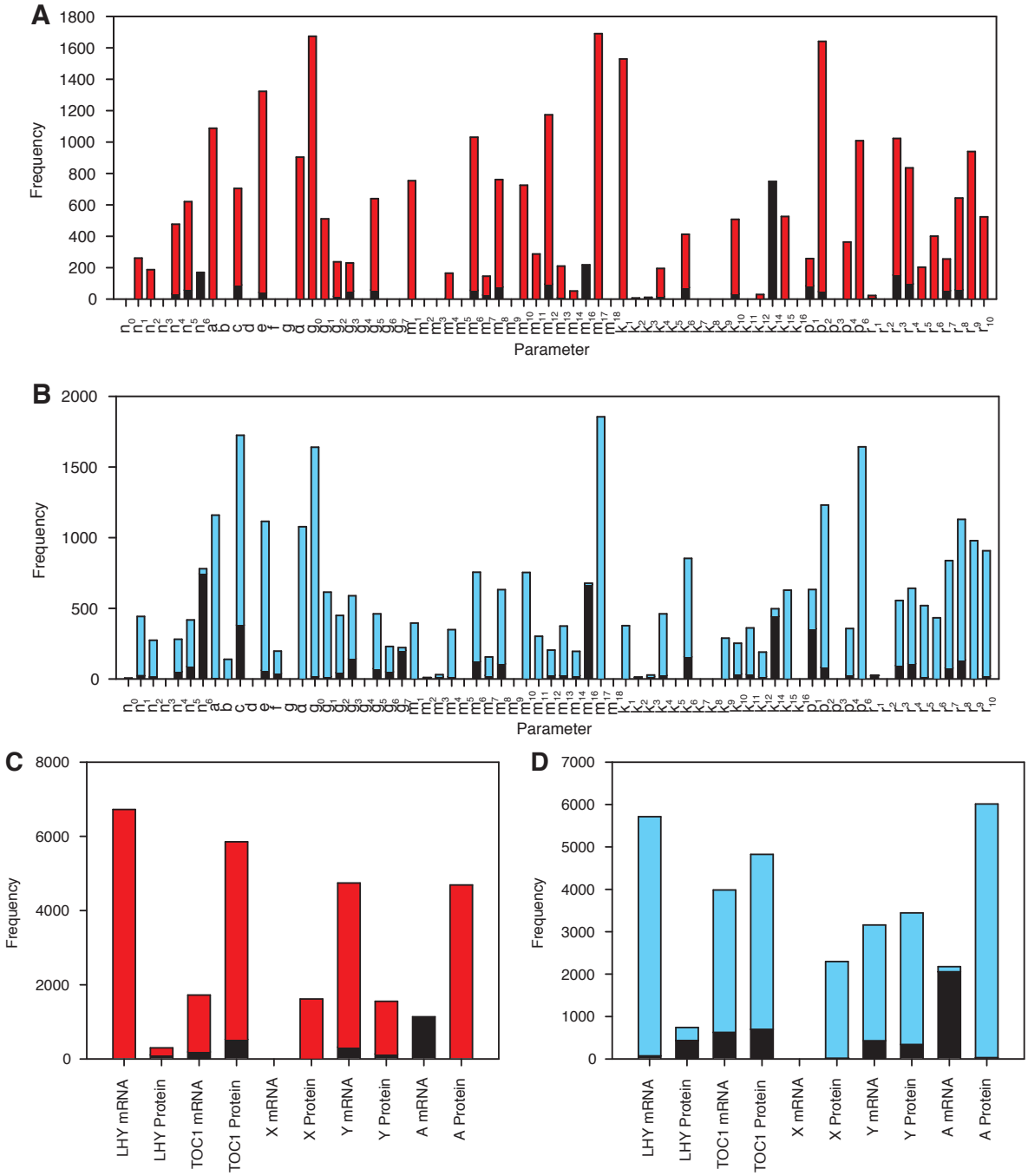

Figure 5.16: Distribution of candidate perturbations over the parameters and components of the *Three Loop Model*.
Perturbations to the *Three Loop Model* (Locke *et al.*, 2006) analysed for the resulting change in gene expression 6 hours after simulated induction of ADPR cyclase. (A,C) Transient and (B,D) constant perturbations considered candidates if $f_{\mathrm{LHY}} < 0.1$, $f_{\mathrm{TOC1}} \in [0.5, 2]$ and $f_{\mathrm{Y}} > 2.5$, and remain rhythmic when simulated in LL (Figure 5.7). Dark portions of each bar represent candidates for $f_{\mathrm{A}} > 2$, and light portions for $f_{\mathrm{A}} < 2$. (A,B) Frequency of each model parameter considered candidate. (C,D) Frequency of each component mRNA or protein directly influenced by candidate parameter perturbation.

[cADPR] respectively.

Randomly weighted two-parameter linear combinations were perturbed according to each profile, and assessed for a goodness of fit to published fold changes of gene expression (Eqn. 5.4; Figure 5.1D; Sánchez *et al.*, 2004). The restriction on the number of parameters allowed to vary represents a potential flaw of the parameter perturbation methods used in this chapter. Also, as the number of model parameters is large and the published data comprises only a single data-point, we expect a large number of perturbations to achieve a close fit. In addition, the time at which *XVE:ADPRc* is induced was not known. The high level of uncertainty might explain the inconsistencies between target predictions from the additive and multiplicative perturbation methods (Figures 5.6 and 5.15). In spite of this, simulations of transient activation, constant activation and constant suppression yielded predictions about circadian phenotypes over the set of candidate pairwise parameter perturbations. Success of pairwise perturbations was also analysed with respect to the time of simulated induction of ADPR cyclase.

Two models were used to simulate clock transcript abundance in response to inducible expression of *Aplysia* ADPR cyclase: the *Interlocked Feedback Loop Model* (Locke *et al.*, 2005b), and the *Three Loop Model* (Locke *et al.*, 2006). In Section 5.3.1, parameters were perturbed additively, ($\hat{p}(t) = p + \delta(t)$), while multiplicative perturbations ($\hat{p}(t) = p\delta(t)$) were investigated in Section 5.3.2. The results remained moderately consistent between the two models and the perturbation definition (additive or multiplicative) used to simulate clock transcript abundance. After transient perturbations (a transient increase in [cADPR]), oscillation phase was unaffected (Figures 5.8, 5.11), while constant perturbations (constantly high [cADPR]) led to a shorter circadian period (Figures 5.9, 5.12) and constant perturbations with the amplitude inverted (constantly low [cADPR]) led to a lengthening of circadian period (Figures 5.10, 5.13). Furthermore, these predictions correspond well with experimental observations after cADPR levels have been altered *in vivo*, as transient induction of *XVE:ADPRc* does not alter circadian period of phase (Figure 5.1H), and inhibition of cADPR synthesis with nicotinamide increases circadian period in LL (Figure 5.1E).

5.4.1 Transient stimulation of cADPR-regulated transcripts does not affect circadian period

The set of candidate transient (exponential profile) parameter perturbations were applied to simulations of gene expression in plants entrained to L12/D12 cycles before being transferred to LL. These simulations indicated how transient alterations in transcript abundance will not affect the free-running oscillation shape, providing that the alteration isn't so large that the state trajectory leaves the basin of attraction of the limit cycle (Figure 5.7A). Since induction of *XVE:ADPRc* does not lead to a change in the period of oscillation for leaf position, we can conclude that the change in gene expression is not large enough for loss of rhythmicity. The transient effect therefore does not affect circadian period, but there is a possibility of a phase change as a result of the excursion of the state trajectory from its nominal oscillation. By considering the range of parameter perturbations that yield the same alterations in transcript abundance of core clock components, the distribution of the resulting phase change was approximated, despite not knowing the actual cADPR targets (Figures 5.8 and 5.11). Transient perturbations which peaked after 6 hours gave distributions clearly centred around 0, though also had a considerable proportion of examples where the deviation from the nominal oscillation phase was large. Therefore, it is not possible to conclude with any certainty whether we might expect transient elevations in cADPR to alter circadian phase.

From these analyses, it was found that the central oscillator mechanism was phase robust to a large subset of transient perturbations corresponding to transient stimulation of the proposed cADPR-based feedback loop. In constant conditions (LL) the difference between the oscillation phase of the perturbed and unperturbed trajectories of the *Three Loop model* was less than approximately 1.5 h in almost 30% of candidate perturbations (Figure 5.11B). Therefore, in the face of large alterations to transcript and protein abundance, up to 24 hours in duration, the *Arabidopsis* circadian clock can maintain a steady free-running behaviour. Possessing phase robustness to transient signalling events (or any uncertainty) is a major advantage for a circadian oscillator, as varied external conditions should induce signalling pathways (such as those involving cADPR and $[Ca^{2+}]_{cyt}$) but should not affect the timing of circadian clock gene expression in general.

Robustness of oscillation properties is pervasive in circadian networks and has been observed in response to a wide range of molecular or environmental uncertainties. The autonomy

of mammalian circadian oscillators is thought to be robust to mutations in circadian clock genes as unstable oscillators are compensated for by intercellular coupling (Liu *et al.*, 2007). Mathematical analysis of 3', 5'-cyclic monophosphate (cAMP) oscillations during the *Dictyostelium discoideum* aggregation phase of starvation-induced development has also indicated that periodic robustness is enhanced by the presence of molecular noise and intercellular coupling (Kim *et al.*, 2007a). It has been suggested that robustness properties also result from a complex network of interactions. However, Rand *et al.* (2004, 2006) and Stelling *et al.* (2004) suggest that complex circadian networks offer precision and flexibility, whilst also preventing catastrophic failure such as the loss of autonomous oscillations in favour of a stable steady state. The results discussed in this section appear to offer an observation of precision. Somehow the *Arabidopsis* circadian network is able to recover from large perturbations in gene expression resulting from cytosolic signalling events involving important second messengers cADPR and Ca^{2+}, whilst also maintaining accurate phase tracking.

5.4.2 Constant activation and suppression of cADPR-regulated transcripts alters circadian period

A constant change in the rate constants of an oscillatory nonlinear system will change the free-running period in general. Due to these rate constant modifications, the state variables will undergo an alternative trajectory and converge on a new limit cycle oscillation (or a stable steady state), and so oscillation properties such as period, phase and amplitude are likely to change. Equivalent analyses to transient perturbations were performed for constant perturbations, in order to see how period might be affected given the observed changes in clock gene expression (Sánchez *et al.*, 2004). This analysis corresponds to the situation in which there is constitutive affect on cADPR-regulated genes, of similar magnitude to that observed 6 hours after *XVE:ADPRc* induction. Figure 5.9 indicated that (additive) constant parameter perturbations were able to reproduce the target fold changes in gene expression (Sánchez *et al.*, 2004) more often when imposed at ZT15 than at ZT0. In addition, the distribution of period resulting from alternative induction times showed almost opposite results, with a short period predicted for ZT0, and long period predicted for ZT15. (Multiplicative) constant parameter perturbations were applied to both models of the central oscillator considered (Figure 5.12). In this analysis, both distributions were bimodal, showing two peaks both less than the nominal period of os-

cillation. In general, the analysis presented indicates that we would expect to see a shortened period in LL following constitutive regulation downstream of cADPR.

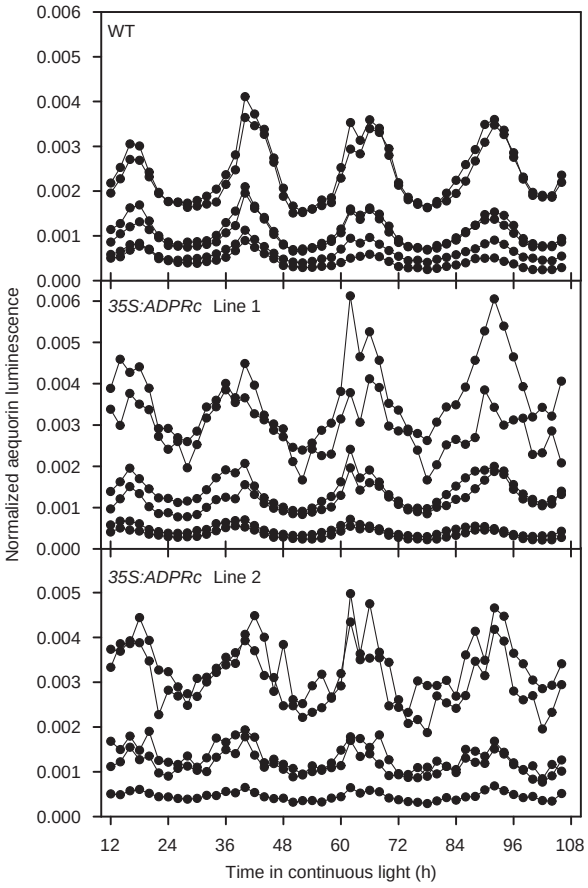

Figure 5.17: Overexpression of ADPR cyclase disrupts circadian oscillations of $[Ca^{2+}]_{cyt}$.
Overexpression of ADP ribosyl cyclase in two independent lines reduced the robustness of circadian $[Ca^{2+}]_{cyt}$oscillations relative to the wild type. Each trace is the aequorin luminescence from one cluster of 15-20 seedlings (Love *et al.*, 2004). Seedlings were previously entrained for 10 d to cycles of 12 h light and 12 h darkness. The luminescence signal was normalised to the total aequorin content of the seedling cluster to compensate for higher aequorin content in Line 2. Total aequorin was measured by discharging available aequorin using 2 M $CaCl_2$ dissolved in 20 % ethanol (Dodd *et al.*, 2006). Modified from Dodd *et al.* (2007).

Circadian rhythms were measured in *Arabidopsis* plants expressing the ADPR cyclase enzyme from *Aplysia kurodai* under the control of a constitutive Cauliflower Mosaic Virus (CaMV) 35S promoter (*35S:ADPRc*; Figure 5.17; Dodd *et al.*, 2007). Circadian oscillations of $[Ca^{2+}]_{cyt}$ appeared to have increased variability when ADPR cyclase was constitutively expressed, though they were still rhythmic, with the same period and phase of wild-type lines (Figure 5.17). One explanation for the increased variability (or loss of robustness) is that the expression of *35S:ADPRc* and/or [cADPR] may not be homogenous across different cells/cell types. Such variability would be averaged when measurements are conducted at the whole-plant level, and it is likely that the same average period and phase could be observed. An alternative ex-

planation is that increased variability results from hypersensitivity to aberrant fluctuations in the environment, as the 'gain' of the feedback loop is increased when ADPR cyclase is more abundant. Circadian oscillations in leaf position were also measured in the *35S:ADPRc* lines and showed peaks that were slightly earlier than the wild-type control, though neither the deviations in period or phase were statistically significant (Figure 5.18; Dodd *et al.*, 2007). This means that neither $[Ca^{2+}]_{cyt}$ nor leaf movement data reflect the period-shortening phenotype predicted by simulation. However, increased variability was seen in leaf position between different experiments, providing a further demonstration of the regulation of circadian clock output by a cADPR-based pathway (Figure 5.18C).

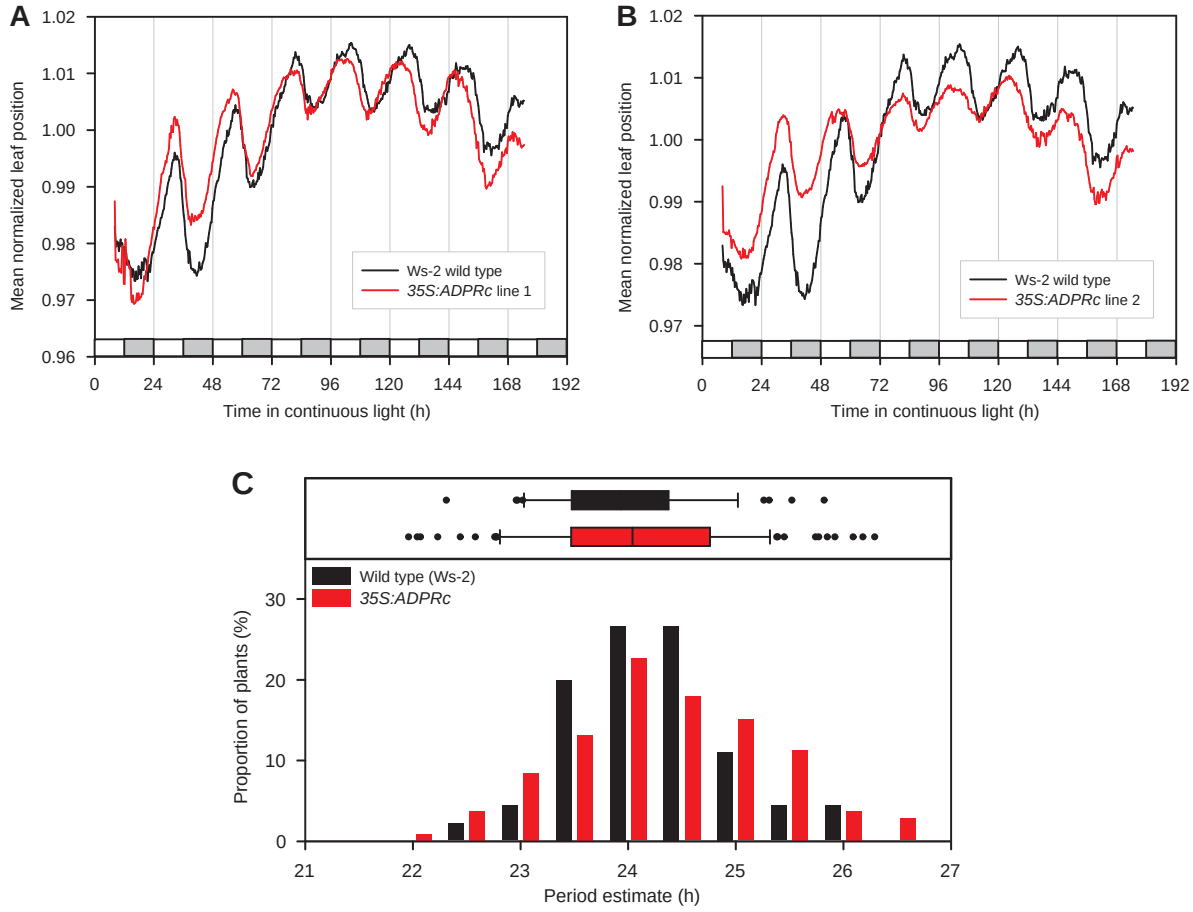

Figure 5.18: Overexpression of ADPR cyclase disrupts circadian rhythms in leaf position. Circadian rhythms of leaf position in two independently transformed lines that constitutively overexpress *Aplysia* ADPR cyclase *35S:ADPRc* (red lines/bars) compared with Ws-2 wild-type (black lines/bars). Seedlings grown for 10 days in 12 h light, 12 h dark cycles before transfer to continuous light conditions (t=0). (A,B) Traces indicate averages of experiments from each *35S:ADPRc* expressing line, with corresponding wild-type controls, n = 52-54. Bars on x-axis in indicate light during subjective daytime (white bars) and subjective night-time (hatched bars). (C) Histogram and box-plot indicates the distribution of oscillation period in individual plants from each genotype. All data collected by Katharine Hubbard, University of Cambridge, UK. Figure modified from Dodd *et al.* (2007).

The effect of suppressing the cADPR-dependent pathway was also investigated. The mag-

nitudes of each candidate parameter perturbation were inverted, and then applied again to simulations of LL after entrained L12/D12 cycles. For negated additive perturbations (Figure 5.10), the candidate set from ZT0 (cluster A) gave a circadian period which was longer than for the unperturbed oscillation (Figure 5.10A), while the set from ZT15 (cluster B) gave periodic invariance on average (Figure 5.10B). The reciprocated multiplicative perturbations (Figure 5.13) gave a more conclusive picture, showing a strong tendency towards a lengthening of circadian period in LL. This prediction agrees very well with the long period behaviour of plants treated continuously with the cADPR inhibitor nicotinamide (Figures 5.1E–G).

The simulations of constant activation/suppression of cADPR-regulated genes have been selected based on the same data for transient perturbations. In particular, the ability to reproduce the changes in gene expression resulting from a transient increase in cADPR after induction of *XVE:ADPRc*. Therefore, we have assumed that constant perturbations should behave the same as transient perturbations in the short term, a shortfall of this parameter perturbation method. It would be interesting to measure gene expression comparing wild-type with *35S:ADPRc* and untreated with nicotinamide treated, so that we can build a better model of the cADPR-dependent pathway. With such data, it would be possible to generate clear predictions of the target(s) of the pathway, which could be validated with the experimentally observed behaviours.

5.4.3 Time of induction of ADPR cyclase affects downstream response

The set of candidate perturbations were analysed for the parameters, states and induction times that were well-represented. Due to the very small quantity of data available to guide the selection process, no parameters or states were largely over-represented (Figures 5.5, 5.6, 5.15, 5.16). However, across all methods and models tested, there was a strikingly consistent distribution in the time of simulated induction of candidate perturbations. The induction time distribution resulting from the *Interlocked Feedback Loop Model* (Locke *et al.*, 2005b) had large peaks centred at ZT15 (Figures 5.4 & 5.14A,B). The equivalent analysis for the *Three Loop Model* (Locke *et al.*, 2006) showed almost all candidate perturbations to lie between ZT10 and ZT21. In all cases, inducing *XVE:ADPRc* during the night led to closer matches to the target fold changes in gene expression. This suggests that the effects of cADPR are time-specific. Interestingly, the times of candidate perturbations coincide with the times during which [cADPR] is low. It would

be interesting to investigate a variety of induction times experimentally, and to plot the corresponding phase response curve (PRC). This would enable a more stringent test of the central oscillators phase robustness to transient elevations in [cADPR].

5.4.4 Summary

Despite knowing little about how the cADPR-dependent feedback loop exerts it's effect on the central oscillator, the series of simulations presented in this chapter have agreed well with measured circadian phenotypes *in vivo*. The most important concept illustrated in this chapter is that changes in gene expression do not necessarily lead to changes in period or phase. A transient change will not lead to a change in period, provided measurements are taken sufficiently long after the transient behaviour. A phase robustness of the central oscillator has been observed where accurate phase-tracking persists after extensive perturbations. Also observed was that the constant suppression of the proposed feedback loop with nicotinamide has important consequences for the circadian control of physiology. Computer simulations have helped to explain why a variety (and sometimes an absence) of behaviours can result from a variety of system manipulations. As knowledge of the molecular mechanisms which underpin biological systems improves, computer simulations will become increasing informative. The demonstration of a cADPR-based feedback loop within the *Arabidopsis* circadian network represents a novel demonstration of the incorporation of cytosolic elements in circadian clocks.

CHAPTER 6

General Discussion

The aim of this thesis was to build mathematical models of the interactions between the circadian clock and physiological input/output pathways in *Arabidopsis*, to test hypotheses proposed from prior experimental work and increase functional understanding at a systems level. Resting levels of $[Ca^{2+}]_{cyt}$ appear to be regulated by both circadian clock dependent and distinct light-dependent pathways (Xu *et al.*, 2007). A strong logical derivation of simple mathematical models revealed that these pathways are necessary to describe existing experimental observations *in silico*, though operate on different timescales and dominate $[Ca^{2+}]_{cyt}$ regulation at different frequencies (Chapter 2). $[Ca^{2+}]_{cyt}$ might mediate a proposed cADPR-based feedback loop with the central oscillator, as treating plants with the cADPR inhibitor nicotinamide abolishes circadian oscillations of $[Ca^{2+}]_{cyt}$ in LL (Dodd *et al.*, 2007). A random pairwise parameter perturbation method was used to demonstrate that transient elevations in [cADPR] can lead to large changes in central oscillator transcript abundance without affecting free-running period, while constant suppression of a cADPR-based loop increases circadian period (Chapter 5; Dodd *et al.*, 2007). The observation that circadian $[Ca^{2+}]_{cyt}$ oscillations in LL are also abolished in plants grown in the presence of exogenous sucrose (Johnson *et al.*, 1995) motivated investigation of the effect of exogenous sucrose on the circadian clock. In constant dark, oscillations of *CCA1* and *TOC1* expression were absent when exogenous sucrose was not supplemented to the growth media (see Figure 3.1). The results of Chapter 3 suggested that *GI* transcription

is up-regulated by sucrose, with the *N5 model* defined as a correction to the *Three Loop Model* (Locke *et al.*, 2006) to account for an absence of exogenous sucrose by reducing the rate of *GI* transcription. Also, the necessity of a functional *GI* in conferring sucrose-responsiveness was demonstrated by measuring sucrose-dependent DD oscillations of *CAB2* expression in wild-type and *gi*-11 loss of function mutants. The mechanism through which sucrose modulates *GI* expression was explored in Chapter 4, with evidence for transcriptional regulation presented. However, dark-induced GI proteolysis was also shown to be a candidate target of sucrose with the rate of GI degradation being correlated with simulated sucrose availability *in silico*, suggesting *GI* may be controlled at both transcriptional and post-translational levels (Chapter 4). These results form a basis for a systems approach to understanding a complex network of interactions between the central oscillator, the light signalling network, carbohydrate metabolism and Ca^{2+}-based cytosolic signalling.

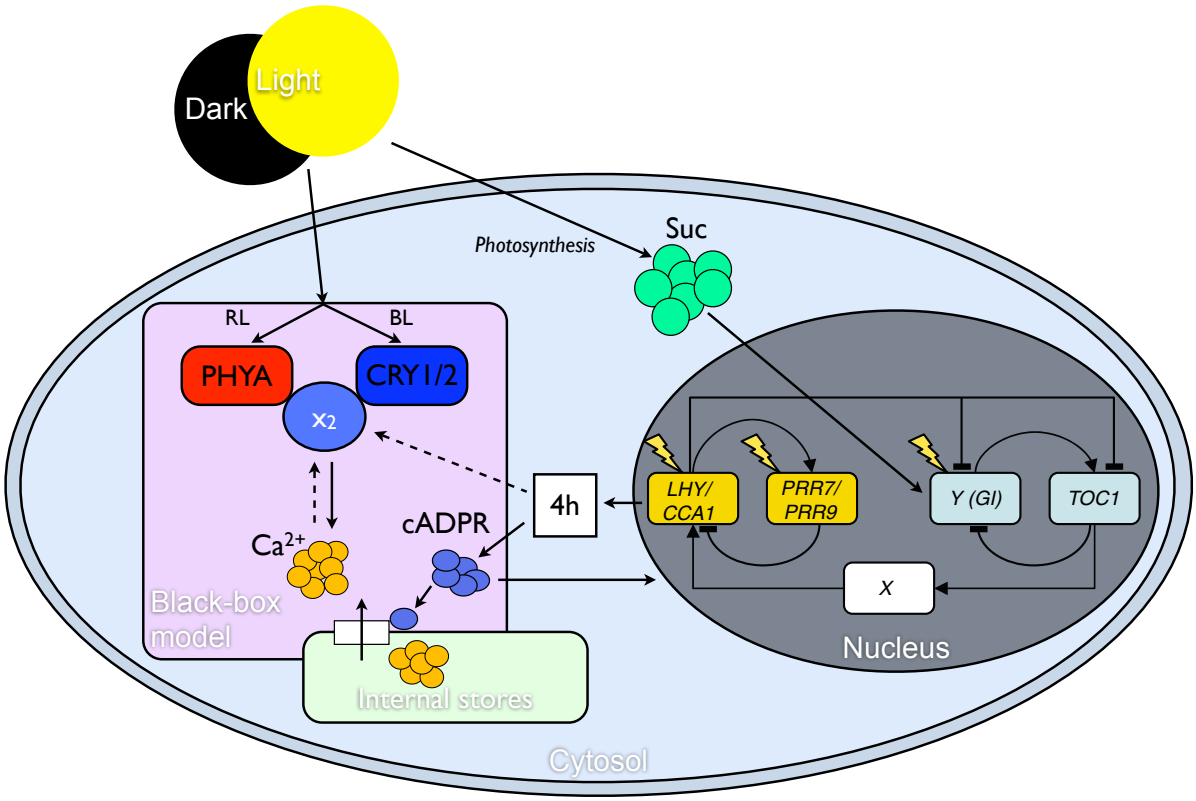

Figure 6.1: *Arabidopsis* circadian clock network as demonstrated through mathematical modelling. Diagram depicting the major findings presented in this Thesis. $[Ca^{2+}]_{cyt}$ is regulated by a *CCA1*-dependent pathway of duration 4 h and a light/dark-dependent pathway with no delay (Chapter 2). A hidden state (*X*2) is also required for model accuracy and represents biochemical components including PHYA. cADPR is an important component in the circadian clock-$[Ca^{2+}]_{cyt}$ network, acting as a mediator of the *CCA1*-dependent pathway and forming a feedback loop with the central oscillator (Chapter 5). Finally, sucrose regulates the central oscillator via changes in *GI* expression (Chapter 3). *GI* is regulated at the transcriptional or possibly also at the post-translational level (Chapter 4).

6.1 Linear systems identification reveals properties of the dual regulation of $[Ca^{2+}]_{cyt}$ by the circadian central oscillator and light

Systems identification theory provides a powerful tool for estimation of dynamical models from input-output data alone (Ljung, 1999). The basic theory enables direct estimation of discrete-time linear systems, with unknown system components or delays being accounted for by hidden variables. With a suitable transformation, the discrete-time formulation can be converted to a continuous-time linear system. The provision of hidden variables in systems identification methods enabled the derivation of a surprisingly accurate linear systems representation of the regulation of $[Ca^{2+}]_{cyt}$ by the circadian clock and an independent light/dark input pathway (Chapter 2). Predictive capability was ensured through a strong logical model derivation, as estimation was conducted from only a single input-output dataset, leaving all remaining data for cross-validation. In this way, model properties which could not be estimated directly with PEM such as the values of delay parameters used to represent the uncharacterised input pathways (τ_{CCA1} and τ_{light}) and the optimal number of state variables n could be assessed. In particular, it was found that *CCA1*-dependent modulation of $[Ca^{2+}]_{cyt}$ occurs after a lag of 3–4 h while changes in the availability of light are transduced within an hour. As the number of hidden variables was increased, model performance with respect to the estimation data improved and sensitivity to τ_{CCA1} decreased indicating that beyond $n = 2$ (optimal after cross-validation), additional state variables were accounting for the delay between *CCA1* expression and changes in $[Ca^{2+}]_{cyt}$. The second, necessary state variable (termed $X2$) may therefore represent one or a number of other components/factors, such as a biochemical component not explicitly defined in the model that is regulated by the circadian clock, light/dark availability, or both. e.g. cADPR, PHY, CRY (Figure 6.1). An approximation to an essential nonlinearity, such as an interaction in the input pathways, or a density-dependent change in $[Ca^{2+}]_{cyt}$ may also be represented by $X2$.

A drawback of LTI state-space systems is the loss of structural information between state variables when there is at least one hidden state, as can be seen by applying a similarity transformation T which preserves the measured state variables and redefines hidden variables as arbitrary linear combinations of all state variables. A further consequence of the degrees of freedom in LTI state-space models is that the dynamics of hidden variables are not fixed. However,

a family of simulations was presented in (Section 2.3.6) which represents the possible input-output behaviour when the hidden component is dysfunctional (set constant). Comparison of the simulated dynamics with measurements of $[Ca^{2+}]_{cyt}$ in a range of mutant *Arabidopsis* lines enabled identification of PHYA to be a candidate component for $X2$, despite non-uniqueness of the simulated dynamics. When taken together with the findings of Xu *et al.* (see Figure 1.3; 2007), the biological interpretation of these results is that $X2$ represents the signal transduction of the red-light sensing PHYs and the blue-light sensing CRYs to $[Ca^{2+}]_{cyt}$ and may also incorporate circadian signals. Additionally, $X2$ and $[Ca^{2+}]_{cyt}$ may form a feedback loop, suggesting that at least one of the components represented by $X2$ is itself regulated by $[Ca^{2+}]_{cyt}$ (see Figure 6.1 for an overview of these conclusions). It remains unclear at which point the two input pathways converge with respect to cADPR, which may be accounted for by τ_{CCA1}, or $X2$. Measurement of AEQUORIN luminescence from plants treated with 50 mM nicotinamide and placed in light-dark cycles may elucidate whether cADPR mediates the light/dark regulation of $[Ca^{2+}]_{cyt}$, as nicotinamide suppresses cADPR-mediated $[Ca^{2+}]_{cyt}$ oscillations in LL (Dodd *et al.*, 2007).

6.2 Demonstration of a cADPR-dependent feedback loop in the circadian clock network by a pairwise parameter perturbation method

A simplistic view of circadian clock architecture is a three-stage system comprising input pathways, a central oscillator mechanism and output pathways (Dunlap, 1999). Transcriptome analyses have demonstrated a ubiquitous cellular regulation by circadian clocks in *Arabidopsis*, quoting values of 5–95% of transcripts undergoing rhythmic control (Harmer *et al.*, 2000; Edwards *et al.*, 2006; Covington & Harmer, 2007; Covington *et al.*, 2008). Several physiological outputs of the circadian clock have been well characterised at a component level, such as the photoperiodic control of flowering time, in which *FT* undergoes a photoperiod-dependent regulation by the coincidence of *CO* expression and light (Suárez-López *et al.*, 2001). The notion of a return integration of physiological signals into circadian clock gene expression is now emerging in chronobiology as cytosolic feedback loops have been proposed in plants and mammals which are associated with $[Ca^{2+}]_{cyt}$ (Chapter 5; Dodd *et al.*, 2007; O'Neill *et al.*, 2008; Hastings

et al., 2008). There is a clear benefit for circadian clocks to respond to signalling pathways, incorporating environmental information that may enable frequency of amplitude modulation of the circadian rhythm. Using pairwise parameter perturbations in a mathematical model of the *Arabidopsis* circadian clock, we showed that manipulating levels of the Ca^{2+}-mobilising cADPR *in vivo* may lead to a variety of behaviours in circadian clock function (Chapter 5; Dodd *et al.*, 2007). In particular, transient manipulations to the proposed cADPR-based loop leads to large changes in clock gene expression (Sánchez *et al.*, 2004) without affecting circadian period or phase of $[Ca^{2+}]_{cyt}$ or leaf movements (Dodd *et al.*, 2007). However, sustained changes can affect circadian period, demonstrating further that cADPR regulates the central oscillator mechanism. These results indicate that the central oscillator mechanism can incorporate cytosolic messages, while achieving some degree of period and phase robustness to these same signals. A similar cytosolic loop has been demonstrated in SCN neurons, in which a cAMP/Ca^{2+}-dependent loop interacts with the transcriptional/post-translational oscillator network (O'Neill *et al.*, 2008).

6.2.1 Does $[Ca^{2+}]_{cyt}$ mediate circadian clock regulation by cADPR?

A functional significance for the circadian regulation of basal $[Ca^{2+}]_{cyt}$ has not been established, as few downstream elements have been identified. However, recent work conducted in the Webb laboratory has found that a putative Ca^{2+}-reponsive *cis* element mediates Ca^{2+}-induced *LHY* expression (Dr. M. J. Gardner unpublished). The ABA-responsive element (ABRE; CACGTG[T/C/G]) was identified as a Ca^{2+}-sensor while probing transcriptional responses to changes in $[Ca^{2+}]_{cyt}$ resulting from treatment with CaM antagonists and Ca^{2+} channel blockers (Kaplan *et al.*, 2006). It was also shown in this study that a tetramer of ABRE elements is sufficient to confer transcriptional activation in response to Ca^{2+} transients (Kaplan *et al.*, 2006). *LHY* transcriptional activation in response to Ca^{2+} transients was reduced in transgenic *Arabidopsis* with a 110 bp deletion in the *LHY* promoter which spans the location of ABRE elements in the *LHY* sequence, providing evidence that the ABRE confers Ca^{2+}-responsiveness in *LHY*. ABRE elements are also found in the promoters of circadian clock genes *CCA1*, *PRR7*, *PRR9* and *LUX*, though not in the promoters of *TOC1*, *GI*, *PRR5*, *ZTL*, *ELF3* or *ELF4*. Therefore, the proposed cADPR-Ca^{2+} pathway may feed back into multiple points of the central oscillator network, and is seemingly more associated with the *CCA1/LHY-PRR7/9* morning loop. The hypothesis that a cADPR-associated pathway targets the morning loop of the *Arabidopsis*

clock agrees with the prediction from Chapter 5 when considering perturbations which approximately matched the target changes in gene expression of all model components. i.e. The *PRR7/9* component must be increased following transient cADPR increases in addition to the reduction in *CCA1/LHY*, the increase in *Y/GI* and invariance of *TOC1*. A large proportion of these perturbations suggested *PRR7/9* mRNA to be the most likely point of entry for the proposed cADPR-based loop (see Figure 5.16).

An experimental study conducted concurrently with this research identified the putative Ca^{2+}-sensors CML23 and CML24 as potential mediators of cADPR feedback to the central oscillator (Hubbard, 2008). A *cml23*-2 *cml24*-4 double mutant was found to have a circadian period approximately 2 h longer than wild-type. However, when treated with 50 mM nicotinamide, the period phenotype of the *cml23*-2 *cml24*-4 double mutant could not be seen with respect to nicotinamide-treated wild-type plants, both of which had approximately 28 h circadian periods. These results suggest that CML23 and CML24 belong to the same feedback loop as, and act downstream of, cADPR, though they do not confer the total extent of central oscillator Ca^{2+}-responsiveness. A compelling hypothesis suggested by these results is that a cADPR–Ca^{2+}–CML23/24 pathway induces morning oscillator gene expression via an interaction with the ABRE promoter element (Figure 6.2).

The ABRE and CML23/24 studies provide a basis for the construction of a mathematical model of the *Arabidopsis* circadian clock network incorporating the proposed cytosolic feedback loop. Such a model could be used to further investigate the central oscillator's period and phase robustness to Ca^{2+} transients. Also, using a similar strategy to that used by Locke *et al.* (2005b), it may be possible to incorporate hypothetical components to represent unknown pathway intermediates in the network, then infer properties which may be used to predict their identities*. For example, in Figure 2 a delay of 3–4 h was used to represent an unknown pathway connecting *CCA1* expression and a resulting increase in $[Ca^{2+}]_{cyt}$. This delay could be replaced by hypothetical genes according to the mRNA–cytoplasmic protein–nuclear protein formalism employed by Locke *et al.* (2006; see Eqns. A.14–A.29). In this way, it may be possible to predict properties of genes encoding ADPR cyclase enzymes, as no homologs of mammalian ADPR cyclases have been found in *Arabidopsis* thus far. Hypothetical components may also be

*In deriving the *Interlocked Feedback Loop* model, J. C. Locke and colleagues defined hypothetical components *X* and *Y* to provide a network capable of reproducing experimental observations (Locke *et al.*, 2005b). They went on to demonstrate that the dynamics of *Y* showed a biphasic oscillation similar to that seen for the expression of *GI*. Further experimental testing revealed that *GI* may contribute 70–100% of the component *Y* (Locke *et al.*, 2006).

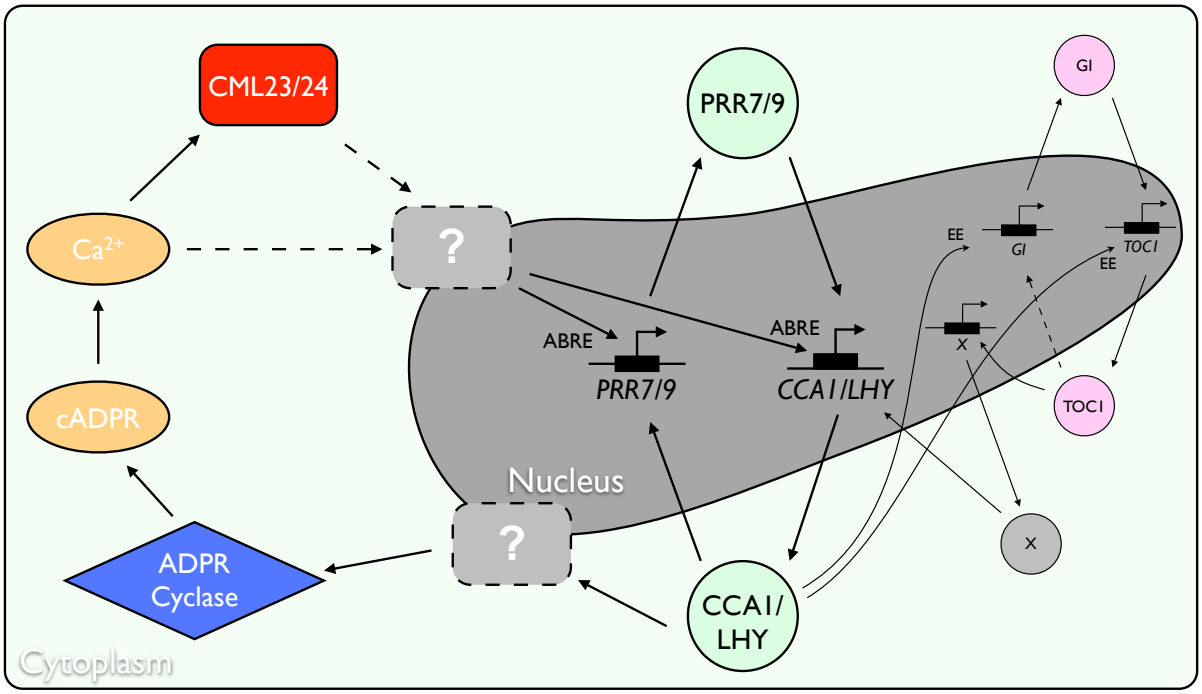

Figure 6.2: The *Arabidopsis* circadian clock may incorporate a cADPR–Ca^{2+}–CML23/24 cytosolic loop. Diagram shown describes the *Three Loop Model* of the central oscillator (Locke *et al.*, 2006), with an additional feedback loop involving an assumed ADPR cyclase enzyme, cADPR, Ca^{2+}, and CML23/24, as proposed by Hubbard (2008). Black symbols in the nucleus (shaded region) represent mRNA, while in the cytoplasm are proteins (circles), enzymes (diamonds), small molecules (ellipses) and unknown biochemical components (dashed outline rectangles). Unknown components are placed overlapping the nucleus and cytoplasm, as their location is unknown. Arrows may indicate activation or inactivation, while dashed arrows represent possible interactions which have not been demonstrated experimentally.

incorporated into candidate models to test hypotheses concerning the network of interactions which precede ABRE-mediated transcriptional control downstream of cADPR. In particular, do CML23 and/or CML24 mediate the Ca^{2+}-responsiveness of ABRE or regulate the central oscillator through an alternative mechanism? Also, to what extent are additional unknown components responsible for cADPR-feedback to the central oscillator?

6.3 Possible roles for sucrose up-regulation of *GI*

In Chapters 3 & 4, it was investigated how in constant darkness the availability of exogenous sucrose was required for *Arabidopsis* seedlings to exhibit stable oscillations in the expression of central oscillator genes *CCA1* and *TOC1* (see Figure 3.1). A relationship between sucrose and the transcriptional activation of *Y* (*GI*) was shown to be accountable for experimental observations *in silico*, and was also demonstrated *in vivo*. It was also demonstrated that a post-translational GI mechanism may confer additional or all sucrose-sensing in the circadian clock

network, though experimental work is still ongoing (Chapter 4). An appealing hypothesis is that sucrose-sensing is integrated to central oscillator function via a pathway mediated by *SFR6*, as *sfr6* mutants have reduced expression of *TOC1* and *GI* in the presence of sucrose relative to wild-type *Arabidopsis* (Knight *et al.*, 2008). In this publication, the authors speculate a role for *GI* in sucrose-sensing and observe that a reduction in model parameters corresponding to *GI* expression can account in part for the dynamics of *sfr6* plants. However, they do not consider gene expression in DD, which may provide more distinguishable observations, as was seen in this thesis.

As investigations into sucrose-sensing by the circadian clock are in their infancy, there have been few suggestions for a physiological role of such a pathway connecting sucrose to the central oscillator. A simple proposal is that the circadian clock may adapt timing or amplitude in response to the current metabolic state at the cellular level, in order to optimise the starch:sucrose balance. It is known that starch degradation enzymes are under the control of the circadian clock in *Arabidopsis* (Lu *et al.*, 2005), indicating that there is feedback between the central oscillator and the carbohydrate metabolic network. Is it possible that this feedback loop is capable of generating oscillations? This possibility provides an explanation for the observable circadian oscillations of *GI:luc* in DD in the absence of exogenous sucrose (Figure 3.1E), as a sucrose/starch–clock feedback loop may generate approximately circadian oscillations. If true, this further suggests that sucrose and starch content may continue to oscillate in DD when seedlings are not exposed to exogenous sucrose. Furthermore, this may represent an early mechanism for the optimisation of photosynthetic output, which precedes the development of a transcriptional oscillator in photosynthetic organisms.

Sucrose accumulates during photosynthesis and therefore may act as a proxy for a light signal. In Chapter 4, it was demonstrated that sucrose is a *zeitgeber* for *GI* which confers stable oscillations in many, if not all, circadian regulated processes (see Figure 4.6). As light is an important *zeitgeber* in circadian systems, sucrose may provide environmental cues for cells which do not perceive light. i.e. root tissue. It has recently been shown that a circadian clock functions in root tissue, which is a slave version of the known network in aerial tissue[†] (James *et al.*, 2008). The root clock differs functionally from the clock in shoots, as there is no EE inhibition

[†]The majority of circadian research is conducted using *luciferase* imaging and gene expression data from whole plants. As aerial tissue comprises a significant proportion of developing *Arabidopsis* seedlings, we may attribute the known biochemical interactions to a large subset of aerial tissue types.

by CCA1/LHY heterodimers, and critically depends on a sucrose-related signal for synchronization to the shoot clock, as addition of sucrose disrupts circadian oscillations in roots. As *GI* is transcriptionally regulated by sucrose, *GI* may also mediate shoot–root synchronization of circadian oscillations by sucrose. If so, then *gi*-11 null mutants may show impaired oscillations or arrhythmicity in LD cycles, depending on the extent to which *GI* mediates the sucrose signal. This provides an alternative physiological role of sucrose input to the central oscillator, though it is likely that both are important.

6.4 A Light–Carbohydrate–Circadian Clock model

Mathematical modelling could be used to further understand the functional relationship between sugar metabolism and the circadian clock. Based on the results of Chapter 3, the rate of *GI* transcription is positively correlated with $[\text{Suc}]_i$ (see Section 3.3.3). Functional understanding could be increased by constructing a mathematical model of carbohydrate metabolism subject to light availability (as an input). It may then be possible to couple this model with the *N5 model* (or a refined model of the *Arabidopsis* clock in the absence of exogenous sucrose) to predict functional forms of *GI* transcriptional activation by sucrose. It may also be possible to test the hypothesis that SFR6 mediates the sucrose-based connection between these two subsystems. Further subsystems may then be connected, such as a model of red- and blue-light photoreception via PHY and CRY and/or the cADPR–Ca^{2+}–CML23/24 cytosolic loop proposed by Hubbard (2008).

6.5 Conclusions

The results of this thesis have demonstrated how the *Arabidopsis* circadian clock network responds to signalling and metabolic pathways, and suggests mechanisms through which these responses are perceived. Mathematical methods have been shown to elucidate biological function at the molecular level when the complete interaction network is unknown. Importantly, the molecular mechanisms uncovered by this thesis have important consequences at the cellular and organismal levels, many of which have been demonstrated experimentally. The results of this thesis demonstrate why there is a growing interplay between mathematical and experimental methods for investigating biological systems.

CHAPTER 7

Bibliography

Akaike, H. (1974). A new look at the statistical model selection. *IEEE Trans. Automatic Control*, **19**, 716–723.

Al-Sady, B., Ni, W., Kircher, S., Schäfer, E. & Quail, P.H. (2006). Photoactivated phytochrome induces rapid PIF3 phosphorylation prior to proteasome-mediated degradation. *Mol Cell*, **23**, 439–446.

Alabadí, D., Oyama, T., Yanovsky, M.J., Harmon, F.G., Más, P. & Kay, S.A. (2001). Reciprocal regulation between *TOC1* and *LHY/CCA1* within the *Arabidopsis* circadian clock. *Science*, **293**, 880–883.

Alabadí, D., Yanovsky, M.J., Más, P., Harmer, S.L. & Kay, S.A. (2002). Critical role for CCA1 and LHY in maintaining circadian rhythmicity in *Arabidopsis*. *Curr Biol*, **12**, 757–761.

Allen, G.J., Muir, S.R. & Sanders, D. (1995). Release of Ca^{2+} from individual plant vacuoles by both $InsP_3$ and cyclic ADP-ribose. *Science*, **268**, 735–737.

Allen, G.J., Kwak, J.M., Chu, S.P., Llopis, J., Tsien, R.Y., Harper, J.F. & Schroeder, J.I. (1999). Cameleon calcium indicator reports cytoplasmic calcium dynamics in *Arabidopsis* guard cells. *Plant J*, **19**, 735–747.

Allen, G.J., Chu, S.P., Harrington, C.L., Schumacher, K., Hoffmann, T., Tang, Y.Y., Grill, E. &

Schroeder, J.I. (2001). A defined range of guard cell calcium oscillation parameters encodes stomatal movements. *Nature*, **411**, 1053–1057.

Apkarian, A.V., Darbar, A., Krauss, B.R., Gelnar, P.A. & Szeverenyi, N.M. (1999). Differentiating cortical areas related to pain perception from stimulus identification: temporal analysis of fMRI activity. *J Neurophysiol*, **81**, 2956–2963.

Aton, S.J., Colwell, C.S., Harmar, A.J., Waschek, J. & Herzog, E.D. (2005). Vasoactive intestinal polypeptide mediates circadian rhythmicity and synchrony in mammalian clock neurons. *Nat Neurosci*, **8**, 476–483.

Barratt, D.H., Barber, L., Kruger, N.J., Smith, A.M., Wang, T.L. & Martin, C. (2001). Multiple, distinct isoforms of sucrose synthase in pea. *Plant Physiol*, **127**, 655–664.

Bartness, T.J., Song, C.K. & Demas, G.E. (2001). SCN efferents to peripheral tissues: implications for biological rhythms. *J Biol Rhythms*, **16**, 196–204.

Baud, S., Vaultier, M.N. & Rochat, C. (2004). Structure and expression profile of the sucrose synthase multigene family in *Arabidopsis*. *J Exp Bot*, **55**, 397–409.

Baum, G., Long, J.C., Jenkins, G.I. & Trewavas, A.J. (1999). Stimulation of the blue light phototropic receptor NPH1 causes a transient increase in cytosolic Ca^{2+}. *Proc Natl Acad Sci U S A*, **96**, 13554–13559.

Berridge, M.J., Bootman, M.D. & Roderick, H.L. (2003). Calcium signalling: dynamics, homeostasis and remodelling. *Nat Rev Mol Cell Biol*, **4**, 517–529.

Bezprozvanny, I., Watras, J. & Ehrlich, B.E. (1991). Bell-shaped calcium-response curves of Ins(1,4,5)P_3- and calcium-gated channels from endoplasmic reticulum of cerebellum. *Nature*, **351**, 751–754.

Bläsing, O.E., Gibon, Y., Günther, M., Höhne, M., Morcuende, R., Osuna, D., Thimm, O., Usadel, B., Scheible, W.R. & Stitt, M. (2005). Sugars and circadian regulation make major contributions to the global regulation of diurnal gene expression in *Arabidopsis*. *Plant Cell*, **17**, 3257–3281.

Bognár, L.K., Hall, A., Adám, E., Thain, S.C., Nagy, F. & Millar, A.J. (1999). The circadian clock

controls the expression pattern of the circadian input photoreceptor, phytochrome B. *Proc Natl Acad Sci U S A*, **96**, 14652–14657.

Boss, P.K., Bastow, R.M., Mylne, J.S. & Dean, C. (2004). Multiple pathways in the decision to flower: enabling, promoting, and resetting. *Plant Cell*, **16 Suppl**, S18–S31.

Bowler, C., Neuhaus, G., Yamagata, H. & Chua, N.H. (1994). Cyclic GMP and calcium mediate phytochrome phototransduction. *Cell*, **77**, 73–81.

Buchanan, B., Gruissem, W. & Jones, R. (2002). *Biochemistry & Molecular Biology of Plants*. Wiley, 1st edn.

Canty, N., O'Mahony, T., O'Connor, B. & Kelly, P. (2006). Comparison of direct and indirect continuous-time system identification methods on a pasteurisation process. In *Irish Signals and Systems Conference, 2006. IET*, 427–432.

Chen, C. (1998). *Linear System Theory and Design: Theory and Design*. Oxford University Press.

Chen, M., Chory, J. & Fankhauser, C. (2004). Light signal transduction in higher plants. *Annu Rev Genet*, **38**, 87–117.

Clapper, D.L., Walseth, T.F., Dargie, P.J. & Lee, H.C. (1987). Pyridine nucleotide metabolites stimulate calcium release from sea urchin egg microsomes desensitized to inositol trisphosphate. *J Biol Chem*, **262**, 9561–9568.

Covington, M.F. & Harmer, S.L. (2007). The circadian clock regulates auxin signaling and responses in *Arabidopsis*. *PLoS Biol*, **5**, e222.

Covington, M.F., Panda, S., Liu, X.L., Strayer, C.A., Wagner, D.R. & Kay, S.A. (2001). ELF3 modulates resetting of the circadian clock in *Arabidopsis*. *Plant Cell*, **13**, 1305–1315.

Covington, M.F., Maloof, J.N., Straume, M., Kay, S.A. & Harmer, S.L. (2008). Global transcriptome analysis reveals circadian regulation of key pathways in plant growth and development. *Genome Biol*, **9**, R130.

Daniel, X., Sugano, S. & Tobin, E.M. (2004). CK2 phosphorylation of CCA1 is necessary for its circadian oscillator function in *Arabidopsis*. *Proc Natl Acad Sci U S A*, **101**, 3292–3297.

David, K.M., Armbruster, U., Tama, N. & Putterill, J. (2006). *Arabidopsis* GIGANTEA protein is post-transcriptionally regulated by light and dark. *FEBS Lett*, **580**, 1193–1197.

De Young, G.W. & Keizer, J. (1992). A single-pool inositol 1,4,5-trisphosphate-receptor-based model for agonist-stimulated oscillations in Ca^{2+} concentration. *Proc Natl Acad Sci U S A*, **89**, 9895–9899.

Deshaies, R.J. (1999). SCF and Cullin/Ring H2-based ubiquitin ligases. *Annu Rev Cell Dev Biol*, **15**, 435–467.

Devlin, P.F. (2002). Signs of the time: environmental input to the circadian clock. *J Exp Bot*, **53**, 1535–1550.

Devlin, P.F. & Kay, S.A. (2000). Cryptochromes are required for phytochrome signaling to the circadian clock but not for rhythmicity. *Plant Cell*, **12**, 2499–2510.

Dijkwel, P.P., Huijser, C., Weisbeek, P.J., Chua, N.H. & Smeekens, S.C. (1997). Sucrose control of phytochrome A signaling in *Arabidopsis*. *Plant Cell*, **9**, 583–595.

Ding, Z., Millar, A.J., Davis, A.M. & Davis, S.J. (2007). *TIME FOR COFFEE* encodes a nuclear regulator in the *Arabidopsis* circadian clock. *Plant Cell*, **19**, 1522–1536.

Dodd, A.N., Love, J. & Webb, A.A.R. (2005a). The plant clock shows its metal: circadian regulation of cytosolic free Ca^{2+}. *Trends Plant Sci*, **10**, 15–21.

Dodd, A.N., Salathia, N., Hall, A., Kévei, E., Tóth, R., Nagy, F., Hibberd, J.M., Millar, A.J. & Webb, A.A.R. (2005b). Plant circadian clocks increase photosynthesis, growth, survival, and competitive advantage. *Science*, **309**, 630–633.

Dodd, A.N., Jakobsen, M.K., Baker, A.J., Telzerow, A., Hou, S.W., Laplaze, L., Barrot, L., Poethig, R.S., Haseloff, J. & Webb, A.A.R. (2006). Time of day modulates low-temperature Ca signals in *Arabidopsis*. *Plant J*, **48**, 962–973.

Dodd, A.N., Gardner, M.J., Hotta, C.T., Hubbard, K.E., Dalchau, N., Love, J., Assie, J.M., Robertson, F.C., Jakobsen, M.K., Gonçalves, J., Sanders, D. & Webb, A.A.R. (2007). The *Arabidopsis* circadian clock incorporates a cADPR-based feedback loop. *Science*, **318**, 1789–1792.

Dowson-Day, M.J. & Millar, A.J. (1999). Circadian dysfunction causes aberrant hypocotyl elongation patterns in *Arabidopsis*. *Plant J*, **17**, 63–71.

Doyle, M.R., Davis, S.J., Bastow, R.M., McWatters, H.G., Kozma-Bognár, L., Nagy, F., Millar, A.J. & Amasino, R.M. (2002). The *ELF4* gene controls circadian rhythms and flowering time in *Arabidopsis thaliana*. *Nature*, **419**, 74–77.

Dunlap, J.C. (1999). Molecular bases for circadian clocks. *Cell*, **96**, 271–290.

Edwards, K.D., Lynn, J.R., Gyula, P., Nagy, F. & Millar, A.J. (2005). Natural allelic variation in the temperature-compensation mechanisms of the *Arabidopsis thaliana* circadian clock. *Genetics*, **170**, 387–400.

Edwards, K.D., Anderson, P.E., Hall, A., Salathia, N.S., Locke, J.C.W., Lynn, J.R., Straume, M., Smith, J.Q. & Millar, A.J. (2006). FLOWERING LOCUS C mediates natural variation in the high-temperature response of the *Arabidopsis* circadian clock. *Plant Cell*, **18**, 639–650.

Endo, M., Tanaka, M. & Ogawa, Y. (1970). Calcium induced release of calcium from the sarcoplasmic reticulum of skinned skeletal muscle fibres. *Nature*, **228**, 34–36.

Falcke, M. (2003). On the role of stochastic channel behavior in intracellular Ca^{2+} dynamics. *Biophys J*, **84**, 42–56.

Farré, E.M., Harmer, S.L., Harmon, F.G., Yanovsky, M.J. & Kay, S.A. (2005). Overlapping and distinct roles of PRR7 and PRR9 in the *Arabidopsis* circadian clock. *Curr Biol*, **15**, 47–54.

Forger, D.B. & Peskin, C.S. (2003). A detailed predictive model of the mammalian circadian clock. *Proc Natl Acad Sci U S A*, **100**, 14806–14811.

Fowler, S., Lee, K., Onouchi, H., Samach, A., Richardson, K., Morris, B., Coupland, G. & Putterill, J. (1999). *GIGANTEA*: a circadian clock-controlled gene that regulates photoperiodic flowering in *Arabidopsis* and encodes a protein with several possible membrane-spanning domains. *EMBO J*, **18**, 4679–4688.

Franklin, K.A. & Whitelam, G.C. (2005). Phytochromes and shade-avoidance responses in plants. *Ann Bot (Lond)*, **96**, 169–175.

Franklin, K.A., Larner, V.S. & Whitelam, G.C. (2005). The signal transducing photoreceptors of plants. *Int J Dev Biol*, **49**, 653–664.

Friel, D.D. (1995). $[Ca^{2+}]_i$ oscillations in sympathetic neurons: an experimental test of a theoretical model. *Biophys J*, **68**, 1752–1766.

Galione, A., Lee, H.C. & Busa, W.B. (1991). Ca^{2+}-induced Ca^{2+} release in sea urchin egg homogenates: modulation by cyclic ADP-ribose. *Science*, **253**, 1143–1146.

Gardner, M.J., Hubbard, K.E., Hotta, C.T., Dodd, A.N. & Webb, A.A.R. (2006). How plants tell the time. *Biochem J*, **397**, 15–24.

Garnier, H. & Mensler, M. (2000). The CONTSID toolbox: a matlab toolbox for continuous-time system identification. In *12th IFAC Symposium on System Identification*, 851–856.

Goldbeter, A. (1995). A model for circadian oscillations in the *Drosophila* period protein (PER). *Proc Biol Sci*, **261**, 319–324.

Goldbeter, A., Dupont, G. & Berridge, M.J. (1990). Minimal model for signal-induced Ca^{2+} oscillations and for their frequency encoding through protein phosphorylation. *Proc Natl Acad Sci U S A*, **87**, 1461–1465.

Gonçalves, J. & Yi, T.M. (2004). Drosophila circadian rhythms: Stability robustness analysis and model reduction. In *Symposium on Mathematical Theory of Networks and Systems*, Leuven, Belgium.

Gorton, H.L., Williams, W.E. & Assmann, S.M. (1993). Circadian rhythms in stomatal responsiveness to red and blue light. *Plant Physiol*, **103**, 399–406.

Gould, P.D., Locke, J.C.W., Larue, C., Southern, M.M., Davis, S.J., Hanano, S., Moyle, R., Milich, R., Putterill, J., Millar, A.J. & Hall, A. (2006). The molecular basis of temperature compensation in the *Arabidopsis* circadian clock. *Plant Cell*, **18**, 1177–1187.

Green, R.M. & Tobin, E.M. (1999). Loss of the circadian clock-associated protein 1 in *Arabidopsis* results in altered clock-regulated gene expression. *Proc Natl Acad Sci U S A*, **96**, 4176–4179.

Hall, A., Kozma-Bognár, L., Tóth, R., Nagy, F. & Millar, A.J. (2001). Conditional circadian regulation of *PHYTOCHROME A* gene expression. *Plant Physiol*, **127**, 1808–1818.

Hall, A., Bastow, R.M., Davis, S.J., Hanano, S., McWatters, H.G., Hibberd, V., Doyle, M.R., Sung, S., Halliday, K.J., Amasino, R.M. & Millar, A.J. (2003). The *TIME FOR COFFEE* gene maintains the amplitude and timing of *Arabidopsis* circadian clocks. *Plant Cell*, **15**, 2719–2729.

Harada, A. & Shimazaki, K. (2007). Phototropins and blue light-dependent calcium signaling in higher plants. *Photochem Photobiol*, **83**, 102–111.

Harada, A., Sakai, T. & Okada, K. (2003). phot1 and phot2 mediate blue light-induced transient increases in cytosolic Ca^{2+} differently in *Arabidopsis* leaves. *Proc Natl Acad Sci U S A*, **100**, 8583–8588.

Harmer, S.L. & Kay, S.A. (2005). Positive and negative factors confer phase-specific circadian regulation of transcription in arabidopsis. *Plant Cell*, **17**, 1926–1940.

Harmer, S.L., Hogenesch, J.B., Straume, M., Chang, H.S., Han, B., Zhu, T., Wang, X., Kreps, J.A. & Kay, S.A. (2000). Orchestrated transcription of key pathways in *Arabidopsis* by the circadian clock. *Science*, **290**, 2110–2113.

Harmon, F., Imaizumi, T. & Gray, W.M. (2008). CUL1 regulates TOC1 protein stability in the *Arabidopsis* circadian clock. *Plant J*, **55**, 568–579.

Harrisingh, M.C. & Nitabach, M.N. (2008). Circadian rhythms. integrating circadian timekeeping with cellular physiology. *Science*, **320**, 879–880.

Harrisingh, M.C., Wu, Y., Lnenicka, G.A. & Nitabach, M.N. (2007). Intracellular Ca^{2+} regulates free-running circadian clock oscillation *in vivo*. *J Neurosci*, **27**, 12489–12499.

Hastings, M.H., Maywood, E.S. & O'Neill, J.S. (2008). Cellular circadian pacemaking and the role of cytosolic rhythms. *Curr Biol*, **18**, R805–R815.

Hazen, S.P., Schultz, T.F., Pruneda-Paz, J.L., Borevitz, J.O., Ecker, J.R. & Kay, S.A. (2005). *LUX ARRHYTHMO* encodes a Myb domain protein essential for circadian rhythms. *Proc Natl Acad Sci U S A*, **102**, 10387–10392.

Heintzen, C., Nater, M., Apel, K. & Staiger, D. (1997). AtGRP7, a nuclear RNA-binding protein as a component of a circadian-regulated negative feedback loop in *Arabidopsis thaliana*. *Proc Natl Acad Sci U S A*, **94**, 8515–8520.

Herz, A.V., Bonhoeffer, S., Anderson, R.M., May, R.M. & Nowak, M.A. (1996). Viral dynamics *in vivo*: limitations on estimates of intracellular delay and virus decay. *Proc Natl Acad Sci U S A*, **93**, 7247–7251.

Hetherington, A.M. & Brownlee, C. (2004). The generation of Ca^{2+} signals in plants. *Annu Rev Plant Biol*, **55**, 401–427.

Higashida, H., Hashii, M., Yokoyama, S., Hoshi, N., Chen, X.L., Egorova, A., Noda, M. & Zhang, J.S. (2001). Cyclic ADP-ribose as a second messenger revisited from a new aspect of signal transduction from receptors to ADP-ribosyl cyclase. *Pharmacol Ther*, **90**, 283–296.

Hotta, C.T. (2007). *Positioning Ca^{2+} within the circadian signalling networks*. Ph.D. thesis, University of Cambridge.

Hotta, C.T., Gardner, M.J., Hubbard, K.E., Baek, S.J., Dalchau, N., Suhita, D., Dodd, A.N. & Webb, A.A.R. (2007). Modulation of environmental responses of plants by circadian clocks. *Plant Cell Environ*, **30**, 333–349.

Hubbard, K. (2008). *Identification of Calcium Signalling Elements in the* Arabidopsis *Circadian Network*. Ph.D. thesis, University of Cambridge.

Hudson, M.E. & Quail, P.H. (2003). Identification of promoter motifs involved in the network of phytochrome A-regulated gene expression by combined analysis of genomic sequence and microarray data. *Plant Physiol*, **133**, 1605–1616.

Hunt, L., Otterhag, L., Lee, J.C., Lasheen, T., Hunt, J., Seki, M., Shinozaki, K., Sommarin, M., Gilmour, D.J., Pical, C. & Gray, J.E. (2004). Gene-specific expression and calcium activation of *Arabidopsis thaliana* phospholipase C isoforms. *New Phytologist*, **162**, 643–654.

Huq, E., Tepperman, J.M. & Quail, P.H. (2000). GIGANTEA is a nuclear protein involved in phytochrome signaling in *Arabidopsis*. *Proc Natl Acad Sci U S A*, **97**, 9789–9794.

Hurvich, C.M. & Tsai, C.L. (1989). Regression and time series model selection in small samples. *Biometrika*, **76**, 297–307.

Ikeda, M., Sugiyama, T., Wallace, C.S., Gompf, H.S., Yoshioka, T., Miyawaki, A. & Allen, C.N. (2003). Circadian dynamics of cytosolic and nuclear Ca^{2+} in single suprachiasmatic nucleus neurons. *Neuron*, **38**, 253–263.

Imaizumi, T. & Kay, S.A. (2006). Photoperiodic control of flowering: not only by coincidence. *Trends Plant Sci*, **11**, 550–558.

Imaizumi, T., Tran, H.G., Swartz, T.E., Briggs, W.R. & Kay, S.A. (2003). FKF1 is essential for photoperiodic-specific light signalling in *Arabidopsis*. *Nature*, **426**, 302–306.

Imaizumi, T., Kay, S.A. & Schroeder, J.I. (2007). Circadian rhythms. daily watch on metabolism. *Science*, **318**, 1730–1731.

Ingalls, B.P. (2004). Autonomously oscillating biochemical systems: parametric sensitivity of extrema and period. *Syst Biol (Stevenage)*, **1**, 62–70.

Ingalls, B.P. & Sauro, H.M. (2003). Sensitivity analysis of stoichiometric networks: an extension of metabolic control analysis to non-steady state trajectories. *J Theor Biol*, **222**, 23–36.

James, A.B., Monreal, J.A., Nimmo, G.A., Kelly, C.L., Herzyk, P., Jenkins, G.I. & Nimmo, H.G. (2008). The circadian clock in arabidopsis roots is a simplified slave version of the clock in shoots. *Science*, **322**, 1832–1835.

Johnson, C.H., Knight, M.R., Kondo, T., Masson, P., Sedbrook, J., Haley, A. & Trewavas, A. (1995). Circadian oscillations of cytosolic and chloroplastic free calcium in plants. *Science*, **269**, 1863–1865.

Jones, T.L. & Ort, D.R. (1997). Circadian regulation of sucrose phosphate synthase activity in tomato by protein phosphatase activity. *Plant Physiol*, **113**, 1167–1175.

Kaplan, B., Davydov, O., Knight, H., Galon, Y., Knight, M.R., Fluhr, R. & Fromm, H. (2006). Rapid transcriptome changes induced by cytosolic Ca^{2+} transients reveal ABRE-related sequences as Ca^{2+}-responsive cis elements in *Arabidopsis*. *Plant Cell*, **18**, 2733–2748.

Kay, S.A. & Millar, A.J. (1992). *The Molecular Genetics of Biological Rhythms*, chap. 4. Circadian-Regulated *cab* Gene Transcription in Higher Plants, 73–89. Dekker, New York.

Keener, J. & Sneyd, J. (2001). *Mathematical Physiology*. Springer, 1st edn.

Khalil, H.K. (2002). *Nonlinear Systems*. Prentice Hall.

Kikis, E.A., Khanna, R. & Quail, P.H. (2005). ELF4 is a phytochrome-regulated component of a negative-feedback loop involving the central oscillator components CCA1 and LHY. *Plant J*, **44**, 300–313.

Kim, J., Heslop-Harrison, P., Postlethwaite, I. & Bates, D.G. (2007a). Stochastic noise and synchronisation during dictyostelium aggregation make camp oscillations robust. *PLoS Comput Biol*, **3**, e218.

Kim, J., Bates, D.G., Postlethwaite, I., Heslop-Harrison, P. & Cho, K.H. (2008a). Linear time-varying models can reveal non-linear interactions of biomolecular regulatory networks using multiple time-series data. *Bioinformatics*, **24**, 1286–1292.

Kim, J., Kim, Y., Yeom, M., Kim, J.H. & Nam, H.G. (2008b). FIONA1 is essential for regulating period length in the *Arabidopsis* circadian clock. *Plant Cell*, **20**, 307–319.

Kim, J.Y., Song, H.R., Taylor, B.L. & Carré, I.A. (2003). Light-regulated translation mediates gated induction of the *Arabidopsis* clock protein LHY. *EMBO J*, **22**, 935–944.

Kim, W.Y., Fujiwara, S., Suh, S.S., Kim, J., Kim, Y., Han, L., David, K., Putterill, J., Nam, H.G. & Somers, D.E. (2007b). ZEITLUPE is a circadian photoreceptor stabilized by GIGANTEA in blue light. *Nature*, **449**, 356–360.

Kirkpatrick, S., Gelatt, C.D. & Vecchi, M.P. (1983). Optimization by simulated annealing. *Science*, **220**, 671–680.

Knight, H., Trewavas, A.J. & Knight, M.R. (1996). Cold calcium signaling in *Arabidopsis* involves two cellular pools and a change in calcium signature after acclimation. *Plant Cell*, **8**, 489–503.

Knight, H., Trewavas, A.J. & Knight, M.R. (1997). Calcium signalling in *Arabidopsis thaliana* responding to drought and salinity. *Plant J*, **12**, 1067–1078.

Knight, H., Thomson, A.J.W. & McWatters, H.G. (2008). SENSITIVE TO FREEZING 6 (SFR6) integrates cellular and environmental inputs to the plant circadian clock. *Plant Physiol*.

Kurepa, J., Smalle, J., Montagu, M.V. & Inzé, D. (1998). Effects of sucrose supply on growth and paraquat tolerance of the late-flowering *gi*-3 mutant. *Plant Growth Regulation*, **26**, 91–96.

Laub, A. (1981). Efficient multivariable frequency response computations. *Automatic Control, IEEE Transactions on*, **26**, 407–408.

Leckie, C.P., McAinsh, M.R., Allen, G.J., Sanders, D. & Hetherington, A.M. (1998). Abscisic acid-induced stomatal closure mediated by cyclic ADP-ribose. *Proc Natl Acad Sci U S A*, **95**, 15837–15842.

Lee, H.C. (1997). Mechanisms of calcium signaling by cyclic ADP-ribose and NAADP. *Physiol Rev*, **77**, 1133–1164.

Lee, H.C. & Aarhus, R. (1991). ADP-ribosyl cyclase: an enzyme that cyclizes NAD^+ into a calcium-mobilizing metabolite. *Cell Regul*, **2**, 203–209.

Lee, H.C. & Aarhus, R. (1993). Wide distribution of an enzyme that catalyzes the hydrolysis of cyclic ADP-ribose. *Biochim Biophys Acta*, **1164**, 68–74.

Lee, H.C., Walseth, T.F., Bratt, G.T., Hayes, R.N. & Clapper, D.L. (1989). Structural determination of a cyclic metabolite of NAD^+ with intracellular Ca^{2+}-mobilizing activity. *J Biol Chem*, **264**, 1608–1615.

Leloup, J.C. & Goldbeter, A. (2003). Toward a detailed computational model for the mammalian circadian clock. *Proc Natl Acad Sci U S A*, **100**, 7051–7056.

Leloup, J.C., Gonze, D. & Goldbeter, A. (1999). Limit cycle models for circadian rhythms based on transcriptional regulation in *Drosophila* and *Neurospora*. *J Biol Rhythms*, **14**, 433–448.

Li, Q.H. & Yang, H.Q. (2007). Cryptochrome signaling in plants. *Photochem Photobiol*, **83**, 94–101.

Lidder, P., Gutiérrez, R.A., Salomé, P.A., McClung, C.R. & Green, P.J. (2005). Circadian control of messenger RNA stability. association with a sequence-specific messenger RNA decay pathway. *Plant Physiol*, **138**, 2374–2385.

Liu, A.C., Welsh, D.K., Ko, C.H., Tran, H.G., Zhang, E.E., Priest, A.A., Buhr, E.D., Singer, O., Meeker, K., Verma, I.M., Doyle, F.J., Takahashi, J.S. & Kay, S.A. (2007). Intercellular coupling confers robustness against mutations in the SCN circadian clock network. *Cell*, **129**, 605–616.

Liu, X.L., Covington, M.F., Fankhauser, C., Chory, J. & Wagner, D.R. (2001). ELF3 encodes a circadian clock-regulated nuclear protein that functions in an *Arabidopsis* PHYB signal transduction pathway. *Plant Cell*, **13**, 1293–1304.

Ljung, L. (1999). *Systems Identification: Theory for the User*. Prentice Hall.

Locke, J.C.W., Millar, A.J. & Turner, M.S. (2005a). Modelling genetic networks with noisy and varied experimental data: the circadian clock in *Arabidopsis thaliana*. *J Theor Biol*, **234**, 383–393.

Locke, J.C.W., Southern, M.M., Kozma-Bognár, L., Hibberd, V., Brown, P.E., Turner, M.S. & Millar, A.J. (2005b). Extension of a genetic network model by iterative experimentation and mathematical analysis. *Mol Syst Biol*, **1**, 2005.0013.

Locke, J.C.W., Kozma-Bognár, L., Gould, P.D., Fehér, B., Kevei, E., Nagy, F., Turner, M.S., Hall, A. & Millar, A.J. (2006). Experimental validation of a predicted feedback loop in the multi-oscillator clock of *Arabidopsis thaliana*. *Mol Syst Biol*, **2**, 59.

Love, J., Dodd, A.N. & Webb, A.A.R. (2004). Circadian and diurnal calcium oscillations encode photoperiodic information in *Arabidopsis*. *Plant Cell*, **16**, 956–966.

Lu, Y., Gehan, J.P. & Sharkey, T.D. (2005). Daylength and circadian effects on starch degradation and maltose metabolism. *Plant Physiol*, **138**, 2280–2291.

Lunn, J.E. & MacRae, E. (2003). New complexities in the synthesis of sucrose. *Curr Opin Plant Biol*, **6**, 208–214.

Lunn, J.E., Ashton, A.R., Hatch, M.D. & Heldt, H.W. (2000). Purification, molecular cloning, and sequence analysis of sucrose-6F-phosphate phosphohydrolase from plants. *Proc Natl Acad Sci U S A*, **97**, 12914–12919.

Macqueen, J. (1967). Some methods of classification and analysis of multivariate observations. In *Proceedings of the Fifth Berkeley Symposium on Mathematical Statistics and Probability*, 281–297.

MacRobbie, E.A. (2000). ABA activates multiple Ca^{2+} fluxes in stomatal guard cells, triggering vacuolar $K^{+}(Rb^{+})$ release. *Proc Natl Acad Sci U S A*, **97**, 12361–12368.

Martínez-García, J.F., Huq, E. & Quail, P.H. (2000). Direct targeting of light signals to a promoter element-bound transcription factor. *Science*, **288**, 859–863.

McClung, C.R. (2001). Circadian rhythms in plants. *Annu Rev Plant Physiol Plant Mol Biol*, **52**, 139–162.

McWatters, H.G., Bastow, R.M., Hall, A. & Millar, A.J. (2000). The *ELF3* zeitnehmer regulates light signalling to the circadian clock. *Nature*, **408**, 716–720.

McWatters, H.G., Kolmos, E., Hall, A., Doyle, M.R., Amasino, R.M., Gyula, P., Nagy, F., Millar, A.J. & Davis, S.J. (2007). ELF4 is required for oscillatory properties of the circadian clock. *Plant Physiol*, **144**, 391–401.

Metropolis, N., Rosenbluth, A.W., Rosenbluth, M.N., Teller, A.H. & Teller, E. (1953). Equations of state calculations by fast computing machines. *The Journal of Chemical Physics*, **21**, 1087–1092.

Mettetal, J.T., Muzzey, D., Gómez-Uribe, C. & van Oudenaarden, A. (2008). The frequency dependence of osmo-adaptation in *Saccharomyces cerevisiae*. *Science*, **319**, 482–484.

Michael, T.P. & McClung, C.R. (2002). Phase-specific circadian clock regulatory elements in *Arabidopsis*. *Plant Physiol*, **130**, 627–638.

Michael, T.P. & McClung, C.R. (2003). Enhancer trapping reveals widespread circadian clock transcriptional control in *Arabidopsis*. *Plant Physiol*, **132**, 629–639.

Millar, A.J., Carré, I.A., Strayer, C.A., Chua, N.H. & Kay, S.A. (1995). Circadian clock mutants in *Arabidopsis* identified by luciferase imaging. *Science*, **267**, 1161–1163.

Mizoguchi, T. & Coupland, G. (2000). ZEITLUPE and FKF1: novel connections between flowering time and circadian clock control. *Trends Plant Sci*, **5**, 409–411.

Mizoguchi, T., Wheatley, K., Hanzawa, Y., Wright, L., Mizoguchi, M., Song, H.R., Carré, I.A. & Coupland, G. (2002). *LHY* and *CCA1* are partially redundant genes required to maintain circadian rhythms in *Arabidopsis*. *Dev Cell*, **2**, 629–641.

Mizoguchi, T., Wright, L., Fujiwara, S., Cremer, F., Lee, K., Onouchi, H., Mouradov, A., Fowler, S., Kamada, H., Putterill, J. & Coupland, G. (2005). Distinct roles of GIGANTEA in promoting flowering and regulating circadian rhythms in *Arabidopsis*. *Plant Cell*, **17**, 2255–2270.

Mizuno, T. & Nakamichi, N. (2005). Pseudo-response regulators (PRRs) or true oscillator components (TOCs). *Plant Cell Physiol*, **46**, 677–685.

Más, P., Alabadí, D., Yanovsky, M.J., Oyama, T. & Kay, S.A. (2003a). Dual role of TOC1 in the control of circadian and photomorphogenic responses in *Arabidopsis*. *Plant Cell*, **15**, 223–236.

Más, P., Kim, W.Y., Somers, D.E. & Kay, S.A. (2003b). Targeted degradation of TOC1 byZTL modulates circadian function in *Arabidopsis thaliana*. *Nature*, **426**, 567–570.

Nakamichi, N., Kita, M., Ito, S., Sato, E., Yamashino, T. & Mizuno, T. (2005a). The *Arabidopsis* pseudo-response regulators, PRR5 and PRR7, coordinately play essential roles for circadian clock function. *Plant Cell Physiol*, **46**, 609–619.

Nakamichi, N., Kita, M., Ito, S., Yamashino, T. & Mizuno, T. (2005b). PSEUDO-RESPONSE REGULATORS, PRR9, PRR7 and PRR5, together play essential roles close to the circadian clock of *Arabidopsis thaliana*. *Plant Cell Physiol*, **46**, 686–698.

Navazio, L., Mariani, P. & Sanders, D. (2001). Mobilization of Ca^{2+} by cyclic ADP-ribose from the endoplasmic reticulum of cauliflower florets. *Plant Physiol*, **125**, 2129–2138.

Nelson, D.E. & Takahashi, J.S. (1991). Sensitivity and integration in a visual pathway for circadian entrainment in the hamster (*Mesocricetus auratus*). *J Physiol*, **439**, 115–145.

Neuhaus, G., Bowler, C., Kern, R. & Chua, N.H. (1993). Calcium/calmodulin-dependent and -independent phytochrome signal transduction pathways. *Cell*, **73**, 937–952.

Ni, M., Tepperman, J.M. & Quail, P.H. (1998). PIF3, a phytochrome-interacting factor necessary for normal photoinduced signal transduction, is a novel basic helix-loop-helix protein. *Cell*, **95**, 657–667.

Ni, M., Tepperman, J.M. & Quail, P.H. (1999). Binding of phytochrome B to its nuclear signalling partner PIF3 is reversibly induced by light. *Nature*, **400**, 781–784.

Oguchi, T., Sage-Ono, K., Kamada, H. & Ono, M. (2004). Characterization of transcriptional oscillation of an *Arabidopsis* homolog of PnC401 related to photoperiodic induction of flowering in *Pharbitis nil*. *Plant Cell Physiol*, **45**, 232–235.

Onai, K. & Ishiura, M. (2005). *PHYTOCLOCK* 1 encoding a novel GARP protein essential for the *Arabidopsis* circadian clock. *Genes Cells*, **10**, 963–972.

O'Neill, J.S., Maywood, E.S., Chesham, J.E., Takahashi, J.S. & Hastings, M.H. (2008). cAMP-dependent signaling as a core component of the mammalian circadian pacemaker. *Science*, **320**, 949–953.

Ouyang, Y., Andersson, C.R., Kondo, T., Golden, S.S. & Johnson, C.H. (1998). Resonating circadian clocks enhance fitness in cyanobacteria. *Proc Natl Acad Sci U S A*, **95**, 8660–8664.

Park, D.H., Somers, D.E., Kim, Y.S., Choy, Y.H., Lim, H.K., Soh, M.S., Kim, H.J., Kay, S.A. & Nam, H.G. (1999). Control of circadian rhythms and photoperiodic flowering by the *Arabidopsis GIGANTEA* gene. *Science*, **285**, 1579–1582.

Perko, L. (2001). *Differential Equations and Dynamical Systems*. Springer.

Pittendrigh, C.S. (1954). On temperature independence in the clock system controlling emergence time in *Drosophila*. *Proc Natl Acad Sci U S A*, **40**, 1018–1029.

Rand, D.A., Shulgin, B.V., Salazar, D. & Millar, A.J. (2004). Design principles underlying circadian clocks. *J R Soc Interface*, **1**, 119–130.

Rand, D.A., Shulgin, B.V., Salazar, J.D. & Millar, A.J. (2006). Uncovering the design principles of circadian clocks: mathematical analysis of flexibility and evolutionary goals. *J Theor Biol*, **238**, 616–635.

Robert, C.P. & Casella, G. (2004). *Monte Carlo Statistical Methods*. Springer, 2nd edn.

Roenneberg, T. & Morse, D. (1993). Two circadian oscillators in one cell. *Nature*, **362**, 362–364.

Sai, J. & Johnson, C.H. (1999). Different circadian oscillators control Ca^{2+} fluxes and *Lhcb* gene expression. *Proc Natl Acad Sci U S A*, **96**, 11659–11663.

Salomé, P.A. & McClung, C.R. (2005a). *PSEUDO-RESPONSE REGULATOR 7* and *9* are partially redundant genes essential for the temperature responsiveness of the *Arabidopsis* circadian clock. *Plant Cell*, **17**, 791–803.

Salomé, P.A. & McClung, C.R. (2005b). What makes the arabidopsis clock tick on time? A review on entrainment. *Plant, Cell & Environment*, **28**, 21–38.

Sánchez, J.P., Duque, P. & Chua, N.H. (2004). ABA activates ADPR cyclase and cADPR induces a subset of ABA-responsive genes in *Arabidopsis*. *Plant J*, **38**, 381–395.

Sanders, D., Pelloux, J., Brownlee, C. & Harper, J.F. (2002). Calcium at the crossroads of signaling. *Plant Cell*, **14 Suppl**, S401–S417.

Sawa, M., Nusinow, D.A., Kay, S.A. & Imaizumi, T. (2007). FKF1 and GIGANTEA complex formation is required for day-length measurement in *Arabidopsis*. *Science*, **318**, 261–265.

Schaffer, R., Ramsay, N., Samach, A., Corden, S., Putterill, J., Carré, I.A. & Coupland, G. (1998). The *late elongated hypocotyl* mutation of *Arabidopsis* disrupts circadian rhythms and the photoperiodic control of flowering. *Cell*, **93**, 1219–1229.

Schaffer, R., Landgraf, J., Accerbi, M., Simon, V., Larson, M. & Wisman, E. (2001). Microarray analysis of diurnal and circadian-regulated genes in *Arabidopsis*. *Plant Cell*, **13**, 113–123.

Seber, G.A.F. (2004). *Multivariate Observations*. John Wiley and Sons.

Sethi, J.K., Empson, R.M. & Galione, A. (1996). Nicotinamide inhibits cyclic ADP-ribose-mediated calcium signalling in sea urchin eggs. *Biochem J*, **319 (Pt 2)**, 613–617.

Shampine, L.F. & Reichelt, M.W. (1997). The MATLAB ODE Suite. *SIAM J. Sci. Comp.*, **18**, 1–22.

Sharrock, R.A. & Clack, T. (2002). Patterns of expression and normalized levels of the five *Arabidopsis* phytochromes. *Plant Physiol*, **130**, 442–456.

Sinha, N.K. (2000). Identification of continuous-time systems from samples of input-output data: An introduction. *Sãdhanã*, **25**, 75–83.

Somers, D.E., Devlin, P.F. & Kay, S.A. (1998a). Phytochromes and cryptochromes in the entrainment of the *Arabidopsis* circadian clock. *Science*, **282**, 1488–1490.

Somers, D.E., Webb, A.A., Pearson, M. & Kay, S.A. (1998b). The short-period mutant, *toc1*-1, alters circadian clock regulation of multiple outputs throughout development in *Arabidopsis thaliana*. *Development*, **125**, 485–494.

Somers, D.E., Schultz, T.F., Milnamow, M. & Kay, S.A. (2000). *ZEITLUPE* encodes a novel clock-associated PAS protein from *Arabidopsis*. *Cell*, **101**, 319–329.

Srikusalanukul, W., Bruyne, F.D. & McCullagh, P. (2000). Modelling of peripheral lymphocyte migration: system identification approach. *Immunol Cell Biol*, **78**, 288–293.

Sriram, K. & Gopinathan, M.S. (2004). A two variable delay model for the circadian rhythm of *Neurospora crassa*. *J Theor Biol*, **231**, 23–38.

Srividhya, J. & Gopinathan, M.S. (2006). A simple time delay model for eukaryotic cell cycle. *J Theor Biol*, **241**, 617–627.

Staiger, D. & Apel, K. (1999). Circadian clock-regulated expression of an RNA-binding protein in *Arabidopsis*: characterisation of a minimal promoter element. *Mol Gen Genet*, **261**, 811–819.

Staiger, D., Zecca, L., Kirk, D.A.W., Apel, K. & Eckstein, L. (2003). The circadian clock regulated RNA-binding protein AtGRP7 autoregulates its expression by influencing alternative splicing of its own pre-mRNA. *Plant J*, **33**, 361–371.

Staxen, I., Pical, C., Montgomery, L.T., Gray, J.E., Hetherington, A.M. & McAinsh, M.R. (1999). Abscisic acid induces oscillations in guard-cell cytosolic free calcium that involve phosphoinositide-specific phospholipase C. *Proc Natl Acad Sci U S A*, **96**, 1779–1784.

Stelling, J., Gilles, E.D. & Doyle, F.J. (2004). Robustness properties of circadian clock architectures. *Proc Natl Acad Sci U S A*, **101**, 13210–13215.

Sugano, S., Andronis, C., Green, R.M., Wang, Z.Y. & Tobin, E.M. (1998). Protein kinase CK2 interacts with and phosphorylates the *Arabidopsis* circadian clock-associated 1 protein. *Proc Natl Acad Sci U S A*, **95**, 11020–11025.

Suárez-López, P., Wheatley, K., Robson, F., Onouchi, H., Valverde, F. & Coupland, G. (2001). CONSTANS mediates between the circadian clock and the control of flowering in *Arabidopsis*. *Nature*, **410**, 1116–1120.

Tang, R.H., Han, S., Zheng, H., Cook, C.W., Choi, C.S., Woerner, T.E., Jackson, R.B. & Pei, Z.M. (2007). Coupling diurnal cytosolic Ca^{2+} oscillations to the CAS-IP3 pathway in *Arabidopsis*. *Science*, **315**, 1423–1426.

Tang, Y. & Othmer, H.G. (1994). A model of calcium dynamics in cardiac myocytes based on the kinetics of ryanodine-sensitive calcium channels. *Biophys J*, **67**, 2223–2235.

Thain, S.C., Hall, A. & Millar, A.J. (2000). Functional independence of circadian clocks that regulate plant gene expression. *Curr Biol*, **10**, 951–956.

Thain, S.C., Murtas, G., Lynn, J.R., McGrath, R.B. & Millar, A.J. (2002). The circadian clock that controls gene expression in *Arabidopsis* is tissue specific. *Plant Physiol*, **130**, 102–110.

Trané, C. (2008). *Robustness Analysis of Intracellular Oscillators with Application to the Circadian Clock*. Ph.D. thesis, KTH School of Electrical Engineering.

Tymowska-Lalanne, Z. & Kreis, M. (1998). Expression of the *Arabidopsis thaliana* invertase gene family. *Planta*, **207**, 259–265.

Tóth, R., Kevei, E., Hall, A., Millar, A.J., Nagy, F. & Kozma-Bognár, L. (2001). Circadian clock-regulated expression of phytochrome and cryptochrome genes in *Arabidopsis*. *Plant Physiol*, **127**, 1607–1616.

Ueda, H.R., Hagiwara, M. & Kitano, H. (2001). Robust oscillations within the interlocked feedback model of *Drosophila* circadian rhythm. *J Theor Biol*, **210**, 401–406.

Unbehauen, H. & Rao, G.P. (1998). A review of identification in continuous-time systems. *Annual Reviews in Control*, **22**, 145–171.

Valverde, F., Mouradov, A., Soppe, W., Ravenscroft, D., Samach, A. & Coupland, G. (2004). Photoreceptor regulation of constans protein in photoperiodic flowering. *Science*, **303**, 1003–1006.

Wang, L., Gawthrop, P., Chessari, C., Podsiadly, T. & Giles, A. (2004). Indirect approach to continuous time system identification of food extruder. *Journal of Process Control*, **14**, 603–615.

Wang, Z.Y. & Tobin, E.M. (1998). Constitutive expression of the *CIRCADIAN CLOCK ASSOCIATED 1 (CCA1)* gene disrupts circadian rhythms and suppresses its own expression. *Cell*, **93**, 1207–1217.

Wang, Z.Y., Kenigsbuch, D., Sun, L., Harel, E., Ong, M.S. & Tobin, E.M. (1997). A Myb-related transcription factor is involved in the phytochrome regulation of an *Arabidopsis Lhcb* gene. *Plant Cell*, **9**, 491–507.

Webb, A.A.R. (2003). The physiology of circadian rhythms in plants. *New Phyt.*, **160**, 281–303.

Webb, A.A.R. (2008). The chloroplast as a regulator of Ca^{2+} signalling. *New Phytol*, **179**, 568–570.

Weinl, S., Held, K., Schlücking, K., Steinhorst, L., Kuhlgert, S., Hippler, M. & Kudla, J. (2008). A plastid protein crucial for Ca^{2+}-regulated stomatal responses. *New Phytol*, **179**, 675–686.

Wood, N.T., Haley, A., Viry-Moussaïd, M., Johnson, C.H., van der Luit, A.H. & Trewavas, A.J. (2001). The calcium rhythms of different cell types oscillate with different circadian phases. *Plant Physiol*, **125**, 787–796.

Wu, Y., Kuzma, J., Maréchal, E., Graeff, R., Lee, H.C., Foster, R. & Chua, N.H. (1997). Abscisic acid signaling through cyclic ADP-ribose in plants. *Science*, **278**, 2126–2130.

Xu, X., Hotta, C.T., Dodd, A.N., Love, J., Sharrock, R., Lee, Y.W., Xie, Q., Johnson, C.H. & Webb, A.A.R. (2007). Distinct light and clock modulation of cytosolic free Ca^{2+} oscillations and rhythmic *CHLOROPHYLL A/B BINDING PROTEIN2* promoter activity in *Arabidopsis*. *Plant Cell*, **19**, 3474–3490.

Yakir, E., Hilman, D., Harir, Y. & Green, R.M. (2007). Regulation of output from the plant circadian clock. *FEBS J*, **274**, 335–345.

Yildirim, M.A. & Vidal, M. (2008). Systems engineering to systems biology. *Mol Syst Biol*, **4**, 185.

Yin, L., Wu, N., Curtin, J.C., Qatanani, M., Szwergold, N.R., Reid, R.A., Waitt, G.M., Parks, D.J., Pearce, K.H., Wisely, G.B. & Lazar, M.A. (2007). Rev-erbα, a heme sensor that coordinates metabolic and circadian pathways. *Science*, **318**, 1786–1789.

Young, M.W. & Kay, S.A. (2001). Time zones: a comparative genetics of circadian clocks. *Nat Rev Genet*, **2**, 702–715.

Zeilinger, M.N., Farré, E.M., Taylor, S.R., Kay, S.A. & Doyle, F.J. (2006). A novel computational model of the circadian clock in *Arabidopsis* that incorporates PRR7 and PRR9. *Mol Syst Biol*, **2**, 58.

Zhong, H.H., Painter, J.E., Salomé, P.A., Straume, M. & McClung, C.R. (1998). Imbibition, but not release from stratification, sets the circadian clock in *Arabidopsis* seedlings. *Plant Cell*, **10**, 2005–2017.

APPENDIX A

Central Oscillator Models

A.1 Interlocked Feedback Loop model

A.1.1 Equations

$$\frac{dc_L^{(m)}}{dt} = \Theta(t)q_1c_P^{(n)} + \frac{n_1c_X^{(n)^a}}{g_1^a + c_X^{(n)^a}} - \frac{m_1c_L^{(m)}}{k_1 + c_L^{(m)}} \tag{A.1}$$

$$\frac{dc_L^{(c)}}{dt} = p_1c_L^{(m)} - r_1c_L^{(c)} + r_2c_L^{(n)} - \frac{m_2c_L^{(c)}}{k_2 + c_L^{(c)}} \tag{A.2}$$

$$\frac{dc_L^{(n)}}{dt} = r_1c_L^{(c)} - r_2c_L^{(n)} - \frac{m_3c_L^{(n)}}{k_3 + c_L^{(n)}} \tag{A.3}$$

$$\frac{dc_T^{(m)}}{dt} = \left(\frac{n_2c_Y^{(n)^b}}{g_2^b + c_Y^{(n)^b}}\right)\left(\frac{g_3^c}{g_3^c + c_L^{(n)^c}}\right) - \frac{m_4c_T^{(m)}}{k_4 + c_T^{(m)}} \tag{A.4}$$

$$\frac{dc_T^{(c)}}{dt} = p_2c_T^{(m)} - r_3c_T^{(c)} + r_4c_T^{(n)} - ((1 - \Theta(t))m_5 + m_6)\frac{c_T^{(c)}}{k_5 + c_T^{(c)}} \tag{A.5}$$

$$\frac{dc_T^{(n)}}{dt} = r_3c_T^{(c)} - r_4c_T^{(n)} - ((1 - \Theta(t))m_7 + m_8)\frac{c_T^{(n)}}{k_6 + c_T^{(n)}} \tag{A.6}$$

$$\frac{dc_X^{(m)}}{dt} = \frac{n_3c_T^{(n)^d}}{g_4^d + c_T^{(n)^d}} - \frac{m_9c_X^{(m)}}{k_7 + c_X^{(m)}} \tag{A.7}$$

$$\frac{dc_X^{(c)}}{dt} = p_3c_X^{(m)} - r_5c_X^{(c)} + r_6c_X^{(n)} - \frac{m_{10}c_X^{(c)}}{k_8 + c_X^{(c)}} \tag{A.8}$$

$$\frac{dc_X^{(n)}}{dt} = r_5 c_X^{(c)} - r_6 c_X^{(n)} - \frac{m_{11} c_X^{(n)}}{k_9 + c_X^{(n)}} \tag{A.9}$$

$$\frac{dc_Y^{(m)}}{dt} = \left(\Theta(t) q_2 c_P^{(n)} + \frac{(\Theta(t) n_4 + n_5) g_5^e}{g_5^e + c_T^{(n)^e}}\right)\left(\frac{g_6^f}{g_6^f + c_L^{(n)^f}}\right) - \frac{m_{12} c_Y^{(m)}}{k_{10} + c_Y^{(m)}} \tag{A.10}$$

$$\frac{dc_Y^{(c)}}{dt} = p_4 c_Y^{(m)} - r_7 c_Y^{(c)} + r_8 c_Y^{(n)} - \frac{m_{13} c_Y^{(c)}}{k_{11} + c_Y^{(c)}} \tag{A.11}$$

$$\frac{dc_Y^{(n)}}{dt} = r_7 c_Y^{(c)} - r_8 c_Y^{(n)} - \frac{m_{14} c_Y^{(n)}}{k_{12} + c_Y^{(n)}} \tag{A.12}$$

$$\frac{dc_P^{(n)}}{dt} = (1 - \Theta(t)) p_5 - \frac{m_{15} c_P^{(n)}}{k_{13} + c_P^{(n)}} - q_3 \Theta(t) c_P^{(n)} \tag{A.13}$$

A.1.2 Parameters

Table A.1: Optimal parameter set for Interlocked Feedback Loop model equations, determined by simulated annealing (Locke *et al.*, 2005b)

Name	Value	Description
q_1	2.4515	Coupling constant of light activation of LHY transcription
n_1	5.1694	Maximum light-independent LHY transcription rate
a	3.3064	Hill coefficient of activation by protein X
g_1	0.8767	Constant of activation by protein X
m_1	1.5283	Maximum rate of LHY mRNA degradation
k_1	1.8170	Michaelis constant of LHY mRNA degradation
p_1	0.8295	Rate constant of LHY mRNA translation
r_1	16.8363	Rate constant of LHY transport into nucleus
r_2	0.1687	Rate constant of LHY transport out of nucleus
m_2	20.4400	Maximum rate of cytoplasmic LHY degradation
k_2	1.5644	Michaelis constant of cytoplasmic LHY degradation
m_3	3.6888	Maximum rate of nuclear LHY degradation
k_3	1.2765	Michaelis constant of nuclear LHY degradation
n_2	3.0087	Maximum TOC1 transcription rate
b	1.0258	Hill coefficient of activation by protein Y
g_2	0.0368	Constant of activation by protein Y
g_3	0.2658	Constant of repression by LHY
c	1.0258	Hill coefficient of repression by protein Y
m_4	3.8231	Maximum rate of TOC1 mRNA degradation
k_4	2.5734	Michaelis constant of TOC1 mRNA degradation
p_2	4.3240	Rate constant of TOC1 mRNA translation
r_3	0.3166	Rate constant of TOC1 transport into nucleus
r_4	2.1509	Rate constant of TOC1 transport out of nucleus

Continued on next page

Table A.1: *Continued from previous page*

Name	Value	Description
m_5	0.0013	Maximum rate of light-dependent cytoplasmic TOC1 degradation
m_6	3.1741	Maximum rate of light-independent cytoplasmic TOC1 degradation
k_5	2.7454	Michaelis constant of cytoplasmic TOC1 degradation
m_7	0.0492	Maximum rate of light-dependent nuclear TOC1 degradation
m_8	4.0424	Maximum rate of light-independent nuclear TOC1 degradation
k_6	0.4033	Michaelis constant of nuclear TOC1 degradation
n_3	0.2431	Maximum transcription rate of protein X
d	1.4422	Hill coefficient of activation by TOC1
g_4	0.5388	Constant of activation by TOC1
m_9	10.1132	Maximum rate of degradation of protein X mRNA
k_7	6.5585	Michaelis constant of protein X mRNA degradation
p_3	2.1470	Rate constant of X mRNA translation
r_5	1.0352	Rate constant of protein X transport into nucleus
r_6	3.3017	Rate constant of protein X transport out of nucleus
m_{10}	0.2179	Maximum rate of degradation of cytoplasmic protein X
k_8	0.6632	Michaelis constant of cytoplasmic protein X degradation
m_{11}	3.3442	Maximum rate of degradation of nuclear protein X
k_9	17.1111	Michaelis constant of nuclear protein X degradation
q_2	2.4017	Coupling constant of light activation of Y mRNA transcription
n_4	0.0857	Light-dependent component of Y transcription
n_5	0.1649	Light-independent component of Y transcription
g_5	1.1780	Constant of repression by TOC1
g_6	0.0645	Constant of repression by LHY
e	3.6064	Hill coefficient of repression by TOC1
f	1.0237	Hill coefficient of repression by LHY
m_{12}	4.2970	Maximum rate of degradation of protein Y mRNA
k_{10}	1.7303	Michaelis constant of protein Y mRNA degradation
p_4	0.2485	Rate constant of Y mRNA translation
r_7	2.2123	Rate constant of protein Y transport into nucleus
r_8	0.2002	Rate constant of protein Y transport out of nucleus
m_{13}	0.1347	Maximum rate of degradation of cytoplasmic protein Y
k_{11}	1.8258	Michaelis constant of cytoplasmic protein Ydegradation
m_{14}	0.6114	Maximum rate of degradation of nuclear protein Y
k_{12}	1.8066	Michaelis constant of nuclear protein Y degradation
p_5	0.5000	Light-dependent production of protein P
k_{13}	1.2000	Michaelis constant of protein P degradation
m_{15}	1.2000	Maximum rate of protein P degradation
q_3	1.0000	Coupling constant of light activation of protein P degradation

A.2 Three Loop model

A.2.1 Equations

$$\frac{dc_L^{(m)}}{dt} = \left(\frac{g_0^{\alpha}}{g_0^{\alpha} + c_A^{(n)^{\alpha}}}\right)\left(\Theta_{\text{light}}(t)\left(q_1 c_P^{(n)} + n_0\right) + \frac{n_1 c_X^{(n)^a}}{g_1^a + c_X^{(n)^a}}\right) - \frac{m_1 c_L^{(m)}}{k_1 + c_L^{(m)}} \tag{A.14}$$

$$\frac{dc_L^{(c)}}{dt} = p_1 c_L^{(m)} - r_1 c_L^{(c)} + r_2 c_L^{(n)} - \frac{m_2 c_L^{(c)}}{k_2 + c_L^{(c)}} \tag{A.15}$$

$$\frac{dc_L^{(n)}}{dt} = r_1 c_L^{(c)} - r_2 c_L^{(n)} - \frac{m_3 c_L^{(n)}}{k_3 + c_L^{(n)}} \tag{A.16}$$

$$\frac{dc_T^{(m)}}{dt} = \left(\frac{n_2 c_Y^{(n)^b}}{g_2^b + c_Y^{(n)^b}}\right)\left(\frac{g_3^c}{g_3^c + c_L^{(n)^c}}\right) - \frac{m_4 c_T^{(m)}}{k_4 + c_T^{(m)}} \tag{A.17}$$

$$\frac{dc_T^{(c)}}{dt} = p_2 c_T^{(m)} - r_3 c_T^{(c)} + r_4 c_T^{(n)} - ((1 - \Theta_{\text{light}}(t))m_5 + m_6)\frac{c_T^{(c)}}{k_5 + c_T^{(c)}} \tag{A.18}$$

$$\frac{dc_T^{(n)}}{dt} = r_3 c_T^{(c)} - r_4 c_T^{(n)} - ((1 - \Theta_{\text{light}}(t))m_7 + m_8)\frac{c_T^{(n)}}{k_6 + c_T^{(n)}} \tag{A.19}$$

$$\frac{dc_X^{(m)}}{dt} = \frac{n_3 c_T^{(n)^d}}{g_4^d + c_T^{(n)^d}} - \frac{m_9 c_X^{(m)}}{k_7 + c_X^{(m)}} \tag{A.20}$$

$$\frac{dc_X^{(c)}}{dt} = p_3 c_X^{(m)} - r_5 c_X^{(c)} + r_6 c_X^{(n)} - \frac{m_{10} c_X^{(c)}}{k_8 + c_X^{(c)}} \tag{A.21}$$

$$\frac{dc_X^{(n)}}{dt} = r_5 c_X^{(c)} - r_6 c_X^{(n)} - \frac{m_{11} c_X^{(n)}}{k_9 + c_X^{(n)}} \tag{A.22}$$

$$\frac{dc_Y^{(m)}}{dt} = \left(\Theta_{\text{light}}(t) q_2 c_P^{(n)} + \frac{(\Theta_{\text{light}}(t) n_4 + n_5) g_5^e}{g_5^e + c_T^{(n)^e}}\right)\left(\frac{g_6^f}{g_6^f + c_L^{(n)^f}}\right) - \frac{m_{12} c_Y^{(m)}}{k_{10} + c_Y^{(m)}} \tag{A.23}$$

$$\frac{dc_Y^{(c)}}{dt} = p_4 c_Y^{(m)} - r_7 c_Y^{(c)} + r_8 c_Y^{(n)} - \frac{m_{13} c_Y^{(c)}}{k_{11} + c_Y^{(c)}} \tag{A.24}$$

$$\frac{dc_Y^{(n)}}{dt} = r_7 c_Y^{(c)} - r_8 c_Y^{(n)} - \frac{m_{14} c_Y^{(n)}}{k_{12} + c_Y^{(n)}} \tag{A.25}$$

$$\frac{dc_P^{(n)}}{dt} = (1 - \Theta_{\text{light}}(t))p_5 - \frac{m_{15} c_P^{(n)}}{k_{13} + c_P^{(n)}} - q_3 \Theta_{\text{light}}(t) c_P^{(n)} \tag{A.26}$$

$$\frac{dc_A^{(m)}}{dt} = \Theta_{\text{light}}(t) q_4 c_P^n + \frac{n_6 c_L^{(n)^g}}{g_7^g + c_L^{(n)^g}} - \frac{m_{16} c_A^{(m)}}{k_{14} + c_A^{(m)}} \tag{A.27}$$

$$\frac{dc_A^{(c)}}{dt} = p_6 c_A^{(m)} - r_9 c_A^{(c)} + r_{10} c_A^{(n)} - \frac{m_{17} c_A^{(c)}}{k_{15} + c_A^{(c)}} \tag{A.28}$$

$$\frac{dc_A^{(n)}}{dt} = r_9 c_A^{(c)} - r_{10} c_A^{(n)} - \frac{m_{18} c_A^{(n)}}{k_{16} + c_A^{(n)}} \tag{A.29}$$

A.2.2 Parameters

Table A.2: Optimal parameter set for Three Loop model equations, determined by simulated annealing (Locke *et al.*, 2006)

Name	Value	Description
q_1	4.1954	Coupling constant of light activation of LHY transcription
n_0	0.05	Maximum light-dependent LHY transcription rate
g_0	1.0	Constant of repression by APRR7/9
α	4.0	Hill coefficient of repression by APRR7/9
n_1	7.8142	Maximum light-independent LHY transcription rate
a	1.2479	Hill coefficient of activation by protein X
g_1	3.1383	Constant of activation by protein X
m_1	1.999	Maximum rate of LHY mRNA degradation
k_1	2.392	Michaelis constant of LHY mRNA degradation
p_1	0.8295	Rate constant of LHY mRNA translation
r_1	16.8363	Rate constant of LHY transport into nucleus
r_2	0.1687	Rate constant of LHY transport out of nucleus
m_2	20.4400	Maximum rate of cytoplasmic LHY degradation
k_2	1.5644	Michaelis constant of cytoplasmic LHY degradation
m_3	3.6888	Maximum rate of nuclear LHY degradation
k_3	1.2765	Michaelis constant of nuclear LHY degradation
n_2	3.0087	Maximum TOC1 transcription rate
b	1.0258	Hill coefficient of activation by protein Y
g_2	0.0368	Constant of activation by protein Y
g_3	0.2658	Constant of repression by LHY
c	1.0258	Hill coefficient of repression by protein Y
m_4	3.8231	Maximum rate of TOC1 mRNA degradation
k_4	2.5734	Michaelis constant of TOC1 mRNA degradation
p_2	4.3240	Rate constant of TOC1 mRNA translation
r_3	0.3166	Rate constant of TOC1 transport into nucleus
r_4	2.1509	Rate constant of TOC1 transport out of nucleus
m_5	0.0013	Maximum rate of light-dependent cytoplasmic TOC1 degradation
m_6	3.1741	Maximum rate of light-independent cytoplasmic TOC1 degradation
k_5	2.7454	Michaelis constant of cytoplasmic TOC1 degradation
m_7	0.0492	Maximum rate of light-dependent nuclear TOC1 degradation
m_8	4.0424	Maximum rate of light-independent nuclear TOC1 degradation
k_6	0.4033	Michaelis constant of nuclear TOC1 degradation
n_3	0.2431	Maximum transcription rate of protein X

Continued on next page

Table A.2: *Continued from previous page*

Name	Value	Description
d	1.4422	Hill coefficient of activation by TOC1
g_4	0.5388	Constant of activation by TOC1
m_9	10.1132	Maximum rate of degradation of protein X mRNA
k_7	6.5585	Michaelis constant of protein X mRNA degradation
p_3	2.1470	Rate constant of X mRNA translation
r_5	1.0352	Rate constant of protein X transport into nucleus
r_6	3.3017	Rate constant of protein X transport out of nucleus
m_{10}	0.2179	Maximum rate of degradation of cytoplasmic protein X
k_8	0.6632	Michaelis constant of cytoplasmic protein X degradation
m_{11}	3.3442	Maximum rate of degradation of nuclear protein X
k_9	17.1111	Michaelis constant of nuclear protein X degradation
q_2	2.4017	Coupling constant of light activation of Y mRNA transcription
n_4	0.0857	Light-dependent component of Y transcription
n_5	0.1649	Light-independent component of Y transcription
g_5	1.1780	Constant of repression by TOC1
g_6	0.0645	Constant of repression by LHY
e	3.6064	Hill coefficient of repression by TOC1
f	1.0237	Hill coefficient of repression by LHY
m_{12}	4.2970	Maximum rate of degradation of protein Y mRNA
k_{10}	1.7303	Michaelis constant of protein Y mRNA degradation
p_4	0.2485	Rate constant of Y mRNA translation
r_7	2.2123	Rate constant of protein Y transport into nucleus
r_8	0.2002	Rate constant of protein Y transport out of nucleus
m_{13}	0.1347	Maximum rate of degradation of cytoplasmic protein Y
k_{11}	1.8258	Michaelis constant of cytoplasmic protein Y degradation
m_{14}	0.6114	Maximum rate of degradation of nuclear protein Y
k_{12}	1.8066	Michaelis constant of nuclear protein Y degradation
p_5	0.5000	Light-dependent production of protein P
k_{13}	1.2000	Michaelis constant of protein P degradation
m_{15}	1.2000	Maximum rate of protein P degradation
q_3	1.0000	Coupling constant of light activation of protein P degradation
q_4	2.4514	Coupling constant of light activation of LHY transcription
g	1.0258	Hill coefficient of activation by LHY
n_6	8.0706	Maximum light-independent APRR7/9 transcription rate
g_7	0.0004	Constant of activation by LHY
m_{16}	12.2398	Maximum rate of APRR7/9 mRNA degradation
k_{14}	10.3617	Michaelis constant of APRR7/9 mRNA degradation
p_6	0.2907	Rate constant of APRR7/9 mRNA translation
r_9	0.2528	Rate constant of APRR7/9 protein movement out of nucleus

Continued on next page

Table A.2: *Continued from previous page*

Name	Value	Description
r_{10}	0.2212	Rate constant of APRR7/9 protein movement into the nucleus
m_{17}	4.4505	Maximum rate of degradation of cytoplasmic protein APRR7/9
k_{15}	0.0703	Michaelis constant of cytoplasmic protein APRR7/9 degradation
m_{18}	0.0156	Maximum rate of degradation of nuclear protein APRR7/9
k_{16}	0.6104	Michaelis constant of cytoplasmic protein APRR7/9 degradation

APPENDIX B

Dodd *et al.*, (2007) – Published in *Science*

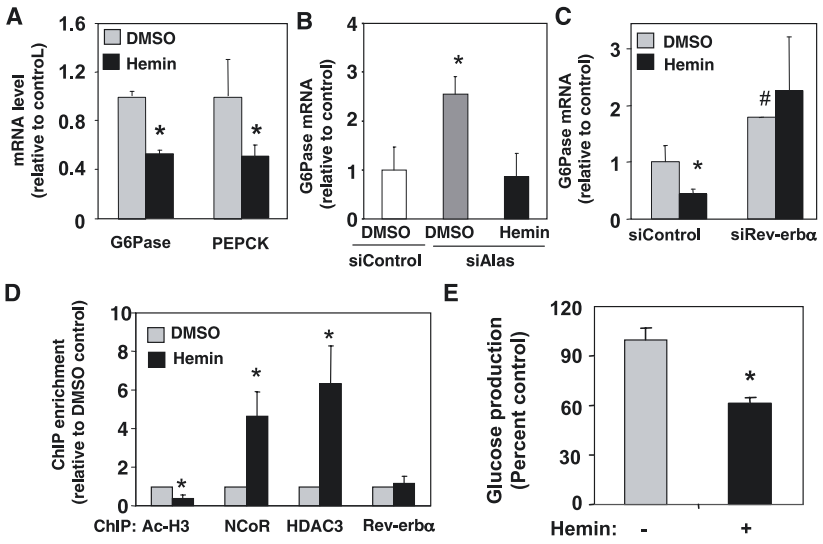

Fig. 5. Suppression of the expression of gluconeogenic genes and glucose production in liver cells treated with hemin. (**A**) Expression of G6Pase and PEPCK genes in HepG2 cells treated with either DMSO or hemin (6 μM) for 6 hours. Amounts of mRNA were quantitated by RT-PCR and normalized to cyclophilin. Mean ± SD of three independent experiments is shown. *$P < 0.05$ compared with control by Student's t test. (**B**) Expression of G6Pase gene in HepG2 cells treated with control or ALAS1-targeting siRNA and then stimulated with DMSO or hemin for 16 hours. Mean ± SD ($n = 3$),*$P < 0.05$ compared with siRNA control treated with DMSO. (**C**) Effect of hemin on the expression of G6Pase gene in cells depleted of Rev-erbα. Mean ± SD ($n = 3$), *P <0.05 compared with DMSO-treated cells transfected with control siRNA. Pound symbol indicates $P < 0.05$ compared with DMSO-treated cells transfected with control siRNA. (**D**) Effect of hemin on the occupancy of Rev-erbα, HDAC3, NCoR, or acetylated H3 (Ac-H3) at the *G6Pase* promoter in cells. Results of hemin-treatment are normalized to DMSO results. Mean ± SD ($n = 4$). *$P < 0.05$ compared with control. (**E**) Primary mouse hepatocytes were treated with dexamethasone and 8-(4-chlorophenyl-thio)-adenosine 3′,5′-cyclic monophosphate along with DMSO or hemin for 16 hours, then glucose in the medium was measured. Mean ± SD of triplicate samples is shown, and four independent experiments gave similar results. *$P < 0.05$ compared with control.

BMAL1-NPAS2–dependent transcription activation (*19*–*21*) while enhancing Rev-erbα–mediated transcription repression, providing a potential means of maintaining the amplitude of circadian rhythms.

Expression of the gene encoding ALAS1, the rate-limiting enzyme in heme biosynthesis, increased in response to peroxisome proliferator activated receptor coactivator–1α (*29*), a regulator of mitochondriogenesis that increases flux through the Krebs cycle (*30*). This first and rate-limiting enzyme in heme biosynthesis requires succincyl CoA, a Krebs cycle intermediate (*17*, *29*). Gluconeogenesis competes with the Krebs cycle for metabolic intermediates whose depletion compromises heme biosynthesis as well as mitochondrial oxidative metabolism (fig. S13). The ability of Rev-erbα to function as a receptor for heme could provide a general mechanism for coordinating these processes.

References and Notes

1. F. Gachon, E. Nagoshi, S. A. Brown, J. Ripperger, U. Schibler, *Chromosoma* **113**, 103 (2004).
2. S. M. Reppert, D. R. Weaver, *Annu. Rev. Physiol.* **63**, 647 (2001).
3. P. L. Lowrey, J. S. Takahashi, *Annu. Rev. Genomics Hum. Genet.* **5**, 407 (2004).
4. A. Kohsaka, J. Bass, *Trends Endocrinol. Metab.* **18**, 4 (2007).
5. M. Stratmann, U. Schibler, *J. Biol. Rhythms* **21**, 494 (2006).
6. M. Akashi, T. Takumi, *Nat. Struct. Mol. Biol.* **12**, 441 (2005).
7. N. Preitner *et al.*, *Cell* **110**, 251 (2002).
8. T. K. Sato *et al.*, *Neuron* **43**, 527 (2004).
9. L. Yin, M. A. Lazar, *Mol. Endocrinol.* **19**, 1452 (2005).
10. M. F. Ceriani *et al.*, *J. Neurosci.* **22**, 9305 (2002).
11. K. Oishi *et al.*, *J. Biol. Chem.* **278**, 41519 (2003).
12. S. Panda *et al.*, *Cell* **109**, 307 (2002).
13. K. Oishi *et al.*, *FEBS Lett.* **580**, 127 (2006).
14. R. D. Rudic *et al.*, *PLoS Biol.* **2**, e377 (2004).
15. F. W. Turek *et al.*, *Science* **308**, 1043 (2005); published online 21 April 2005 (10.1126/science.1108750).
16. H. Atamna, *Ageing Res. Rev.* **3**, 303 (2004).
17. P. Ponka, *Am. J. Med. Sci.* **318**, 241 (1999).
18. A. S. Tsiftsoglou, A. I. Tsamadou, L. C. Papadopoulou, *Pharmacol. Ther.* **111**, 327 (2006).
19. E. M. Dioum *et al.*, *Science* **298**, 2385 (2002); published online 20 November 2002 (10.1126/science.1078456).
20. K. Kaasik, C. C. Lee, *Nature* **430**, 467 (2004).
21. D. Boehning, S. H. Snyder, *Science* **298**, 2339 (2002).
22. E. de Rosny *et al.*, *Biochemistry* **45**, 9727 (2006).
23. J. Reinking *et al.*, *Cell* **122**, 195 (2005).
24. S. Sassa, A. Kappas, *J. Clin. Investig.* **71**, 625 (1983).
25. Y. Zhu, T. Hon, W. Ye, L. Zhang, *Cell Growth Differ.* **13**, 431 (2002).
26. J. A. Ripperger, *Chronobiol. Int.* **23**, 135 (2006).
27. G. Adelmant, A. Begue, D. Stehelin, V. Laudet, *Proc. Natl. Acad. Sci. U.S.A.* **93**, 3553 (1996).
28. L. Yin, J. Wang, P. S. Klein, M. A. Lazar, *Science* **311**, 1002 (2006).
29. C. Handschin *et al.*, *Cell* **122**, 505 (2005).
30. S. C. Burgess *et al.*, *J. Biol. Chem.* **281**, 19000 (2006).

31. We thank R. Gampe, D. Steger, T. Stanley, M. Walker, J. Williams, and T. Willson for helpful discussions. This work was supported by National Institute of Diabetes and Digestive and Kidney Diseases grant R01 DK45586 (M.A.L.).

Supporting Online Material

www.sciencemag.org/cgi/content/full/1150179/DC1
Materials and Methods
Figs. S1 to S13
References

6 September 2007; accepted 28 September 2007
Published online 15 November 2007;
10.1126/science.1150179
Include this information when citing this paper.

The *Arabidopsis* Circadian Clock Incorporates a cADPR-Based Feedback Loop

Antony N. Dodd,[1] Michael J. Gardner,[1] Carlos T. Hotta,[1] Katharine E. Hubbard,[1] Neil Dalchau,[1] John Love,[1]* Jean-Maurice Assie,[1] Fiona C. Robertson,[1] Mia Kyed Jakobsen,[1]† Jorge Gonçalves,[2] Dale Sanders,[3] Alex A. R. Webb[1]‡

Transcriptional feedback loops are a feature of circadian clocks in both animals and plants. We show that the plant circadian clock also incorporates the cytosolic signaling molecule cyclic adenosine diphosphate ribose (cADPR). cADPR modulates the circadian oscillator's transcriptional feedback loops and drives circadian oscillations of Ca^{2+} release. The effects of antagonists of cADPR signaling, manipulation of cADPR synthesis, and mathematical simulation of the interaction of cADPR with the circadian clock indicate that cADPR forms a feedback loop within the plant circadian clock.

Circadian clocks are adaptations to the daily rotation of the planet. In plants and cyanobacteria, benefits occur when the clock is resonant with the environment (*1*–*3*). This requires the oscillator to be robust yet flexible, which may explain the evolution of molecular clocks with multiple feedback loops (*4*–*6*). We tested the hypothesis that plant circadian oscillators also incorporate cytosolic signaling molecules because there are circadian rhythms in the

concentration of cytosolic free Ca^{2+} ($[Ca^{2+}]_{cyt}$) (*7*, *8*). We investigated the function within the plant circadian system of cyclic adenosine diphosphate ribose (cADPR), a cytosolic ligand that promotes the release of Ca^{2+} into the cytosol from internal stores through cation channels (*9*).

To identify potential interactions between plant circadian and Ca^{2+} signaling pathways, we examined the overlap between a circadian transcriptome and transcriptomes for known regulators of $[Ca^{2+}]_{cyt}$ (table S1) (*10*). We obtained a new near whole-genome transcriptome in constant light (LL) under conditions allowing circadian $[Ca^{2+}]_{cyt}$ oscillations (*10*, *11*). This was necessary because previous circadian transcript analyses used plants grown on 3% sucrose (*12*, *13*), which abolishes circadian $[Ca^{2+}]_{cyt}$ oscillations (*7*). On the basis of a threshold multiple measures–corrected probability of rhythmicity (pMMC) of 0.15, 2282 (12.08%) transcripts were circadian-regulated (spreadsheet S1 and fig. S1) (*12*, *14*).

A cADPR-regulated transcript set (*15*) had the most statistically significant overlap with our circadian transcriptome [(Fig. 1A and table S1) $P = 5.15 \times 10^{-52}$]. The overlap was significantly larger than the 93 transcripts expected for a chance overlap of two similarly sized datasets selected randomly from the *Arabidopsis* genome. We noted that 252 transcripts were both circadian- and cADPR-regulated (Fig. 1A and spreadsheet S2). There was a phase relation between circadian- and cADPR-regulation of transcript abundance: The majority of cADPR–up-regulated rhythmic transcripts reached peak abundance at zeitgeber time (ZT) ZT8 or ZT12, and the majority of cADPR-repressed rhythmic transcripts reached peak abundance between ZT20 and ZT4 (Fig. 1B).

Because a phase relation existed between circadian- and cADPR-regulated genes and the circadian-regulated evening element was significantly overrepresented in cADPR–up-regulated genes (spreadsheet S3), we reasoned that cADPR signaling might be circadian-regulated (*12*, *15*). We measured [cADPR] in extracts of aerial tissues of seedlings in LL (*10*). [cADPR] was circadian-regulated, because [cADPR] was significantly higher during subjective light (mean ± SEM, 0.27 ± 0.04 pmol · μg $protein^{-1}$) than subjective dark (0.16 ± 0.02 pmol · μg $protein^{-1}$) (Fig. 2, A and B, and fig. S2), [cADPR] variations persisted through the second and third days of LL and were eliminated in plants overexpressing *CIRCADIAN CLOCK ASSOCIATED1* (*CCA1*-ox) (Fig. 2A). *CCA1*-ox abolishes all known plant circadian rhythms (*2*, *16*).

We tested whether circadian [cADPR] variations cause circadian rhythms of $[Ca^{2+}]_{cyt}$. Under LL, we monitored $[Ca^{2+}]_{cyt}$ in seedlings treated every 3 hours with Ca^{2+} signaling antagonists (Fig. 2, C and D). Nicotinamide (10 mM) reduced the amplitude of the $[Ca^{2+}]_{cyt}$ oscillation, and 50 mM nicotinamide abolished the oscillation (Fig. 2C) (*10*). Nicotinamide is an antagonist of cADPR signaling that, at 50 mM, inhibits the synthesis of cADPR from NAD^+ by adenosine diphosphate ribosyl cyclase (ADPRc) (*17*). Circadian $[Ca^{2+}]_{cyt}$ oscillations were unaltered by $GdCl_3$, which inhibits extracellular Ca^{2+} influx (*18*) (Fig. 2D), and the phospholipase C (PLC) inhibitor U73122, which inhibits production of inositol 1,4,5-trisphosphate (IP_3) at 1 μM (*19*) (Fig. 2D). *Arabidopsis* ADPRc activity (*10*, *20*) was inhibited in vitro by 40 mM nicotinamide (fig. S3), which suggests that nicotinamide prevents cADPR synthesis in plants. Because 50 mM nicotinamide abolished circadian $[Ca^{2+}]_{cyt}$ oscillations, and circadian [cADPR] and $[Ca^{2+}]_{cyt}$ alterations had a similar phase, circadian cADPR oscillations are likely to drive circadian $[Ca^{2+}]_{cyt}$ rhythms.

Several genes encoding components of the circadian clock are cADPR-regulated (*15*). *GIGANTEA* (*GI*), *CRYPTOCHROME2* (*CRY2*), *GLYCINE-RICH BINDING PROTEIN7* (*GRP7*), *GRP8*, and *PSEUDO-RESPONSE REGULATOR5* (*PRR5*) and *PRR7* are cADPR–up-regulated, and *LATE ELONGATED HYPOCOTYL* (*LHY*) and *CCA1* are down-regulated. *TIMING OF CHLOROPHYLL A/B BINDING PROTEIN* (*TOC1*) is unaffected (spreadsheet S2) (*15*). To understand how circadian function might be affected by cADPR-induced changes in transcript abundance, we performed a simulation using a previously described mathematical model (*21*). In that model, 13 equations define an approximation for the *Arabidopsis* circadian oscillator. We controlled the parameters of this model to constrain *CCA1/LHY*, *GI*, and *TOC1* transcripts to adopt the fold-changes that are caused by cADPR in plants (figs. S4 and S5) (*10*, *15*). First, we constrained the parameters transiently, because increasing cADPR synthesis by inducing the *Aplysia ADPR cyclase* gene, fused to a β-estradiol–inducible promoter (*XVE:ADPRc*), causes transient alterations in clock transcripts although [cADPR] remains elevated (*15*). Depending on the parameters that were constrained, there was a short disruption to the modeled oscillator that sometimes caused phase changes, but the period remained 24 hours (Fig. 3A and fig. S5C). Next, we constrained the parameters continuously to evaluate the effects of continuous cADPR-induced alteration in clock transcripts. Depending on the parameters that were constrained, the circadian period often changed and remained altered throughout the simulation (Fig. 3B). Finally, we inverted the permanent constraint of the parameters to understand the possible effects of removal of cADPR-regulation of clock transcripts. Most of the parameters that did not lead to arrhythmia caused the simulations to run with a longer period (Fig. 3C). These simulated outcomes provided a framework with which to interpret the effects of cADPR on the plant circadian clock.

We experimentally tested how transient [cADPR]-induced alterations in circadian clock transcripts affect circadian behavior. We elevated [cADPR] in two independent lines by inducing the *XVE:ADPRc* transgene (*15*) with 100 μM β-estradiol. [cADPR] increased 13.5-fold (line 1) and 27-fold (line 2) relative to controls (fig. S6). The circadian period and phase of leaf position were unaltered when *XVE:ADPRc* was induced at ZT2 under LL (Fig. 4A and fig. S7, A, B, and G), or at two times during the final LD cycle before LL (fig. S7, C to G). Circadian $[Ca^{2+}]_{cyt}$ oscillations were unaltered by *XVE:ADPRc* induction (Fig. 4B). The invariance of circadian period may be explained by the simulated evidence that transient cADPR-induced alterations in oscillator transcripts do not alter circadian period. This invariance also reveals remarkable stability of the oscillator.

We investigated whether continuous [cADPR] synthesis alters circadian behavior. We overexpressed *Aplysia ADPRc* using the constitutive 35*S* promoter (*35S:ADPRc*) (*10*). This approximately doubled [cADPR] [0.38 ± 0.09 pmol · μg $protein^{-1}$ (line 1); 0.45 ± 0.13 pmol · μg

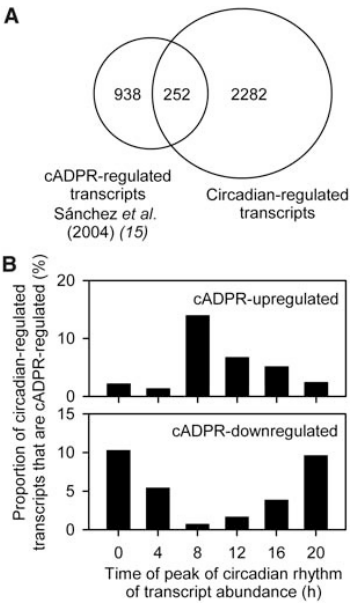

Fig. 1. Circadian- and cADPR-regulated transcripts overlap significantly. (**A**) The numbers of circadian- and cADPR-regulated transcripts (*15*), and the number common to both transcriptomes. (**B**) The proportion of circadian-regulated transcripts that were cADPR-regulated, binned according to the circadian peak of abundance.

[1]Department of Plant Sciences, University of Cambridge, Downing Street, Cambridge CB2 3EA, UK. [2]Department of Engineering, University of Cambridge, Trumpington Street, Cambridge CB2 1PZ, UK. [3]Department of Biology, University of York, York YO10 5YW, UK.

*Present address: School of Biosciences, Geoffrey Pope Building, University of Exeter EX4 4QD, UK.

†Present address: Institute for Plant Biology, Copenhagen University, Thorvaldsensvej 40, 1871 Frederiksberg, Denmark.

‡To whom correspondence should be addressed. E-mail: alex.webb@plantsci.cam.ac.uk

protein^{-1} (line 2), 0.23 ± 0.05 pmol · μg protein^{-1} (wild type); n = 5]. [cADPR] was not measured over a circadian time course because of poor *35S:ADPRc* plant growth, which was consistent with a lesion to stress and circadian signaling (*2*, *3*). The mean period of circadian rhythms in leaf position was unaltered in *35S:ADPRc* [P = 0.51 by two-sample t test (fig. S8, A and B)]. However, there was a broader period length distribution compared with the wild type when all replicates with all lines were considered, as indicated by both the spread and significantly different standard deviation [(Fig. 4C) Ws-2 wild type: SD = 0.71 hours, spread = 22.3 to 25.8 hours, n = 45; *35S:ADPRc*: SD = 0.96 hours, spread = 21.9 to 26.3 hours, n = 106; test of homogeneity of variances Levene statistic = 5.81, P = 0.017**]. ADPRc overexpression disturbed the sinusoidal circadian $[Ca^{2+}]_{cyt}$ oscillations (fig. S9) and increased the relative amplitude error (RAE) (*22*) of the oscillations [(Fig. 4D) wild-type RAE, 0.28 ± 0.02; line 1, 0.42 ± 0.03; line 2, 0.55 ± 0.06]. The greater RAE indicated a poorer Fourier fit to the data. Because $[Ca^{2+}]_{cyt}$ images were obtained from groups of 15 to 20 seedlings (*23*), the increased RAE of circadian $[Ca^{2+}]_{cyt}$ oscillations could reflect increased variability of the $[Ca^{2+}]_{cyt}$ oscillation period between individuals. The simulations suggested that oscillator period is affected by high [cADPR] (Fig. 3B). We found that *35S:ADPRc* affected oscillator period by increasing variability, which might be a consequence of differing levels of cADPR between seedlings and cells having different effects on period.

Finally, we investigated how continuously suppressed cADPR signaling affected the clock by treating seedlings with nicotinamide. The circadian period of rhythms of leaf position was significantly longer with 10 mM or 50 mM nicotinamide compared with water and osmotic controls. The period increase was nicotinamide concentration–dependent [(Fig. 4, E and F, and table S2) control period 23.6 ± 0.3 hours; 10 mM nicotinamide, 24.5 ± 0.3 hours, $P < 0.001$; 50 mM nicotinamide, 26.6 ± 0.4 hours, P = 0.002; comparisons by two-sample t tests]. Circadian rhythms of leaf position were unaltered by other chemical modifiers of Ca^{2+} signaling [$CaCl_2$, $GdCl_3$, $LaCl_3$, EGTA, or U73122 (table S2)]. At 50 mM, nicotinamide also lengthened circadian period of *CAB2:luciferase* luminescence [nicotinamide, 25.3 ± 0.4 hours; 50 mM mannitol, 26.6 ± 0.5 hours (Fig. 4G and fig. S10)], the

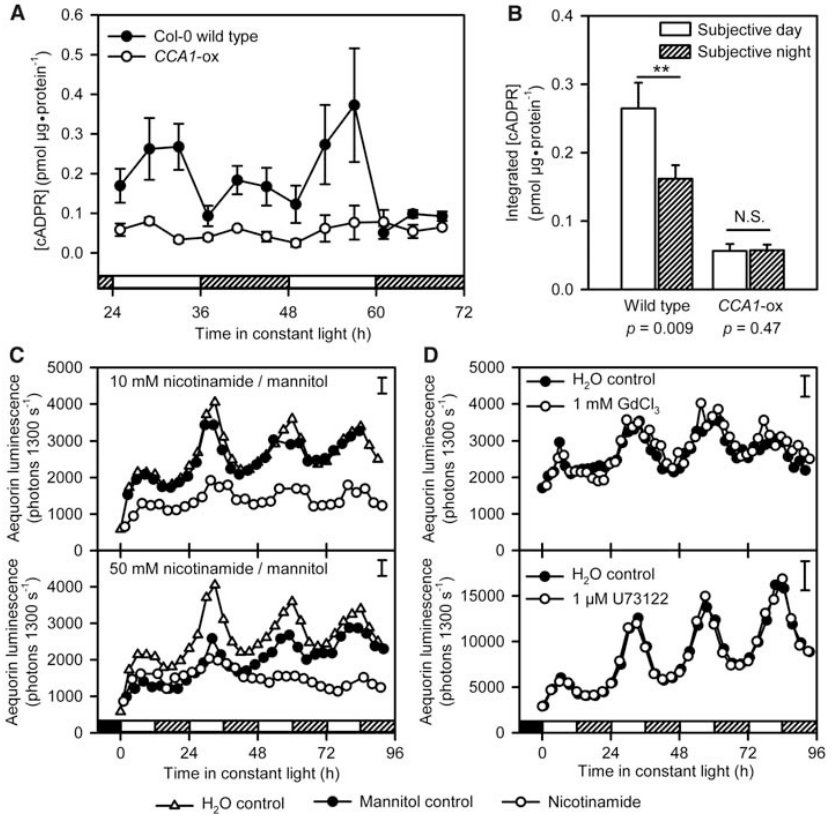

Fig. 2. [cADPR] oscillates with a circadian rhythm and a cADPR signaling antagonist inhibits circadian $[Ca^{2+}]_{cyt}$ oscillations. (**A**) [cADPR] during 48 hours of constant light in Col-0 wild type and arrhythmic *CCA1*-ox (n = 5; ± SEM). Seedlings were transferred to LL 24 hours before sampling. (**B**) Data from (A) binned according to subjective day and night, P values from two-sample t tests indicated. (**C** and **D**) Circadian $[Ca^{2+}]_{cyt}$ oscillations in 11-day-old seedlings dosed every 3 hours with (C) nicotinamide, mannitol (osmotic control), or water; (D) $GdCl_3$ and U73122. n = 12; greatest SEM for each panel at top right. On x axes are black bars, darkness; white bars, light, hatched bars, subjective dark under LL.

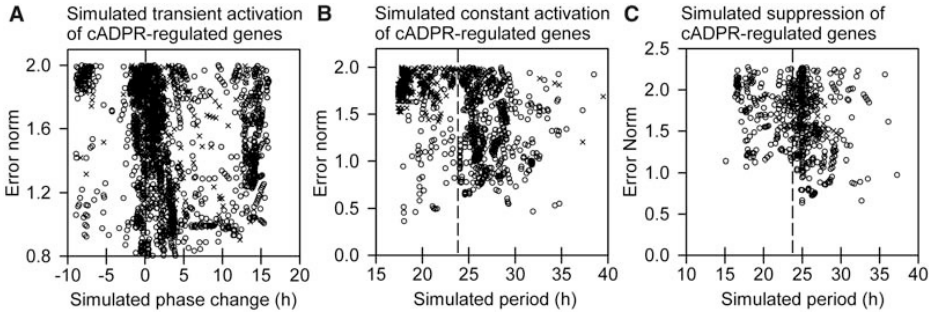

Fig. 3. Constraint of a mathematical model for the *Arabidopsis* circadian clock (*21*) to explore how cADPR-induced alterations in *CCA1/LHY*, *GI*, and *TOC1* transcript abundance alter clock function. (**A**) Transient constraint of model parameters to impose cADPR-induced alterations in clock transcript abundance caused variable phase changes that depended on parameters constrained. (**B** and **C**) For uniform parameter constraints analogous to continuous cADPR signaling (B) and repression (C), the period changed by a magnitude that depended on the parameters constrained. (A to C) Each point represents a different parameter pair that correctly constrained simulated transcripts when cADPR synthesis was induced between ZT20 to 6 or ZT20 to 24 (crosses) and ZT11 to 19 (circles); explained in fig. S5B. Broken lines indicate period or phase of unperturbed simulated oscillator. Phase and period calculated after simulated 480 hours in LL; arrhythmic simulations excluded from plots because perturbation of cADPR signals in plants (Fig. 4) did not cause arrhythmia.

period of *CAB2* transcript abundance [(Fig. 4H) 50 mM nicotinamide, 26.0 hours; H_2O control, 23.3 hours; 50 mM mannitol, 22.3 hours], and *CCA1*, *TOC1*, and *LHY* transcript abundance (Fig. 4H) (*10*). Inhibition of cADPR synthesis, therefore, lengthened the period of the clock and its outputs.

Our data demonstrate the existence of a feedback loop within the plant circadian clock that incorporates cADPR, because [cADPR] is regulated by the circadian oscillator and cADPR, in turn, regulates the abundance of clock gene transcripts. Circadian oscillations in [cADPR] also regulate circadian $[Ca^{2+}]_{cyt}$ oscillations. It has been suggested that diurnal variations in $[Ca^{2+}]_{cyt}$ are regulated by the Ca^{2+} sensor CAS through an IP_3-mediated system (*24*). Our data indicate that IP_3 does not contribute to the control of circadian $[Ca^{2+}]_{cyt}$ oscillations (Fig. 2D). The circadian feedback loop incorporating cADPR may interface the clock with exogenous stimuli that transiently elevate intracellular [cADPR] and $[Ca^{2+}]_{cyt}$ and so optimize the adaptive value of circadian control during unpredictable short-term environmental variations. We have established that cytosolic signaling molecules represent a hitherto unrecognized class of circadian clock components.

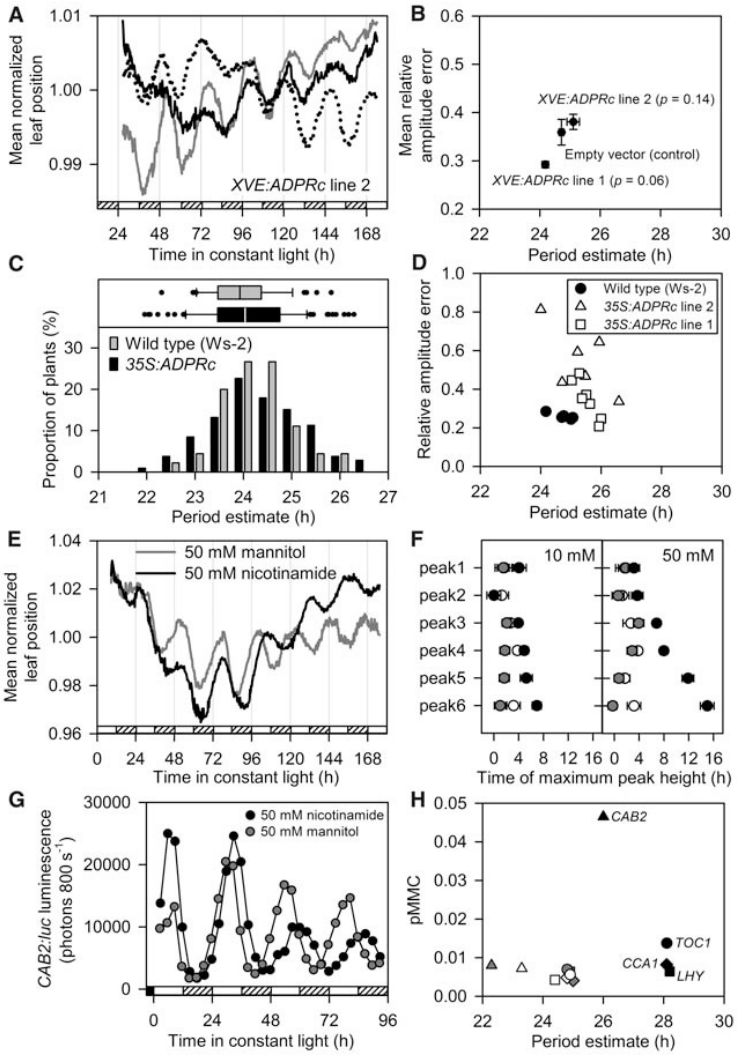

Fig. 4. The circadian clock and its outputs are altered by continuous disruption of cADPR signaling. (**A** and **B**) *XVE:ADPRc* induction at ZT2 on day 1 of LL, (A) circadian rhythm of leaf position (n = 30 to 32) and (B) analysis of circadian $[Ca^{2+}]_{cyt}$ oscillations; P values from two-sample t test comparisons of period to control are indicated and were not significant. Relative amplitude error quantifies the rhythmic robustness (0 is sine wave and 1 is poor Fourier fit; n = 4; mean ± SEM). In (A), black is 100 μM β-estradiol (XVE inducer), gray is empty vector control (P = 0.38 in two-sample t test period comparison with induced plants), broken line, 0.1% DMSO solvent control (P = 0.32). (**C** and **D**) In *35S:ADPRc*, (C) distribution of period lengths of circadian rhythms of leaf position for all replicates and both lines; (D) analysis of circadian $[Ca^{2+}]_{cyt}$ oscillations for *35S:ADPRc* line 1, line 2, and Ws-2 wild type. (**E**) Circadian rhythm of leaf position of seedlings treated at ZT2 with a single dose of 50 mM nicotinamide or 50 mM mannitol (n = 46). (**F**) Time of circadian peaks of leaf position in seedlings treated as for (E) (n = 5 to 26). (**G**) Circadian rhythm of *CAB2:luciferase* luminescence in seedlings dosed every 3 hours with 50 mM nicotinamide (mannitol control shown for clarity). (**H**) Circadian period of *CAB2* (triangles), *TOC1* (circles), *LHY* (squares), and *CCA1* (diamonds) transcript abundance in seedlings dosed every 3 hours with 50 mM nicotinamide. (E to H) Treatment designations: open is H_2O control; gray is mannitol control; black is nicotinamide. For comparability with (E and F), alterations in circadian rhythms of $[Ca^{2+}]_{cyt}$ and *CAB2* promoter activity after single doses of 50 mM nicotinamide are in fig. S10.

References and Notes

1. Y. Ouyang, C. R. Andersson, T. Kondo, S. S. Golden, C. H. Johnson, *Proc. Natl. Acad. Sci. U.S.A.* **95**, 8660 (1998).
2. A. N. Dodd *et al.*, *Science* **309**, 630 (2005).
3. R. M. Green, S. Tingay, Z. Y. Wang, E. M. Tobin, *Plant Physiol.* **129**, 576 (2002).
4. D. A. Rand, B. V. Shulgin, J. D. Salazar, A. J. Millar, *J. Theor. Biol.* **238**, 616 (2006).
5. S. Panda, J. B. Hogenesch, S. A. Kay, *Nature* **417**, 329 (2002).
6. D. Alabadí *et al.*, *Science* **293**, 880 (2001).
7. C. H. Johnson *et al.*, *Science* **269**, 1863 (1995).
8. M. Ikeda *et al.*, *Neuron* **38**, 253 (2003).
9. G. J. Allen, S. R. Muir, D. Sanders, *Science* **268**, 735 (1995).
10. Materials and methods are available on *Science* Online.
11. Microarray data deposited at ArrayExpress (www.ebi.ac.uk/arrayexpress/), accession E-TABM-331.
12. S. L. Harmer *et al.*, *Science* **290**, 2110 (2000).
13. K. D. Edwards *et al.*, *Plant Cell* **18**, 639 (2006).
14. M. Straume, *Methods Enzymol.* **383**, 149 (2004).
15. J. P. Sánchez, P. Duque, N. H. Chua, *Plant J.* **38**, 381 (2004).
16. Z. Y. Wang, E. M. Tobin, *Cell* **93**, 1207 (1998).
17. J. K. Sethi, R. M. Empson, A. Galione, *Biochem. J.* **319**, 613 (1996).
18. A. A. Véry, J. M. Davies, *Proc. Natl. Acad. Sci. U.S.A.* **97**, 9801 (2000).
19. I. Staxén *et al.*, *Proc. Natl. Acad. Sci. U.S.A.* **96**, 1779 (1999).
20. R. M. Graeff, T. F. Walseth, K. Fryxell, W. D. Branton, H. C. Lee, *J. Biol. Chem.* **269**, 30260 (1994).
21. J. C. Locke *et al.*, *Mol. Syst. Biol.* **1**, E9 (2005).
22. J. D. Plautz *et al.*, *J. Biol. Rhythms* **12**, 204 (1997).
23. J. Love, A. N. Dodd, A. A. R. Webb, *Plant Cell* **16**, 956 (2004).
24. R. H. Tang *et al.*, *Science* **315**, 1423 (2007).

25. The authors thank N.-H. Chua for inducible *XVE:ADPRc* lines; H. Okamoto, S. Takasawa, H.-C. Lee, and R. Graeff for *Aplysia ADPRc*; H.-C. Lee, R. Graeff, E. Zocchi, and S. Bruzzone for advice; B. Handley for programming assistance; and J. C. Gray, E. A. C. MacRobbie, and J. Carr for critical reading. Research funded by the U.K. Biotechnology and Biological Sciences Research Council (BBSRC), the Royal Society of London, the Broodbank Foundation Cambridge, the Gates Foundation, Corpus Christi College Cambridge, Coordenação de Aperfeiçoamento de Pessoal de Nível Superior (CAPES) Brazil, and the Danish Research Council.

Supporting Online Material

www.sciencemag.org/cgi/content/full/1146757/DC1
Materials and Methods
Figs. S1 to S10
Tables S1 to S2
References
Spreadsheets S1 to S3

20 June 2007; accepted 27 September 2007
Published online 15 November 2007;
10.1126/science.1146757
Include this information when citing this paper.

Supporting Figures

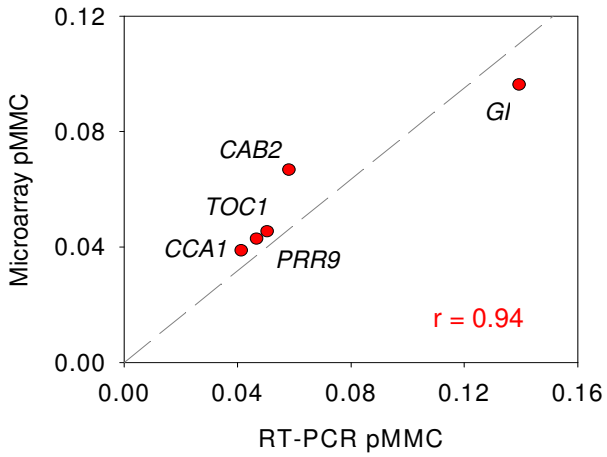

Supporting Fig. S1. Verification of microarray analysis by comparison of the multiple measures-corrected probability statistic of rhythmicity (pMMC) of selected array transcripts with RT-PCR analysis on the same mRNA samples.

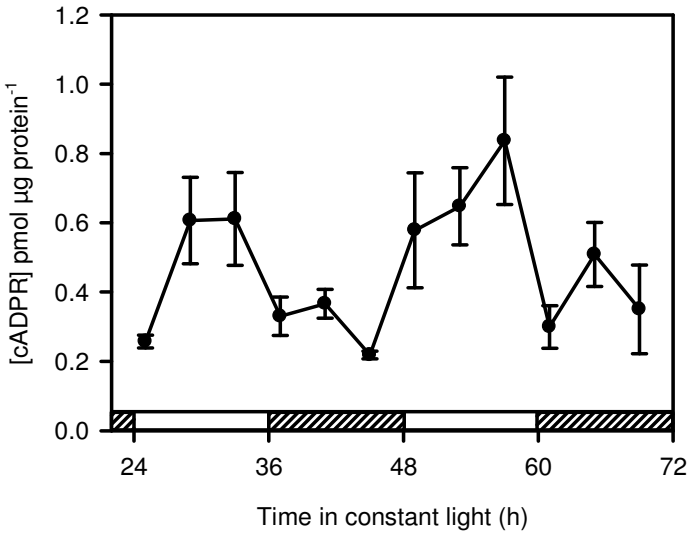

Supporting Fig. S2. Circadian oscillations of [cADPR] measured in an identical but independent experiment from Fig. 2A. [cADPR] during 48 h of constant light in Col-0 wild type (n = 5; ± s.e.m.), measured using a coupled cycling assay (described in this Supporting Material). Tissue was from seedlings germinated/grown on 0.5 x MS, 0.8 % (w/v) agar for 3 weeks under 12 h light, 12 h dark and transferred to continuous light 24 h before sampling.

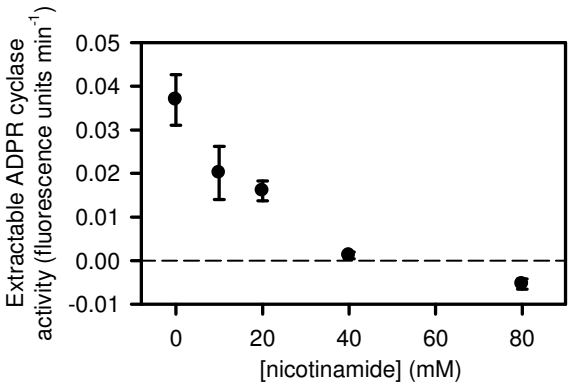

Supporting Fig. S3. Nicotinamide inhibits ADPRc activity from Arabidopsis tissue extracts, *in vitro*. ADPRc activity was measured by monitoring ADPRc-mediated synthesis of fluorescent cyclic GDP-ribose from nicotinamide guanine dinucleotide *(1)* (n = 5; ± s.e.m.).

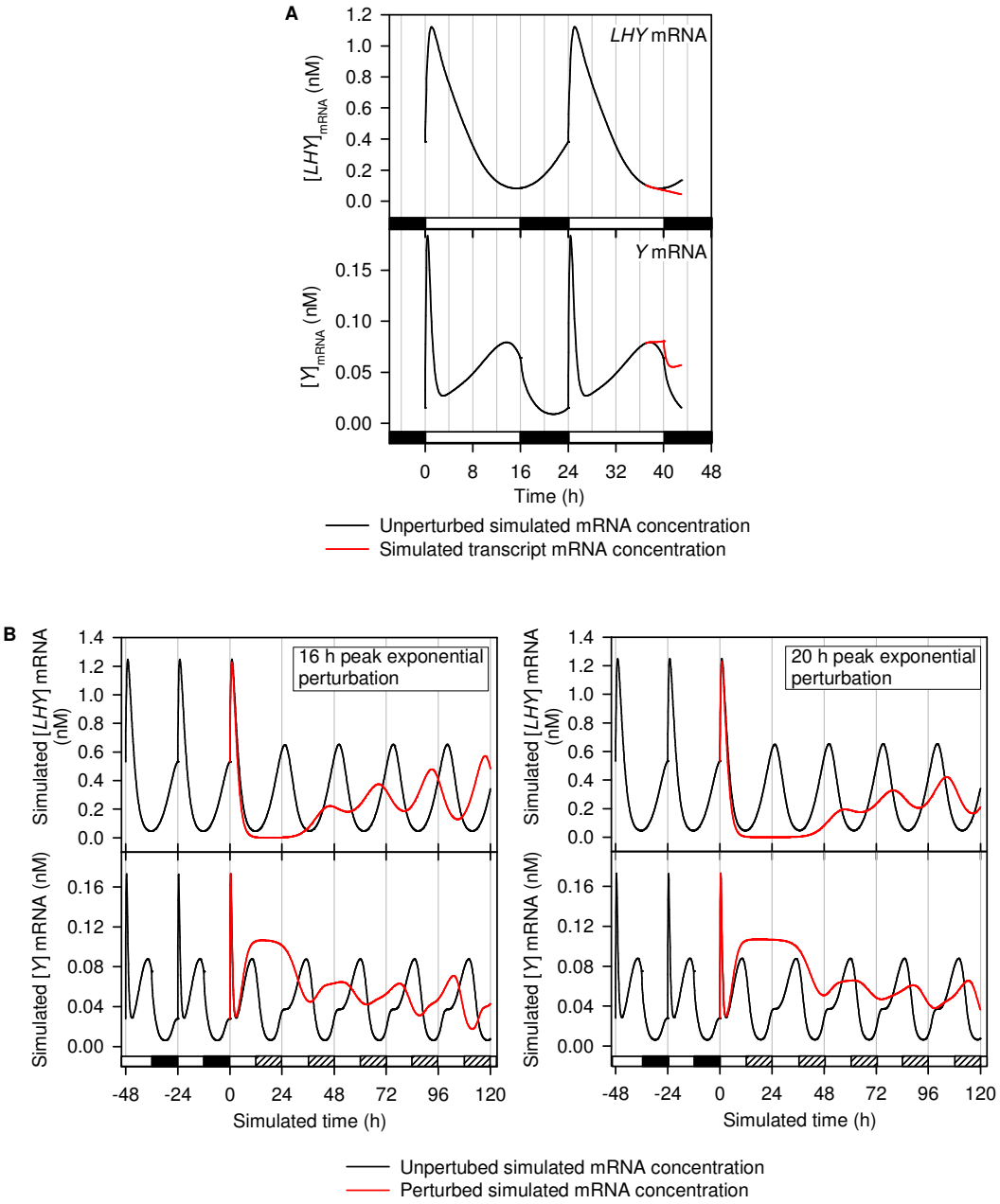

Supporting Fig. S4. Examples of estimation and simulation of cADPR-induced alterations to a model *(2)* of the circadian clock. **A,** Under 16 h light / 8 h dark, estimation of cADPR-induced *(3)* alterations in *LHY* and *Y* (*GI*) transcript abundance, for the parameter pair with the lowest error norm (goodness-of-fit of simulated to real data). This best fit was a perturbation that commenced at ZT13 and peaked 6 h later. **B,** For exponential perturbation profiles that commenced at 0 h and peaked at 16 h or 20 h, simulated oscillations in *LHY* and *Y* mRNA concentration for perturbation of the parameter pair with the lowest error norm.

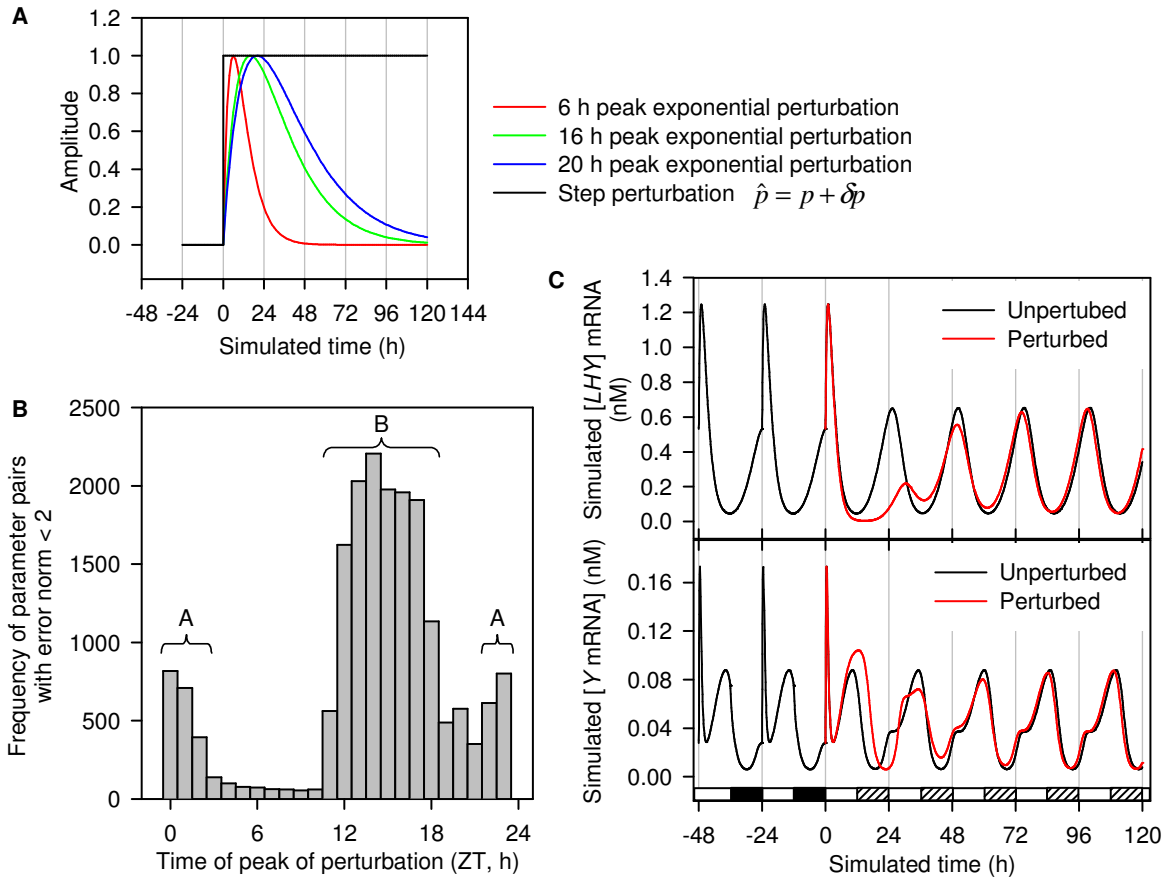

Supporting Fig. S5. Systematic perturbation of a mathematical model for the Arabidopsis circadian oscillator *(2)*, to investigate how cADPR-mediated changes in clock transcript abundance alter clock function. **A,** parameter perturbation profiles used to simulate changes in cADPR signal magnitude ($\hat{p} = p - \delta p$ profile for cADPR pathway suppression not shown). **B,** The number of perturbed parameter-pairs leading to changes in clock transcript abundance with error norm < 2 depended on time of induction, and separated into two clusters (marked A and B). **C,** Simulated oscillations in [*LHY*] and [*Y*] mRNA for perturbation of the parameter pair with lowest error norm, for an exponential (transient) perturbation profile that commenced at 0 h and peaked at 6 h. Note the period invariance. Error norm is the goodness-of-fit of simulated to real data *(3)*. cADPR-induced changes in oscillator transcript abundance: lower values indicate a closer match. Black bars on abscissa indicate darkness, white bars: light, hatched: subjective dark under LL.

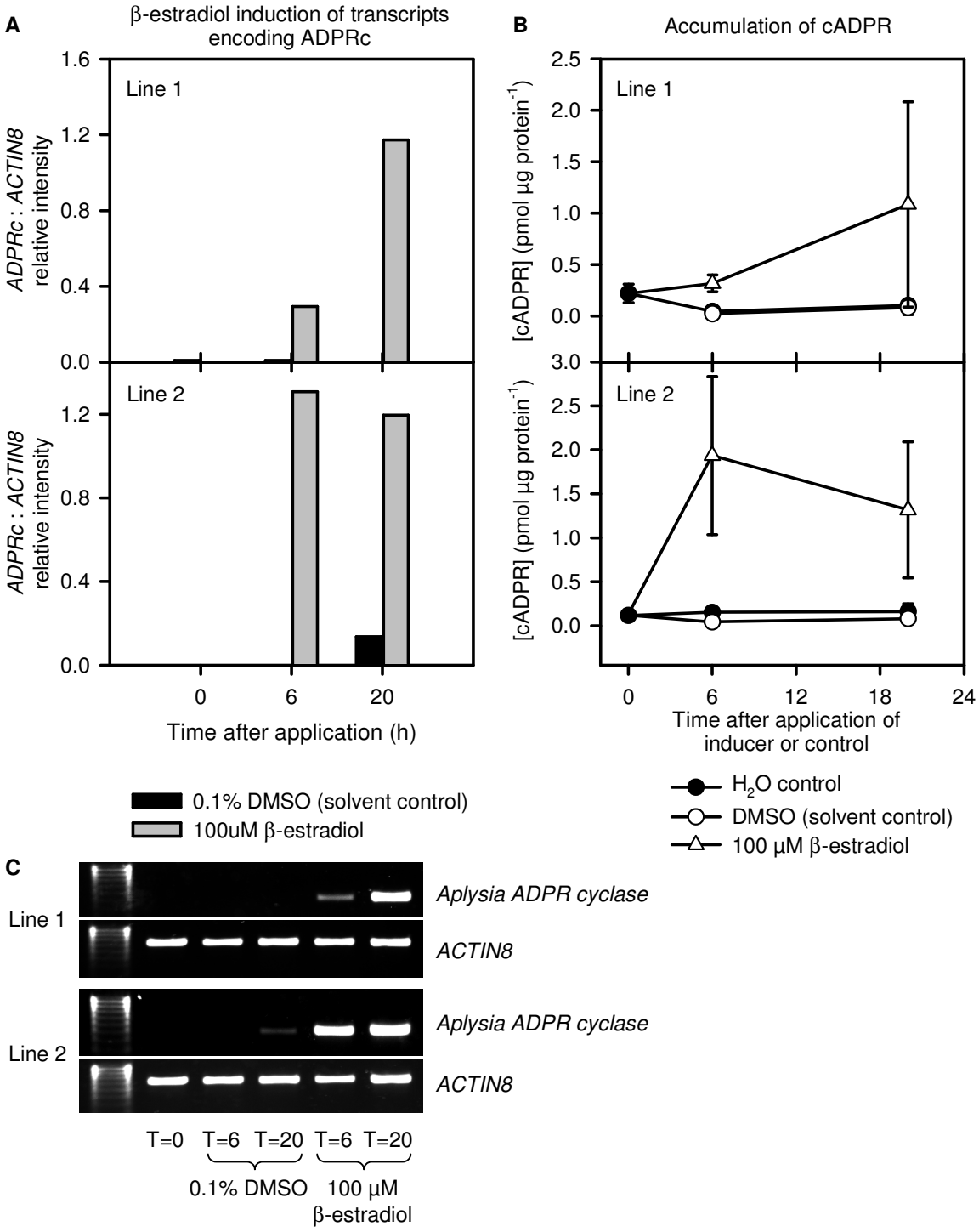

Supporting Fig. S6. [cADPR] was increased by induction of *Aplysia* ADPR cyclase in two lines independently transformed with *XVE:ADPRc (3)*. **A,B,** Magnitude of *ADPRc* transcript induction by 100 µM β-estradiol, compared to 0.1% DMSO solvent control, determined using semiquantitative RT-PCR (**A**) normalized to *ACTIN8*, (**B**) [cADPR] in the samples used for RT-PCR (n = 5 ± s.e.m.; mRNA pooled for RT-PCR), (**C**) RT-PCR products separated by agarose gel electrophoresis.

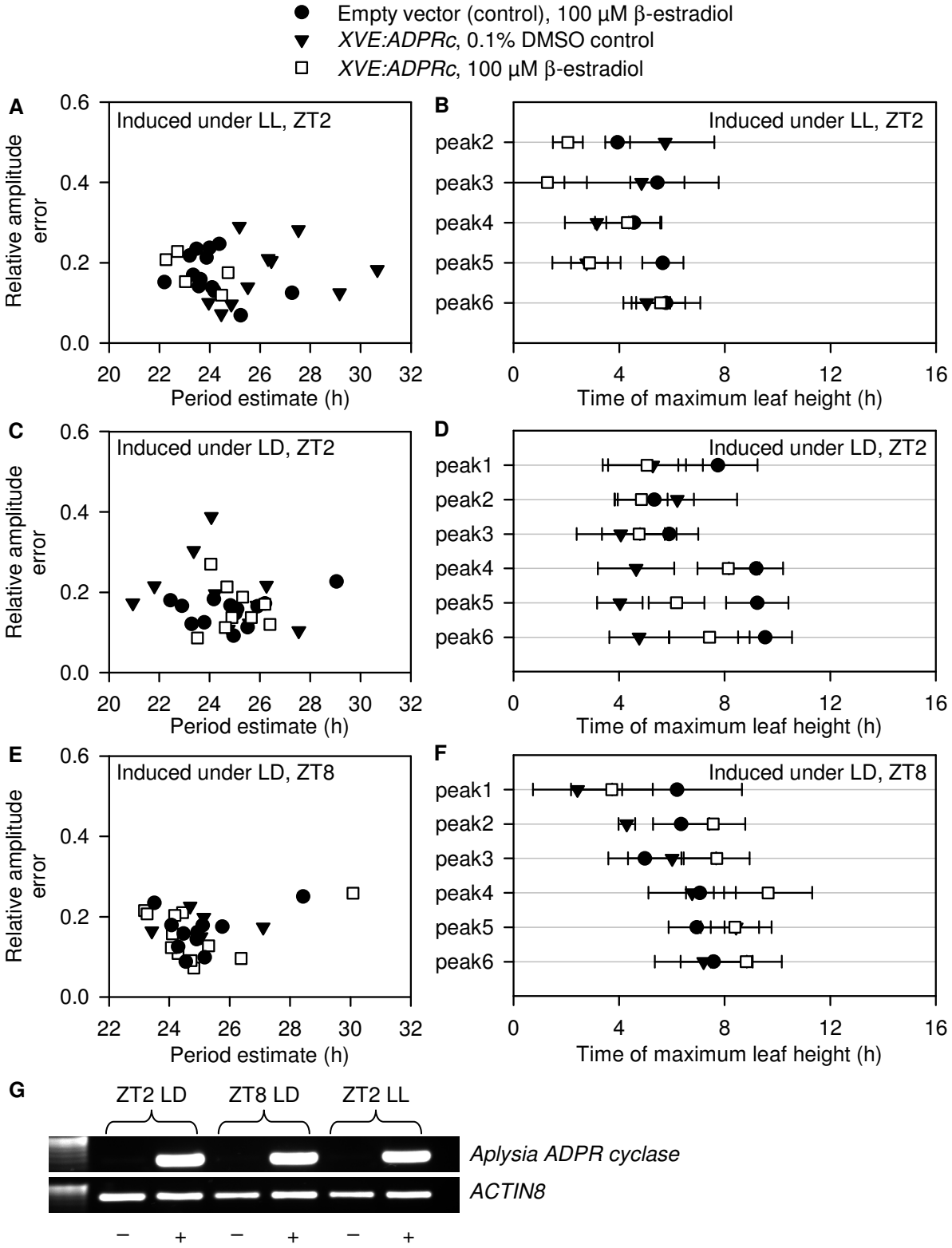

Supporting Fig. S7. Circadian rhythms of leaf position were unaltered by induction of *Aplysia* ADPR cyclase *(3)*. Seedlings transformed with *XVE:ADPRc* or *XVE:*[Empty vector] were dosed with 100 µM β-estradiol or 0.1% DMSO solvent control A**,B,** two hours after the onset of constant light, **C,D,** two hours or **E,F,** six hours after dawn on the final light-dark cycle before transfer to continuous light.

Time-lapse imaging commenced 24 h after β-estradiol application. **A,C,E,** Variation in period estimates in rhythmic replicate seedlings (*n* = 5 – 13). **B,D,F,** Time of circadian peak of leaf position for each 24 h period (n = 5 – 16; mean ± s.e.m.). **G,** *ADPRc* transcripts were verified by semiquantitative RT-PCR to have been induced in representative seedlings used to monitor leaf position for each induction time. The induction time (ZT), and whether induction occurred under the final light-dark cycle before constant light (LD) or on Day 1 of constant light (LL), is indicated above the gel. Identical samples were either induced with 100 μM β-estradiol or treated as a control with 0.1 % DMSO (+ and – below gel, respectively).

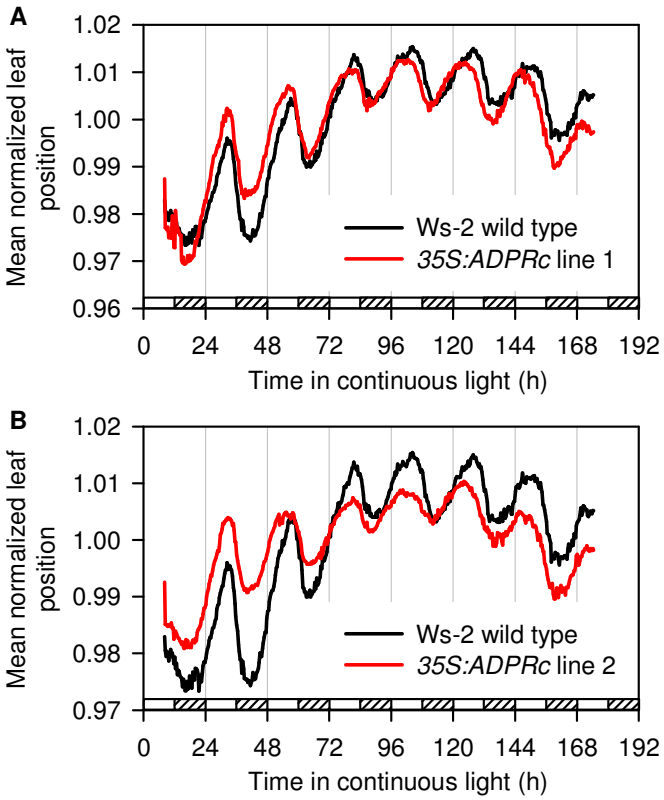

Supporting Fig. S8. Circadian rhythms of leaf position in two lines (**A,B**) that constitutively overexpressed *Aplysia* ADPR cyclase (*35S:ADPRc*). n = 52 - 54.

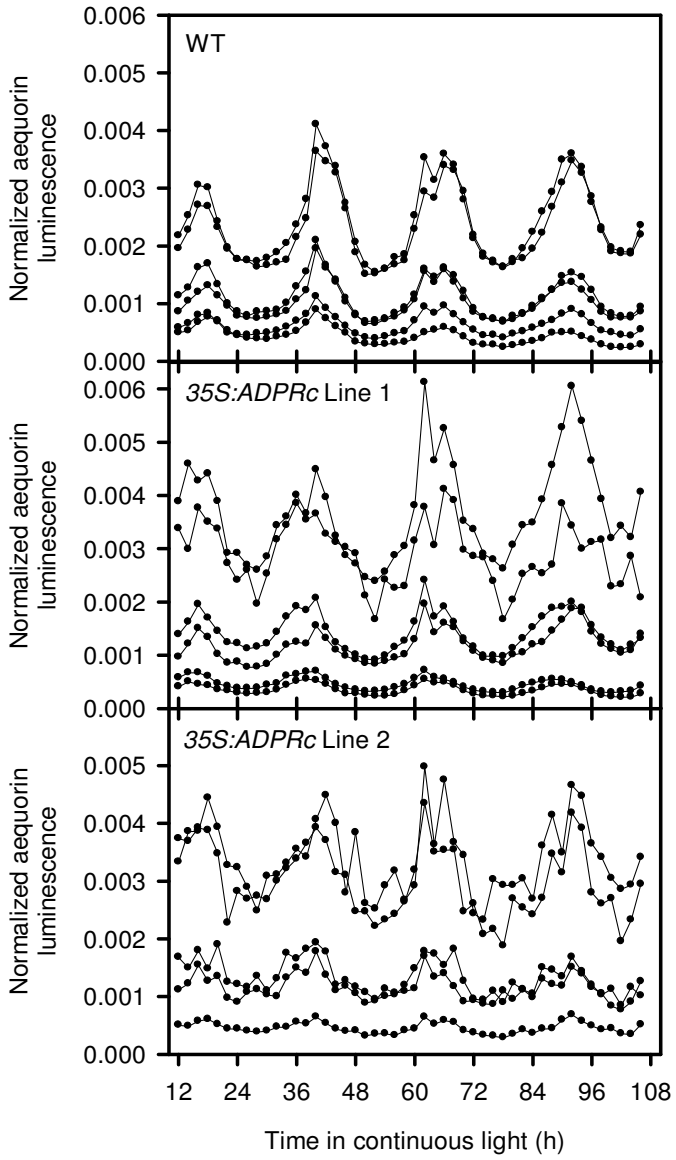

Supporting Fig. S9. Overexpression of ADP ribosyl cyclase in two independent lines reduced the robustness of circadian $[Ca^{2+}]_{cyt}$ oscillations relative to the wild type. Each trace is the aequorin luminescence from one cluster of 15-20 seedlings *(4)*. Seedlings were previously entrained for 10 d to cycles of 12 h light and 12 h darkness. The luminescence signal was normalized to the total aequorin content of the seedling cluster to compensate for higher aequorin content in Line 2. Total aequorin was measured by discharging available aequorin using 2 M $CaCl_2$ dissolved in 20 % ethanol *(5)*.

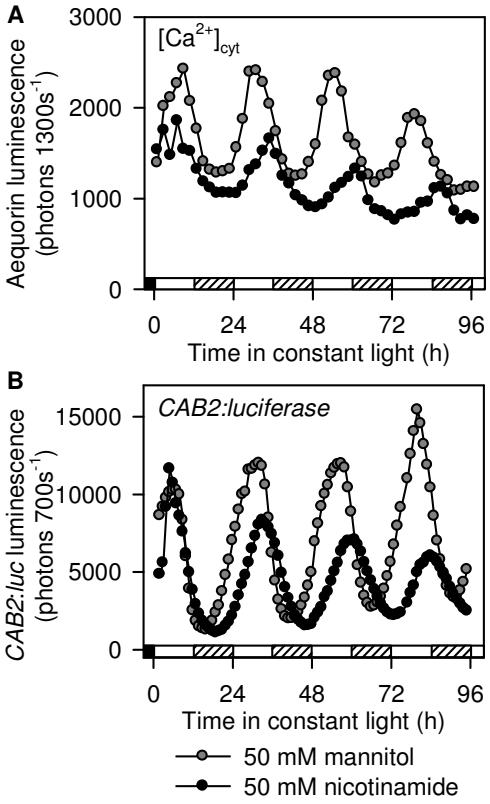

Supporting Fig. S10. Circadian $[Ca^{2+}]_{cyt}$ oscillations were partially inhibited by discontinuous application of 50 mM nicotinamide, which caused the circadian oscillator to adopt a longer period. These data indicate that partial inhibition of circadian $[Ca^{2+}]_{cyt}$ oscillations by nicotinamide was sufficient to alter the functioning of the circadian clock. **A,** Rhythms of aequorin luminescence had a longer circadian period and lower amplitude than controls when dosed 48 h and 24 h before constant light with 50 mM nicotinamide (period estimates: 50 mM nicotinamide, 24.6 ± 0.7 h, n = 20; 50 mM mannitol, 23.6 ± 0.4 h; n = 8; H_2O control, omitted from **(A)** for clarity, 23.8 ± 0.4 h; n = 20; period of $[Ca^{2+}]_{cyt}$ in presence of 50 mM nicotinamide is significantly different from the other two treatments (one-way ANOVA, $p < 0.0001$ with Tukey-Kramer post-test, $p < 0.001$ for both controls). **B,** Circadian rhythm of *CAB2:luciferase* luminescence after single dose of 50 mM nicotinamide at ZT2 (mannitol control shown for clarity; H_2O control was comparable; period estimates: 50 mM nicotinamide, 25.7 h ± 0.1 h; H_2O control, 24.4 h ± 0.1 h; 50 mM mannitol, 24.7 h ± 0.1 h). **A, B** Grey circles = 50 mM mannitol, black circles = 50 mM nicotinamide.

Supporting Tables

Treatment	Overlap with circadian		Significance		Significance
	Observed	Expected	(*p*-value)		(E-value)
Blue light	145	135	2.38×10^{-02}		1.62
Brassinolide *(7)*	63	41	1.80×10^{-04}		3.74
Brassinolide *(8)*	59	33	8.93×10^{-06}	*	5.05
cADPR	252	93	5.15×10^{-52}	*	51.28
cGMP	133	100	1.60×10^{-04}		3.79
Cold	195	92	1.23×10^{-24}	*	23.91
IAA *(7)*	32	27	5.05×10^{-02}		1.29
IAA *(8)*	51	40	1.64×10^{-02}		1.79
LPS	76	48	1.77×10^{-05}		4.75
OG	28	26	7.70×10^{-02}		1.11
Red light	237	96	6.64×10^{-41}	*	40.17
SNAP	75	40	9.50×10^{-08}	*	7.02

Supporting Table S1. Comparison of circadian-regulated transcripts to transcripts regulated by blue light *(6)*, brassinolide *(7, 8)*, cADPR *(3)*, cyclic guanosine monophosphate (cGMP) *(9)*, cold *(10)*, indole-3-acetic acid (IAA) *(7, 8)*, lipopolysaccharide (LPS) *(11)*, oligogalcturonide (OG) (12), red light *(13)* and S-Nitroso-N-acetylpenicillamine, (SNAP, a nitric oxide donor) (14). Transcripts regulated by cADPR shared both the greatest numerical overlap and the most statistically significant overlap with circadian-regulated transcripts. Red light- and cold-regulated transcripts had large but less significant overlaps with the set of circadian-regulated transcripts. The threshold for statistical significance was considered to be $p < 1 \times 10^{-5}$, as indicated by single asterisks on the table.

	Antagonist			H_2O control				Additional control [a]			
	Rhythmic seedlings (%)	Period (h) ± s.e.m	*n*	Rhythmic seedlings (%)	Period (h) ± s.e.m	*n*	Statistical significance	Rhythmic seedlings (%)	Period (h) ± s.e.m	*n*	Statistical significance
10 mM $CaCl_2$	72.9	23.81 ± 0.3	16	66.7	24.09 ± 0.6	14	p=0.68				
50 mM EGTA	68.2	24.25 ± 0.4	17	71.7	23.56 ± 0.3	20	p=0.16	65.2	24.19 ± 0.7	16	p=0.94
1 mM $GdCl_3$	62.5	24.18 ± 0.6	13	66.7	24.09 ± 0.6	14	p=0.92				
10 mM $LaCl_3$	60.9	24.15 ± 0.6	17	71.7	23.56 ± 0.3	20	p=0.40	80.4	23.83 ± 0.3	15	p=0.65
10 mM nicotinamide	80.4	24.50 ± 0.3	21	71.7	23.56 ± 0.3	20	p=0.03*	80.4	23.83 ± 0.3	15	p=0.12
50 mM nicotinamide[b]	65.2	25.60 ± 0.3	21	71.7	23.56 ± 0.2	20	p<0.01**	65.2	24.19 ± 0.6	16	p=0.06
50 mM nicotinamide[b]	76.6	26.59 ± 0.4	8	93.8	23.79 ± 0.3	15	p<0.01**	81.3	24.08 ± 0.5	14	p<0.01**
1 µM U73122	87.5	24.90 ± 0.7	12	93.8	23.79 ± 0.2	15	p=0.14	71.9	24.78 ± 0.3	10	p=0.88

[a] Additional controls for EGTA, $LaCl_3$ and nicotinamide were appropriate concentrations of mannitol; control for U73122 was inactive analogue of antagonist U73343; control for $CaCl_2$ and $GdCl_3$ was H_2O.

[b] Results from two independent experiments with 50 mM nicotinamide.

Supporting Table S2. Effect of pharmacological modifiers of Ca^{2+} homeostasis on circadian rhythms of leaf position. Total replicate numbers and nature of controls specified in table. The pharmacological agents were used modify $[Ca^{2+}]_{cyt}$ as follows: External $CaCl_2$ causes transient elevations in $[Ca^{2+}]_{cyt}$ *(15)*; EGTA reduces the magnitude of stimulus-induced $[Ca^{2+}]_{cyt}$ transients *(16)*; $GdCl_3$ and $LaCl_3$ inhibit extracellular Ca^{2+} influx by blocking plasma membrane ion channels *(17)*; 50 mM nicotinamide inhibits ADP ribosyl cyclase-dependent synthesis of cADPR (Fig. 2E, *(18)*); 1 µM U73122 inhibits InsP3 synthesis by phospholipase C *(19)*. *p*-values are outcome from two-sample t-test comparison of the period of inhibitor-treated seedlings against controls.

Supporting Materials & Methods

Microarray analysis of mature leaf circadian transcriptome

Arabidopsis thaliana Col-0 seeds were germinated in 48-unit trays containing a 1:1 mix of potting compost and vermiculite. Seeds were stratified at 4 °C for 48 h and germinated and grown at 20 °C under 12 h light / 12 h dark; 150 µmol photons m^{-2} s^{-1}. Plants were transferred to LL after 26 days growth, and harvesting of leaf material commenced 48 h after the start of LL. When harvesting began, no incipient inflorescences were visible within rosettes, rosettes were not senescent, and all aerial tissue was harvested with the exception of any dead cotyledons. Tissue was subsequently harvested every 4 h for a 24 h period.

RNA isolation was performed using TRIzol Reagent (Invitrogen, UK). Contaminating DNA was degraded by 30 min incubation at 37 °C with RQ1 RNase-free DNase 1 (Promega), and RNA purified using an RNeasy column (Qiagen, Germany). Poly(A)$^+$ RNA was isolated from 500 µg total RNA using PolyATract (Promega). RNA was reverse transcribed (RT) into cDNA with Superscript II RNase H$^-$ reverse transcriptase (Invitrogen), using 2.4 µg DNase-treated total RNA with 1 µg oligo (dT)12-18 primer and 200 U Superscript II RT, at 42 °C for 50 min. RT was then inactivated by incubation at 65 °C for 10 min.

Double-stranded cDNA synthesis *(20)* was performed using 3 µg total RNA and 100 ng anchored Eberwine oligo(dT)$_{21}$-T7 primer (5′-GCA TTA GCG GCC AAA TTA ATA CGA CTC ACT ATA GGG AGA T_{21} V-3′; V = A, C or G). Double-stranded cDNA was extracted using phase-lock gel heavy tubes (Eppendorf, Germany), and purified from primers and unincorporated nucleotides using BioGel P-6 microspin columns (BioRad, USA). cDNA was linearly amplified and labelled with amino-allyl UTP by *in vitro* transcription for 5 h at 37°C using the RiboMax™ kit (Promega, USA). Fluorescent dyes were chemically conjugated onto the amino-allyl labelled targets *(21)*. Labelled cRNA was purified from unincorporated dyes using Qiagen RNeasy Cleanup columns (Qiagen, Germany). The appropriate Cy3- and Cy5-labelled samples were subsequently combined and hydrolysed into 60 - 600 bp fragments by incubation for 15 min in RNA fragmentation buffer (Ambion, UK).

Oligonucleotide microarrays were obtained from D. Galbraith (Univ. Arizona). To reduce technical variation, all microarray slides were from a single print batch

(02.07.02.072-110). Circadian analysis was based on a common reference design: all cRNA samples from plants from 48 h to 72 h in LL were hybridized against the same reference (48 h) sample. Three biological replicates were used for each time-point. Labelled cDNA was added to 36 µl preheated (42°C) formamide-based hybridization buffer (MWG Biotech, Germany) and pipetted onto microarray slides. Slides were incubated at 42°C for 18 h in a light-proof water bath. Arrays were then washed in light proof slide boxes: twice for 5 min in 2 x SSC (saline sodium citrate), 0.5% (v/v) SDS preheated to 55°C, three times for 5 min in 0.5 x SSC at room temperature and twice for 5 min in 0.05 x SSC at room temperature. 20 x SSC was 3 M sodium chloride, 0.3 M sodium citrate, pH 7.0.

Slides were scanned (Axon 4000B Scanner, Axon Instruments, USA) and spot finding performed with GenePix Pro 5 (Axon) using diameters between 10 µm and 20 µm. Microarray elements were re-annotated using the latest *A. thaliana* genome annotations from The Arabidopsis Information Resource (TAIR, http://www.arabidopsis.org). Data were normalised and microarrays compared using GeneSpring (Silicon Genetics, USA). Transcripts with circadian rhythms were identified using a modified version of COSOPT *(22, 23)*, with a period window of 16 - 32 h, and all patterns with multiple measure corrected probability (pMMC) ≤ 0.15 were considered to be circadian regulated and used for further analysis. 18,891 transcripts were consistently detected across the seven timepoints.

Transcriptome comparison and analysis

Circadian-regulated transcripts were placed into groups (bins) according to the zeitgeber time of their maximal relative abundance. The TAIR IDs of transcripts in each bin were then compared to those found in the total dataset for cADPR-regulated transcripts using a custom Python script (http://www.python.org). The absolute number of transcripts in common in each comparison was expressed as a percentage of the total number of transcripts in each circadian time bin. We used SIFT *(24)* to identify motifs that were over-represented in the promoter regions of genes regulated by cADPR. The evening element (AAAATATCT, *(22)*) was the most significantly over-represented motif in the promoters of genes encoding cADPR-upregulated transcripts. The element occurred in the 1 kb upstream regions of 119 of 578 (20.6%) genes encoding transcripts up-regulated by cADPR. The binomial distribution

implemented in SIFT reported the probability of this occurrence as $2x10^{-28}$ (sequences with associated probabilities lower than $1x10^{-5}$ are regarded as significant). In contrast, the evening element occurred in only 19 of the 354 (5.4%) promoters of genes encoding transcripts down-regulated by cADPR. This was below the expected background frequency for the motif. Additionally, the second most significant motif recognised by SIFT in the promoters of genes encoding transcripts up-regulated by cADPR was the G-box (CACGTG), an abscisic acid response element (ABRE)-related sequence, which had an associated probability of just $4.17x10^{-11}$.

Determination of [cADPR] and ADP ribosyl cyclase activity

For measurement of [cADPR] over a circadian timecourse, Col-0 seedlings were grown on 0.5 x MS, 0.8 % (w/v) agar for 20 days under 12 h light, 12 h dark and transferred to continuous light 24 h before sampling, to ensure that the [cADPR] timecourse incorporated the second and third days under constant conditions. cADPR was extracted from 0.2 g of previously powdered and liquid N_2-frozen aerial tissue. cADPR was extracted in 0.7 M perchloric acid and measured using a fluorescence-based cycling assay *(25)*. The cADPR-dependent increase in fluorescence was measured over an 8 hour period at 25 °C, and a parallel assay was performed for each replicate to control for potential incomplete enzymatic removal of NAD^+ *(25)*. [cADPR] was normalized to the protein concentration of the extract. ADP ribosyl cyclase activity was determined using the fluorescent surrogate of NAD^+, NGD^+ *(1)*, using 1 g of fresh aerial tissue that was desalted using Sephadex G25 (Amersham PD-10 columns) and subsequently concentrated using protein concentration spin columns (VivaScience VS0291). ADP ribosyl cyclase activity was measured at 25 °C.

Imaging of aequorin and luciferase activities

Circadian rhythms of aequorin and luciferase luminescence were measured using a Photek IFS32 photon counting camera as described previously *(4)*. Sterile solutions of Ca^{2+}-signalling antagonists mixed with 5 µM coelenterazine or 5 mM luciferin were applied topically to seedlings either immediately after each integration time-point, or in a single dose mixed with 5 µM coelenterazine, depending on the type of experiment being performed. It was ensured that the aerial tissue of seedlings (leaves, cotyledons and hypocotyls) were coated with the inhibitor solution. Circadian period and phase estimates, and relative amplitude errors (RAE), were obtained using Fast-

Fourier Transform (non-liner least squares method) conducted with the Biological Rhythms Analysis Software System (BRASS, http://millar.bio.ed.ac.uk/PEBrown/BRASS/BrassPage.htm) *(26)*. For measurement of *CAB2:luciferase* rhythms in the presence of 50 mM nicotinamide, 50 mM nicotinamide was applied 48 h and 24 h before transfer to LL, to ensure comparability with equivalent measurements of circadian rhythms in leaf position.

Semi-quantitative RT-PCR to determine abundance of circadian-regulated transcripts and transgenic ADP ribosyl cyclase

For circadian timecourses, aerial portions of inhibitor-treated seedlings were harvested every 4 h for 48 h after 24 h in LL. Total RNA was extracted with TRIzol (Invitrogen, Paisley, UK) and treated with RQ1 DNase I (Promega, Madison, WI) for 30 min at 37 ^{o}C. RNA was purified using RNeasy Columns (Qiagen GmbH, Hilden, Germany) according to manufacturer's instructions. 2.5 µg RNA was combined with 1 µg oligo $(dT)_{12-18}$ primer (Roche, Lewes, UK), heat denatured at 70 ^{o}C for 10 min, and reverse transcribed into first-strand cDNA using SuperScript II (Invitrogen). For PCR, 1 µl first-strand cDNA was amplified with 0.2 µM of each of the forward and reverse primers for *CCA1* (5′ - ACTTTCGCCTCATCATTT - 3′ and 5′ - ACCATTGGTGCCATCC- 3′), *LHY* (5′ - GTGGCTCAAATACACCTTC- 3′ and 5′ - CAACACCGATCATTACTACTC- 3′), *TOC1* (5′ - CACATTCCCTTGAGCG- 3′ and 5′ - TTCCTAACAAACTGACCCT- 3′), *CAB2* (5′ - CCCTGGAGACTACGGATGG- 3′ and 5′ - AAGCGTTGTTGTTGACTGGAT- 3′) and *ACTIN 8* (5′ - CTCCAGCTATGTATGTTGCCATTC- 3′ and 5′ - CATACTCTGCCTTAGAGATCCAC- 3′). *Aplysia ADPR cyclase* transcripts were quantified using the primers 5' - GTTGGAGAATGTGTTCCTTGG - 3' (FP) and 5' - TAAGCTGGTACCTTGGGATTC - 3'. The linear range of amplification was between 22 and 32 cycles, so all products were quantified after 28 cycles. RT-PCR products were separated on a 1.5 % (w/v) agarose gel and band intensities were measured using ImageQuant (Amersham, UK). Mean band intensities from two replicates were normalised to *ACTIN8* and plotted as mean-centred values. Period estimates were obtained using the COSOPT algorithm *(23)*.

Imaging circadian rhythms of leaf position

Seeds were surface-sterilized *(4)* and plated onto media comprising 1 x Murashige & Skoog (MS) medium, and 1% (w/v) agar, then stratified for 4 days at 4 ^{o}C. Seeds were germinated and initially grown under LL (20 - 30 µmoles photons m^{-2} s^{-1}, 21 ^{o}C) for 6 days in a Sanyo MLR350 growth chamber, then entrained in 12 h light/12 h dark cycles for 6 days (75 - 100 µmoles m^{-2} s^{-1}, 21 ^{o}C). Inhibitor solutions were applied 24 and 48 h before transfer to LL, with 200 µl of each solution applied to each seedling. 1.5 cm^2 agar blocks that supported each seedling were transferred to vertical 25-well tissue culture dishes *(27)*. Treatments were randomized within each vertical plate and within the growth chamber to eliminate positional effects. The vertical plates were transferred to LL (100 µmoles m^{-2} s^{-1}, 21 ^{o}C) and circadian rhythms of leaf position were recorded with time-lapse image capture using an array of video cameras synchronised via a video switching unit that was controlled by custom MetaMorph™ journals (Universal Imaging Corp., *(27)*). Leaf position data was extracted from time-lapse sequences using MetaMorph™. Rhythmic traces were analysed using the BRASS software package (described in imaging section above and *(26)*), and scored as having a circadian period if the principal rhythmic component exhibited a period between 15 h and 35 h *(27)*. Period estimates excluded the first 24 h of data, and were calculated from individuals with a minimum of three complete 24 h cycles. Peak time analysis was conducted using traces from all individuals (replicate numbers for any given experiment are therefore dependent on the type of analysis).

Constitutive expression of* Aplysia *ADP ribosyl cyclase

Aplysia californica ADPRc was PCR-amplified from pPIC9 (Invitrogen) using primers (FP: 5'-ACTCGCGAGTTGGAGAATGTGTTC-3'; RP: 5'-TTATAAACCTCTAACGAAACGCCTC-3') that excluded the first 78 nucleotides of ADPRc which encode an animal signal peptide *(3)*. The PCR fragment was cloned into the pBIN35S:H2B-mYFP binary vector (a gift from Dr. Jim Haseloff, Department of Plant Sciences, University of Cambridge) from which the H2B-mYFP sequence had been excised. The construct was transferred from *E. coli* strain DH5α to *Agrobacterium tumefaciens* strain DB3.1. Arabidopsis plants were transformed using floral dips into *Agrobacterium* cultures in order to obtain kanamycin-resistant T_1 progeny. Homozygous stably-transformed lines were subsequently transformed with

pJAA *35S:APOAEQUORIN,* which conferred phosphinothricin resistance for selection of *35S:APOAEQUORIN* transformed lines.

Simulation of effect of cADPR on the* Arabidopsis *circadian clock

Simulating transient effects of cADPR upon the oscillator

Inducible expression of ADPRc by β-estradiol leads to transient alterations in circadian clock transcript abundance. To characterize the signal of this pathway, the parameters of the Locke model equations for the plant circadian clock *(2)* were perturbed as time-varying functions $\hat{p}(t) = p+\delta(t)$, where $\hat{p}$ is the vector of perturbed model parameters, p the nominal parameter vector, and δ the perturbation profiles (Fig. 3A). These profiles are characterised by two distinct classes. The first class reflects the observed transient nature of the pathway after induction of *XVE:ADPRc*, and will be referred to as the *exponential* profile due to the exponential function in its definition.

$$\delta(t)= \frac{Ate^{-\beta t}}{\beta} \qquad (1)$$

where A is the amplitude of the perturbation at its peak, $t=\beta$. To remain consistent with the published data *(3)*, three peak times were tested. [cADPR] peaked 20 hours after induction, the activity of the ADPR cyclase enzyme at 16 hours, and peak ADPRc transcript abundance occurred, in general, at 6 hours. The other class of perturbations assumes a constant and immediate change in cellular processes (δ = constant), and will be referred to as the *step-change* perturbation.

Selection of candidate Locke model parameters

Published cADPR-induced fold-changes in clock gene transcript abundance *(3)* were used to assess the goodness of fit of each pair of parameters under the time-varying profiles of Fig. 3A. The Locke model equations *(2)* were simulated under long day conditions (16 hours light, 8 hours dark), in line with the experimental conditions used by Sánchez *et al. (3).* These simulations were performed both with and without the perturbation imposed, and the fold change in the concentration of mRNA for each component calculated 6 hours after the start of the perturbation. A variety of

perturbation amplitudes were tested in an effort to cover as much of parameter space as possible. The calculated fold changes were then compared with the target values found experimentally through evaluation of a cost function, namely the 2-norm of the error vector *e*.

$$\|e\|_2 = \sqrt{(f_{LHY} - 0.056)^2 + (f_{TOC1} - 1)^2 + (f_Y - 3.732)^2} \quad (2)$$

The target value for *LHY/CCA1*, 0.056, was calculated as the arithmetic mean of the fold changes in *LHY* and *CCA1* transcript abundance. Similarly, the value for *Y* was taken to be the fold change in *GI*. Since *TOC1* was not found to be regulated significantly by cADPR *(3)*, the target value was set as 1. No restriction was imposed on the change in X mRNA. Parameters were retained as candidates if they achieved a cost function score less than 2.

Simulations of the parameter pairs with lowest observed cost are plotted for the exponential perturbations (peaking at 6 hours after induction) in Supplementary Figure 3a. The red traces (perturbed simulation) clearly show suppression of *LHY* along with upregulation of *Y* (*GI*). It is important to note that the time in the diurnal cycle at which the seedlings were treated with β-estradiol is not known, and so simulations were carried out at each integer time (Fig. S5B).

Calculation of phase for unsustained perturbations

To assess the extent to which the phase of oscillation was changed, each perturbation was simulated for 480 hours. The time of the final peak value of *LHY* mRNA, $t_{\max}^{(p)}$, was noted and compared with the unperturbed equivalent, $t_{\max}^{(u)}$. The differences $t_{\max}^{(p)} - t_{\max}^{(u)}$ reflect the phase change and are plotted against the error norm score (Eqn. 2) calculated for parameter perturbation cluster A (induction at ZT0) and B (induction at ZT15) in Fig. 3A. Candidate parameters from the exponential perturbation profile peaking after 6 hours do not alter the phase of oscillation significantly for cluster A (4 hours). However, cluster B perturbations appear to lie in two groups: one of which does not alter phase, and one that does alter phase. The corresponding analyses for the exponential perturbations which peak after 16 and 20 hours are shown in Supporting Fig. S4B.

Calculation of period for sustained (step-change) perturbations

The candidate parameter pairs for the step-change perturbation were analysed through simulation for 480 hours, and the period was calculated as being the difference in time of the final two peak values of *LHY* mRNA. Here the choice of component and of location in the state trajectory is arbitrary, so these choices were made for convenience of computation. The duration of the simulation was chosen to be sufficiently long that any transient behaviour had disappeared at the point of calculation. The period for each candidate parameter pair is plotted against the error norm score (Eqn. 2) for parameter clusters A and B in Fig. 3B. Periods below 15 hours and above 40 hours were deemed non-circadian and removed from these graphs, in addition to the cases where the state trajectory tended to steady state.

This analysis corresponds to simulating continuous activation of transcripts regulated by cADPR, and observing effects on oscillator period under constant light conditions. Continuous suppression of cADPR-regulated transcripts was simulated by negating each parameter perturbation about the nominal values ($\hat{p}=p-\delta$). Oscillator period was calculated using the same method as before for parameter clusters A and B and is plotted against the error norm score in Fig. 3C.

References for Supporting Online Material

1. R. M. Graeff *et al*. *J. Biol. Chem.* **269**, 30260-30267 (1994).

2. J. C. Locke *et al*. *Mol. Syst. Biol.* Epub 2005 Jun 28 (2005).

3. J. P. Sánchez, P. Duque, N. H. Chua. J. P. Sánchez, P. Duque, N. H. Chua. *Plant J.* **38**, 381-395 (2004).

4. J. Love, A. N. Dodd, A. A. R. Webb. *Plant Cell* **16**, 956-966 (2004).

5. A. N. Dodd *et al. Plant J.* **48**, 962-973 (2006).

6. Y. Jiao *et al. Plant Physiol.* **133,** 1480-1493 (2003).

7. H. Goda *et al. Plant Physiol.* **134**, 1555-1573 (2004).

8. J. L. Nemhauser, T. C. Mockler, J. Chory PLoS Biol 2: e258. doi:10.1371/journal.pbio.0020258 (2004).

9. F. J. M. Maathuis. *Plant J*. **45**, 700-711 (2006).

10. J. T. Vogel *et al*. *Plant J*. **41**, 195-211 (2005).

11. D. Zelder *et al. Proc. Natl. Acad. Sci. USA*. **101**, 15811-15816 (2004).

12. R. Moscatiello, P. Marianai, D. Sanders, F.J.M. Maathius. *J. Exp. Bot.* **57,** 2846-2865 (2006).

13. J. M. Tepperman, T. Zhu, H. S. Chang, X. Wang, P. H. Quail. *Proc. Natl. Acad. Sci. USA* **98**, 9437-9442 (2001).

14. M Parani *et al. Plant Biotech. J.* **2**, 359-366 (2004).

15. M. R. McAinsh, A. A. R. Webb, Taylor, J. E., A. M. Hetherington. *Plant Cell* **7**, 1207-1219 (1995).

16. A. Haley *et al. Proc. Natl. Acad. Sci. USA* **92**, 4124-4128 (1995).

17. A. A. Véry, J. M. Davies. *Proc. Natl. Acad. Sci. USA* **97**, 9801-9806 (2000).

18. J. K. Sethi, R. M. Empson, A. Galione. *Biochem. J.* **319**, 613-617 (1996).

19. I. Staxén *et al. Proc Natl. Acad. Sci. USA* **96**, 1779-1784.

20. L. R. Baugh, A. A. Hill, E. L. Brown, C. P. Hunter. *Nucleic Acids Res.* **29**, E29 (2001).

21. P. A. C. 't Hoen, F. de Kort, G. J. B. van Ommen, J. T. den Dunnen. *Nucleic Acids Res.* **31,** E20 (2003).

22. S. L. Harmer *et al. Science* **290**, 2110-2113 (2000).

23. M. Straume. *Meth. Enzymol.* **383**, 149-166 (2004).

24. M. E. Hudson, P. H. Quail, P.H. *Plant Physiol.* **133**, 1605-1616 (2003).

25. R. M. Graeff, H. C. Lee. *Biochem. J.* **361**, 379-384 (2002).

26. J. D. Plautz *et al*. *J. Biol. Rhythms* **12**, 204-217 (1997).

27. M. J. Dowson-Day, A. J. Millar. *Plant J.* **17**, 63-71 (1999).